A few experiments using cold atoms: dipolar quantum gases, guided atom optics, and quantum engineering with single Rydberg atoms

Thierry Lahaye

Université Paris 11 **Institut d'Optique Graduate School**

Mémoire d'habilitation à diriger des recherches

présenté par

Thierry Lahaye

A few experiments using cold atoms: dipolar quantum gases, guided atom optics, and quantum engineering with single Rydberg atoms

Soutenue le 11 mai 2015
devant le jury composé de :

M.	**C. Fabre**	Président du jury
M.	**O. Gorceix**	Rapporteur
M.	**P. Pillet**	Rapporteur
M.	**J. Vigué**	Rapporteur
M.	**A. Browaeys**	Examinateur
M.	**J. Dalibard**	Examinateur
M.	**T. Pfau**	Examinateur

Acknowlegements

Writing a *Mémoire d'habilitation à diriger des recherches* is an interesting exercise in itself, allowing one to look back at the past and try to discern the logic at work in the first part of a research career. However, one of its main interests probably lies in the fact that it is above all an ideal way to realize the importance of human relationships in research —as probably in any human endeavor. I have been lucky, at all the stages of my research career, to interact with many outstanding individuals, who all have had a major impact not only on my research, but beyond that, on my conception of science. I am glad that some of them could make it to take part in my jury, or to attend the defense.

Let me start by thanking all the members of the jury for having bothered to read this document in details, and asked many interesting questions. I now want to thank more specifically people with whom I have worked more or less closely during the last 15 years, and for that I will somehow follow the chronological order —maybe that's a way to minimize the risk of forgetting someone!

I had my first real contact with research after my first year at ÉNS, when I spent one month as an intern in Jacques Vigué's group, working on the early version of his atom interferometer and, more importantly, sharing his office. I could not have dreamed of a better mentor in atomic physics. When I joined the LCAR many years later, Jacques was the director of the lab, and I greatly benefited from his help and advice at a time when not-so-easy decisions had to be made. I want to thank him for that, and I only regret we could not have more discussions about physics.

After my internship in John Doyle's group at Harvard during my master, I was convinced to continue working in atomic physics. Joining the cold atom group at Labortoire Kastler–Brossel of ÉNS for my PhD was thus an obvious choice. There, I had the opportunity to benefit from two supervisors, Jean Dalibard and David Guéry-Odelin.

There is no way to emphasize enough the qualities that make Jean an ideal supervisor: not only he is the brilliant physicist and excellent teacher that everybody knows, but, and maybe even more importantly, he also knows how to listen, guide, encourage a young student and allow him to gain confidence and become a scientist. I thank him for his numerous pieces of advice that were crucial, at several stages of my career. Through a day-to-day close supervision, David taught me during my PhD the basics of experimental cold atoms physics, and countless interesting theoretical curiosities. I also want to thank the various post-docs and PhD students on the experiment: Christian Roos, Johnny Vogels, Gaël

Reinaudi, Zhaoying Wang, Antoine Couvert... They all had very different personalities, and contributed to making my PhD time a very enjoyable experience. Beyond the team, I want to thank all the members of the cold atom group. Attending the weekly group meeting, led by Claude Cohen-Tannoudji, Christophe Salomon, Jean Dalibard, Yvan Castin, Michèle Leduc, was the best AMO physics school one could dream of. Finally, I benefited from the help of the technical services, and in particular I want to thank Jean-François Point and Didier Courtiade.

After my PhD, I moved on to Stuttgart for a post-doc in Tilman Pfau's group. These two and a half years were very productive, and played a major role in my maturation as a scientist. Tilman's enthusiasm for physics, allied with an impressive ability to follow very closely all the progress in the lab, despite the size of the group, made my time in his institute very enjoyable. I also want to thank him warmly for his understanding when I had to spend a few weeks back in France with my wife and my new-born son. Not every 'boss' would have had his attitude! In Stuttgart I also had the chance to interact with a wonderful team: Marco Fattori, Tobias Koch, Bernd Fröhlich, Jonas Metz, and Axel Griesmaier. It was a pleasure to tame the Chromium BEC machine with them. I also enjoyed a lot the interactions with the other members of the institute, and in particular with Robert Löw, as well as with our theory colleagues Luis Santos and Hans-Peter Büchler. Many thanks also to Karin Otter for having fought the central administration of the university for me.

I joined the LCAR in Toulouse in 2008. There, I worked very closely with Renaud Mathevet. I have learned at lot from him, not only about all kinds of very valuable technical skills, but also a lot of physics, especially in optics, electronics, thermodynamics. I admire his vast culture, his energy for hard work, and his taste for always trying to explain physics in the simplest (but rigorous) way. Working with him in the lab was a pleasure, and our work on the replication of Fizeau's æther-drag experiment will remain a highlight of my time at LCAR. The cold atom team on the experiment was composed of Gianluca Gattobigio, Pierrick Cheiney, Charlotte Fabre: with them we shared all the hard times one encounters when building an experiment, but also the rewards when the setup was running. I also thank François Vermersch who, supervised by David, did a lot of numerics to simulate our experiments. I also had the chance to interact with many other members of the lab: Jacques, of course, but also Jean-Marc L'Hermite, Pierre Labastie... Special thanks to Béatrice Chatel for having organized a lot of outreach activities for the general public, in which I took part and which I enjoyed a lot. Among the staff of the technical services, I want to thank warmly Gilles Bailly and Stéphane Faure for all they have taught me.

My final move was to Palaiseau, where I arrived at the beginning of 2012. This was made possible by several people whom I want to thank here: Jacques Vigué, Jean-Marc L'Hermite, Christian Chardonnet, Pascale Roubin, and Bertrand Girard. Working with Antoine Browaeys is a great privilege. His deep culture allied with strong modesty makes any scientific interaction with him a real pleasure. I appreciate a lot his way of managing his team, in a way that makes everybody feel that his work is important for collective

achievements. When I joined the group, the Rydberg team was composed of Lucas Béguin and Aline Vernier. I consider myself very lucky to have had such a 'dream team' to start working on single atoms. When both of them were about to leave the group, we had the pleasure to welcome, almost at the same time, the current members of another dream team: Sylvain Ravets, Henning Labuhn, and Daniel Barredo. Working for three years with all those five extremely talented students and post-docs, moreover in a very friendly atmosphere, was extremely enjoyable, and led to many results. We also benefited from a lot of help by Florence Nogrette, who spent a long time developing the SLM system and then, when it became fun, had to let us play with it on the setup. Mondher Besbes helped us a lot for the finite-element modeling of our electrodes, and I thank him for all the time he has spent on that. Charles Adams spent a one-month sabbatical stay in our team in 2014 and it was extremely enriching to interact with him. I also want to thank Yvan Sortais, not only for being the group's reference on optics, but also for many enjoyable discussions about physics. Thanks also to Ronan Bourgain, Joseph Pellegrino, and Stephan Jennewein for interesting interactions. Finally, let me thank all the technical and administrative services for their efficiency and kindness, with special thanks to Christian Beurthe and André Guilbaud.

Finally, I want to express my gratitude to people that, while being outside of the field of research itself, made it possible for me to undertake and/or pursue my passion for research. I had the chance to have several outstanding teachers, who contributed to my interest in science, and knowledge in general. Among them, Henri Lluel stood out, and I had the great pleasure to show him our lab in Toulouse a few years ago. My parents have no connections with science, but I know how much all they taught me as a kid turned out to be essential. Last but not least, I want to thank to my wife Irina and my son Maxime for reminding me constantly that there is life also outside of the lab.

Contents

Introduction

This *Mémoire d'habilitation à diriger des recherches* summarizes the research activities that I have pursued over the last nine years, from my postdoc (included), to the present day.

After my PhD at Laboratoire Kastler–Brossel of ENS Paris, under the joint supervision of David Guéry-Odelin and Jean Dalibard, and entitled *Evaporative cooling of a magnetically guided atomic beam*, I joined in 2006 Tilman Pfau's group, at Stuttgart University, to work on dipolar quantum gases. More precisely, a Bose–Einstein condensate of chromium had been obtained in the group about one year before. Chromium has, in its ground state, a strong magnetic dipole moment of $6\mu_{\mathrm{B}}$, where μ_{B} is the Bohr magneton, and thus, in addition to the short-range, isotropic contact interaction usually at work in BECs, the long-range, anisotropic dipole-dipole interaction influences significantly the properties of chromium BECs. However these dipolar effects remained a small perturbation as compared to the contact interactions. The group had also demonstrated that several (relatively narrow) Feshbach resonances exist in the collisions of ^{52}Cr atoms. This led to the possibility to use controlled magnetic fields in order to enhance the relative effects of the dipolar interactions, by tuning the contact interaction to zero close to a Feshbach resonance, and thus realize a purely dipolar quantum gas. This is exactly what the team achieved during my post-doc, during which we thus studied the properties of purely dipolar quantum gases, in particular their geometry-dependent stability and their collapse dynamics when they are unstable.

In October 2008, I joined, as a CNRS researcher, the newly-founded cold atom group of David Guéry-Odelin, at Laboratoire Collisions, Agrégats, Réactivité, in Toulouse. The first months where devoted to preparing the new lab space, and then to moving, from LKB to Toulouse, David's experimental setup, which was a modified version of the one developed during my PhD thesis, but now used for the all-optical generation of BECs of ^{87}Rb. We then rebuilt from scratch this setup in Toulouse, with some substantial changes. In the course of this rather technical work, a highlight was the development, led by Renaud Mathevet, then an assistant professor in the group, of a Zeeman slower using a transverse magnetic field created by permanent magnets in a Halbach configuration. Once the BEC apparatus was again operational, we chose to perform *guided atom optics* experiments: by outcoupling a BEC in a horizontal, single-beam dipole trap acting as waveguide, one gets a matterwave analogue of a pulsed laser, propagating in a "fiber" made of light. In

particular, we studied in details the reflection of such a matterwave on an attractive, one-dimensional optical lattice, the equivalent of the fiber Bragg gratings widely used in guided photonics. After a few years in Toulouse, I decided to reorient my research activity and move to Laboratoire Charles Fabry of Institut d'Optique.

I thus joined Antoine Browaeys' team in Palaiseau, in January 2012, to take the responsibility of a setup still under construction, and funded by the ERC starting grant that Antoine had just obtained. The long-term goal is to use the Rydberg blockade to engineer interesting quantum states of a system of single atoms held in arrays of optical microtraps, or tweezers, with arbitrary geometries. Since then, we have moved forward towards this goal, by demonstrating single-atom loading in such arrays containing tens of tweezers, and by studying in great details the interactions between small numbers (two and three) of single Rydberg atoms.

This manuscript is organized as follows. Chapter 1 deals with the main results on dipolar quantum gases; chapter 2 is devoted to the work performed in Toulouse; and chapter 3 reports on the experiments on single Rydberg atoms done in Palaiseau. In these chapters, I have tried to avoid repeating the details that one can readily find in the published papers (the main ones being reproduced in the text for convenience). I chose to (i) give a broad introduction to the field, suitable for non-specialists, (ii) provide sometimes information about some technical tricks that were important for the experiments, but were too technical for being discussed in published papers, and (iii) when applicable, try to look, after a few years, at the possible impact of the results obtained. Chapter 3 on the Rydberg experiments is obviously the most developed one, as it deals with my current research interests. A final chapter, *passage obligé* of a HDR, summarizes administrative data about my research career. I have decided to add an appendix about a part of my work which, despite being small at the quantitative level, is important —and enjoyable— for me, namely outreach activities.

Chapter 1

Dipolar quantum gases

... Bien sûr, ce n'est pas la Seine
Ce n'est pas le Bois de Vincennes
Mais c'est bien joli tout de même,
À Vaihingen, à Vaihingen... [1]

1.1 Introduction

The realization of Bose–Einstein condensates (BECs) of dilute atomic vapors in 1995, quickly followed by that of degenerate Fermi gases, has triggered a huge amount of theoretical and experimental studies of the properties of quantum gases over the last twenty years [100]. Despite the fact that such gases are extremely dilute, with densities n rarely exceeding $n \sim 10^{14}\,\mathrm{cm}^{-3}$, most of their striking properties, such as superfluidity for instance, are governed by binary interactions between the constituent atoms.

For the vast majority of atomic species, the actual interatomic potential between two atoms can be replaced, at ultracold temperatures, by a contact pseudo-potential proportional to the *scattering length* a characterizing the two-body scattering problem. For instance, the mean-field description of the time-dependent behaviour of a BEC with a macroscopic wavefunction ψ relies on the Gross-Pitaevskii equation

$$i\hbar\frac{\partial\psi}{\partial t} = -\frac{\hbar^2}{2m}\triangle\psi + V(\boldsymbol{r})\psi + g|\psi|^2\psi, \tag{1.1}$$

where $V(\boldsymbol{r})$ is the external trapping potential, and

$$g = \frac{4\pi\hbar^2 a}{m} \tag{1.2}$$

the interaction strength, proportional to the scattering length a. Here, and in all this chapter, we chose to normalize the macroscopic wavefunction ψ to the number N of particles in the condensate:

$$\int |\psi|^2\,\mathrm{d}\boldsymbol{r} = N. \tag{1.3}$$

[1] Slightly adapted from Barbara, *Göttingen* (1964). For the reader not familiar with the geography of Stuttgart, let me mention that Vaihingen is the district of Stuttgart were the University campus is located.

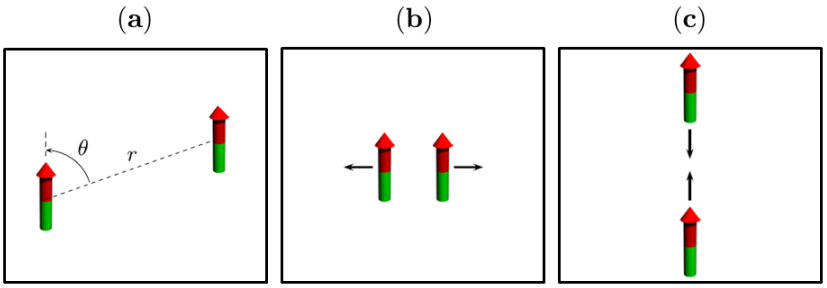

Figure 1.1: (a): Two interacting magnetic dipoles. (b) Side-by-side dipoles repel each other, while head-to-tail ones attract each other (c).

More recently, ultracold atoms have been used to study strongly correlated systems, that cannot be described in a mean-field approach: for instance bosons in optical lattices realize the Bose-Hubbard hamiltonian giving rise to the Mott transition, or fermions with interactions that can be tuned via Feshbach resonances allow the study of the BEC–BCS cross over [16]. However, in all those cases, the underlying interaction is still a short-range, isotropic contact interaction. The typical order of magnitude of the scattering length for an atom like ^{87}Rb is $a \sim 100a_0$, where a_0 is the Bohr radius. For the typical densities of quantum gases, the magnitude of the mean-field interaction gn is then on the order of 10 kHz.

In principle, for paramagnetic atoms, another type of interaction plays a role: the magnetic dipole-dipole interaction (DDI) between the magnetic moments of the particles. For two atoms with parallel magnetic moments $\boldsymbol{\mu}$ separated by $\boldsymbol{r}$, the magnetic DDI takes the familiar form

$$U_{\mathrm{dd}} = \frac{\mu_0 \mu^2}{4\pi} \frac{1 - 3\cos^2\theta}{r^3}, \tag{1.4}$$

where θ is the angle between the direction of the dipoles and the interatomic axis (Fig. 1.1a). The DDI is *long-range* as it decays as $1/r^3$, and *anisotropic*: two dipoles side by side repel each other, while two dipoles in a head-to-tail configuration attract each other (Fig. 1.1b and c). Due to these properties opposite to the ones of the contact interaction, quantum gases in which dipolar interactions play an important or even dominant role acquire unique features, and several pioneering articles in the early 2000's studied the physics of dipolar BECs, which are governed by the non-local generalization of the Gross-Piteavskii equation (1.1):

$$i\hbar\frac{\partial\psi}{\partial t} = \left[-\frac{\hbar^2}{2m}\triangle + V(\boldsymbol{r}) + g|\psi|^2 + \int U_{\mathrm{dd}}(\boldsymbol{r}-\boldsymbol{r}')|\psi(\boldsymbol{r}')|^2\,\mathrm{d}\boldsymbol{r}'\right]\psi. \tag{1.5}$$

Early theoretical proposals showed from equation (1.5) that the properties of a dipolar BEC are strikingly different from the ones of a contact-interacting condensate. As a first example, the stability of the condensate was predicted to depend strongly on the trapping geometry: for an oblate (i.e. pancake-shaped) BEC with the dipoles pointing out of the plane, the DDI is essentially repulsive, and the condensate is stable, while for a prolate (i.e. cigar-shaped) BEC with the dipoles aligned along the axis, the attractive

character of the DDI makes the condensate unstable and prone to collapse [43, 114]. Another early prediction about the effects of dipolar interactions is that they qualitatively change the spectrum of the elementary excitations of the system; for instance, a quasi-two-dimensionnal dipolar BEC is predicted to exhibit, instead of the usual Bogoliubov spectrum, a non-monotonous spectrum for the elementary excitations, with a local roton minimum, analog to the one observed in superfluid Helium [113]. For dipolar bosons loaded into optical lattices, a variety of exotic phases, such as supersolids or checkerboard insultors, are predicted to occur [44, 63].

In order for the dipolar effects to play a role, however, a necessary condition is that the DDI is non-negligible as compared to the contact interaction. A convenient way to quantify the strength of the DDI is to define a length scale, the *dipolar length*, by

$$a_{\mathrm{dd}} = \frac{\mu_0 \mu^2 m}{12\pi\hbar^2} \tag{1.6}$$

where the numerical prefactor is chosen in such a way that a *homogeneous* BEC with both contact and dipolar interactions with $a_{\mathrm{dd}} > a$ is unstable due to the attractive character of the DDI. A trapped quantum gas with $a_{\mathrm{dd}} \sim a$ should show marked dipolar effects, and for $a_{\mathrm{dd}} \gg a$ the gas can be considered as purely dipolar. For alkali atoms, with $\mu = \mu_{\mathrm{B}}$ where μ_{B} is the Bohr magneton, the typical value of a_{dd} is very small, around a_0, which means that dipolar effects are negligible.

At the end of 2004, after several years of development of original cooling techniques, a Bose–Einstein condensate of chromium atoms was obtained in Tilman Pfau's group in Stuttgart [122]. In its ground state, ^{52}Cr has a spin $S = 3$ and a magnetic moment of $6\mu_{\mathrm{B}}$. The dipolar effects are thus expected to be ~ 36 times stronger than in the alkali. The ratio

$$\varepsilon_{\mathrm{dd}} \equiv \frac{a_{\mathrm{dd}}}{a} \tag{1.7}$$

reaches $\varepsilon_{\mathrm{dd}} \simeq 0.16$, which means that sizable dipolar effects can be observed in a Cr BEC. Indeed, soon after the realization of the first Cr BEC, the anisotropic character of the DDI was observed in the expansion of a chromium condensate [45]: due to the DDI, the condensate elongates along the orientation of the dipoles, and this magnetostrictive effect persists even during the expansion in free space. This means that the time evolution of the aspect ratio of the condensate depends on the orientation of the dipoles with respect to the eigenaxes of an anisotropic trap (see Fig. 1.3a, in section 1.2 below). However, due to the relatively small value of $\varepsilon_{\mathrm{dd}}$, these dipolar effects remained a small perturbation of the contact-interaction-driven expansion.

When I joined the group in july 2006, our first goal thus was to go beyond perturbative effects by increasing $\varepsilon_{\mathrm{dd}}$. To do that, we used one of the 14 Feshbach resonances previously identified in the group by studying losses in a thermal cloud [130], and tuned the scattering length a close to zero.

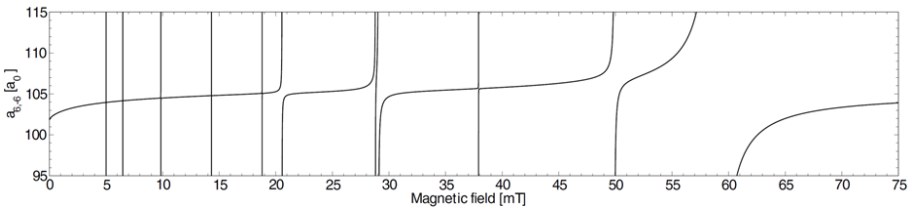

Figure 1.2: Scattering length for two chromium atoms as a function of the applied magnetic field. Figure taken from [130]. Note the limited scale of the y-axis.

1.2 Realizing a purely dipolar quantum gas

Close to a Feshbach resonance, the scattering length depends on the applied field B as

$$a = a_{\mathrm{bg}} \left(1 - \frac{\Delta}{B - B_0}\right), \tag{1.8}$$

where a_{bg} is the background value of the scattering length, B_0 denotes the position of the resonance and Δ its width. By tuning the field close to $B = B_0 + \Delta$, the scattering length almost vanishes, and the gas becomes almost purely dipolar.

Figure 1.2 shows the variation of the scattering length for two Cr atoms in their ground state, as a function of the applied magnetic field. The broadest resonance, or, to be more precise, the least narrow, at a field of $B_0 \simeq 589$ G, had a predicted width $\Delta \simeq 1.7$ G. The requirements in terms of magnetic field stability to tune the scattering length to zero are therefore demanding: to tune a to 1% of its background value requires to control the field with an uncertainty δB better than $\Delta/100$, i.e. $\delta B \sim 17$ mG, at a field of almost 600 G! The needed relative stability of the field is thus at the 10^{-5} level, which requires an active stabilization of the magnetic field. Moreover, the large number of resonances at smaller fields, together with the associated inelastic losses, makes it impractical to first produce a BEC at low fields and then switch on the magnetic field to $B_0 + \Delta$, as this would reduce the atom number and increase the temperature of the cloud.

We thus upgraded the —already quite complex— experimental setup to be able to produce and study a Cr BEC in a high field. The technical details are described in depth in Bernd Fröhlich's *Diplomarbeit* [37] and in Tobias Koch's PhD thesis [61]. In brief, the main steps were the following.

- **Installation of an active control of the magnetic field.** To apply a homogeneous field $B \sim 600$ G, we ran about 400 A in the bias coils of the cloverleaf Ioffe-Pritchard trap (that was used in the BEC sequence for precooling, by RF-induced evaporation, the Cr cloud before the transfer to the dipole trap). In order to achieve the required stability, a low-noise, high-linearity current meter from Dan-Fysik was used to measure the current running through the coils, and a homemade PID controller was used for feedback on the current. The actuator was a pair of water-cooled IGBTs in parallel, used in the linear part of their characteristics. The

large power dissipated in the IGBTs lead to numerous failures during the debugging phase, and for a while, IGBTs almost became consumables! We finally reached a stability in current better than 10^{-5}, after realizing the importance of "tiny" details such as the CMRR of differential amplifiers used in the PID controller, and using Agilent power supplies with less noise than the ones initially installed.

- **Achievement of BEC of Cr above 600 G.** The high magnetic field was turned on, in a few milliseconds, just after the optical pumping step that follows the transfer of the cold Cr cloud from the magnetic trap to the optical dipole trap. At this stage, the density of the trapped sample is still low and the effect of inelastic losses is small. Forced evaporation in the crossed dipole trap is then performed[2]. Initial attempts failed due to the residual field curvature of the bias coils, which provided a very weak radial trapping acting against gravity and preventing the evaporated atoms to leave the trap completely. We thus added a power supply providing a small opposite current through the pinch coils to compensate for the residual curvature.

- **Implementation of high-field imaging of the condensate.** For initial experiments, we decided to image the BEC in high field in order to avoid crossing all resonances with the BEC before imaging. However, due to geometrical constraints, we could not use a σ^+ polarization for imaging, which reduced the absorption cross-section by a factor of two. In later experiments on the dipolar collapse (see section 1.4), we decided to image in low field, as it turned out that with a sufficiently fast switching off (on a timescale of ~ 100 μs), losses were negligible.

Equipped with these tools, we managed to realize what we named a "quantum ferrofluid", i.e. a quantum gas with strong dipolar interactions [69]. This paper is reproduced at the end of the chapter (see page 26).

We first located the resonance, by measuring the scattering length a as a function of the applied magnetic field B when approaching the resonance from above or from below (Fig. 1 of [69] on page 26). In order to extract a, we studied the expansion of the condensate, which is driven by contact and dipolar interactions. In the Thomas–Fermi regime, the density of a contact-interacting BEC varies during free expansion in a self-similar way, keeping the shape of an inverted parabola. The time-dependent Gross–Pitaevskii equation reduces to a set of three ordinary differential equations governing the scaling parameters that give the Thomas–Fermi radii of the BEC [20]. It can be shown that this property still holds in the presence of dipole-dipole interactions [93]. This means that from a measurement of the atom number and of the Thomas–Fermi radii of the BEC after expansion, one can infer in a rather simple way the scattering length a. By varying B around $B_0 = 589$ G, we could vary a over more than one order of magnitude, an in particular reduce it to 15% of the background value. In the vicinity of the resonance, inelastic three-body losses

[2]Having 400 A running in the bias coils for ~ 10 seconds leads to significant thermal effects in the coils, but we could circumvent them by taking them into account in our calibration of the fields.

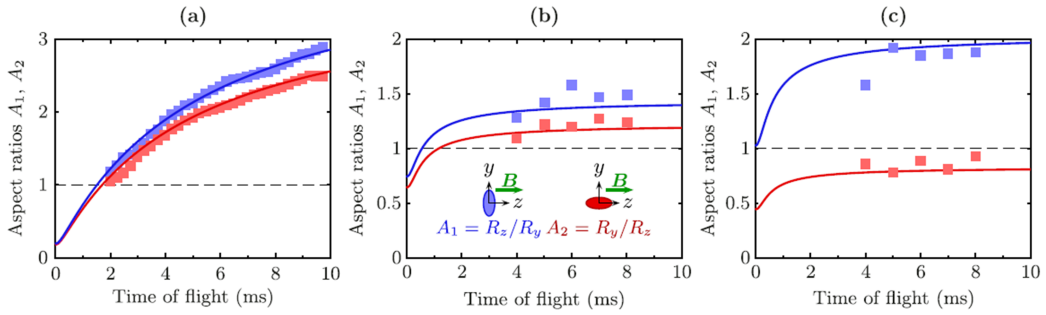

Figure 1.3: Anisotropic expansion of a Cr BEC. The aspect ratio of the cloud is plotted as a function of the time of flight, for two orientations of the dipoles with respect to the trap axes. Solid symbols are experimental data; the solid lines are the prediction of the scaling equations, without any adjustable parameter. (a): Perturbative effects obtained in the pioneering experiment of [45], at low fields, for $\varepsilon_{\rm dd} = 0.16$. (b): In high field, but far from the resonance: the dipolar effects have a size similar to the case (a). (c): Very close to the zero-crossing of the resonance, for $\varepsilon_{\rm dd} \simeq 0.75$, the expansion dynamics depends drastically on the orientation of the dipoles. The inversion of ellipticity during time of flight, the usual "smoking gun" for BEC, can even be inhibited.

get enhanced, but the loss rates remain sufficiently small for the BEC to remain in a quasi-equilibrium state.

We could thus study how the aspect ratio of the condensate evolves when increasing the dipolar parameter all the way to $\varepsilon_{\rm dd} \sim 1$. The anisotropic expansion of the condensate for two orientations of the dipoles with respect to the trap eigenaxes now shows very pronounced effects close to resonance (see Fig. 1.3). In particular, for strong dipolar interactions, the inversion of ellipticity of the BEC during time-of-flight, the usual "smoking gun" for BEC, can be inhibited.

This way of enhancing the relative effects of dipolar interactions by reducing the contact interaction close to a zero-crossing of the scattering length was subsequently used in other groups to observe very weak dipolar effects in alkali condensates : in ^{39}K at LENS [35] and in ^{7}Li at Rice [101]. However, there, the absolute strength of the dipolar interactions is very weak, while in our case of a Cr condensate, dipolar effects can lead to dramatic effects, as we now see.

1.3 Stability of a dipolar quantum gas

Due to the fact that the DDI has a partially attractive character, one expects that a homogeneous purely dipolar condensate is unstable, and collapses. Indeed, a homogeneous condensate with attractive contact interactions, i.e. with a scattering length $a < 0$, is unstable as the frequency of long-wavelength Bogoliubov excitations (phonons) is imaginary[3].

[3]The Bogoliubov speed of sound is given by $c = \sqrt{gn/m}$, where $g = 4\pi\hbar^2 a/m$, and becomes imaginary when $a < 0$.

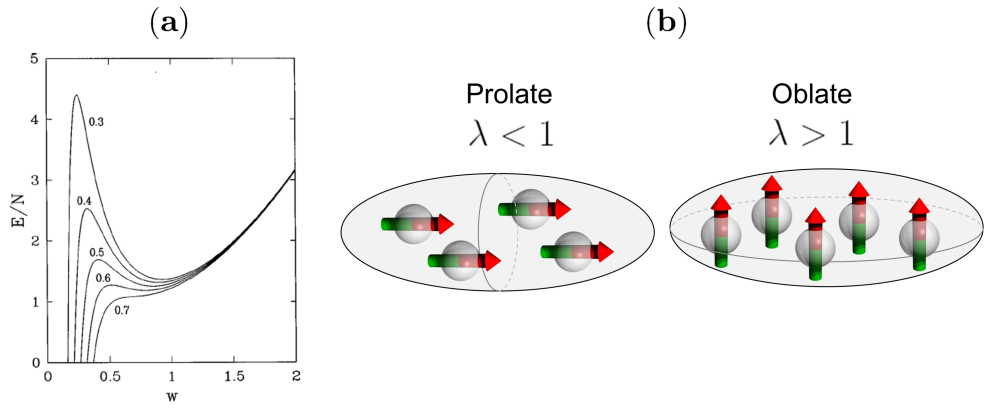

Figure 1.4: (a): Variational approach to the stability of a spherical, contact-interacting BEC. The energy of the condensate, obtained by inserting into the Gross-Pitaevskii energy functional a Gaussian trial wavefunction of size w, is plotted as a function of w for various values of the parameter $N|a|/a_{\mathrm{ho}}$. Beyond a certain value, the local minimum that existed at finite w (corresponding to a metastable condensate) vanishes, indicating that the condensate collapses. (b): Intuitive picture of the geometry-dependent stability of a dipolar BEC: in a prolate (i.e. cigar-shaped, $\lambda \ll 1$) trap with the dipoles oriented along the weak axis of the trap, the attractive part of the DDI destabilzes the condensate, even in the presence of a small, positive scattering length. On the contrary, in an oblate (i.e. pancake-shaped, $\lambda \gg 1$) trap with the dipoles perpendicular to the plane, the dipoles essentially repel each other, and the condensate is stable even for a small negative scattering length.

The presence of a trap can stabilize a BEC with attractive interactions, as long as there are not too many particles: if the number N of atoms in the condensate remains below $ka_{\mathrm{ho}}/|a|$, where a_{ho} is the harmonic oscillator length corresponding of the trap and k a constant of order unity, the kinetic energy due to confinement can be strong enough to prevent collapse, and the condensate is in a metastable state.

A simple way to obtain this threshold is to use a variational approach to find a local minimum of the energy functional that is equivalent to the Gross-Pitaevskii equation (1.1). The energy per particle calculated for a trial Gaussian wavefunction of width wa_{ho} has the form [100]:

$$\frac{E}{N\hbar\omega} = \frac{3}{4}\left(\frac{1}{w^2} + w^2\right) - \frac{1}{\sqrt{2\pi}}\frac{Na}{a_{\mathrm{ho}}}\frac{1}{w^3}, \tag{1.9}$$

where ω is the frequency of the trap (assumed to be isotropic for simplicity). The first term is the kinetic energy, the second one the potential energy in the harmonic trap, and the last one the contribution of the contact interaction (proportional to the atomic density, whence the w^{-3} scaling). Figure 1.4(a) shows $E(w)/(N\hbar\omega)$ for different values of the parameter $N|a|/a_{\mathrm{ho}}$: when this increases beyond ~ 0.67, the local minimum that existed at finite w vanishes, which means that the condensate is unstable. These predictions were observed in pioneering experiments with ^{7}Li in Randy Hulet's group [19], and the critical atom number beyond which the BEC is unstable, on the order of 10^3, was in good agreement with the above estimate.

For a BEC with both contact and dipolar interactions, it is intuitive that the stability

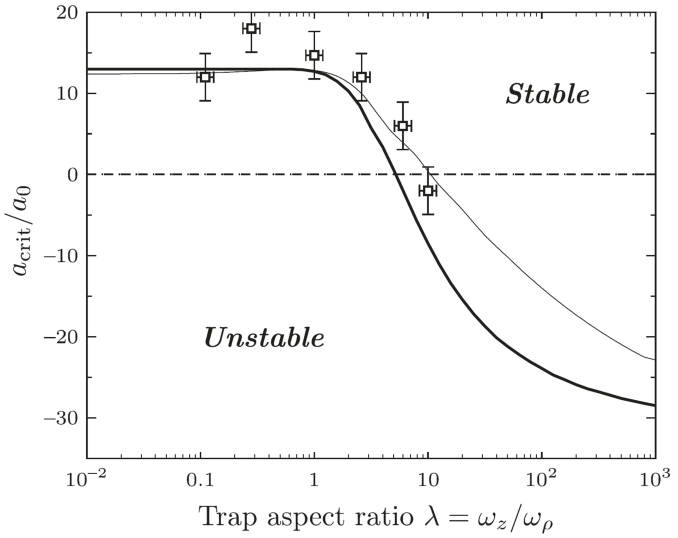

Figure 1.5: Geometry-dependent stability of a dipolar BEC. Critical scattering length $a_{\rm crit}$, in units of the Bohr radius a_0, below which the condensate becomes unstable, as a function of the trap aspect ratio λ. The open squares are the experimental data; the thick solid line is the result of a very simple variational calculation (see text and [62]), and the thin solid line is obtained by a numerical calculation [18].

of the condensate in the presence of confinement depends strongly on the trap geometry, as can be seen on Fig. 1.4(b). Consider a BEC in a trap which is cylindrically symmetric around the z axis, with the dipoles pointing along z. We denote by $\lambda = \omega_z/\omega_\perp$ the ratio of the axial to radial frequencies. In a prolate (i.e. cigar-shaped) trap ($\lambda \ll 1$), the net effect of the dipolar interactions is attractive, one thus expects the instability of the BEC to occur even in the presence of a small, positive scattering length (smaller than $a_{\rm dd}$, as we shall see). On the contrary, for an oblate (i.e. pancake-shaped) trap, the dipolar interaction has a repulsive net effect, and the BEC is stable even with a weak (precisely, $|a| < 2a_{\rm dd}$) attractive contact interaction. This geometry-dependent stability is a distinctive feature of the dipolar BEC, and was studied theoretically in the pioneering work of [114], as well as in a number of subsequent papers (see e.g. references 4–7 of [62], reproduced on page 30).

We therefore investigated experimentally this geometry-dependent stability of a dipolar condensate. The basic idea was to load the BEC in a trap of a given geometry, then, using the Feshbach resonance, to decrease the scattering length in about 10 ms to a final value, and see if the BEC was still stable. In order to be able to vary the aspect ratio λ over a wide range, we decided to superimpose, onto the usual crossed optical dipole trap, a large-period, one-dimensional optical lattice obtained by crossing two beams with wavelength $\lambda_{\rm L} = 1064$ nm under a small angle $\theta = 4°$. This combined trap allowed us to vary λ over two orders of mangitude, while keeping the average trapping frequency almost constant.

For a given λ, we measured the number N of atoms in the BEC as a function of the final scattering length a of the ramp, and observed a sharp threshold below which the BEC

disappeared: only a dilute cloud survived. The critical value of the scattering length was extracted by fitting the data to the empirical law $N \propto (a - a_{\rm crit})^{\beta}$. We then studied how $a_{\rm crit}$ depends on the aspect ratio λ. The results are shown as open squares on Fig. 1.5. As expected from the discussion above, we observe that for prolate traps, $a_{\rm crit} \sim a_{\rm dd}$. For an oblate trap with $\lambda \sim 10$, the critical scattering length is slightly negative. We thus could realize the first purely dipolar quantum gas.

To compare our experimental data for the variation of $a_{\rm crit}$ as a function of λ with theory, we performed a variational calculation using an anisotropic Gaussian trial wavefunction in the Gross-Piteavskii energy functional with the non-local dipole-dipole term. The result of this two-parameter variational calculation is shown as a thick solid line on Fig. 1.5. The agreement between the data and this very crude model is quite satisfactory. These results were published in [62], and are reproduced here on page 30. This paper motivated a certain number of theoretical investigations; in particular, numerical solutions of the Gross-Pitaevskii equation, obtained in the group of John Bohn at JILA [18] were in very good agreement with our experimental data (thin line on Fig. 1.5).

1.4 Collapse dynamics of a dipolar quantum gas

When studying the geometry-dependent stability of a dipolar condensate, a natural question arises: what happens when one crosses the stability threshold? For the case of contact-interacting condensates, the collapse dynamics has been studied in pioneering experiments with ^{6}Li and ^{85}Rb at Rice and at JILA [110, 41, 30]. When the condensate parameters are quenched abruptly into an unstable region, the BEC first collapses quickly due to the attractive interactions. The very high densities reached in this phase lead to fast three-body collisions, inducing rapid atom losses, as well as some heating. The small number of remaining condensed atoms, called the remnant, then expand outwards due to the quantum pressure which overwhelms the interactions. This collapse, followed by an explosion of the BEC, has been dubbed a 'Bose-Nova', by analogy with the gravitational collapse of a star giving rise to the explosion of supernovæ.

For the case of a dipolar BEC, at the time we were studying the stability of the BEC, no detailed prediction of what one should expect concerning the collapse dynamics had been published. Intuitively, it was clear that the anisotropy of the DDI should be reflected in the collapse dynamics. We therefore decided to investigate the collapse dynamics of an almost spherically symmetric dipolar BEC [71] by using faster ($\sim$ 1 ms) ramps of magnetic field to bring the scattering length significantly below the critical value $a_{\rm crit}$, and waiting a variable holding time before relaesing the confinement. The observed clouds had low optical densities, of about 10%, due to the fact that the number of remaining atoms was small (on the order of a few 10^3), and we had to improve the signal-to-noise ratio of the absorption images by (i) getting rid of unwanted residual interference fringes[4];

[4] An almost trivial, but particularly efficient way to reduce such fringes, that are due to the interference between the imaging beam and light scattered on dust particles lying on the optical elements of the system,

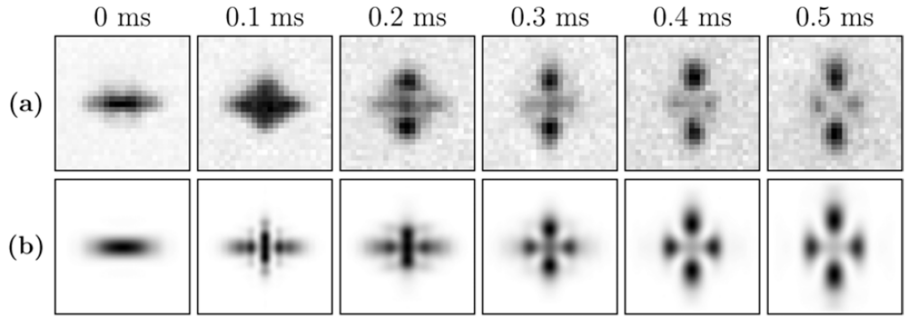

Figure 1.6: Collapse dynamics of a Cr BEC. (a): experimental images; (b): numerical simulation without any adjustable parameter. The dipoles are aligned along the horizontal axis of the figures.

(ii) averaging several images to decrease the effect of photon shot noise (iii) subtracting a broad thermal background.

The top row of Fig. 1.6 shows the observed density distribution after a fixed time of flight, when varying the holding time. The dipoles are oriented along the horizontal axis of the image. One clearly observes an anisotropic collapse, where the cloud, initally elongated along the magnetization direction, evolves at longer times to display a cloverleaf-like pattern reminiscent of the d-wave symmetry of the DDI. At the same time, the number of atoms in the condensate decreases abruptly during the collapse, by a factor ~ 3.

In order to go beyond the mere observation of the collapse, the group of Masahito Ueda in Tokyo collaborated with us to perform a complete numerical simulation of the dynamics, taking as inputs only the experimentally measured parameters. They performed a 3D simulation of the time-dependent, non-local Gross-Piteaevskii equation, where a loss term proportional to $L_3|\psi|^4\psi$ was added to account for three-body losses (L_3 is the measured three-body loss coefficient). Due to the wide variation in the condensate size during the collapse dynamics, an algorithm with an adaptive grid size was needed. When we first compared the simulation results with the experimental data, a systematic shift in the timing, of about 500 μs, was observed. We then realized that this had to do with eddy currents induced in the vacuum chamber by the magnetic field ramp. After we measured the effects of eddy currents by Zeeman spectroscopy on the atom cloud, and included them in the simulation, we finally obtained an excellent agreement between the data and the simulation, without any adjustable parameter, as can be seen on Fig. 1.6. In addition, the time-dependence of the atom number in the BEC during collapse was also well reproduced by the numerics.

The simulation gave insight into phenomena that we could not access experimentally. In particular, it revealed the mechanism of the formation of the d-wave pattern during the collapse: due to the attractive interactions, the cloud initially collapses radially, and becomes a very dense, needle-shaped cloud. Extremely fast three-body losses then occur,

turned out to simply reduce the diameter of the imaging beam impinging on all these elements to about 1 mm. For this, it was enough to use an iris, conjugated with the plane of the atoms.

leaving an almost non-interacting cloud, strongly confined in the radial direction, which thus expands radially due to the quantum pressure. At the same time, axially, the cloud goes on shrinking. This difference in the time scales between the axial and radial dynamics is what explains the formation of the cloverleaf-like density distribution. It also leads to the formation of two vortex rings encircling the axial lobes of the cloud. However, observing these vortex rings experimentally has remained elusive so far.

In a series of subsequent experiments, we then studied the collapse dynamics for various trap aspect ratios, including in the presence of the 1D optical lattice [80], which allowed us to confirm the coherent character of the remnant condensate. Here again, the collapse dynamics, which remains qualitatively similar to the one above, agrees very well with the simulations.

1.5 Dipolar quantum gases in triple-well potentials

During my stay in Stuttgart, we often discussed informally in the group the theory papers predicting exotic phases for dipolar bosons loaded in optical lattices [44]. These phases arise due to the existence of dipolar interactions between the atoms residing on different sites of the lattice. In particular, the possibility to observe supersolids, i.e. phases displaying at the same time off-diagonal and diagonal long-range order, appeared fascinating. Another interesting phase, revealing directly the long-range character of the dipolar interaction, is the checkerboard isolator, where an isolating phase is observed at half filling on a square lattice, with a boson occupying one every second site. Unfortunately, even in a short-period optical lattice, the dipolar interaction between two single chromium atoms in nearest-neighbour sites is only of a few Hertz. This means that to observe these exotic phases, the tunneling rates and the contact interaction must be on the same order of magnitude, or even smaller, implying very low temperatures. Thus, systems of polar molecules seemed to be required to observe these predicted phases. Moreover, theoretical studies indicated that a large number of low-energy, metastable states occurred in such systems, implying that reaching the ground state would prove challenging [79].

We thus started to consider whether a different approach could allow us to study a minimalistic version of those exotic phases using Chromium atoms, and realized that loading a Cr BEC with a mesoscopic number of atoms ($N \sim 10^2$ to 10^3) in a triple-well potential would constitute a toy-model for these phases[5]: the ratio of interactions to tunelling is enhanced by a factor N, and thus starts to be non-negligible for realistic parameters. These informal discussions finally gave birth to a theoretical proposal [72] written in collaboration with Luis Santos from Hannover.

The corresponding setup is shown on Fig. 1.7(a): a dipolar BEC of N atoms, with the dipoles polarized along z, is loaded in a trapping potential consisting of three wells that are close enough, and separated by a low enough barrier, such that tunneling can

[5]For a BEC in a double-well potential, adding dipolar interactions only renormalizes the parameters of the system, but does not lead to new effects.

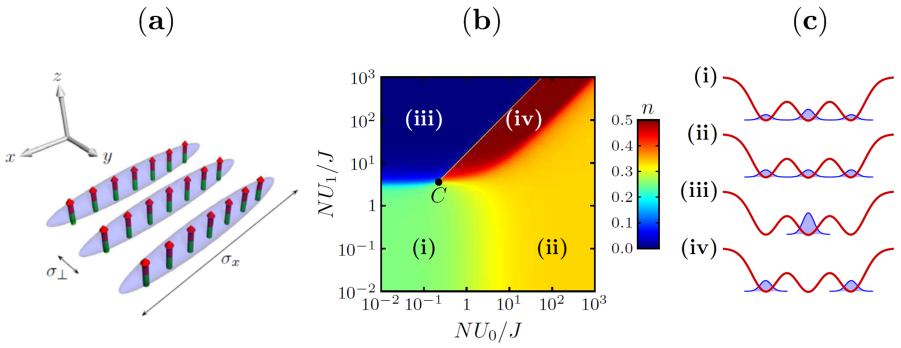

Figure 1.7: (a): Schematic view of the proposed triple-well setup. The three wells are separated by a distance ℓ. (b): The mean-field "phase diagram" of the dipolar BEC in the triple-well potential, as a function of the onsite U_0 and intersite U_1 interactions. (c): Pictorial representation of the various "phases" occurring in (b).

occur between adjacent sites, with a rate J. Due to both contact and dipolar interactions, particles on the same site interact, with a strength U_0. Moreover, due to the long-range character of the DDI, particles in different sites also interact, with a strength U_1 for adjacent sites.

In second quantization, the Hamiltonian of the system reads

$$\hat{H} = -J\left(\hat{a}_1^\dagger \hat{a}_2 + \hat{a}_2^\dagger \hat{a}_3 + \text{h.c}\right) + \frac{U_0}{2}\sum_{i=1}^{3} \hat{n}_i(\hat{n}_i - 1) + U_1\left(\hat{n}_1\hat{n}_2 + \hat{n}_2\hat{n}_3 + \frac{\hat{n}_1\hat{n}_3}{\alpha}\right), \quad (1.10)$$

which is a minimalistic version of the extended Bose-Hubbard hamiltonian. Here, α is a dimensionless number depending on the geometry of the system, and ranging from 4 (for elongated clouds with a size σ_x much larger than the spacing ℓ between traps) to 8 (when the onsite wavefunctions have an extension along x much smaller than the spacing between wells). One obtains (1.10) in the usual way, by using the single-mode approximation which consists in expanding the field operator as $\hat{\psi}(\boldsymbol{r}) = \sum_i \phi_i(\boldsymbol{r})\hat{a}_i$, where $\phi_i(\boldsymbol{r})$ is the "Wannier function" localized on site i, and then inserting this expression in the second-quantized hamiltonian expressed as a function of $\hat{\psi}(\boldsymbol{r})$ and $\hat{\psi}^\dagger(\boldsymbol{r})$. The interaction terms U_0 and U_1 then have simple expressions as a function of the onsite wavefunctions; for instance:

$$U_1 = \int \mathrm{d}\boldsymbol{r}\mathrm{d}\boldsymbol{r}'\, |\phi_1(\boldsymbol{r})|^2 |\phi_2(\boldsymbol{r}')|^2 U_{\text{dd}}(\boldsymbol{r} - \boldsymbol{r}'). \quad (1.11)$$

A first insight can be gained into the physics of a system described by (1.10) using a mean-field approach. It consists in assuming that the N atoms share the same macroscopic wavefunction $\psi = \sqrt{N}\left(\sqrt{n}\phi_1 + \sqrt{1-2n}\phi_2 + \sqrt{n}\phi_3\right)$. The "order parameter" n describing the different "phases" is obtained by minimizing the total energy, as a function of the two interaction parameters NU_0/J and NU_1/J. Figure 1.7(b) shows the resulting "phase diagram", with Fig. 1.7(c) giving a pictorial representation of the corresponding density distributions. Phases (i) and (ii), obtained at small values of the intersite interactions U_1, correspond respectively to non-interacting particles and to a state with reduced density

inhomogeneities due to onsite repulsive interactions. However, when $NU_1 \gg 1$, one observes new phases such as (iii) and (iv), which directly reveal the long-range character of the DDI. For instance, phase (iv) displays in a striking manner the long-range character of the DDI, and can be thought of as minimalistic realization of a supersolid. The fact that the relevant parameter to be compared to the tunneling rate J is NU_1, and not U_1, means that even for weakly interacting dipoles such as Chromium atoms, such effects should be observable when the number of particles is on the order of a few 10^2, in accordance with the initial motivation for our work.

In our paper [72], we studied beyond-mean field effects, and found that for $U_{0,1} > 0$ the qualitative picture obtained in the mean-field approach still holds. We investigated also the possibility to have attractive onsite and intersite interactions, which, not surprisingly, gives rise to new ground states, not captured by a mean-field approach, for instance to the possibility to create "Schrödinger cats", i.e. mesoscopic superpositions of states. However in practice, losses make such states decohere extremely fast and they are unlikely to be observed experimentally, unless one uses a very small number of particles. In the final part of our study, we made numerical estimates to assess the possibility to implement experimentally such triple well systems with typically 10^3 Cr atoms, using tightly-focused, slightly overlapping Gaussian beams. The waists and spacings required to observe sizeable effects of intersite interactions are on the order of ~ 1 μm and $\ell \sim 1.7$ μm, respectively, which is not unrealistic.

In this initial study, we restricted ourselves to the single-mode approximation: the wavefunction ϕ_i on site i is assumed to be independent of the number of atoms on this site. This approximation is valid for the case of very small atom numbers, but for experimentally relevant ranges of parameters, it may break down, which casts some doubts about the possibility to realize experimentally the "phases" predicted above. In [97], the authors thus studied a more refined model, where the effects of the interactions on the onsite wavefucntions were taken into account. The conclusion of this work is that the phases predicted above can probably be observed, but that the range of parameters for which they do exist is significantly reduced as compared to the case where the single-mode approximation is performed. Based on these conclusions, the new setup being built in Stuttgart to work with Dysprosium atoms (see below) was designed in order to be able to study such a triple-well system.

Despite its simplicity, this model is quite rich, as many parameters, such as the trapping geometry, the orientation of the dipoles, and so on, can be varied. Our proposal triggered a significant theoretical activity, aiming at studying in more details the possibilities offered by the setup, and about thirty theory papers about dipolar BECs in triple-well potentials have been published in the last four years.

1.6 Recent achievements in the field of dipolar gases

This final section summarizes briefly recent landmarks in the experimental study of dipolar quantum gases since 2008. This is not meant to be an exhaustive review, and many important experimental and theoretical papers will not be mentioned.

After I left the group, the Cr team in Stuttgart studied the stability [88] and the in-TOF collapse dynamics [13] of a Cr BEC loaded in a 1D lattice where the effect of intersite interactions could be observed experimentally. In a series of impressive experiments in low field, the Villetaneuse group observed the anisotropic character of the DDI in the collective oscillations of the cloud [15] and in sound propagation [14], and made first steps in the study of quantum magnetism by loading a spinor Cr BEC in a 3D optical lattice [29].

Recently, the study of dipolar quantum gases using highly magnetic atoms has been extended to two new species: the rare-earth elements Dysprosium (which has a magnetic moment of $10\mu_B$ in its ground state) and Erbium (with a dipole moment of $7\mu_B$). Both have attractive features, in particular a rich electronic level structure allowing the implementation of new laser cooling schemes, and the existence of bosonic and fermionic isotopes. Bose–Einstein condensates [76] and degenerate Fermi gases (DFG) [75] of Dysprosium have been obtained in Ben Lev's group, and similar results were reported in Erbium ($7\mu_B$) in Francesca Ferlaino's group, with both a BEC [2] and a DFG [1]. These groups have already reported exciting physics, with e.g. the observation of the d-wave collapse in Er [2], or the achievement of Fermi degeneracy by direct evaporation of a polarized sample [1], this being possible due to the long-range character of the DDI, which implies that, unlike for the contact-interaction case, collisions between identical dipolar fermions do not freeze out at zero temperature. As mentioned above, the Stuttgart Cr setup has been rebuilt in view of cooling and trapping Dy, with the goal, among other ones, to explore triple-well physics. Another Dy setup is currently being built at LKB/Collège de France, in the team of Jean Dalibard and Sylvain Nascimbène, with the aim of studying topological superfluids.

Another promising platform to study dipolar quantum gases is to use polar molecules. There, one expects much stronger dipolar effects than in the case of magnetic dipoles, as the interaction strength between two electric dipoles (on the order of one Debye) exceeds that between two atomic magnetic moments (on the order of the Bohr magneton) by a factor $\sim 1/\alpha^2$ where $\alpha \simeq 1/137$ is the fine-structure constant. Moreover, the strength of the dipole-dipole interaction can be varied by tuning the strength of the electric field which orients the molecules in the lab frame. In recent years, samples of ultracold polar fermionic molecules, with densities such that the system is close to quantum degeneracy, have been obtained in Jun Ye's and Debbie Jin's groups at JILA. Starting from an ultracold mixture of fermionic ^{40}K and bosonic ^{87}Rb atoms, they created weakly-bound Feshabch molecules, and then transferred them to their ground state using two Raman lasers phase-locked using a frequency comb. Clear effects of the long-range, anisotropic interaction between the molecules could be observed, e.g. in the rate of inelastic collisions [59]. More recently, loading the molecules in a 3D optical lattice allowed to implement a lattice spin model,

where the DDI yields spin-exchange interaction between the internal degrees of freedom of molecules pinned at the lattice sites [134].

Finally, Rydberg atoms open exciting prospects for the study of quantum many-body systems with dipolar interactions. A first approach is *Rydberg dressing*, which consists in coupling off-resonantly the ground state of the ultracold atoms of interest to a Rydberg state. The dressed atoms then interact via a soft-core, long-range potential, while keeping a long lifetime [102]. Due to the prospects of achieving exotic states of matter, such as supersolids, Rydberg dressing is the subject of active experimental efforts, but remains experimentally challenging so far as one needs to minimize heating [5]. Another approach to study long-range-interacting quantum many-body systems consists in promoting cold, single atoms held in optical tweezers to Rydberg states: the interactions strengths can be very large, on the order of tens of MHz for separations of a few microns, which allow to study coherent dynamics despite the limited lifetime of the Rydberg states, on the order of ~ 100 μs. This subject will be addressed in detail in chapter 3 of this manuscript.

1.7 Published articles

I list below the articles I have co-authored about dipolar quantum gases. The main ones are reproduced in the following pages.

- B. Fröhlich *et al.*, Rev. Sci. Inst. **78**, 043101 (2007);
- T. Lahaye *et al.*, Nature **448**, 672 (2007), reproduced on page 26;
- T. Koch *et al.*, Nat. Phys. **4**, 218 (2008), reproduced on page 30;
- T. Lahaye *et al.*, Phys. Rev. Lett. **101**, 080401 (2008), reproduced on page 35;
- J. Metz *et al.*, New. J. Phys **11**, 055032 (2009);
- T. Lahaye *et al.*, Rep. Prog. Phys. **72**, 126401 (2009). This is a review paper on the physics of dipolar bosonic quantum gases (41 pages, 368 references), written in collaboration with T. Pfau, L. Santos, C. Menotti and M. Lewenstein. It is not reprinted in this manuscript;
- T. Lahaye *et al.*, Phys. Rev. Lett. **104**, 170404 (2010), reproduced on page 39.

nature Vol 448|9 August 2007|doi:10.1038/nature06036

LETTERS

Strong dipolar effects in a quantum ferrofluid

Thierry Lahaye[1], Tobias Koch[1], Bernd Fröhlich[1], Marco Fattori[1], Jonas Metz[1], Axel Griesmaier[1], Stefano Giovanazzi[1] & Tilman Pfau[1]

Symmetry-breaking interactions have a crucial role in many areas of physics, ranging from classical ferrofluids to superfluid ^{3}He and *d*-wave superconductivity. For superfluid quantum gases, a variety of new physical phenomena arising from the symmetry-breaking interaction between electric or magnetic dipoles are expected[1]. Novel quantum phases in optical lattices, such as chequerboard or supersolid phases, are predicted for dipolar bosons[2,3]. Dipolar interactions can also enrich considerably the physics of quantum gases with internal degrees of freedom[4–6]. Arrays of dipolar particles could be used for efficient quantum information processing[7]. Here we report the realization of a chromium Bose–Einstein condensate with strong dipolar interactions. By using a Feshbach resonance, we reduce the usual isotropic contact interaction, such that the anisotropic magnetic dipole–dipole interaction between ^{52}Cr atoms becomes comparable in strength. This induces a change of the aspect ratio of the atom cloud; for strong dipolar interactions, the inversion of ellipticity during expansion (the usual 'smoking gun' evidence for a Bose–Einstein condensate) can be suppressed. These effects are accounted for by taking into account the dipolar interaction in the superfluid hydrodynamic equations governing the dynamics of the gas, in the same way as classical ferrofluids can be described by including dipolar terms in the classical hydrodynamic equations. Our results are a first step in the exploration of the unique properties of quantum ferrofluids.

A quantum ferrofluid is a superfluid quantum gas consisting of polarized dipoles, either electric or magnetic. The first option (using polarized electric dipoles) might be achieved for instance with polar molecules in their vibrational ground state, aligned by an electric field. Progress has been made recently in the slowing and trapping of polar molecules (see ref. 8 and references therein), but the densities and temperatures achieved to date are far away from the quantum-degenerate regime. The use of Feshbach resonances to create polar molecules from two ultracold atomic species[9] is a promising, actively explored alternative[10]; however it is a challenging task to bring those heteronuclear molecules to their vibrational ground state[11]. Alternatively, atomic electric dipoles induced by dc fields[12] or by light[13] could be used. The second option, chosen here, relies on the magnetic dipole–dipole interaction (MDDI) between atoms with a large magnetic moment, such as chromium, for which a Bose–Einstein condensate (BEC) was achieved recently[14]. The relative strength of the MDDI to the contact interaction is conveniently expressed by the dimensionless ratio

$$\varepsilon_{\mathrm{dd}} = \frac{\mu_0 \mu^2 m}{12\pi\hbar^2 a} \qquad (1)$$

where m is the atomic mass, a is the s-wave scattering length, μ_0 is the permeability of a vacuum, $\hbar$ is $h/2\pi$, and μ is the magnetic moment (numerical factors in $\varepsilon_{\mathrm{dd}}$ are such that a homogenous BEC with $\varepsilon_{\mathrm{dd}} > 1$ is unstable against dipolar collapse). Chromium has a large dipole moment, $\mu = 6\mu_{\mathrm{B}}$, and a background scattering length in the fully polarized case of $a \approx 100\, a_0$ (μ_{B} is the Bohr magneton, and a_0 the Bohr radius), yielding[15] $\varepsilon_{\mathrm{dd}} \approx 0.16$. Although this value is typically 36 times larger than in standard alkali quantum gases, the MDDI is still a small perturbation compared to the contact interaction. A perturbative mechanical effect of the MDDI has been demonstrated by analysing the expansion of a chromium BEC from an anisotropic trap for various orientations of the dipoles[16].

The existence of Feshbach resonances[17] allows us to increase $\varepsilon_{\mathrm{dd}}$ and go beyond the perturbative limit. Indeed, close to a resonance, the scattering length varies with the applied magnetic field B as

$$a = a_{\mathrm{bg}}\left(1 - \frac{\Delta}{B - B_0}\right) \qquad (2)$$

where a_{bg} is the background scattering length, B_0 the resonance position, and Δ the resonance width. For B approaching $B_0 + \Delta$, the scattering length tends to zero, thus enhancing $\varepsilon_{\mathrm{dd}}$. This gives the possibility of reaching an MDDI-dominated quantum gas.

We report here the observation of strong dipolar effects in a chromium BEC in the vicinity of the broadest Feshbach resonance at

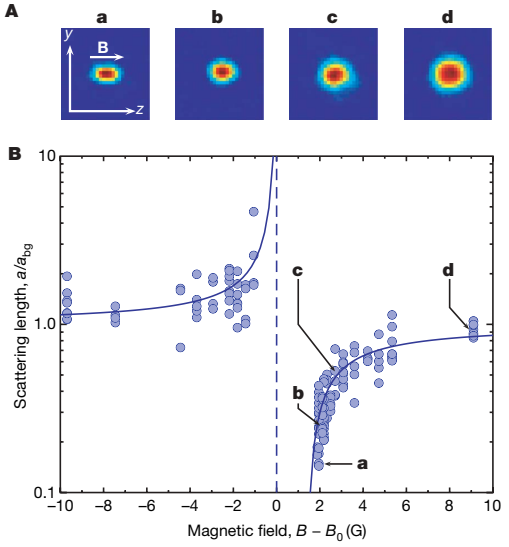

Figure 1 | Tuning the chromium scattering length. A, Absorption images (field of view 260 μm by 260 μm) of the condensate after 5 ms of expansion, for different fields B above resonance ($B - B_0$ is 2, 2.2, 2.7 and 9 G for **a**, **b**, **c** and **d**, respectively). Reducing a slows down the mean-field driven expansion. The change in aspect ratio for small a is a direct signature of strong MDDI. **B**, Variation of a across the resonance, inferred from the mean-field energy released during expansion. The line is a fit to equation (2), yielding $\Delta = 1.4 \pm 0.1$ G.

[1]5. Physikalisches Institut, Universität Stuttgart, Pfaffenwaldring 57, D-70550 Stuttgart, Germany.

$B_0 \approx 589$ G. We measure the dispersive behaviour of the scattering length, and observe that the change in a is accompanied by enhanced inelastic losses. Close to the zero-crossing of a, we observe a large modification of the aspect ratio of the cloud when ε_{dd} increases, which is direct evidence for strong dipolar effects. We finally show that the usual inversion of ellipticity of the condensate during expansion is inhibited for large enough MDDI.

We modified our experimental set-up, which has been described in detail elsewhere[14], in order to be able to produce Cr condensates in high field, close to B_0 (see Methods). Once the condensate is obtained, the magnetic field is ramped close to its final value B in 10 ms, and held there for 2 ms to let it settle down. The trap is then switched off, and the condensate expands freely for 5 ms before being imaged by absorption of resonant light in high field. Figure 1A shows a series of images taken when approaching the resonance from above, and clearly displays a reduction of the cloud size, as well as a change in its aspect ratio.

From the measured optical density profiles, we extract the BEC atom number N, as well as the Thomas–Fermi radii R_z (along the magnetization direction) and R_y (along the vertical axis). Without MDDI, one could easily obtain the scattering length a from these measurements, as the Thomas–Fermi radii after a time of flight would scale as $(Na)^{1/5}$. In our case, we take into account the MDDI using the hydrodynamic formulation of the Gross–Pitaevskii equation, including both contact and dipole–dipole interactions[18] (see Methods for the assumptions underlying our analysis). Figure 1B shows the measured variation of $a(B)$ across the resonance, showing a characteristic dispersive shape[19]. A fit according to equation (2) yields $\Delta = 1.4 \pm 0.1$ G, in good agreement with the prediction $\Delta = 1.7$ G of multi-channel calculations[17]. The position $B_0 \approx 589$ G of the resonance coincides with the one obtained by observing inelastic losses in a thermal cloud[16]. We can tune a by more than one order of magnitude, with a reduction by a factor of five above the resonance.

Close to the resonance, we observe on both sides enhanced inelastic processes resulting in a decay of the condensate. We studied the BEC atom number as a function of the time spent at the final magnetic field B, and fitted the corresponding curves by an exponential decay law (this functional form being chosen for simplicity). The 1/e BEC lifetime obtained in this way is shown in Fig. 2 as a function of B (the initial peak atomic density is 3×10^{14} cm^{-3}). Enhanced inelastic losses close to a Feshbach resonance have been observed with other species, for example, sodium[20]. Here the losses are small enough to allow us to observe the effect of the enhanced relative strength of the MDDI on the equilibrium shape of the condensate.

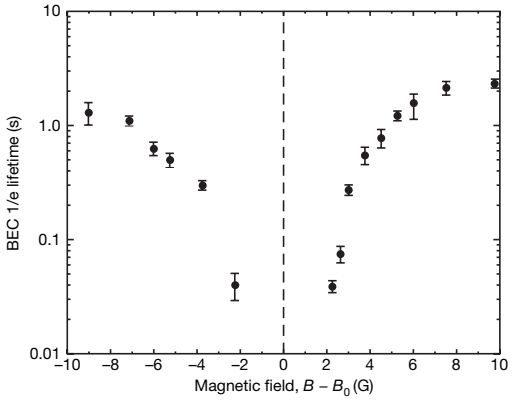

Figure 2 | Inelastic losses close to the resonance. The 1/e lifetime of the condensate is plotted as a function of the magnetic field B. Error bars correspond to one standard deviation; the lifetime was determined by fitting the atom number remaining in the BEC after a variable holding time with an exponential decay law. The losses are small enough to allow for the observation of enhanced dipolar interactions (see Methods).

Figure 3 shows the aspect ratio R_y/R_z of the cloud as a function of the value of ε_{dd} obtained from the measured a, and constitutes the main result of this Letter. The aspect ratio decreases when ε_{dd} increases: the cloud becomes more elongated along the direction of magnetization z, as can be seen unambiguously in Fig. 1A. This is a clear signature of the MDDI, as for pure contact interaction, the aspect ratio is independent of the scattering length (provided the Thomas–Fermi approximation is valid). The solid line in Fig. 3 shows the aspect ratio after time of flight calculated using the hydrodynamic theory including MDDI[18], without any adjustable parameter. The agreement between our data and the theoretical prediction is excellent, given the dispersion of data points and the uncertainty in the theoretical prediction arising from the measurements of trap frequencies. The highest value of ε_{dd} we could reach reliably is about 0.8, corresponding to a fivefold reduction of the scattering length. For our trap geometry, the condensate is expected to become unstable with respect to dipolar collapse[21,22] for values of ε_{dd} slightly above one (the exact value depending on the trap anisotropy, but also on the atomic density).

As an application of the tunability of the dipolar parameter, we study the expansion of the condensate for two orthogonal orientations of the dipoles with respect to the trap, as was done in ref. 16, but now as a function of ε_{dd}. In practice, for the large fields required to approach the Feshbach resonance, we cannot change the magnetic field orientation, which is always along z. We therefore use two different trap configurations, with interchanged y and z frequencies, and identical frequencies along x: trap 1 has frequencies $(\omega_x,\omega_y,\omega_z)/2\pi \approx (660,370,540)$ Hz, while trap 2 has $(\omega_x,\omega_y,\omega_z)/2\pi \approx (660,540,370)$ Hz. We then measure the aspect ratio of the cloud (defined as $A_1 = R_z/R_y$ for trap 1, and $A_2 = R_y/R_z$ for trap 2) as a function of the time of flight, for different values of B (and hence of ε_{dd}). This protocol is equivalent to a mere rotation of the magnetization direction with respect to the trap axes.

Figure 4 presents the results. In order to check that the two trap configurations only differ by an exchange of the y and z frequencies, we first perform the expansion experiment without switching on the

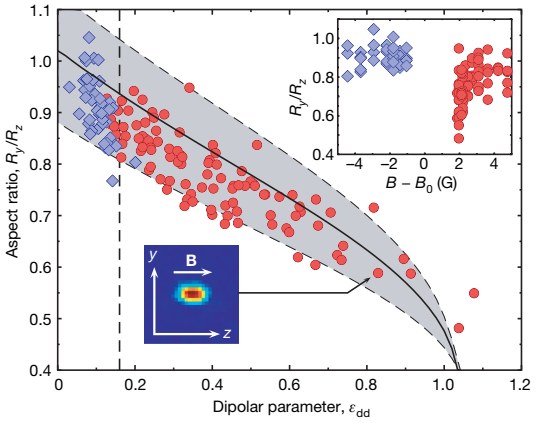

Figure 3 | Increasing the dipolar parameter. Main plot, condensate aspect ratio after 5 ms of expansion plotted against the measured ε_{dd}. Diamonds (circles) correspond to data taken below (above) resonance. The solid line is the prediction of hydrodynamic theory including MDDI, without adjustable parameters (the grey-shaded area corresponds to the uncertainties in the trap frequencies). The dashed line indicates the off-resonant ε_{dd} value. Top right inset, a subset of the same data points plotted against the magnetic field. The condensate elongates appreciably along B only just above resonance, when a approaches zero. Bottom left inset, sample absorption image giving an example of a condensate with strong MDDI.

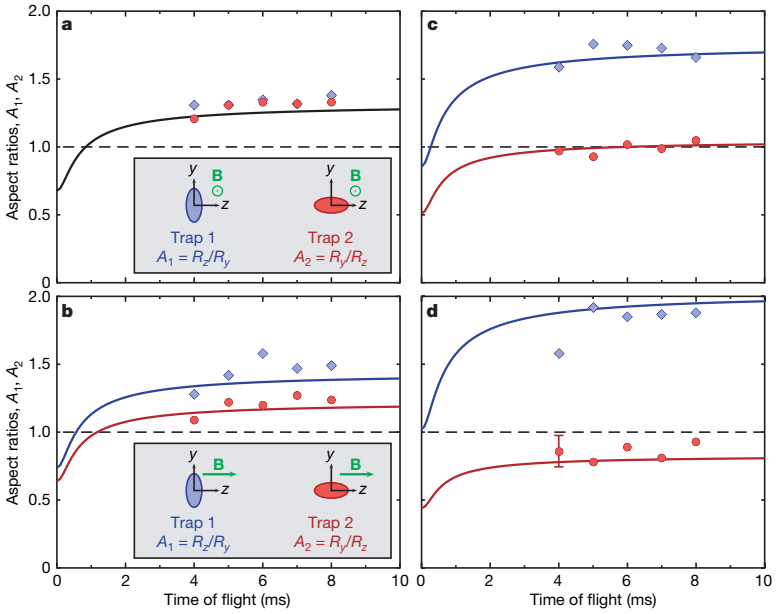

Figure 4 | MDDI-dominated BEC expansion. Aspect ratio of the condensate versus time of flight, for two traps with interchanged y and z frequencies (see text). The solid lines are theoretical predictions without adjustable parameters. The error bar (in **d**) gives the typical dispersion over several runs. **a**, Dipoles perpendicular to the observation plane (see inset sketching the in-trap BEC shape); both configurations yield the same aspect ratio. **b**–**d**, Dipoles along z (see inset in **b**); ε_{dd} takes the values 0.16 (**b**), 0.5 (**c**) and 0.75 (**d**). The MDDI induces larger and larger effects, even inhibiting (**d**) the inversion of ellipticity.

large magnetic field along z, but with a small (11.5 G) field along x (the line of sight of the imaging). The magnetization is therefore perpendicular to the observation plane, and changing the trap configuration does not affect the aspect ratios, as the difference between the two situations is simply a rotation of the trap around the magnetization axis. Figure 4a shows the equality $A_1 = A_2$, confirming the equivalence of the two configurations. We then study the expansion with the large magnetic field B along z. In this case, the MDDI induces a change in the aspect ratios, and $A_1 \neq A_2$. Far from resonance, $\varepsilon_{dd} \approx 0.16$ and we recover the perturbative dipolar effect already observed in ref. 16 (see Fig. 4b). However, for values of B approaching $B_0 + \Delta$, ε_{dd} increases and, correspondingly, the difference between A_1 and A_2 becomes very large (Fig. 4c and d, where ε_{dd} is 0.5 ± 0.1 and 0.75 ± 0.1, respectively). The lines correspond to the prediction of the hydrodynamic theory without adjustable parameters, and show again a very good agreement with the data. The effect of the dipolar interaction is far beyond the perturbative regime, and induces very strong deviations from what one expects for contact interaction. In particular, for $\varepsilon_{dd} \approx 0.75$, the aspect ratio A_2 always remains smaller than unity during the time of flight: the strong anisotropic dipolar interaction inhibits the inversion of ellipticity, the 'smoking gun' evidence for BECs with contact interaction.

In conclusion, the use of a Feshbach resonance to reduce the s-wave scattering length of chromium allowed us to realize a BEC with strong dipolar interaction, and to study the hydrodynamics of this novel quantum ferrofluid. This work opens up many avenues towards the study of dipolar quantum gases beyond the perturbative regime. Structured density profiles are predicted for dipolar condensates in anisotropic traps[23], including biconcave density distributions in pancake-shaped traps[24]. A clear direction for future work is thus to use a one-dimensional optical lattice, creating a stack of pancake-shaped traps. A condensate with dipoles perpendicular to the trap plane is then stable with respect to dipolar collapse, which should allow entry to the regime $\varepsilon_{dd} \gg 1$. In particular, the investigation of the unusual, roton-like excitation spectrum predicted in this system[25] is a fascinating possibility. The creation of Cr_2 molecules by ramping over the Feshbach resonance is another appealing experiment. In a two-dimensional trap, the repulsive interaction between the molecules, due to their large magnetic moment, might stabilize them against inelastic losses. Another possible extension of this work is the study of degenerate fermions with strong dipolar interactions, which may display new types of pairing mechanisms (ref. 1, and references therein). Finally, the behaviour of strongly correlated dipolar quantum gases in three-dimensional optical lattices is an interesting open field, with many connections to fundamental questions in condensed-matter physics—such as the study of supersolid phases, whose experimental observation in helium is still debated (see, for example, ref. 26).

METHODS SUMMARY

We modified our experimental sequence[14] to produce chromium condensates in high field. For this, we switch on quickly (in less than 5 ms) a large field (~600 G) during forced evaporation in the dipole trap. The low atomic density at this stage of evaporation allows for small losses. The current in the coils used to produce the field is actively stabilized; care is taken to ensure a high homogeneity of the field. Evaporation is then resumed until an almost pure condensate of 3×10^4 atoms is obtained. The trap is then adjusted to obtain frequencies $(\omega_x,\omega_y,\omega_z)/2\pi \approx (840,600,580)$ Hz (measured by exciting the centre of mass motion of the cloud, with an accuracy of 5%).

In our data analysis to extract the scattering length a (Fig. 1), we assumed that no external forces act on the atoms during the time of flight, that the condensate stays in equilibrium during the magnetic field ramp, and finally that the hydrodynamic (Thomas–Fermi) approximation is valid even for small a. These assumptions are largely fulfilled for all our parameters.

Full Methods and any associated references are available in the online version of the paper at www.nature.com/nature.

Received 4 May; accepted 15 June 2007.

1. Baranov, M., Dobrek, Ł., Góral, K., Santos, L. & Lewenstein, M. Ultracold dipolar gases — a challenge for experiments and theory. *Phys. Scr.* **T102**, 74–81 (2002).

2. Góral, K., Santos, L. & Lewenstein, M. Quantum phases of dipolar bosons in optical lattices. *Phys. Rev. Lett.* **88,** 170406 (2002).
3. Menotti, C., Trefzger, C. & Lewenstein, M. Metastable states of a gas of dipolar bosons in a 2D optical lattice. *Phys. Rev. Lett.* **98,** 235301 (2007).
4. Kawaguchi, Y., Saito, H. & Ueda, M. Einstein–de Haas effect in dipolar Bose-Einstein condensates. *Phys. Rev. Lett.* **96,** 080405 (2006).
5. Santos, L. & Pfau, T. Spin-3 chromium Bose-Einstein condensates. *Phys. Rev. Lett.* **96,** 190404 (2006).
6. Yi, S. & Pu, H. Spontaneous spin textures in dipolar spinor condensates. *Phys. Rev. Lett.* **97,** 020401 (2006).
7. DeMille, D. Quantum computation with trapped polar molecules. *Phys. Rev. Lett.* **88,** 067901 (2002).
8. Doyle, J., Friedrich, B., Krems, R. V. & Masnou-Seeuws, F. (eds) Special issue on ultracold molecules. *Eur. Phys. J. D* **31,** 149–445 (2004).
9. Köhler, T., Góral, K. & Julienne, P. S. Production of cold molecules via magnetically tunable Feshbach resonances. *Rev. Mod. Phys.* **78,** 1311–1361 (2006).
10. Ospelkaus, C. *et al.* Ultracold heteronuclear molecules in a 3D optical lattice. *Phys. Rev. Lett.* **97,** 120402 (2006).
11. Sage, J., Sainis, S., Bergeman, T. & DeMille, D. Optical production of ultracold polar molecules. *Phys. Rev. Lett.* **94,** 203001 (2005).
12. Marinescu, M. & You, L. Controlling atom-atom interaction at ultralow temperatures by dc electric fields. *Phys. Rev. Lett.* **81,** 4596–4599 (1998).
13. Giovanazzi, S., O'Dell, D. & Kurizki, G. Density modulations of Bose-Einstein condensates via laser-induced interactions. *Phys. Rev. Lett.* **88,** 130402 (2002).
14. Griesmaier, A., Werner, J., Hensler, S., Stuhler, J. & Pfau, T. Bose-Einstein condensation of chromium. *Phys. Rev. Lett.* **94,** 160401 (2005).
15. Griesmaier, A. *et al.* Comparing contact and dipolar interactions in a Bose-Einstein condensate. *Phys. Rev. Lett.* **97,** 250402 (2006).
16. Stuhler, J. *et al.* Observation of dipole-dipole interaction in a degenerate quantum gas. *Phys. Rev. Lett.* **95,** 150406 (2005).
17. Werner, J., Griesmaier, A., Hensler, S., Stuhler, J. & Pfau, T. Observation of Feshbach resonances in an ultracold gas of ^{52}Cr. *Phys. Rev. Lett.* **94,** 183201 (2005).
18. Giovanazzi, S. *et al.* Expansion dynamics of a dipolar Bose-Einstein condensate. *Phys. Rev. A* **74,** 013621 (2006).
19. Inouye, S. *et al.* Observation of Feshbach resonances in a Bose-Einstein condensate. *Nature* **392,** 151–154 (1998).
20. Stenger, J. *et al.* Strongly enhanced inelastic collisions in a Bose-Einstein condensate near Feshbach resonances. *Phys. Rev. Lett.* **82,** 2422–2425 (1999).
21. Santos, L., Shlyapnikov, G. V., Zoller, P. & Lewenstein, M. Bose-Einstein condensation in trapped dipolar gases. *Phys. Rev. Lett.* **85,** 1791–1794 (2000).
22. Góral, K., Rzążewski, K. & Pfau, T. Bose-Einstein condensation with magnetic dipole-dipole forces. *Phys. Rev. A* **61,** 051601(R) (2000).
23. Dutta, O. & Meystre, P. Ground-state structure and stability of dipolar condensates in anisotropic traps. *Phys. Rev. A* **75,** 053604 (2007).
24. Ronen, S., Bortolotti, D. C. E. & Bohn, J. L. Radial and angular rotons in trapped dipolar gases. *Phys. Rev. Lett.* **98,** 030406 (2007).
25. Santos, L., Shlyapnikov, G. V. & Lewenstein, M. Roton-maxon spectrum and stability of trapped dipolar Bose-Einstein condensates. *Phys. Rev. Lett.* **90,** 250403 (2003).
26. Sasaki, S., Ishiguro, R., Caupin, F., Maris, H. J. & Balibar, S. Superfluidity of grain boundaries and supersolid behavior. *Science* **313,** 1098–1100 (2006).

Acknowledgements We thank L. Santos for discussions and J. Stuhler for contributions in the initial phases of the experiment. We acknowledge financial support by the German Science Foundation (SFB/TRR21) and the EU (Marie-Curie fellowship to T.L.).

Author Information Reprints and permissions information is available at www.nature.com/reprints. The authors declare no competing financial interests. Correspondence and requests for materials should be addressed to T.L. (t.lahaye@physik.uni-stuttgart.de) or T.P. (t.pfau@physik.uni-stuttgart.de).

Stabilization of a purely dipolar quantum gas against collapse

T. KOCH, T. LAHAYE, J. METZ, B. FRÖHLICH, A. GRIESMAIER AND T. PFAU*

5. Physikalisches Institut, Universität Stuttgart, Pfaffenwaldring 57, 70550 Stuttgart, Germany

*e-mail: t.pfau@physik.uni-stuttgart.de

Published online: 24 February 2008; doi:10.1038/nphys887

Although the phenomenon of Bose–Einstein condensation[1] is a purely statistical effect that also appears in an ideal gas, the physics of Bose–Einstein condensates (BECs) of dilute gases is considerably enriched by the presence of interactions among the atoms. In usual experiments with BECs, the only relevant interaction is the isotropic and short-range contact interaction, which is described by a single parameter, the scattering length *a*. In contrast, the dipole–dipole interaction between particles possessing an electric or magnetic dipole moment is of long-range character and anisotropic, which gives rise to new phenomena[2,3]. Most prominently, the stability of a dipolar BEC depends not only on the value of the scattering length, *a*, but also strongly on the geometry of the external trapping potential[4–7]. Here, we report on the experimental investigation of the stability of a dipolar BEC of ^{52}Cr as a function of the scattering length and the trap aspect ratio. We find good agreement with a universal stability threshold arising from a simple theoretical model. Using a pancake-shaped trap with the dipoles oriented along the short axis of the trap, we are able to tune the scattering length to zero, stabilizing a purely dipolar quantum gas.

In the case of a homogeneous Bose–Einstein condensate (BEC) with pure contact interaction, the existence of a stable ground state depends on the modulus and sign of the interaction. For repulsive interaction ($a > 0$), the BEC is stable, whereas for attractive interaction ($a < 0$), the BEC is unstable. This instability can be prevented by an external trapping potential. The tendency of the gas to shrink towards the centre of the trap is in that case counteracted by the repulsive quantum pressure arising from the Heisenberg uncertainty relation. Detailed analysis[8] shows that in a harmonic trap with mean frequency $\bar{\omega}$, a condensate is stable as long as the number of atoms N stays below a critical value N_{crit} given by

$$N_{\mathrm{crit}} = \frac{k a_{\mathrm{ho}}}{|a|}, \qquad (1)$$

where $a_{\mathrm{ho}} = \sqrt{\hbar/(m\bar{\omega})}$ is the harmonic oscillator length and k is a constant of the order of $1/2$. This scaling has been experimentally checked in ref. 9 in a BEC of ^{85}Rb. The dynamics of condensates for $N \geq N_{\mathrm{crit}}$ has been the subject of several experiments with condensates of ^{7}Li (refs 10,11) and ^{85}Rb (ref. 12). In refs 13, 14, the collapse of a Bose–Fermi mixture of ^{87}Rb and ^{40}K was investigated. Some aspects of the dynamics such as the soliton train formation in ^{7}Li (ref. 15) and ^{85}Rb (ref. 16) remain the subject of ongoing research.

Being anisotropic and long range, the dipole–dipole interaction (DDI) differs significantly from the contact interaction, which changes the stability conditions in a system with DDI present. Considering a purely dipolar condensate with homogeneous density polarized by an external field, it is found that owing to the anisotropy of the DDI, the BEC is unstable, independent of how small the dipole moment is[17]. As in the pure contact case, a trap helps to stabilize the system. In the dipolar case, however, it is not only the quantum pressure that prevents the collapse but also the anisotropy of the density distribution imprinted by the trap.

Consider a cylindrically symmetric harmonic trap

$$V_{\mathrm{trap}}(r,z) = \frac{1}{2} m\left(\omega_r^2 r^2 + \omega_z^2 z^2\right)$$

with the dipoles oriented along z, and r being the distance from the symmetry axis. As can be intuitively understood from Fig. 1a, in a pancake-shaped trap (aspect ratio $\lambda = \omega_z/\omega_r > 1$), the dipoles predominantly repel each other and the BEC is stable. In contrast, a cigar-shaped trap ($\lambda < 1$, Fig. 1b) leads to mainly attractive forces and hence to a dipolar collapse. Following this simple argument, we expect that in the prolate case a positive scattering length a is needed to stabilize the BEC, whereas in the oblate case, we can even afford a slightly negative a. The dependence of the stability of a dipolar BEC on the trap aspect ratio λ and scattering length a has been extensively studied theoretically[4–7], and is experimentally investigated here.

Our measurements are carried out with a BEC of ^{52}Cr (ref. 18), which is so far the only experimentally accessible quantum gas with observable DDI[19,20]. To compare contact and dipolar interactions, we introduce a length scale characterizing the magnetic DDI

$$a_{\mathrm{dd}} = \frac{\mu_0 \mu^2 m}{12\pi\hbar^2}.$$

The numerical prefactor in a_{dd} is chosen such that a homogeneous condensate becomes unstable to local density perturbations for $a \leq a_{\mathrm{dd}}$ (ref. 21). As chromium has a magnetic dipole moment of $\mu = 6\mu_{\mathrm{B}}$ (μ_{B} is the Bohr magneton), $a_{\mathrm{dd}} \simeq 15 a_0$, where a_0 is the Bohr radius. Far from Feshbach resonances, a takes its background value $a_{\mathrm{bg}} \simeq 100 a_0$ (ref. 22) and the BEC is stable for any λ. To explore the unstable regime, we thus reduce the scattering length a, which in the vicinity of a Feshbach resonance scales as

$$a = a_{\mathrm{bg}}\left(1 - \frac{\Delta B}{B - B_0}\right)$$

with the applied magnetic field B.

To carry out the measurements, we produce a BEC of approximately 25,000 atoms at a magnetic field that is about 10 G above the broadest Feshbach resonance where the scattering length is approximately $85 a_0$ and the BEC is stable. Once the BEC is

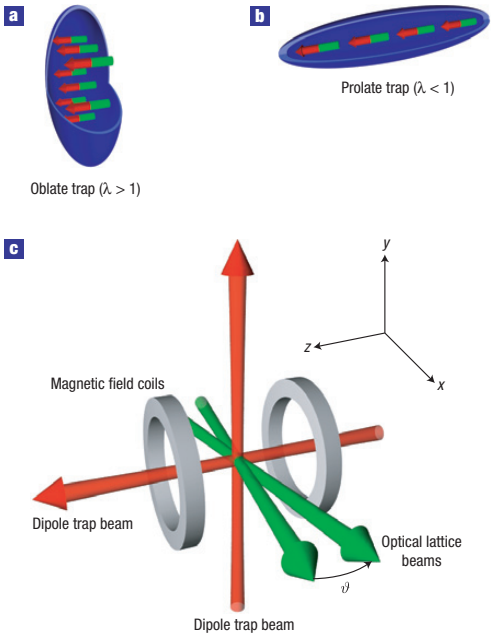

Figure 1 Intuitive picture of the trap geometry dependence of the stability of a dipolar BEC. a,**b**, In an oblate trap (**a**), the dipoles mainly repel each other, whereas in a prolate trap (**b**), the interaction is predominantly attractive. **c**, The different trapping geometries are realized by the crossed optical dipole trap (red) and a further one-dimensional optical lattice (green). The magnetic field is pointing along the symmetry axis *z* of our traps.

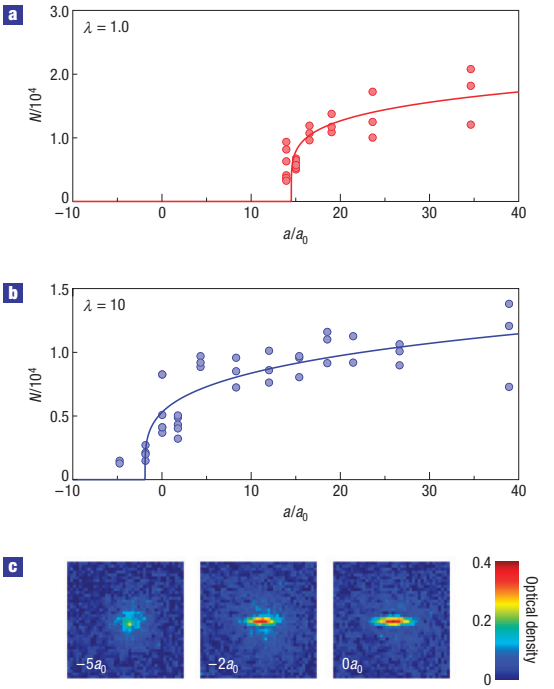

Figure 2 Decrease of the BEC atom number *N* around the critical scattering length a_{crit}. a,**b**, The critical point depends strongly on the aspect ratio λ of the trap. The solid lines are fits to equation (2) used to determine the critical scattering length a_{crit} (see text). **c**, Typical images of the atomic cloud around the critical scattering length for the trap with $\lambda = 10$.

obtained[20,23], we adiabatically shape the trapping potential to the desired aspect ratio λ. To be able to vary λ over a wide range, we generate the trapping potential by a crossed optical dipole trap (ODT) and a superimposed one-dimensional optical lattice along the z direction (see Fig. 1c and Methods section).

We observe two effects when approaching the zero-crossing of the scattering length: the BEC shrinks in both directions owing to the decreasing scattering length and the ellipticity of the cloud changes as a manifestation of the enhanced dipolar effects[20]. Finally, when we decrease the scattering length below some critical value a_{crit}, the BEC atom number (determined from a bimodal fit[24] of the time-of-flight absorption images) abruptly decreases (Fig. 2a,b). The disappearance of the BEC around the instability point is shown in Fig. 2c. Although slightly above a_{crit}, we still see an almost pure BEC, for $a \simeq a_{crit}$ the density shows a bimodal distribution (an anisotropic, dense central peak surrounded by an isotropic gaussian cloud). Just below a_{crit}, the BEC collapses and the density distribution becomes a unimodal, isotropic gaussian. Note that we do not observe the formation of soliton trains as in refs 15,16. This can be attributed to the fact that as our trap is much tighter than in those references, the initial size of our BEC is smaller than any single soliton observed in refs 15,16.

The critical scattering length a_{crit} where the condensate vanishes depends strongly on the trap aspect ratio λ. For an isotropic trap (Fig. 2a), the collapse occurs at $a \simeq 15a_0$, whereas the pancake-shaped trap (Fig. 2b) can even stabilize a purely dipolar BEC ($a \simeq 0$). We repeated this experiment for six different traps (see Table 1), thereby covering a range of two orders of magnitude in the trap aspect ratio λ. To exclude three-body loss processes causing the abrupt decrease in the BEC atom number, we measured the lifetime of the BEC for the different traps just above a_{crit} and found the same lifetime (∼10 ms) for the different scattering lengths.

Table 1 Trap frequencies and aspect ratios of the traps used. The trap frequencies were measured by either exciting the centre-of-mass motion or parametric heating and are accurate to about 10%. Traps 1–3 are provided only by the crossed optical dipole trap, whereas for traps 4–6 the horizontal dipole trap beam and the optical lattice are used.

Trap	$\omega_r/(2\pi)$ (Hz)	$\omega_z/(2\pi)$ (Hz)	$\bar{\omega}/(2\pi)$ (Hz)	$\lambda = \omega_z/\omega_r$
1	1,300	140	620	0.11
2	890	250	580	0.28
3	480*	480	480	1.00
4	530	1,400	730	2.60
5	400	2,400	730	6.00
6	330	3,400	720	10.00

*Trap 3 is not cylindrically symmetric (see the Methods section) and has the trap frequencies $\omega_x = 2\pi \times 610$ Hz and $\omega_y = 2\pi \times 370$ Hz.

By fitting to the observed BEC atom numbers (Fig. 2a,b) the threshold function

$$N = \max\left[0, N_0(a - a_{crit})^{\beta}\right], \qquad (2)$$

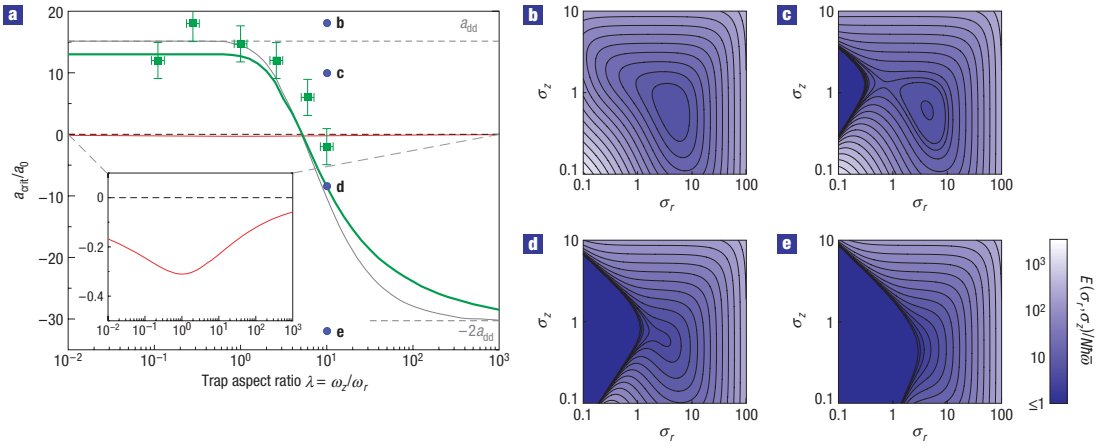

Figure 3 Stability diagram of a dipolar BEC in the a–λ plane. **a**, Experimental (green squares) and theoretical (green line) values of the critical scattering length a_{crit} as a function of the trap aspect ratio. The theory curve is obtained for 20,000 atoms and an average trap frequency $\bar{\omega} = 2\pi \times 700$ Hz (the average values we find for our six traps). The red curve (magnified in the inset) marks the stability threshold for a BEC with pure contact interactions using the same parameters. The asymptotic stability boundary ($Na_{dd}/a_{ho} \gg 1$) which for $\lambda \to 0$ ($\lambda \to \infty$) converges to a_{dd} ($-2a_{dd}$) is plotted in grey. The error bars in λ and a_{crit} result from the uncertainty (estimated one standard deviation) in the trap frequency measurement and the calibration $a(B)$ of the scattering length. **b**–**e**, Behaviour of the energy landscape $E(\sigma_r, \sigma_z)$. Lines of equal energy are plotted for fixed $\lambda = 10$ and four different values of the scattering length a (blue dots in **a**). For $a_{crit} < a < a_{dd}$ (**c**) the collapsed prolate ground state emerges ($\sigma_r \to 0$ at finite σ_z) and the BEC becomes metastable.

where N_0, a_{crit} and β are fitting parameters, we find the critical scattering length a_{crit}. The simple functional form (2) was empirically chosen as it accounts for the fast decreasing BEC atom number at $a \simeq a_{crit}$ and for the slow decrease for $a \gg a_{crit}$. The exponent β describing the steepness of the collapse was found to be $\beta \simeq 0.2$ for all traps. The values of a_{crit} that are plotted in Fig. 3a mark the experimentally obtained stability threshold of a ^{52}Cr BEC in the plane (λ, a). We observe a clear shift towards smaller a as λ increases. For the most oblate trap ($\lambda = 10$), we can reduce the scattering length to zero and hence access the purely dipolar regime experimentally.

To get a more quantitative insight into the collapse threshold $a_{crit}(\lambda)$, we numerically determine the critical scattering length (green curve in Fig. 3a). For this, we use a variational method to minimize the Gross–Pitaevskii energy functional[1]

$$E[\Phi] = \int \left[\frac{\hbar^2}{2m} |\nabla \Phi|^2 + V_{trap} |\Phi|^2 + \frac{2\pi\hbar^2 a}{m} |\Phi|^4 + \frac{1}{2} |\Phi|^2 \int U_{dd}(\mathbf{r}-\mathbf{r}') |\Phi(\mathbf{r}')|^2 d\mathbf{r}' \right] d\mathbf{r}, \quad (3)$$

where

$$U_{dd}(\mathbf{r}) = \frac{\mu_0 \mu^2}{4\pi} \frac{1 - 3\cos^2\theta}{|\mathbf{r}|^3}$$

is the interaction energy of two aligned magnetic dipoles μ, with $\mathbf{r}$ being the relative position of the dipoles and θ the angle between $\mathbf{r}$ and the direction z of polarization.

Similar to the work presented in refs 4–6 and 25, we use a cylindrically symmetric gaussian ansatz to evaluate the energy functional (3) with the radial and axial widths σ_r and σ_z as variational parameters (see the Methods section). To obtain a_{crit}, we lower the scattering length until the energy landscape $E(\sigma_r, \sigma_z)$ does not contain any minimum for finite σ_r and σ_z any more (Fig. 3b–e). Starting with large values $a > a_{dd}$, we find that $E(\sigma_r, \sigma_z)$ supports a global minimum for finite σ_r and σ_z independently of λ and thus the BEC is stable (Fig. 3b). Going below $a \sim a_{dd}$, the absolute ground state is a collapsed infinitely thin cigar-shaped BEC ($\sigma_r \to 0$) and the possible existence of a further local minimum (corresponding to a metastable state) is determined by the trap aspect ratio λ (see Fig. 3c, where $a_{dd} > a > a_{crit}$ and Fig. 3d, where $a = a_{crit}$). Finally, below $a \sim -2a_{dd}$ (Fig. 3e), the local minimum vanishes for any λ and the BEC is always unstable[6,7].

In spite of the simplicity of our model, we find good agreement between experiment and theory (Fig. 3a). We checked that the different atom numbers and mean trap frequencies that we find for the six traps modify the green curve by much less than the error bars.

The behaviour of the critical scattering length a_{crit} as a function of the aspect ratio λ can be understood considering the limit $Na_{dd}/a_{ho} \gg 1$, which is satisfied by our average experimental value of $Na_{dd}/a_{ho} \simeq 23$. Owing to their linear N-scaling, the kinetic energy and the potential energy (equations (5) and (6) in the Methods section) can be neglected and the total energy $E(\sigma_r, \sigma_z)$ is dominated by the interaction term

$$[E_{contact} + E_{DDI}] \propto N^2 \left[\frac{a}{a_{dd}} - f(\kappa) \right].$$

The function f (ref. 25) of the cloud aspect ratio $\kappa = \sigma_r/\sigma_z$ arises from the DDI and is discussed in the Methods section.

In this regime, where the stability is solely governed by the competition between the contact and DDI, the critical scattering length (grey curve in Fig. 3a) is implicitly given by

$$a_{crit}(\lambda) = a_{dd} f(\kappa(\lambda)). \quad (4)$$

The asymptotic behaviour of the theory curve now becomes apparent: an extremely prolate (oblate) trap forces the cloud shape to also be extremely prolate (oblate) and f takes its extremal

value 1 (-2). Hence, we find the asymptotic values $a_{crit} = a_{dd}$ for $\lambda \to 0$ and $a_{crit} = -2a_{dd}$ for $\lambda \to \infty$. Another particular point is $a_{crit} = 0$, marking the aspect ratio λ_c needed to stabilize a purely dipolar BEC. More precisely, as $f(1) = 0$, we search for the trap in which the ground state of a purely dipolar BEC is isotropic. As the DDI tends to elongate the BEC along the z direction and shrink it radially[26], it is clear that the desired trap is oblate. Using our model we obtain the criterion $\lambda > \lambda_c \approx 5.2$ for a purely dipolar BEC to be stable, a result that agrees well with the values found in refs 2,4–7.

The grey curve in Fig. 3a that we obtain by numerically solving equation (4) shows a universal behaviour in the sense that in the large-N limit $a_{crit}(\lambda)$ does not depend anymore on the absolute values of the trap frequencies and N. This fact clearly distinguishes the dipolar collapse from the pure contact case (red curve in Fig. 3a), where the λ-dependence, which is already weak for finite N (ref. 27), completely vanishes in the limit of large N as the stability criterion reads $a_{crit}(\lambda) = 0$ (see equation (1) and red curve in Fig. 3a). Furthermore, the instability threshold obtained here applies for any dipolar system in a harmonic potential, such as, for example, heteronuclear molecules, where the only difference is the specific value of a_{dd}.

In summary, we experimentally mapped the stability diagram of a dipolar BEC. The dependence on scattering length and trap aspect ratio agrees well with a simple model based on the minimization of the energy of a gaussian ansatz. By using a pancake-shaped trap, we were able to enter the regime of purely dipolar quantum gases. Although the lifetime of the purely dipolar BEC is relatively short ($\sim$10 ms), this work opens up the route to new and exciting physics[2]. A clear subject for future studies is the dynamics of the dipolar collapse, which might show anisotropic features. Another remarkable property predicted to appear in a dipolar BEC contained in a pancake-shaped trap is the existence of a roton minimum in its Bogoliubov spectrum[21]. Furthermore, close to the collapse threshold, the existence of structured ground states is predicted[28,29], a precursor for the supersolid phase[30] that is expected to appear in dipolar BECs in three-dimensional optical lattices. Finally, a field that has gained increasing interest in the recent past is the study of unusual vortex lattice patterns in rotating dipolar BECs[31,32].

METHODS

EXPERIMENTAL SET-UP AND PROCEDURE

To be able to vary λ over a wide range, the trapping potential is generated by a crossed ODT[20,23] and a further optical lattice (Fig. 1c). The two lattice beams (wavelength $\lambda_{latt} = 1{,}064$ nm, waist $w_{latt} = 110\,\mu$m, maximum power per beam $P_{latt} = 5$ W) propagate in the x–z plane under a small angle of $\vartheta/2 = 4°$ with respect to the x axis. This configuration creates a standing wave along the z axis with a spacing $d = \lambda_{latt}/[2\sin(\vartheta/2)] = 7.6\,\mu$m. Owing to the large spacing of the lattice and the small size of the BEC (Thomas–Fermi diameter $2R_z^{TF} \simeq 6\,\mu$m), we load at most two sites when ramping up the optical lattice. The resulting change in the atom number (at most dividing by 2) changes the theoretical value of a_{crit} by less than a_0, which is below the size of our experimental error bars. Tunnelling processes are completely negligible on the timescale of our experiments.

By varying the powers in the beams, we are able to provide nearly cylindrically symmetric traps, with aspect ratios λ between $\sim$1/10 and $\sim$10, while keeping the average trap frequency $\bar{\omega} = (\omega_r^2\omega_z)^{1/3}$ approximately constant. More extreme aspect ratios are not used as for extreme oblate (prolate) traps the radial (axial) confinement becomes too weak to hold the atoms against gravity and remaining magnetic field gradients. The properties of the six traps that were used in the experiment are listed in Table 1. The cylindrical symmetry of the oblate traps in the x–y direction is given by the fact that ω_x and ω_y are mainly determined by the horizontal ODT beam, whereas ω_z is given by the lattice and the vertical beam is not used. For prolate traps, ω_x and ω_y are again mainly given by the horizontal ODT beam, whereas the vertical beam determines ω_z and the lattice is not used. For all traps, except trap 3, we find $0.94 < \omega_x/\omega_y < 1.04$. For trap 3, the critical scattering length a_{crit} has been calculated using a gaussian ansatz with the three widths $\sigma_{x,y,z}$ as variational parameters. The obtained value deviates by less than a_0 from the value found with the cylindrically symmetric ansatz.

After the BEC is obtained by forced evaporation in the ODT, the trapping potential is shaped in 25 ms to the desired aspect ratio λ. We then ramp the magnetic field within 10 ms to adjust the value of the scattering length. To tune a accurately, we use the broadest of the resonances in ^{52}Cr (ref. 22), which is located at $B_0 \simeq 589$ G and has a width of $\Delta B \simeq 1.5$ G (ref. 20). The current providing the magnetic field is actively stabilized with a remaining noise of less than 1×10^{-5} r.m.s., which results in a resolution of $\Delta a \sim a_0$ around the zero crossing of the scattering length. After a further holding time of 2 ms, we finally switch off the trap and take an absorption image along the x axis, after a time-of-flight of 5 ms. The BEC atom number N and radii $R_{y,z}$ are obtained by fitting the density profile using a bimodal distribution[23]. The calibration between scattering length and magnetic field is done by solving the hydrodynamic equations for the scattering length a with known N and $R_{y,z}$ (refs 20,26).

CALCULATION OF THE CRITICAL SCATTERING LENGTH

To obtain an estimate of a_{crit}, we calculate the energy $E(\sigma_r, \sigma_z)$ (3) of the cylindrically symmetric gaussian wave function[4–6,25]

$$\Phi(r,z) = \left(\frac{N}{\pi^{3/2}\sigma_r^2\sigma_z a_{ho}^3}\right)^{1/2} \exp\left(-\frac{1}{2a_{ho}^2}\left(\frac{r^2}{\sigma_r^2} + \frac{z^2}{\sigma_z^2}\right)\right)$$

with σ_r and σ_z as variational parameters. Using this ansatz, where $a_{ho} = \sqrt{\hbar/(m\bar{\omega})}$, the contributions to the total energy are[5,6] the zero-point fluctuations

$$\frac{E_{kin}}{\hbar\bar{\omega}} = \frac{N}{4}\left(\frac{2}{\sigma_r^2} + \frac{1}{\sigma_z^2}\right), \tag{5}$$

the potential energy

$$\frac{E_{pot}}{\hbar\bar{\omega}} = \frac{N}{4\lambda^{2/3}}\left(2\sigma_r^2 + \lambda^2\sigma_z^2\right) \tag{6}$$

and the mean-field interaction energy

$$\frac{E_{contact} + E_{DDI}}{\hbar\bar{\omega}} = \frac{N^2 a_{dd}}{\sqrt{2\pi}a_{ho}}\frac{1}{\sigma_r^2\sigma_z}\left(\frac{a}{a_{dd}} - f(\kappa)\right), \tag{7}$$

with

$$f(\kappa) = \frac{1+2\kappa^2}{1-\kappa^2} - \frac{3\kappa^2 \operatorname{artanh}\sqrt{1-\kappa^2}}{(1-\kappa^2)^{3/2}}.$$

The function $f(\kappa)$ is a monotonically decreasing function of the condensate aspect ratio $\kappa = \sigma_r/\sigma_z$ with the asymptotic values $f(0) = 1$ and $f(\infty) = -2$, arising from the non-local term in equation (3) (ref. 25). It vanishes for $\kappa = 1$, implying that for an isotropic density distribution the magnetic DDI does not contribute to the total energy. As the interaction term (7) scales as N^2, it overrules the other terms in the limit $Na_{dd}/a_{ho} \gg 1$.

Received 18 October 2007; accepted 21 January 2008; published 24 February 2008.

References

1. Dalfovo, F., Giorgini, S., Pitaevskii, L. P. & Stringari, S. Theory of Bose–Einstein condensation in trapped gases. *Rev. Mod. Phys.* **71**, 463–512 (1999).
2. Baranov, M., Dobrek, L., Góral, K., Santos, L. & Lewenstein, M. Ultracold dipolar gases—a challenge for experiments and theory. *Phys. Scr. T* **102**, 74–81 (2002).
3. Menotti, C. & Lewenstein, M. Ultra-cold dipolar gases. Preprint at <http://arxiv.org/abs/0711.3406> (2007).
4. Santos, L., Shlyapnikov, G. V., Zoller, P. & Lewenstein, M. Bose–Einstein condensation in trapped dipolar gases. *Phys. Rev. Lett.* **85**, 1791–1794 (2000).
5. Góral, K. & Santos, L. Ground state and elementary excitations of single and binary Bose–Einstein condensates of trapped dipolar gases. *Phys. Rev. A* **66**, 023613 (2002).
6. Yi, S. & You, L. Trapped condensates of atoms with dipole interactions. *Phys. Rev. A* **63**, 053607 (2001).
7. Eberlein, C., Giovanazzi, S. & O'Dell, D. H. J. Exact solution of the Thomas–Fermi equation for a trapped Bose–Einstein condensate with dipole–dipole interactions. *Phys. Rev. A* **71**, 033618 (2005).
8. Ruprecht, P. A., Holland, M. J., Burnett, K. & Edwards, M. Time-dependent solution of the nonlinear Schrödinger equation for Bose-condensed trapped neutral atoms. *Phys. Rev. A* **51**, 4704–4711 (1995).
9. Roberts, J. L. *et al.* Controlled collapse of a Bose–Einstein condensate. *Phys. Rev. Lett.* **86**, 4211–4214 (2001).
10. Sackett, C. A., Gerton, J. M., Welling, M. & Hulet, R. G. Measurements of collective collapse in a Bose–Einstein condensate with attractive interactions. *Phys. Rev. Lett.* **82**, 876–879 (1999).
11. Gerton, J. M., Strekalov, D., Prodan, I. & Hulet, R. G. Direct observation of growth and collapse of a Bose–Einstein condensate with attractive interactions. *Nature* **408**, 692–695 (2000).
12. Donley, E. A. *et al.* Dynamics of collapsing and exploding Bose–Einstein condensates. *Nature* **412**, 295–299 (2001).

13. Modugno, G. *et al.* Collapse of a degenerate Fermi gas. *Science* **297**, 2240–2243 (2002).
14. Ospelkaus, C., Ospelkaus, S., Sengstock, K. & Bongs, K. Interaction-driven dynamics of ^{40}K/^{87}Rb Fermi–Bose gas mixtures in the large particle number limit. *Phys. Rev. Lett.* **96**, 020401 (2006).
15. Strecker, K. E., Partridge, G. B., Truscott, A. G. & Hulet, R. G. Formation and propagation of matter-wave soliton trains. *Nature* **417**, 150–153 (2002).
16. Cornish, S. L., Thompson, S. T. & Wieman, C. E. Formation of bright matter-wave solitons during the collapse of attractive Bose–Einstein condensates. *Phys. Rev. Lett.* **96**, 170401 (2006).
17. Góral, K., Rzążewski, K. & Pfau, T. Bose–Einstein condensation with magnetic dipole–dipole forces. *Phys. Rev. A* **61**, 051601 (2000).
18. Griesmaier, A., Werner, J., Hensler, S., Stuhler, J. & Pfau, T. Bose–Einstein condensation of chromium. *Phys. Rev. Lett.* **94**, 160401 (2005).
19. Stuhler, J. *et al.* Observation of dipole–dipole interaction in a degenerate quantum gas. *Phys. Rev. Lett.* **95**, 150406 (2005).
20. Lahaye, T. *et al.* Strong dipolar effects in a quantum ferrofluid. *Nature* **448**, 672–675 (2007).
21. Santos, L., Shlyapnikov, G. V. & Lewenstein, M. Roton-maxon spectrum and stability of trapped dipolar Bose–Einstein condensates. *Phys. Rev. Lett.* **90**, 250403 (2003).
22. Werner, J. *et al.* Observation of Feshbach resonances in an ultracold gas of ^{52}Cr. *Phys. Rev. Lett.* **94**, 183201 (2005).
23. Griesmaier, A. Generation of a dipolar Bose Einstein condensate. *J. Phys. B* **40**, R91 (2007).
24. Ketterle, W., Durfee, D. S. & Stamper-Kurn, D. M. in *Bose–Einstein Condensation in Atomic Gases* (eds Inguscio, M., Stringari, S. & Wieman, C. E.) 67–176 (Proceedings of the International School of Physics Enrico Fermi, Course CXL, IOS Press, Amsterdam, 1999).
25. Giovanazzi, S., Görlitz, A. & Pfau, T. Ballistic expansion of a dipolar condensate. *J. Opt. B* **5**, 208–211 (2003).
26. Giovanazzi, S. *et al.* Expansion dynamics of a dipolar Bose–Einstein condensate. *Phys. Rev. A* **74**, 013621 (2006).
27. Gammal, A., Frederico, T. & Tomio, L. Critical number of atoms for attractive Bose–Einstein condensates with cylindrically symmetrical traps. *Phys. Rev. A* **64**, 055602 (2001).
28. Ronen, S., Bortolotti, D. C. E. & Bohn, J. L. Radial and angular rotons in trapped dipolar gases. *Phys. Rev. Lett.* **98**, 030406 (2007).
29. Dutta, O. & Meystre, P. Ground-state structure and stability of dipolar condensates in anisotropic traps. *Phys. Rev. A* **75**, 053604 (2007).
30. Góral, K., Santos, L. & Lewenstein, M. Quantum phases of dipolar bosons in optical lattices. *Phys. Rev. Lett.* **88**, 170406 (2002).
31. Cooper, N. R., Rezayi, E. H. & Simon, S. H. Vortex lattices in rotating atomic Bose gases with dipolar interactions. *Phys. Rev. Lett.* **95**, 200402 (2005).
32. Zhang, J. & Zhai, H. Vortex lattices in planar Bose–Einstein condensates with dipolar interactions. *Phys. Rev. Lett.* **95**, 200403 (2005).

Acknowledgements

We would like to thank L. Santos, G. V. Shlyapnikov and H.-P. Büchler for stimulating discussions and M. Fattori for his contributions in earlier stages of the experiment. We acknowledge financial support by the German Science Foundation (SFB/TR 21 and SPP 1116) and the EU (Marie-Curie fellowship contract MEIF-CT-2006-038959 to T.L.).
Correspondence and requests for materials should be addressed to T.P.

Author contributions

T.K., T.L., J.M. and B.F. carried out the experimental work and data analysis, T.K. and T.L. did the calculations on the theoretical model and A.G. and T.P. were responsible for project planning.

d-Wave Collapse and Explosion of a Dipolar Bose-Einstein Condensate

T. Lahaye,[1] J. Metz,[1] B. Fröhlich,[1] T. Koch,[1] M. Meister,[1] A. Griesmaier,[1] T. Pfau,[1] H. Saito,[2] Y. Kawaguchi,[3] and M. Ueda[3,4]

[1]*5. Physikalisches Institut, Universität Stuttgart, Pfaffenwaldring 57, 70550 Stuttgart, Germany*
[2]*Department of Applied Physics and Chemistry, The University of Electro-Communications, Tokyo 182-8585, Japan*
[3]*Department of Physics, University of Tokyo, Tokyo 113-0033, Japan*
[4]*ERATO Macroscopic Quantum Project, JST, Tokyo 113-8656, Japan*

(Received 24 April 2008; published 18 August 2008)

We investigate the collapse dynamics of a dipolar condensate of ^{52}Cr atoms when the *s*-wave scattering length characterizing the contact interaction is reduced below a critical value. A complex dynamics, involving an anisotropic, *d*-wave symmetric explosion of the condensate, is observed. The atom number decreases abruptly during the collapse. We find good agreement between our experimental results and those of a numerical simulation of the three-dimensional Gross-Pitaevskii equation, including contact and dipolar interactions as well as three-body losses. The simulation indicates that the collapse induces the formation of two vortex rings with opposite circulations.

DOI: 10.1103/PhysRevLett.101.080401 PACS numbers: 03.75.Kk, 03.75.Lm

The underlying symmetries of physical systems often determine the nature and dynamics of macroscopic quantum states. For example, the difference between isotropic and *d*-wave pairing of electrons, in conventional and high-T_c superconductors, respectively, leads to fundamentally different properties [1]. Degenerate quantum gases are usually dominated by isotropic (*s*-wave) contact interactions. *Dipolar* quantum gases [i.e., in which the dipole-dipole interaction (DDI) between permanent dipole moments play a significant or even dominant role] are governed by the *d*-wave symmetry of the long-range DDI, which gives rise to novel properties.

Examples of fascinating predictions for polarized dipolar quantum gases range from a roton-maxon spectrum [2] for the elementary excitations of a quasi-two-dimensional dipolar Bose-Einstein condensate (BEC), to the existence of novel quantum phases (such as a ''checkerboard'' insulator, or a supersolid) for dipolar quantum gases in optical lattices [3]. The DDI also modifies the hydrodynamic equations describing the dynamics of a BEC, which has been probed experimentally by studying the expansion of the cloud when released from the trap [4]. Unusual, structured shapes for the BEC have been predicted [5,6]. In the unpolarized case, the DDI dramatically enriches the physics of spinor BECs [7]. Ultracold dipolar fermions also have fascinating properties [8].

A striking example of the new properties of dipolar BECs is given by their stability, which, contrary to the case of contact interaction, depends strongly on the trap geometry. Consider a pancake-shaped trap with the dipole moments of the particles oriented perpendicular to the plane of the trap. The DDI is then essentially repulsive, and the BEC is stable, independently of the atom number. In contrast, a cigar-shaped trap cannot stabilize a purely dipolar BEC. We experimentally studied [9] this geometry-dependent stability of a dipolar quantum gas by using a ^{52}Cr BEC, and mapped out the stability diagram of the condensate as a function of the scattering length a (characterizing the contact interaction) and the trap aspect ratio. In the case of a pure contact interaction, crossing the stability border into the unstable regime $a < 0$ leads to a collapse of the BEC [10–12]. This gives rise to an interesting dynamics involving a fast implosion of the condensate followed by the formation of energetic ''bursts'' of atoms [13], or the formation of soliton trains [14,15].

In this Letter, we investigate experimentally the collapse dynamics of a dipolar ^{52}Cr BEC when the scattering length a is decreased (by means of a Feshbach resonance) below the critical value a_{crit} for stability [9]. We observe a rich dynamics on a time scale shorter than the trap period, with the formation of an expanding structure featuring a *d*-wave symmetry. We study the atom number in the condensate as a function of time, and find an abrupt decrease due to inelastic losses. Finally, we compare our experimental results with a three-dimensional numerical simulation of the Gross-Pitaevskii equation (GPE) including both contact and dipolar interactions, as well as three-body losses. Such a generalized GPE with three-body losses has been demonstrated to explain the main features of ''Bose-nova'' experiments with ^{85}Rb [16]. Here we generalize this model to include the DDI. As shown later, this generalized model accounts very well for the observed *d*-wave collapse.

The experimental setup to produce a ^{52}Cr BEC above the Feshbach resonance located at a magnetic field $B_0 \simeq 589$ G has been described elsewhere [9]. Close to the resonance, the scattering length a varies with the applied magnetic field B as

$$a(B) = a_{\mathrm{bg}}\left(1 - \frac{\Delta}{B - B_0}\right),$$

where $\Delta \simeq 1.5$ G is the resonance width and $a_{\mathrm{bg}} \simeq 100a_0$ the background scattering length (a_0 is the Bohr radius). We calibrate the variation $a(B)$ of the scattering length by measuring, after expansion, the BEC size and atom number

[9]. The reduction of a close to $B_0 + \Delta$ is accompanied by inelastic losses. By measuring the $1/e$ lifetime and the density of the BEC close to resonance, we estimate the three-body loss coefficient to be constant for the range of scattering lengths ($5 \leqslant a/a_0 \leqslant 30$) studied here, with a value $L_3 \sim 2 \times 10^{-40}$ m^6/s.

To study the collapse dynamics, we first create a BEC of typically 20 000 atoms in a trap with frequencies $(\nu_x, \nu_y, \nu_z) \simeq (660, 400, 530)$ Hz at a magnetic field $\sim$10 G above the Feshbach resonance, where the scattering length is $a \simeq 0.9 a_{\rm bg}$. We then decrease a by ramping down B linearly over 8 ms to a value $a_{\rm i} = 30 a_0$ which still lies well above the critical value for collapse, measured to be at $a_{\rm crit} \simeq (15 \pm 3) a_0$ [shaded area on Fig. 1(a)] for our parameters [9]. This ramp is slow enough to be adiabatic ($\dot{a}/a \ll \nu_{x,y,z}$), so that the BEC is not excited during it. After 1 ms waiting time, a is finally ramped down rapidly to $a_{\rm f} = 5 a_0$, which is below the collapse threshold. For this, we ramp linearly in 1 ms the current $I(t)$ in the coils providing the magnetic field $B = \alpha I$. However, due to eddy currents in the metallic vacuum chamber, the actual value of $B(t)$ and hence that of $a(t)$ change in time as depicted in blue on Fig. 1(a). To obtain this curve, we used Zeeman spectroscopy to measure the step response of $B(t)$ to a jump in the current $I(t)$ (corresponding to a $\sim$15 G change in B), and found that the resulting $B(t)$ is well described if $\tau \dot{B} + B = \alpha I(t)$ holds, with $\tau \simeq 0.5$ ms. From this equation and the measured $I(t)$ we determine the actual $a(t)$.

After the ramp, we let the system evolve for an adjustable time $t_{\rm hold}$ and then the trap is switched off. Note that the origin of $t_{\rm hold}$ corresponds to the end of the ramp in $I(t)$. Because of eddy currents, $t_{\rm hold} = 0$ about 0.2 ms *before* the time at which the scattering length crosses $a_{\rm crit}$. However, as we shall see below, even for $t_{\rm hold} < 0.2$ ms a collapse (happening not in trap, but during the time of flight) is observed, since during expansion the scattering length continues to evolve towards $a_{\rm f}$. The large magnetic field along z is rapidly turned off (in less than 300 μs) after 4 ms of expansion, and the condensate expands for another 4 ms in an 11 G field pointing in the x direction, before being imaged by absorption of a resonant laser beam propagating along x. Changing the direction of the field allows us to use the maximum absorption cross section for the imaging (if the latter was done in high field, the absorption cross section would be smaller, thus reducing the signal to noise ratio of the images). We checked that this fast switching has no influence on the condensate dynamics. We observe that the atomic cloud has a clear bimodal structure, with a broad isotropic thermal cloud, well fitted by a Gaussian, and a much narrower, highly anisotropic central feature, interpreted as the remnant BEC [see Figs. 1(b) and 1(c)].

The upper row of Fig. 1(d) shows the time evolution of the condensate when varying $t_{\rm hold}$. The images were obtained by averaging typically five absorption images taken under the same conditions; the thermal background was subtracted, and the color scale was adjusted separately for each $t_{\rm hold}$ for a better contrast. From an initial shape elongated along the magnetization direction z, the condensate rapidly develops a complicated structure with an expanding, torus-shaped part close to the $z = 0$ plane. Interestingly, the angular symmetry of the condensate at some specific times (e.g., at $t_{\rm hold} = 0.5$ ms) is reminiscent of the d-wave angular symmetry $1 - 3\cos^2\theta$ of the DDI. For larger values of $t_{\rm hold}$, we observe that the condensate "refocuses" due to the presence of the trap [17].

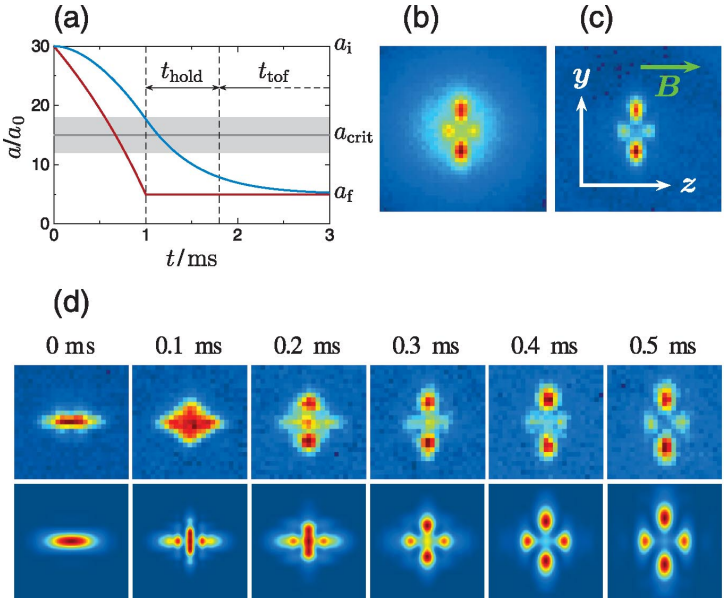

FIG. 1 (color). Collapse dynamics of the dipolar condensate. (a) Timing of the experiment. The red curve represents the time variation of the scattering length $a(t)$ one would have in the absence of eddy currents, while the blue curve is obtained by taking them into account (see text). (b) Sample absorption image of the collapsed condensate for $t_{\rm hold} =$ 0.4 ms, after 8 ms of time of flight, showing a "cloverleaf" pattern on top of a broad thermal cloud. This image was obtained by averaging 60 pictures taken under the same conditions. (c) Same image as (b) with the thermal cloud subtracted. In (b) and (c) the field of view is 270 μm by 270 μm. The green arrow indicates the direction of the magnetic field. (d) Series of images of the condensate for different values of $t_{\rm hold}$ (upper row) and results of the numerical simulation without adjustable parameters (lower row); the field of view is 130 μm by 130 μm.

The lower row of Fig. 1(d) shows the column density $\int |\psi(\boldsymbol{r})|^2 dx$ [where $\psi(\boldsymbol{r})$ is the order parameter of the condensate after time of flight] obtained from a numerical simulation of the three-dimensional GPE

$$i\hbar\frac{\partial\psi}{\partial t} = \left[\frac{-\hbar^2}{2m}\Delta + V_{\text{trap}} + \int U(\boldsymbol{r}-\boldsymbol{r}', t)|\psi(\boldsymbol{r}', t)|^2 d\boldsymbol{r}' - \frac{i\hbar L_3}{2}|\psi|^4\right]\psi,$$

where

$$U(\boldsymbol{r}, t) = \frac{4\pi\hbar^2 a(t)}{m}\delta(\boldsymbol{r}) + \frac{\mu_0\mu^2}{4\pi}\frac{1-3\cos^2\theta}{r^3}$$

stands for the contact and dipolar interactions, θ being the angle between $\boldsymbol{r}$ and the direction of polarization. Here m is the atomic mass, μ_0 the permeability of vacuum, and $\mu = 6\mu_B$ the magnetic moment of a Cr atom (μ_B is the Bohr magneton). The nonunitary term proportional to L_3 describes three-body losses. The scattering length $a(t)$ is changed according to the blue curve in Fig. 1(a) and the trap potential V_{trap} is switched off at the beginning of the 8 ms time of flight. For the simulation, space is discretized into a $128 \times 128 \times 128$ mesh with a step size of 70 nm. For the kinetic part, the Crank-Nicolson scheme is used for the time evolution to avoid numerical instability. For the interaction part, the convolution integral is calculated using a fast Fourier transform. After the trap is switched off, the mesh is extended to $512 \times 512 \times 512$ to describe the expansion of the cloud. When the density becomes low enough so that the nonlinear terms of the GPE can be neglected, the free expansion propagator is used to give the final time-of-flight images. The agreement between the experimental data and the simulation, performed without any adjustable parameter, is excellent.

The cloverleaf patterns seen in Figs. 1(b)–1(d) are caused by the anisotropic collapse and the subsequent dynamics of the system. Figure 2 shows the in-trap evolution of the condensate as a function of t_{hold}. The mechanism of the condensate "explosion" is as follows [18]: When the atomic density grows due to the attractive interaction, three-body losses predominantly occur in the high-density region. The centripetal force then weakens, and the atoms that gathered in this narrow central region are ejected due to the "quantum pressure" arising from the uncertainty principle. The kinetic energy is supplied by the loss of the negative interaction energy. For the contact interaction, the collapse and subsequent atomic explosion is isotropic [18]. In the present case, the collapse occurs mainly in the x-y direction due to anisotropy of the DDI (in the absence of inelastic losses, the condensate would indeed become an infinitely thin cigar-shaped cloud along z, see Fig. 3 of Ref. [9], and the in-trap image at $t_{\text{hold}} = 0.5$ ms in Fig. 2 of this Letter), and therefore the condensate explodes essentially radially, producing the anisotropic shape of the cloud. The numerical simulation reveals that, for $t_{\text{hold}} < 0.5$ ms, the collapse observed in Fig. 1(d) occurs not during the holding time but during the time of flight. We stress that in the absence of three-body losses, the explosion following the collapse would not be observed.

From the images, the atom number N_{BEC} in the condensate is obtained by integrating the optical density. Blue circles in Fig. 3 show N_{BEC} as a function of t_{hold}. The BEC atom number is initially $N_{\text{BEC}}(0) \simeq 16\,000$ and decreases toward its asymptotic value $\sim$6000. Over the same time scale, the atom number N_{thermal} in the thermal cloud (inset of Fig. 3) stays constant. The size of the thermal cloud after expansion is also constant over this period. This suggests that the thermal cloud does not play any significant role in the collapse dynamics. For $t_{\text{hold}} < 0.5$ ms, the collapse actually occurs during the time of flight, which explains the gradual decay of $N_{\text{BEC}}(t_{\text{hold}})$, and why the atom losses are not as large as those when the collapse occurs in trap (in the latter case, 70% of the atoms are lost). The missing atoms have very likely escaped from the trap as energetic molecules and atoms produced in three-body collisions. This is confirmed by the fact that the simulation gives a $N_{\text{BEC}}(t_{\text{hold}})$ curve (solid line in Fig. 3) which matches well the experimental data. Experimental uncertainties in the parameters used in the simulation (trap frequencies, values of L_3 and τ) probably explain the small discrepancy between the experiment and the numerical results.

The numerical simulation gives access not only to the density $|\psi(\boldsymbol{r})|^2$, but also to the phase $S(\boldsymbol{r})$ of the order parameter ψ (i.e., to the velocity field $\boldsymbol{v} = \hbar\boldsymbol{\nabla}S/m$) and reveals the generation of vortex rings [19,20] of charge ± 1. Figure 4(a) shows an in-trap isodensity surface of a condensate at $t_{\text{hold}} = 0.8$ ms and the location of the vortex rings (shown as red curves). Comparing Figs. 2 and 4(a) (at $t_{\text{hold}} = 0.8$ ms), we find that the topological defects encircle the two "leaves" of the "clover." Figure 4(b) shows the velocity field $\boldsymbol{v}(\boldsymbol{r})$ in the $x = 0$ plane. The atoms ejected in the x-y plane flow outward, while the atoms

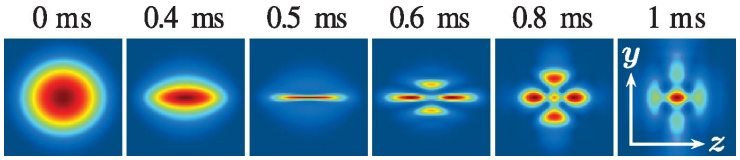

FIG. 2 (color). In-trap column density obtained in the simulation, for different t_{hold}. The field of view is 5 μm by 5 μm. Because of the DDI, the condensate collapses radially, acquiring the shape of a very thin cigar elongated along z. At $t_{\text{hold}} \simeq 0.5$ ms, the collapse occurs, and immediately after, the cloud starts to expand radially.

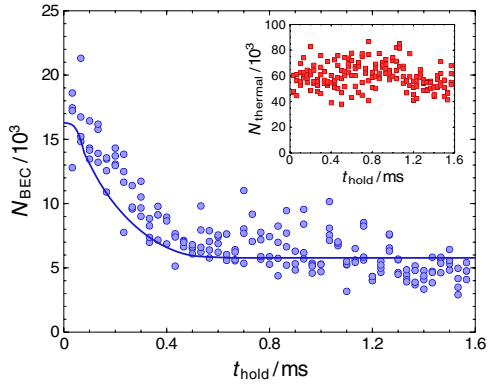

FIG. 3 (color online). Atom losses during collapse. Blue circles: atom number N_{BEC} in the condensate as a function of t_{hold}. The solid curve is the result of the simulation for $L_3 = 2 \times 10^{-40}$ m^6/s, without any adjustable parameter. Inset: the atom number $N_{thermal}$ in the thermal cloud (red squares) remains essentially constant during the collapse.

near the z axis still flow inward, giving rise to the circulation. Thus, the vortex-ring formation is specific to the d-wave collapse induced by the DDI. Although the vortex rings are not observed directly in the experiment, the excellent agreement between the experiment and simulation in Figs. 1 and 3 strongly suggests the creation of vortex rings during the collapse of the condensate.

In conclusion, we have investigated the collapse dynamics of a dipolar BEC. Contrary to the case of an isotropic contact interaction, the DDI induces the formation of a structured cloud featuring a d-wave symmetry. The collapse dynamics is quantitatively reproduced by numerical simulations of the GPE without any adjustable parameter. An interesting subject for future studies is the dependence of the collapse dynamics on the trap geometry: one may wonder if the condensate would collapse in the same way if initially trapped in a very anisotropic (e.g., pancake-shaped) trap. A natural extension of this work would involve detecting, e.g., by interferometric methods [21,22], the vortex rings predicted by the simulation. Finally, whether one can nucleate stable vortex rings by initiating the collapse, and then changing a back to a value corresponding to a stable BEC, is a question which certainly deserves further investigations.

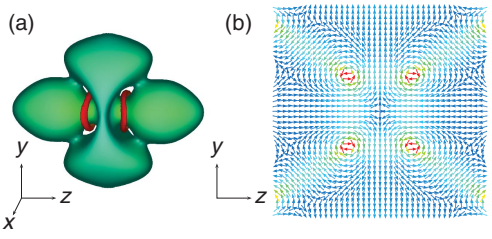

FIG. 4 (color). Vortex rings predicted by the numerical simulation. (a) Isodensity surface of an in-trap condensate at $t_{hold} = 0.8$ ms. The topological defects are shown by the red rings. (b) Velocity field of the atomic flow in the $x = 0$ plane at $t_{hold} = 0.8$ ms. The field of view is 2.5 μm by 2.5 μm; the color scale represents the velocity (red is faster).

We thank H. P. Büchler, S. Giovanazzi, L. Santos, and G. V. Shlyapnikov for useful discussions. We acknowledge support by the German Research Foundation (SFB/TRR 21 and SPP 1116), the Landesstiftung Baden-Württenberg, and the EU (Marie-Curie Grant No. MEIF-CT-2006-038959 to T. L.). H. S., Y. K., and M. U. acknowledge support by the Ministry of Education, Culture, Sports, Science and Technology of Japan (Grants-in-Aid for Scientific Research No. 17071005 and No. 20540388, the 21st century COE program on "Nanometer-Scale Quantum Physics") and by the Matsuo Foundation.

[1] C. C. Tsuei and J. R. Kirtley, Rev. Mod. Phys. **72**, 969 (2000).
[2] L. Santos, G. V. Shlyapnikov and M. Lewenstein, Phys. Rev. Lett. **90**, 250403 (2003).
[3] K. Góral, L. Santos, and M. Lewenstein, Phys. Rev. Lett. **88**, 170406 (2002); C. Menotti, C. Trefzger, and M. Lewenstein, *ibid.* **98**, 235301 (2007).
[4] K. Góral, K. Rzążewski, and T. Pfau, Phys. Rev. A **61**, 051601(R) (2000); L. Santos *et al.*, Phys. Rev. Lett. **85**, 1791 (2000); S. Yi and L. You, Phys. Rev. A **63**, 053607 (2001); S. Giovanazzi, A. Görlitz, and T. Pfau, J. Opt. B **5**, S208 (2003); J. Stuhler *et al.*, Phys. Rev. Lett. **95**, 150406 (2005); T. Lahaye *et al.*, Nature (London) **448**, 672 (2007).
[5] S. Ronen, D. C. E. Bortolotti, and J. L. Bohn, Phys. Rev. Lett. **98**, 030406 (2007).
[6] O. Dutta and P. Meystre, Phys. Rev. A **75**, 053604 (2007).
[7] Y. Kawaguchi, H. Saito, and M. Ueda, Phys. Rev. Lett. **96**, 080405 (2006); L. Santos and T. Pfau, *ibid.* **96**, 190404 (2006); S. Yi and H. Pu, *ibid.* **97**, 020401 (2006); Y. Kawaguchi, H. Saito, and M. Ueda, *ibid.* **97**, 130404 (2006).
[8] M. A. Baranov, Phys. Rep. **464**, 71 (2008).
[9] T. Koch *et al.*, Nature Phys. **4**, 218 (2008).
[10] C. A. Sackett *et al.*, Phys. Rev. Lett. **82**, 876 (1999).
[11] J. M. Gerton *et al.*, Nature (London) **408**, 692 (2000).
[12] J. L. Roberts *et al.*, Phys. Rev. Lett. **86**, 4211 (2001).
[13] E. A. Donley *et al.*, Nature (London) **412**, 295 (2001).
[14] K. S. Strecker *et al.*, Nature (London) **417**, 150 (2002).
[15] S. L. Cornish, S. T. Thompson, and C. E. Wieman, Phys. Rev. Lett. **96**, 170401 (2006).
[16] M. Ueda and H. Saito, J. Phys. Soc. Jpn. **72**, 127 (2003).
[17] See EPAPS Document No. E-PRLTAO-101-008831 for a movie of the collapse for $0 \leqslant t_{hold} \leqslant 1.6$ ms. For more information on EPAPS, see http://www.aip.org/pubservs/epaps.html.
[18] H. Saito and M. Ueda, Phys. Rev. A **65**, 033624 (2002).
[19] B. P. Anderson *et al.*, Phys. Rev. Lett. **86**, 2926 (2001).
[20] N. S. Ginsberg, J. Brand, and L. V. Hau, Phys. Rev. Lett. **94**, 040403 (2005).
[21] M. R. Matthews *et al.*, Phys. Rev. Lett. **83**, 2498 (1999).
[22] F. Chevy *et al.*, Phys. Rev. A **64**, 031601(R) (2001).

Mesoscopic Ensembles of Polar Bosons in Triple-Well Potentials

T. Lahaye,[1,2,3] T. Pfau,[3] and L. Santos[4]

[1]*Université de Toulouse, UPS, Laboratoire Collisions Agrégats Réactivité, IRSAMC; F-31062 Toulouse, France*
[2]*CNRS, UMR 5589, F-31062 Toulouse, France*
[3]*5. Physikalisches Institut, Universität Stuttgart, Pfaffenwaldring 57, 70550 Stuttgart, Germany*
[4]*Institut für Theoretische Physik, Leibniz Universität Hannover, Appelstrasse 2 D-30167, Hannover, Germany*

(Received 27 November 2009; revised manuscript received 25 February 2010; published 28 April 2010)

Mesoscopic dipolar Bose gases in triple-well potentials offer a minimal system for the analysis of the nonlocal character of the dipolar interaction. We show that this nonlocal character may be clearly revealed by a variety of possible ground-state phases. In addition, an appropriate control of short-range and dipolar interactions may lead to novel scenarios for the dynamics of polar bosons in lattices, including the dynamical creation of mesoscopic quantum superpositions, which may be employed in the design of Heisenberg-limited atom interferometers.

DOI: 10.1103/PhysRevLett.104.170404 PACS numbers: 03.75.Kk, 03.75.Lm

Interparticle interactions are crucial in quantum gases [1]. They can usually be described by a short-range isotropic potential proportional to the scattering length a. Recently, dipolar quantum gases, in which the long-range and anisotropic dipole-dipole interaction (DDI) between magnetic or electric dipole moments plays a significant or even dominant role, have attracted a lot of interest as they show fascinating novel properties [2,3]. To date, dipolar effects have been observed experimentally only with atomic magnetic dipoles, being particularly relevant in Bose-Einstein condensates (BECs) of ^{52}Cr where exciting new physics has been observed [4–7]. Dipolar effects have also been reported in spinor BECs [8], and in ^{39}K and ^{7}Li BECs with $a = 0$ [9,10]. Recent experiments with polar molecules [11,12] open fascinating perspectives towards the realization of highly dipolar gases.

Although a very clear and direct demonstration of the anisotropy of the DDI was given by the d-wave collapse of a Cr BEC [6,7], an equivalently obvious "visual" proof of the nonlocal character of the DDI is still missing. Such a nonambiguous qualitative evidence of the nonlocal character of the dipolar interaction could be provided in principle by the observation of novel quantum phases (supersolid, checkerboard) in optical lattices [13]. However, the unambiguous detection of such phases is far from trivial, as is the preparation of the ground state of the system due to a large number of metastable states [14].

In this Letter, we investigate a minimal system, namely, a mesoscopic sample of dipolar bosons in a triple-well potential, which minimizes these restrictions, while still presenting clear visual nonlocal features (see "phase" B below). Nondipolar BECs in double-well potentials have allowed for the observation of Josephson oscillations and nonlinear self-trapping [15], showing clearly that "slicing" a BEC dramatically enhances the effects of interactions. The two-well Josephson physics is affected quantitatively (although not qualitatively) by the DDI [16,17] (the DDI may induce, however, significant intersite effects in coupled 1D and 2D bilayer systems [18–20]). On the contrary, as we show below, the DDI does introduce qualitatively novel physics in the Josephson-like dynamics in three-well systems. We discuss how the DDI leads to various possible ground states, which may visually reveal the nonlocality of the DDI. In addition, we show how this nonlocality leads to a peculiar quantum dynamics characterized by striking new phenomena, including the dynamical formation of mesoscopic quantum superpositions (MQS). MQSs produced in cavity QED or with trapped ions [21] require complex manipulations, whereas in the present system they arise naturally, similar to the MQSs obtained in BECs with attractive interactions in double wells [22,23] or lattices [24]. We then comment on the design of four-site Heisenberg-limited atom interferometers using the dynamical creation of MQS, and finally discuss possible experimental scenarios.

We consider N dipolar bosons in a three-well potential $V_{\rm trap}(\boldsymbol{r})$ [Fig. 1(a)]. The wells are aligned along the y axis, separated by a distance ℓ and an energy barrier V_0. The bosons are polarized by a sufficiently large external field, with a dipole moment $\boldsymbol{d}$ along a given direction. The lattice potential is strong enough compared to other energies (in particular, the interaction energies) such that the on-site wave functions $\phi_{i=1,2,3}(\boldsymbol{r})$ are fixed, being independent of the number of atoms per site. For a large enough V_0 we may assume $\phi_i(\boldsymbol{r}) = \phi(\boldsymbol{r} - \boldsymbol{r}_i)$, where $\boldsymbol{r}_i$ is the center of site i. In addition we may assume ϕ to be a Gaussian with

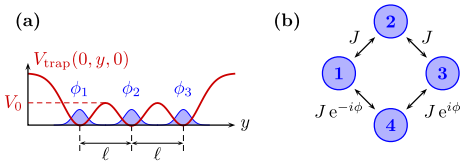

FIG. 1 (color online). (a) Schematic view of the three-well system. (b) MQS interferometer with four wells (see text).

widths $\sigma_{x,y,z}$. We limit to the case where σ_y is small enough with respect to ℓ so that the sites are well defined. Reexpressing the bosonic field operator as $\hat{\psi}(\boldsymbol{r}) = \sum_{i=1}^{3} \phi_i(\boldsymbol{r})\hat{a}_i$, we may write the Hamiltonian as

$$\hat{H} = -J[\hat{a}_2^\dagger(\hat{a}_1 + \hat{a}_3) + \text{H.c.}] + \frac{U_0}{2}\sum_{i=1}^{3}\hat{n}_i(\hat{n}_i - 1) + U_1\left[\hat{n}_1\hat{n}_2 + \hat{n}_2\hat{n}_3 + \frac{1}{\alpha}\hat{n}_1\hat{n}_3\right], \quad (1)$$

where $J = -\int d\mathbf{r}\phi_1(\mathbf{r})[-\hbar^2\nabla^2/2m + V_{\text{trap}}(\mathbf{r})]\phi_2(\mathbf{r})$ is the hopping rate, $U_0 = g\int|\phi_1|^4 d\boldsymbol{r} + \int|\phi_1(\boldsymbol{r})|^2|\phi_1(\boldsymbol{r}')|^2 \times U_{\text{dd}}(\boldsymbol{r}-\boldsymbol{r}')d\boldsymbol{r}d\boldsymbol{r}'$ characterizes the on-site interactions, $U_1 = \int|\phi_1(\boldsymbol{r})|^2|\phi_2(\boldsymbol{r}')|^2 U_{\text{dd}}(\boldsymbol{r}-\boldsymbol{r}')d\boldsymbol{r}d\boldsymbol{r}'$ is the coupling constant for nearest-neighbor DDI, and $\hat{n}_j = \hat{a}_j^\dagger\hat{a}_j$. In the previous expressions $g = 4\pi\hbar^2 a/m$ is the coupling constant for the short-range interactions, with a the s-wave scattering length. The DDI is given by $U_{\text{dd}}(\boldsymbol{r}) = d^2(1 - 3\cos^2\theta)/r^3$, where θ is the angle between $\boldsymbol{r}$ and $\boldsymbol{d}$, $d^2 \equiv \mu_0\mu^2/(4\pi)$ for magnetic dipoles (μ is the magnetic dipole moment) or $d^2 \equiv \bar{d}^2/4\pi\epsilon_0$ for electric dipoles ($\bar{d}$ is the electric dipole moment). The parameter α in Eq. (1) depends on the geometry of $V_{\text{trap}}(\boldsymbol{r})$ ($\alpha = 8$ if the wave functions are well localized in all directions compared to ℓ, and decreases towards $\alpha = 4$ when $\sigma_x/\ell \to \infty$ [25]). In the following we focus on the localized case, i.e., $\alpha = 8$, but all results remain valid for $4 \le \alpha \le 8$. Finally, note that U_0 results from short-range interactions and DDI, and that the ratio between U_0 and U_1 may be easily manipulated by means of Feshbach resonances, by modifying the dipole orientation $\boldsymbol{d}$ and by changing ℓ [25].

Since $\sum_i \hat{n}_i = N$ is conserved by (1), we may rewrite $\hat{H}$ [up to a global energy $U_0 N(N-1)/2$] as an effective Hamiltonian without on-site interactions:

$$\hat{H} = -J[\hat{a}_2^\dagger(\hat{a}_1 + \hat{a}_3) + \text{H.c.}] + (U_1 - U_0)\hat{n}_2[\hat{n}_1 + \hat{n}_3] + \left(\frac{U_1}{8} - U_0\right)\hat{n}_1\hat{n}_3. \quad (2)$$

The gross structure of the ground-state diagram is understood from the $J = 0$ case, where the Fock states $|n_1, n_3\rangle$ are eigenstates of $\hat{H}$, with energy $E(n_1, n_3)$ (since N is conserved, the Fock states are defined by $n_{1,3}$). The minimization of E provides four classical "phases." For $U_0 > 0$ and $U_1 \le 8U_0/15$, and $U_0 < 0$ and $U_1 < -8|U_0|$, phase (A) occurs, with $n_1 = n_3 = \lfloor\bar{n}/2\rfloor$ with $\bar{n} \equiv 16N(U_0 - U_1)/(24U_0 - 31U_1)$ (where $\lfloor\cdot\rfloor$ denotes the integer part). Phase (B) appears for $U_0 > 0$ and $8U_0/15 \le U_1 \le 8U_0$, being characterized by $n_1 = n_3 = N/2$. For $U_0 > 0$ and $U_1 > 8U_0$, and $U_0 < 0$ and $U_1 > -|U_0|$, phase (C) occurs, with $n_2 = N$ (actually states with $n_i = N$ are degenerated, but the degeneracy is broken by tunneling which favors $n_2 = N$). Finally, phase (D) occurs for $U_0 < 0$ and $8U_0 < U_1 < U_0$, being characterized by a broken symmetry, with two degenerated states with $n_1 = \lfloor\bar{n}\rfloor$, $n_3 = 0$ and vice versa.

Figure 2(a) shows $\langle\hat{n}\rangle/N$, with $\hat{n} = \hat{n}_1 + \hat{n}_3$ for $N = 18$. We can see that phases (A)–(D) describe well the gross structure of the ground-state diagram [a similar graph shows, as expected, that the (D) phase shows large fluctuations $\Delta\hat{\delta}$ in $\hat{\delta} = \hat{n}_1 - \hat{n}_3$]. However, tunneling is relevant at low $|U_0|$ and $|U_1|$ and at the phase boundaries. In general, the system is in a quantum superposition of different Fock states $|\psi\rangle = \sum_{n_1=0}^{N}\sum_{n_3=0}^{N-n_1} C(n_1, n_3)|n_1, n_3\rangle$. Figure 2(b) depicts $\Delta\hat{\delta}$ in the region $U_{0,1} > 0$. As expected at small $|U_{0,1}|/J$ tunneling dominates and the product state $(a_1^\dagger/\sqrt{2} + a_2^\dagger/2 + a_3^\dagger/\sqrt{2})^N|\text{vac}\rangle$ is retrieved ($|\text{vac}\rangle$ is the vacuum state). This state transforms into phase (A), which for growing U_0 becomes the Fock state $|N/3, N/3\rangle$. Phase (C) remains the Fock state $|0, 0\rangle$ ($n_2 = N$), and the border (B)–(C) is characterized by a first-order "phase transition" [26], at which n_2 abruptly jumps from 0 to N. Figure 2(c) represents schematically phases (A)–(D).

Phase (B) is characterized by vanishing $\langle\hat{n}_2\rangle$ and Δn_2, and $\langle\hat{n}_1\rangle = \langle\hat{n}_3\rangle$. It strikingly reveals the nonlocal character of the DDI, similarly to the biconcave BECs predicted in [27], but with a much higher "contrast." Note, however, that the actual ground state may significantly depart from $|N/2, N/2\rangle$, since $|\Delta\hat{\delta}|$ is significant at the (B)–(C) transition [Fig. 2(b)]. At $U_1 = 8U_0$, the ground state is a coherent state $(a_1^\dagger + a_3^\dagger)^N|\text{vac}\rangle$; i.e., coherence between the two extremal sites is preserved in spite of the absence of particles in site 2. This coherence is understood from (2), since for $U_1 = 8U_0$ there is no effective interaction between sites 1 and 3. Since $\langle\hat{n}_2\rangle \ll 1$ due to the effective repulsive nearest-neighbor interactions ($U_1 - U_0 > 0$), sites 1 and 3 form an effective noninteracting two-well system coherently coupled by a second-order process through site 2 [with effective hopping $J_{\text{eff}} = J^2/7(N-1)U_0$]. Hence the coherent region extends inside (B) for $|U_1 - 8U_0| \lesssim J_{\text{eff}}$. Thus for larger NU_0 the coherent re-

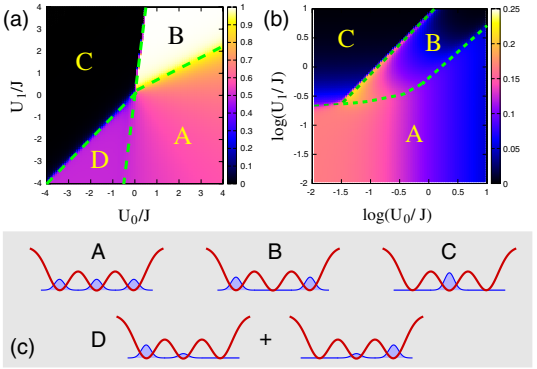

FIG. 2 (color online). (a) $\langle\hat{n}\rangle/N$ as a function of $U_{0,1}$ for $N = 18$. (b) $\Delta\hat{\delta}/N$ in logarithmic scale for $U_{0,1}$. The dashed lines show the boundaries between the classical phases (A)–(D) that are shown schematically in (c).

gion shrinks [reducing to the very vicinity of $U_1 = 8U_0$ as seen in Fig. 2(b)].

Such a 1–3 coherence has important consequences for the quantum dynamics, best illustrated by considering initially all particles at site 3. Interestingly, $\langle \hat{n}_{1,3} \rangle$ show perfect Josephson-like oscillations (with frequency $2J_{\rm eff}/\hbar$), although for any time $\langle \hat{n}_2 \rangle = \Delta \hat{n}_2 \ll 1$. However, $J_{\rm eff}$ decreases with NU_0, and hence the observation of this effect demands a mesoscopic sample, since otherwise the dynamics may become prohibitively slow. Off the $U_1 = 8U_0$ boundary, inside phase (B), the residual 1–3 interaction leads to a damping of the Josephson oscillations (connected to number squeezing). Eventually for $|U_1 - 8U_0| \gg J_{\rm eff}$ self-trapping in 3 occurs.

Phase (D) is characterized by a large $\Delta \hat{\delta}$ and $\langle \hat{n}_2 \rangle \neq 0$, and two degenerated states: $n_3 = 0$ (i) and $n_1 = 0$ (ii). Strictly speaking, the exact ground state is provided by a MQS of these two states, but the gap between the ground state and the first excited one is vanishingly small ($\ll J$) even at the $U_1 = U_0 < 0$ boundary and for N as small as 18. Experimentally, the signature of phase (D) would thus consist in measuring large shot-to-shot fluctuations in $\hat{\delta}$, while never observing simultaneously atoms in both sites 1 and 3. At $U_1 = U_0 < 0$, states (i) and (ii) become coherent superpositions of the form $(a_1^\dagger + a_2^\dagger)^N |\text{vac}\rangle$ and $(a_2^\dagger + a_3^\dagger)^N |\text{vac}\rangle$, respectively. These superpositions may be understood from Eq. (2), which for $U_1 = U_0 < 0$ becomes

$$\hat{H} = -J[\hat{a}_2^\dagger(\hat{a}_1 + \hat{a}_3) + \text{H.c.}] + \frac{7|U_0|}{8}\hat{n}_1\hat{n}_3, \qquad (3)$$

which describes a noninteracting two-well system if $n_1 = 0$ or $n_3 = 0$, leading to the coherent states (i) and (ii).

Hamiltonian (3) leads to an intriguing quantum dynamics characterized by the creation of MQSs. From an initial Fock state $|0, 0\rangle$ ($n_2 = N$), if a particle tunnels into site 1 (state $|1, 0\rangle$), a subsequent tunneling from 2 to 3 (state $|1, 1\rangle$) is produced with a bosonic-enhanced hopping rate $J\sqrt{N-1}$. However, the state $|1, 1\rangle$ has an interaction energy $7|U_0|/8$. Hence, if $J \ll 7|U_0|/8\sqrt{N-1}$, then the tunneling from 2 to 3 remains precluded. On the contrary, the hopping into 1 presents no energy penalty. As a result, if the first particle tunnels into 1, then a coherent 1–2 superposition is established. Of course, if the first particle tunnels into 3, then a 2–3 superposition occurs. Since the initial process is coherently produced in both directions, a MQS $|\Phi(t)\rangle|0\rangle + |0\rangle|\Phi(t)\rangle$ is formed, where $|\Phi(t)\rangle = \sum_{n=0}^{N} C_n(t)|n\rangle$, with the normalization condition $2\sum_{n=1}^{N} |C_n(t)|^2 + 4|C_0(t)|^2 = 1$ [25]. Figure 3(a) shows that $\langle \hat{n}_{1,3} \rangle(t)$ perform a coherent oscillation, which, however, damps for longer times. This damping is again a remarkable consequence of the nonlocal character of the DDI. Virtual hoppings of a single particle from site 2 into site 3 (1) induce a second-order correction of the energy of the states $|n, 0\rangle$ ($|0, n\rangle$): $\Delta E_n = 8J^2(N-n)/7|U_0|n$, which distorts the Josephson Hamiltonian, and leads to a significant damping after a time scale of the order of $\tau \sim 7|U_0|/8J^2N$ (in agreement with our numerics) [25]. At longer times, chaotic dynamics may even occur [28].

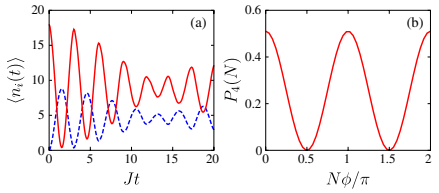

FIG. 3 (color online). (a) $\langle \hat{n}_{1,3}(t) \rangle$ (dashed line) and $\langle \hat{n}_2(t) \rangle$ (solid line), for $U_0 = U_1 = -100J$ and $N = 18$. (b) Probability $P_4(N)$ as a function of ϕ for the interferometric four-site arrangement (see text) with $N = 14$, $U_0 = U_1 = -100$, and $Jt = 2.7$.

The three-well system hence acts as a MQS splitter under the mentioned conditions. We stress, however, that a MQS (although asymmetric) is still created [25], even for unequal hoppings J_{ij} for nearest neighbors, as long as $J_{12,23} \ll 7|U_0|/8\sqrt{N-1}$. We note also that if $U_1 \neq U_0$, a MQS is created if $|U_1 - U_0| \lesssim J$, but nearest-neighbor interactions enhance the damping in each MQS branch. If $|U_1 - U_0| \gg J$, bosons at site 2 remain self-trapped.

The MQS splitter opens fascinating possibilities beyond the three-well system, most relevantly in the context of Heisenberg-limited atom interferometry. We illustrate this possibility by considering a simple interferometer based on a four-well system [Fig. 1(b)]. Initially the bosons are at site 2 (which acts as the input port). Sites 1 and 3 play the role of the interferometer arms, whereas site 4 acts as the output port, where the interferometric signal is read out. We consider hoppings $J_{21} = J_{23} = J$, but $J_{34} = Je^{i\phi} = J_{14}^\star$. We are interested in the ϕ sensitivity of the population at site 4. This arrangement is chosen for its theoretical simplicity (more general arrangements work along similar lines), although it may be implemented also in practice by means of Raman tunneling [29]. Under the MQS conditions [in this case $U_1 = U_0 < 0$ and $J\sqrt{N-1} \ll (2\sqrt{2}-1)|U_0|/2\sqrt{2}$], the system evolves into an entangled MQS formed by Fock states such that $n_i n_j = 0$ for next-nearest neighbors. It is straightforward to show that the probability to find N particles at site 4 depends explicitly on the phase ϕ as $P_4(N) \sim \cos^2(N\phi)$ [$P_4(n \neq N)$ are only indirectly ϕ dependent due to normalization]. Hence, $P_4(N)$ has a modulation of period $\delta\phi = \pi/N$ [Fig. 3(b)], contrary to the period $\delta\phi = \pi$ expected for independent single particles, allowing for a Heisenberg-limited interferometric measurement of the phase ϕ. This superresolution is an unambiguous signature of the coherent character of the MQS thus created [30,31]. $\langle \hat{n}_4 \rangle$ presents a similar modulation (but with poorer contrast). Calculations with a six-site arrangement provide similar results [25].

In the final part of this Letter we discuss experimental feasibility. Triple-well potentials as in Fig. 1 may be con-

trollably implemented with optical potentials. By superimposing, onto a single-beam optical trap which provides the xz confinement, a tightly focused beam (with a waist ~ 1 μm, see, e.g., [32]), one may create a tight "dimple" acting as one well. To realize a triple well (or even more complex configurations), several possibilities exist. Using an acousto-optic modulator (AOM) with several rf frequencies [33,34], several diffracted beams are created, whose intensity and position can be controlled independently. Another option using an AOM consists in toggling the dimple between several positions at high rate, to create almost arbitrary time-averaged potentials [35]. Such an implementation has several advantages: arbitrary, time-dependent energy offsets can be applied to the different sites; the intersite separation ℓ can be changed in real time, easing the preparation of a given atom number in each well (e.g., by performing evaporative cooling with different energy offsets in each site), and the detection of the population in each well (before imaging, V_0 may be increased to freeze out the dynamics and then ℓ increased, thus relaxing constraints on the imaging resolution).

We now evaluate J, U_0, and U_1 for realistic experimental values. Although in our calculations we have just considered N up to 36, similar ground states are expected for larger N [but, as mentioned above, the observation of the quantum features at the (B)–(C) and (D)–(C) boundaries demands small samples]. In particular, consider a triple-well potential formed by three Gaussian beams of waist 1 μm separated by $\ell = 1.7$ μm. For a barrier height $V_0/h \simeq 2500$ Hz, we obtain $J/h \sim 10$ Hz, and the typical value of NU_1/J is then ~ 10 for $N = 2000$ ^{52}Cr atoms. The value of U_0 can be tuned, for a fixed geometry, by means of Feshbach resonances [4], so that one can explore, e.g., the first-order (B)–(C) "transition" with ^{52}Cr by varying U_1/U_0. However, the MQS creation demands small samples, being hence more realistic with polar molecules. For example, for KRb molecules placed at a distance $\ell = 1$ μm and maximally polarized ($d = 0.5$ D) parallel to the joining line between the sites, $U_1/h \simeq -70$ Hz. Under these conditions the MQS condition implies, for $N = 36$ molecules, J/h of a few hertz. Single-atom sensitivity has been achieved with fluorescence imaging [36], so that the relatively small values of N considered here should be detectable.

In summary, we have studied a simple system of dipolar bosons in a triple well, showing that the nonlocality of the DDI leads to qualitatively novel physics that may be explored with a high degree of control over all parameters via the trap geometry, dipole orientation, and Feshbach resonances. We have shown that the ground-state phases present abrupt crossovers induced by the nonlocal nature of the DDI, which may be explored with ^{52}Cr BECs. In addition, the dynamics presents intriguing new scenarios, especially for the case of polar molecules, including the dynamical creation of MQSs, which may be employed for Heisenberg-limited interferometry.

We thank M. K. Oberthaler, H. P. Büchler, D. Guéry-Odelin, and E. Demler for useful discussions. We acknowledge support by the DFG (QUEST and SFB/TRR 21), the ESF (EUROQUASAR), and the EU (Marie-Curie Grant No. MEIF-CT-2006-038959 to T. L.).

[1] I. Bloch, J. Dalibard, and W. Zwerger, Rev. Mod. Phys. **80**, 885 (2008).
[2] M. A. Baranov, Phys. Rep. **464**, 71 (2008).
[3] T. Lahaye *et al.*, Rep. Prog. Phys. **72**, 126401 (2009).
[4] T. Lahaye *et al.*, Nature (London) **448**, 672 (2007).
[5] T. Koch *et al.*, Nature Phys. **4**, 218 (2008).
[6] T. Lahaye *et al.*, Phys. Rev. Lett. **101**, 080401 (2008).
[7] J. Metz *et al.*, New J. Phys. **11**, 055032 (2009).
[8] M. Vengalattore *et al.*, Phys. Rev. Lett. **100**, 170403 (2008).
[9] M. Fattori *et al.*, Phys. Rev. Lett. **101**, 190405 (2008).
[10] S. E. Pollack *et al.*, Phys. Rev. Lett. **102**, 090402 (2009).
[11] K.-K. Ni *et al.*, Science **322**, 231 (2008).
[12] J. Deiglmayr *et al.*, Phys. Rev. Lett. **101**, 133004 (2008).
[13] K. Góral, L. Santos, and M. Lewenstein, Phys. Rev. Lett. **88**, 170406 (2002).
[14] C. Menotti, C. Trefzger, and M. Lewenstein, Phys. Rev. Lett. **98**, 235301 (2007).
[15] M. Albiez *et al.*, Phys. Rev. Lett. **95**, 010402 (2005).
[16] B. Xiong *et al.*, Phys. Rev. A **79**, 013626 (2009).
[17] M. Asad-uz-Zaman and D. Blume, Phys. Rev. A **80**, 053622 (2009).
[18] A. Argüelles and L. Santos, Phys. Rev. A **75**, 053613 (2007).
[19] D. W. Wang, Phys. Rev. Lett. **98**, 060403 (2007).
[20] C. Trefzger, C. Menotti, and M. Lewenstein, Phys. Rev. Lett. **103**, 035304 (2009).
[21] See, e.g., S. Haroche and J.-M. Raimond, *Exploring the Quantum* (Oxford University Press, Oxford, 2006), and references therein.
[22] J. I. Cirac *et al.*, Phys. Rev. A **57**, 1208 (1998).
[23] T.-L. Ho and C. V. Ciobanu, J. Low Temp. Phys. **135**, 257 (2004).
[24] M. W. Jack and M. Yamashita, Phys. Rev. A **71**, 023610 (2005); P. Buonsante, V. Penna, and A. Vezzani, Phys. Rev. A **72**, 043620 (2005); J. Javanainen and U. Shrestha, Phys. Rev. Lett. **101**, 170405 (2008).
[25] See supplementary material at http://link.aps.org/supplemental/10.1103/PhysRevLett.104.170404 for more details.
[26] Strictly speaking, one deals only with a crossover, since the system has a finite size.
[27] S. Ronen, D. C. E. Bortolotti, and J. L. Bohn, Phys. Rev. Lett. **98**, 030406 (2007).
[28] P. Buonsante, R. Franzosi, and V. Penna, Phys. Rev. Lett. **90**, 050404 (2003).
[29] D. Jaksch and P. Zoller, New J. Phys. **5**, 56 (2003).
[30] M. W. Mitchell *et al.*, Nature (London) **429**, 161 (2004).
[31] P. Walther *et al.*, Nature (London) **429**, 158 (2004).
[32] Y. R. P. Sortais *et al.*, Phys. Rev. A **75**, 013406 (2007).
[33] Y. Shin *et al.*, Phys. Rev. Lett. **92**, 050405 (2004).
[34] B. Fröhlich *et al.*, Rev. Sci. Instrum. **78**, 043101 (2007).
[35] K. Henderson *et al.*, New J. Phys. **11**, 043030 (2009).
[36] R. Bücker *et al.*, New J. Phys. **11**, 103039 (2009).

Chapter 2

Guided atom optics

Parfois au fond de moi se raniment
L'eau verte du canal du Midi
Et la brique rouge des Minimes.[1]

2.1 Introduction

I was hired at CNRS as a permanent researcher in October 2008, and joined the Cold Atom group recently founded at Laboratoire Collsions, Agrégats, Réactivité in Toulouse by David Guéry-Odelin, who had been appointed Professor at Université Paul Sabatier a few months earlier. At the time, David's experimental setup was still located at Laboratoire Kastler-Brossel of the ENS, in Paris. The machine, based for a significant part on equipment built during my PhD thesis, was producing all-optical BECs of ^{87}Rb and was used by a post-doc, Gianluca Gattobigio, and a PhD student, Antoine Couvert, to perform atom-optics experiments [27].

The group in Toulouse also included Renaud Mathevet, a *maître de conférence* who had been working previously in the team of the now retired John Weiner, on nanolithography using laser-cooled Cesium atoms. Our early work with Renaud consisted in preparing the lab space that had just been renovated to accommodate the experimental activity of the group. In parallel, the former nanolithography experiments were dismantled to make room for an extension of the lab space of the *atom interferometry* team, and, on my side, I finished some work, started in Stuttgart, related to dipolar gases.

In February 2009, we moved the BEC machine from ENS to Toulouse, and decided to reconstruct it without changes, so as to be operational as soon as possible. In retrospect, this probably was a mistake, as it turned out that several pieces of equipment, from the vacuum chamber to most of the lasers, finally had to be replaced in the end, while the design retained its initial shortcomings, such as a rather limited optical access and a moderate stability of the crossed optical dipole trap.

Two PhD students, Charlotte Fabre and Francois Vermersch, joined the team in

[1] Claude Nougaro, *Toulouse* (1967).

(a) (b)

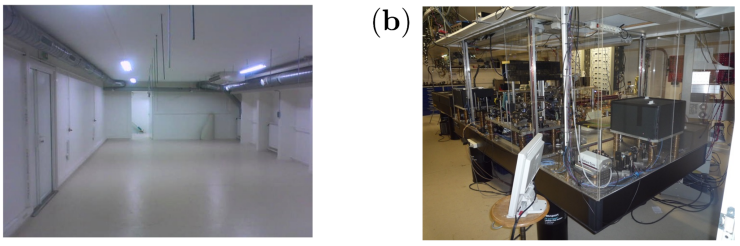

(c)

PRL 107, 230401 (2011) PHYSICAL REVIEW LETTERS week ending 2 DECEMBER 2011

Realization of a Distributed Bragg Reflector for Propagating Guided Matter Waves

C. M. Fabre, P. Cheiney, G. L. Gattobigio, F. Vermersch, S. Faure, R. Mathevet, T. Lahaye, and D. Guéry-Odelin
Université de Toulouse, UPS, Laboratoire Collisions Agrégats Réactivité, IRSAMC, F-31062 Toulouse, France and CNRS, UMR 5589, F-31062 Toulouse, France
(Received 27 July 2011; published 29 November 2011)

Figure 2.1: A quick summary of the early work of the cold atom group at LCAR in Toulouse. (a): The lab just after the renovation was finished (January 2009). (b): The lab at the time when we obtained the first BEC in Toulouse (spring 2010). (c): The first atom optics paper from the group (end of 2011).

September 2009, and Gianluca Gattobigio prolonged his post-doc from Paris to Toulouse. We obtained a first BEC in April 2010, but the system was unreliable as the 1070 nm, 300 W IPG fiber laser at the heart of the machine was slowly dying (its spatial mode kept degrading week after week). After repair of the laser, stable operation of the machine, giving BECs of up to 10^5 atoms every 5 seconds, was achieved at the end of 2010 (figure 2.1).

As a follow-up of the studies performed at ENS, it was decided to continue guided atom optics experiments, and we realized a Bragg reflector for guided matter waves [34]. In parallel, in early 2010 a new experimental setup was designed, in view of replacing the aging one moved from ENS. A PhD student, Pierrick Cheiney, joined the group in September 2010 to work on this project. During the development of the setup, Renaud Mathevet proposed to use permanent magnets for the construction of the Zeeman slower. This turned out to be a fruitful idea, that gave rise to the publication [22].

This chapter is organized as follows. I first describe in section 2.2 our Zeeman slower based on permanent magnets in a Halbach configuration. In section 2.3 I briefly summarize the experimental demonstration of a Bragg reflector for guided matter waves. For details, the reader is referred to the successive PhD theses defended in the group [33, 127, 21].

2.2 A Zeeman slower based on permanent magnets in a Halbach configuration

More than thirty years after its first demonstration [99], the Zeeman slower remains one of the most widely used intense sources of slow atoms in experiments using cold or ultracold atoms. Compared to alternative solutions, it is indeed a very robust system, which can

deliver very high fluxes. Furthermore, for atomic species with high melting points, it is the only practical option, as obtaining a significant vapor pressure requires the operation of a high-temperature oven.

The usual approach to the construction of Zeeman slowers relies on a tapered solenoid, that generates the parabolic magnetic field profile used to compensate, *via* the Zeeman effect, for the changing Doppler shift of the atoms as they decelerate. However this solution often results in cumbersome setups: the construction of a the tapered solenoid creating fields of some hundreds of Gauss takes time and care, and, once built, its power consumption can reach hundreds of watts, which requires relatively expensive power supplies, and, frequently, water cooling. Now, it often turns out that the benefit of using current-carrying wires to generate the B-field, that is the possibility to switch it on and off at will, is not used in actual experiments. Therefore, using strong, rare-earth permanent magnets for creating the magnetic field profile appears as an appealing alternative[2].

However, by using permanent magnets placed around a long cylinder, it is much more convenient to create a field transverse to the axis than a longitudinal one. This in itself is not a problem for the operation of a Zeeman slower; the only difference as compared to traditional, longitudinal-field slowers is that, in this case, one cannot use a purely σ^+ or σ^- polarization for the slowing light. In [94], the construction of a Zeeman slower for Strontium atoms using a transverse field created by permanent magnets was described (without any test of atom slowing, though). Moreover, the transverse uniformity of the magnetic field was quite bad, as, in a given cross-section of the slower, only two dipoles in a head-to-tail configuration, on each side, were used.

We thus proposed to use a different arrangement for the magnets, inspired by the so-called Halbach dipole cylinder [50]. This configuration, shown in Fig 2.2(a), consists of a continuous, radial distribution of magnetization within a cylindrical shell of internal and external radii R_i and R_e, where the angle of the magnetization vector is twice the azimuthal angle. One can show that such a configuration produces a magnetic transverse field, which vanishes for $r > R_\mathrm{e}$, and which is *uniform* inside the cylinder. For $r < R_\mathrm{i}$, the field takes the value

$$B = B_\mathrm{r} \ln\left(\frac{R_\mathrm{e}}{R_\mathrm{i}}\right), \tag{2.1}$$

where B_r is the remnant magnetic field of the magnetic material, which is typically above 1 T for NdFeB magnets. This Halbach dipole cylinder actually is only one of the many Halbach configurations that can be used to produce two-dimensional multipolar fields. A similar, one-dimensional configuration, called a *Halabch array*, in which the orientation of the magnetization vector rotates along a slab, allows the realization of a 'single-sided' magnetic plate[3]. Figure 2.2(b) gives an intuitive explanation of how this non-trivial be-

[2]The typical magnetization of NdFeB magnets with grade N-35 is above 800 kA/m. This means, for instance, that a 5-mm thick slab magnetized out of its plane is equivalent to a loop of wire of the same area, but carrying more than 4000 A!

[3]The reader might have quite a few Halbach arrays on the front of his/her fridge, especially if he/she has kids. Indeed, the ubiquitous 'fridge magnets' or magnetic bumper stickers have the magnetic configuration

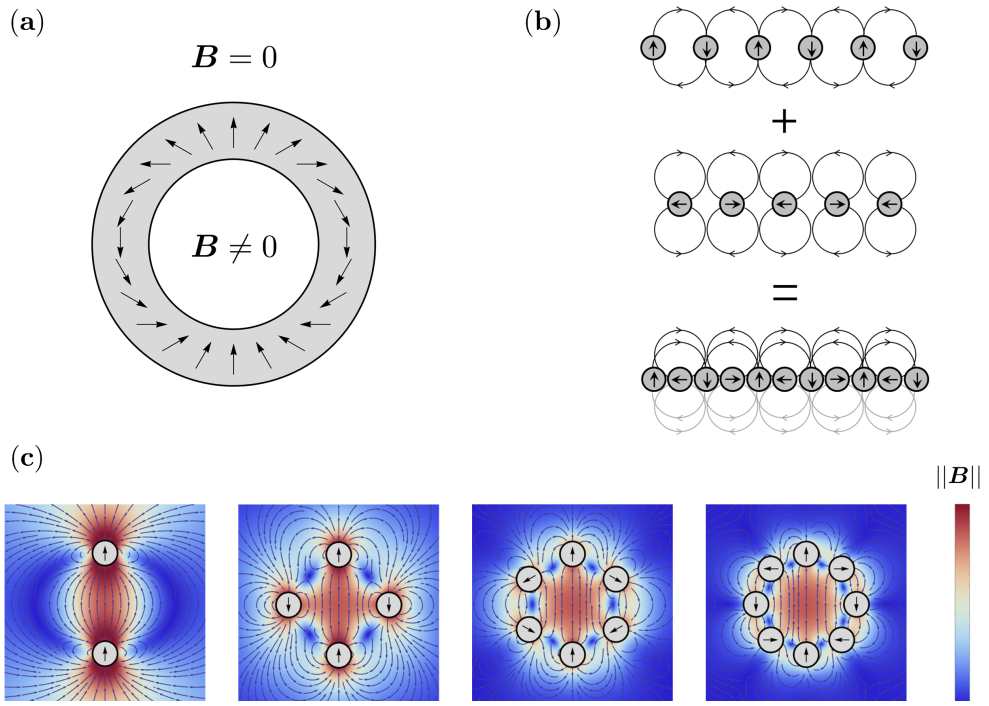

Figure 2.2: (a): The distribution of magnetization for a Halbach dipole cylinder. (b): An intuitive way to understand how a Halbach array generates a 'one-sided flux': on one side, the field produced by the magnetization pointing out of the plane and the one produced by the magnetization pointing in the plane add up, while on the other side they cancel out. In the limit of a continuously rotating magnetization, one gets a perfect one-sided magnetic flux. (c): Discrete approximation of a Halbach cylinder using 2, 4, 6 and 8 poles: one approximates more and more closely an ideal Halbach cylinder, with a uniform field inside the cylinder, and a vanishing field outside.

havior can be obtained, and allows to understand how the Halbach dipole cylinder works: it is essentially a Halbach array rolled up with the appropriate radius such that the inside field is uniform.

We therefore designed a transverse Zeeman slower, of total length 1.2 m, by approximating the Halbach configuration using only eight dipoles with the appropriate orientation [see Figure 2.2(c)]. Elongated bar magnets of size $6 \times 6 \times 148$ mm, with the magnetization oriented along the small side, were arranged in Halbach configuration along the generatrices of a cone: the field is then very uniform, and its strength, controlled locally by the radius of the cone, varies according to the required parabolic profile to a very good approximation.

Based on this design, we build an increasing-field Zeeman slower, with a field varying from 200 G to 590 G, for a total cost of about 1 k€ only. The magnet assembly is enclosed in a soft-iron box, which serves both to hold mechanically the magnets and to

of a Halbach array. This can be checked easily: (i) these magnets 'stick' on a ferromagnetic material only on one side and (ii) if one tries to stick together two such magnets on their magnetic side, this occurs only at discrete positions, separated by about 3 mm: this is the period of the Halbach array.

avoid the leakage of stray magnetic fields outside the slower. An extra advantage of this approach is that the slower, made in two parts, can be fitted around the vacuum chamber *after* the bake-out, allowing for high-temperature baking. We tested the slower not only by demonstrating the slowing down of an atomic beam, but also by loading a magneto-optical trap, with loading rates exceeding 10^{10} at/s when about 100 mW of cycling light and 10 mW of repumper are used[4]. The results are detailed in [22]. Our design has recently been adapted for Sodium atoms, in an experiment under construction in the team of Aurélien Perrin at LPL in Villetaneuse, and is, at the time of writing, being tested [95].

2.3 A Bragg reflector for guided matter waves

A few years after the realization of Bose–Einstein condensation in alkali gases in 1995, several pioneering experiments demonstrated the outcoupling of matterwaves from a trapped BEC, realizing what was to become known as *atom lasers* [81, 3, 49, 17]. The obtained atom lasers were pulsed ones, with initially short bursts of atoms, and in later experiments much longer pulses, with durations of up to $\sim$ 100 ms, that were called *quasi-continuous* atom lasers. In those beautiful illustrations of the wave nature of atoms, the outcoupled matterwave was (i) propagating in free space, and (ii) falling under the influence of gravity. Both aspects are drawbacks in view of atom-optic experiments, as (i) gives rise to a decrease in brightness, while (ii) rapidly makes the de Broglie wavelength of the atoms very small.

Therefore, in a second generation of experiments, the idea emerged to use an horizontal dipole trap beam as a waveguide for matterwaves, to keep the wave transversely confined, and prevent at the same time the acceleration of the atoms due to gravity. In the pioneering work of [47], atoms were outcoupled from a magnetic trap using a RF knife to transfer them to a magnetically-insensitive state, and then guided horizontally. This configuration, where light guides a wave of matter, realizes the complete opposite of the (much more usual) guiding of light waves by matter along an optical fiber.

David Guéry-Odelin's group at ENS had been pursuing for several years the study of evaporative cooling of a magnetically guided atomic beam in view of achieving the operation of a truly CW atom laser. Despite the achievement of the collisional regime for the beam [73] and the demonstration of a gain of ten in phase-space density by RF-induced evaporation [74], it appeared that the achievement of a CW atom laser by evaporation of a beam would be extremely challenging technically. At about the time when I left ENS for Stuttgart, it was thus decided to reorient the activities of the group towards the study of guided, quasi-continuous atom lasers. An all-optical BEC of ^{87}Rb was first obtained in a crossed optical dipole trap, and outcoupling was achieved by controlled spilling of the BEC in the horizontal dipole trap beam. The group demonstrated that a careful control of the outcoupling process allowed to obtain guided atom lasers with very few excited transverse

[4] The repumper frequency is swept at $\sim$ 10 kHz over a range of $\sim$ 2 GHz (otherwise, to get the same flux out of the slower, higher repumping powers, on the order of 50 mW, are needed).

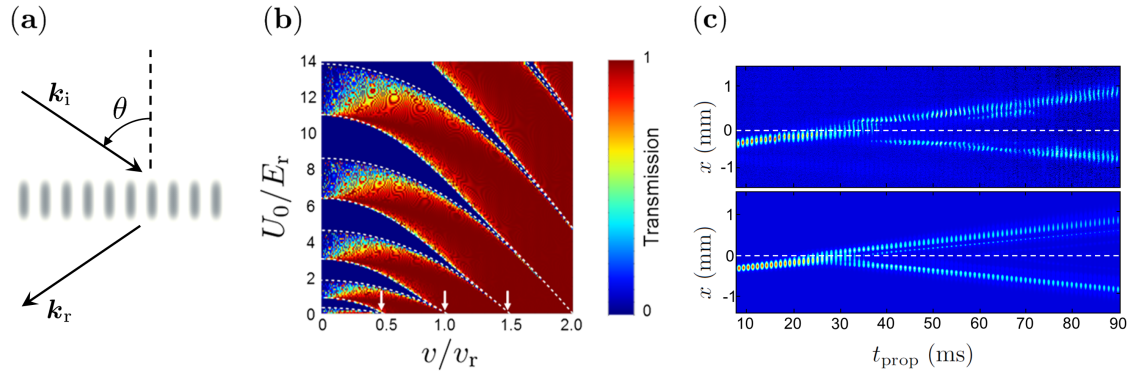

Figure 2.3: (a): Bragg reflection on a sinusoidal grating. (b) Transmission coefficient through a 800-site lattice, as a function of the incident velocity v and of the lattice depth U_0. The white arrows show the Bragg condition $v = nv_r/2$ obtained in the limit of a shallow lattice. (c) Atomic density along the guide after a propagation time t_{prop}: experimental result (top panel) and simulation without any adjustable parameter (bottom panel). The position of the Bragg reflector is shown by the white dashed line.

modes [28], i.e. a quasi-single-mode guided atom laser. The next logical step was then to implement some atom-optical equivalents of mirrors, beamsplitters....

In Toulouse, it was thus decided to pursue the exploration of guided atom optics, by trying to realize one of the simplest non-trivial atom-optical element, namely a distributed Bragg reflector. Bragg mirrors and beamsplitters realized with optical standing waves have been the workhorse of atom interferometry for three decades since their first demonstration in the 1980s [78]. Here, we studied how a matterwave packet interacts with an attractive periodic potential, of depth U_0, and spacing d, obtained by superimposing a one-dimensional optical lattice along the axis of the guiding beam.

The presence of the lattice introduces a typical velocity scale, the *recoil* velocity $v_r = h/(md)$, and an energy scale $E_r = mv_r^2/2$. In usual atom-optics experiments with relatively fast atoms, the periodic potential experienced by the atoms is very shallow as compared to their kinetic energy, and reflection is obtained for the usual Bragg condition

$$2d \sin\theta = n\lambda, \tag{2.2}$$

where n is an integer, d is the lattice spacing, and $\lambda = h/(mv)$ is the de Broglie wavelength of the particle, which impinges on the lattice at an angle θ (see Figure 2.3a). Here, we consider a distributed Bragg reflector with the periodic modulation along the propagation axis ($\theta = \pi/2$), so the Bragg condition (2.2) reads simply $v = nv_r/2$.

In our case, we deal with an ultraslow 'beam', and we thus need to revisit Bragg reflection for lattice potentials that can be deep with respect to the kinetic energy of the incident particles. Figure 2.3b shows the calculated transmission coefficient for a 800-site lattice, as a function of its depth U_0 (in units of E_r) and of the velocity v (in units of v_r) of the incident particle. For vanishing U_0, one recovers full reflection when the Bragg condition $v = nv_r$ is fulfilled (white arrows). However, for a finite depth of the lattice,

the transmission coefficient needs to be calculated by solving the Shrödinger equation in a sinusoidal potential. The Bloch theorem applies, and depending whether the incident energy lies within an allowed band or within a gap, the particle is transmitted or not. For an infinite lattice, one thus expects the transmission coefficient to be either 0 or 1, and, in the parameter plane (v, U_0), the boundaries between the two situations can be obtained by solving the Mathieu equation (dashed lines in Figure 2.3b). For a lattice with a finite number of sites, boundary effects change the picture only marginally at low velocities.

We experimentally implemented a Bragg reflector by intersecting two beams at an angle of about 80°, thus making a longitudinal, one-dimensional lattice along the guide, with a lattice spacing of 650 nm and a Gaussian envelope with a 145 μm rms half-width. We produced an all-optical BEC 350 μm upstream, released it in the guide, and then gave it a kick with a pulsed magnetic gradient, thus imparting it an initial mean velocity of 10 to 15 mm/s. The wavepacket had a velocity dispersion of about 1.3 mm/s set by the repulsive interactions during the initial release of the BEC. The top panel of Figure 2.3c shows the atomic density along the guide, for increasing propagation times. On observes that, when interacting with the lattice, the leading edge of the wavepacket (corresponding to high velocity components) is transmitted, while the trailing edge is reflected. The Bragg reflector thus acts as a dichroic mirror for matter waves, with a sharp cutoff in velocity space. The bottom panel is the result of a simulation of the time-dependent Schödinger equation without any adjustable parameter, and shows good agreement with the data. We also studied systematically the transmission of the reflector as a function of the depth of the optical lattice, and found good agreement with simulations.

2.4 Prospects

At the end of my time in Toulouse, we worked on a generalization of the Bragg reflector, using a time-dependent lattice: when its amplitude is modulated at a high frequency, new velocity classes can be reflected. We used this to demonstrate the principle of a notch velocity filter allowing to select very narrow velocity classes in a guided expanding cloud [24]. In another follow-up experiment, the team demonstrated the *trapping* of a launched BEC in the lattice, with the periodic emission, via tunelling, of wavepackets with a narrow velocity distribution [23].

In the future, it would be interesting to extend these studies along two directions:

- In the experiments described above, the effects of interparticle interactions are negligible. A first subject of study would thus concern the propagation of matter wave streams in the presence of significant interparticle interactions. In this case of *nonlinear* guided atom optics, new interesting effects appear [84].

- The other natural extension of those studies would consist in going beyond proof-of-principle experiments, towards useful applications. An appealing experiment would consist in realizing a matterwave interferometer using optically guided atoms, for

instance in a Mach–Zehnder geometry as proposed in [64]. For such studies, the integrated matter wave circuits recently demonstrated in [108] appear as an ideal platform.

For both goals, the current setup is not well adapted: a more stable experiment, with much more optical access, is needed. Therefore the group is currently working on a new setup, specially designed to overcome the above-mentioned shortcomings [12].

2.5 Published articles

Here, I list the articles I have co-authored about my work in LCAR; the main ones are reproduced in the following pages.

- C.M. Fabre *et al.*, Phys. Rev. Lett. **107**, 230401 (2011), reproduced on page 51.
- P. Cheiney *et al.*, Rev. Sci. Inst. **82** 063115 (2011) reproduced on page 56.
- P. Cheiney *et al.*, Phys. Rev. A. **87**, 013623 (2013).

Realization of a Distributed Bragg Reflector for Propagating Guided Matter Waves

C. M. Fabre, P. Cheiney, G. L. Gattobigio, F. Vermersch, S. Faure, R. Mathevet, T. Lahaye, and D. Guéry-Odelin

Université de Toulouse, UPS, Laboratoire Collisions Agrégats Réactivité, IRSAMC, F-31062 Toulouse, France and CNRS, UMR 5589, F-31062 Toulouse, France

(Received 27 July 2011; published 29 November 2011)

We report on the experimental study of a Bragg reflector for guided, propagating Bose-Einstein condensates. A one-dimensional attractive optical lattice of finite length created by red-detuned laser beams selectively reflects some velocity components of the incident matter wave packet. We find quantitative agreement between the experimental data and one-dimensional numerical simulations and show that the Gaussian envelope of the optical lattice has a major influence on the properties of the reflector. In particular, it gives rise to multiple reflections of the wave packet between two symmetric locations where Bragg reflection occurs. Our results are a further step towards integrated atom-optics setups for quasi-cw matter waves.

DOI: 10.1103/PhysRevLett.107.230401 PACS numbers: 03.75.Kk, 03.75.Lm

The interaction of light with structures having a periodic refractive index profile is ubiquitous in photonics. Applications range from simple antireflection coatings to the fabrication of dielectric mirrors with ultrahigh reflectivities, used for instance in high-finesse cavities, and to semiconductor laser technology with the example of vertical cavity surface-emitting lasers (VCSELs), and distributed feedback or distributed Bragg reflector lasers. In the field of guided optics, fiber Bragg gratings are essential components for the telecommunication industry, as well as for the realization of outcoupling mirrors in high-power fiber lasers. Photonic crystal devices also have a huge range of applications [1].

In matter wave optics and interferometry, interactions of free-space propagating beams or trapped clouds with periodic structures or potentials have been extensively investigated and are commonly used as mirrors and beam splitters [2–4]. In this Letter, we demonstrate, following the proposals of Refs. [5–9], a Bragg reflector for manipulating a guided Bose-Einstein condensate (BEC) propagating in an optical waveguide, i.e., the exact atom-optics counterpart of a photonic fiber Bragg grating. We study the dynamics and the transmission of a probe wave packet as a function of the depth of the optical lattice. As we will develop later on, this quasi-1D configuration clearly exemplifies two textbook features of quantum mechanics: quantum reflection [10–12] and band theory [13,14]. This Letter is organized as follows. We first present a simple model to gain some physical insight into the Bragg reflection of a matter wave packet by a finite-length lattice having a Gaussian envelope. Then we describe our experimental implementation and show quantitative agreement between the data and our model. Finally, we discuss numerical simulations that give access to unresolved details in the experiment.

We consider a BEC with given mean velocity $\bar{v}$ and dispersion Δv propagating in a horizontal waveguide defining the x axis. At some distance, two intersecting laser beams interfere and create an *attractive* quasiperiodic potential of finite length, with lattice spacing d (see Fig. 1).

The potential experienced by the atoms is modeled by

$$U(x) = -U_0 \exp\left(-\frac{2x^2}{\tilde{w}^2}\right)\sin^2\left(\frac{\pi x}{d}\right), \tag{1}$$

whose depth $U_0 > 0$ is proportional to the power of the laser beams. The period d naturally introduces typical scales in velocity $v_R = h/(md)$ and energy $E_R = mv_R^2/2$.

We are interested in a wave packet with finite size and velocity dispersion impinging on a finite-length lattice. Let us consider first the textbook case of an incident plane wave and a square-envelope lattice (see, e.g., [15] for an analytical treatment of the problem). Figure 2(a) shows the transmission coefficient for a lattice of $N = 800$ sites, calculated by solving numerically the corresponding stationary Schrödinger equation. For a given velocity v, one observes that the transmission coefficient essentially

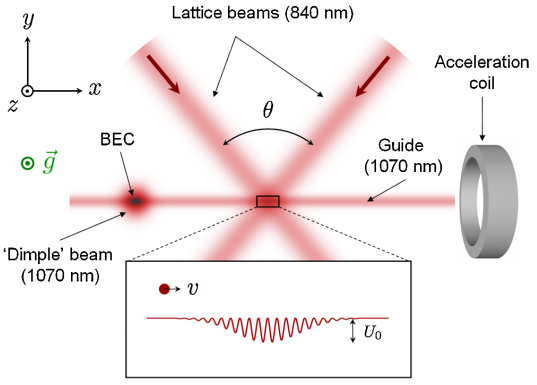

FIG. 1 (color online). Schematic view of the experimental setup (not to scale).

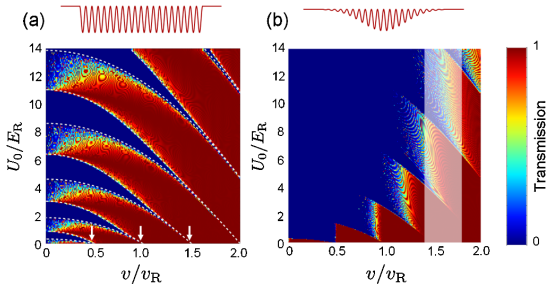

FIG. 2 (color online). Intensity transmission coefficient of the lattice for an incident plane wave of velocity v, as a function of the lattice depth U_0. (a) Square-envelope lattice with 800 sites. The white dashed lines are obtained from the Mathieu characteristic functions; white arrows show the velocities for which the Bragg condition is fulfilled (see text). (b) Lattice with a Gaussian envelope ($1/e^2$ radius $\tilde{w} \simeq 230d$). The vertical shaded stripe corresponds to the relevant velocity components in the wave packet used for the measurements shown in Figs. 3 and 4. The insets on top of (a) and (b) illustrate the shape of the lattice envelope, but the number of sites is reduced to $N = 20$ for clarity.

switches between 0 and 1 as a function of the depth of the lattice U_0. It can be interpreted as follows. At the entrance, the incoming state of energy $E_i = mv^2/2$ is projected onto the eigenstates of the lattice. The associated eigenenergies distribute into energy bands [13] whose position can be expressed in terms of the characteristic functions of the Mathieu equation [16,17] as depicted by the white dashed lines in Fig. 2(a). Reflection occurs if E_i lies in the gap between two allowed energy bands. Because of the finite length of the lattice the energy bands are not strictly continuous and resolve into N separate states for vanishing incident velocity [17]. Undersampling of the image gives rise to the "foamy" aspect of the low-velocity side of transmission bands. Obviously, the reflection by an *attractive* potential is a purely quantum effect, with no classical counterpart.

A second interesting feature appears in the limit of a vanishing potential depth U_0. One still observes reflection but it occurs only for incident velocities of the form $v = nv_R/2$ where n is an integer [see the white arrows in Fig. 2(a)]. This corresponds to Bragg's condition $2d\sin\Theta = n\lambda$ [14], where $\Theta = \pi/2$ for retroreflection, and $\lambda = h/(mv)$ is the incident de Broglie wavelength of the atoms: the reflection amplitude at each lattice site is small, but constructive interference between all the reflected waves results in a macroscopic reflected wave building up. For the range of parameters of Fig. 2(a), quantum reflection by a *single* lattice well occurs only for velocities that are very small as compared to v_R [17] and thus cannot explain the observed features.

Figure 2(b) shows the result of the same calculation, but now for the experimentally relevant case of a lattice having a smooth Gaussian envelope. One clearly observes a drastic change in the dependence of the transmission coefficient: for a fixed velocity v, the transmission is essentially equal to one only *below* a critical value $U_0^{(1)}$ of the lattice depth, and then goes essentially to zero for increasing U_0 (except for very narrow resonances). That critical value corresponds to the smallest one at which total reflection would occur for the square-envelope lattice. Almost no resurgence of the transmission is observed if U_0 is further increased, which gives a "sawtooth" appearance to the boundary between reflection and transmission.

This can be understood as follows. We are in the slowly varying envelope limit as $\tilde{w} \gg d$. The amplitude of the lattice does not change appreciably over a few sites, and thus one can consider that, locally, the matter wave interacts with a constant-amplitude lattice. When $U_0 = U_0^{(1)}$ the reflection condition is met at the center of the lattice, i.e., at $x = 0$. Then, for higher values of U_0, there are some locations $\pm x_{\mathrm{refl}}$, on both sides of the center, for which $U(\pm x_{\mathrm{refl}}) = U_0^{(1)}$. In this case, reflection occurs at $x = -x_{\mathrm{refl}}$. If there were not a second, identical mirror at $x = x_{\mathrm{refl}}$, the transmission of the lattice would strictly vanish for $U_0 > U_0^{(1)}$. However, as in optics, the two local Bragg mirrors actually constitute a Fabry-Perot resonator, analog to a VCSEL cavity for example, and transmission exhibits sharp resonances which gives the same foamy aspect as in Fig. 2(a).

We now come to the experimental realization. Our technique to produce all-optical BECs has been described in detail elsewhere [18]; in what follows we thus simply recall the major steps. We produce an almost pure ^{87}Rb condensate containing typically 5×10^4 atoms by forced evaporation over 4 s in a crossed optical dipole trap. It is made of two intersecting beams with a wavelength of 1070 nm. A horizontal one, with a waist of 50 μm, to be used later as a guide for the BEC, defines the $\hat{x}$ direction. The second, the "dimple" beam, of waist 150 μm, propagates along the diagonal in the (x, z) plane, $\hat{z}$ being the vertical (Fig. 1). Spin distillation using a magnetic field gradient during evaporation [18] results in the BEC being prepared in the state $|F = 1, m_F = 0\rangle$. We then decrease adiabatically the power in the dimple beam by a factor $\sim$20 over 80 ms, thus barely keeping a longitudinal confinement for the BEC, before switching it off abruptly to outcouple a wave packet in the horizontal guide. In this way, we produce a wave packet with a minimal intrinsic longitudinal velocity dispersion [19,20]. To set the wave packet in motion, we then switch on a coil, coaxial with the guide, that produces an inhomogeneous magnetic field. Through the quadratic Zeeman effect the wave packet is accelerated in 15 ms to a final mean velocity $\bar{v} = 11$ mm/s. The residual acceleration of the packet due to stray fields and beam curvature is negligible (we measure an upper bound of 10 mm/s^2).

Centered 350 μm downstream from the dimple location x_0, the optical lattice is produced at the intersection of two

beams with a wavelength $\lambda_L = 840$ nm (red-detuned with respect to the ^{87}Rb $D1$ and $D2$ lines) and a waist $w = 110$ μm, linearly polarized along $\hat{z}$, crossing at an angle $\theta \simeq 81°$. The lattice detuning is large enough so that spontaneous emission does not play any role in our experimental time scales. The resulting lattice spacing is $d = \lambda_L/[2\sin(\theta/2)] \simeq 650$ nm, and the envelope $1/e^2$ radius is $\tilde{w} = w/\cos(\theta/2) \simeq 145$ μm. In a set of preliminary experiments we calibrate the potential depth U_0 using Kapitza-Dirac (KD) diffraction [21,22]. A BEC is created at the position of the lattice and exposed to the lattice potential for a short time τ_{KD}, typically a few tens of microseconds. The diffraction pattern of the BEC after time of flight as a function of τ_{KD} is then compared to numerical simulations of the process. A typical 35 mW per beam results in U_0 up to $15E_R$.

After being launched as described above, the wave packet propagates in the horizontal guide for an adjustable time t_{prop}. Then all the lasers are switched off abruptly and the cloud is imaged by absorption after a 10 ms time of flight. This gives access to the spatial density distribution $n(x, t) = |\psi(x, t)|^2$ of the wave packet with a resolution of about 10 μm limited by the numerical aperture of our collection lens.

In a first set of experiments, the propagation time $t_{\mathrm{prop}} = 100$ ms is sufficiently long so that the interaction with the lattice is completed. We measured in a separate experiment the mean velocity $\bar{v} \simeq 11$ mm/s $\simeq 1.6v_R$ and a rms velocity spread $\Delta v \simeq 1.3$ mm/s $\simeq 0.2v_R$ corresponding to the shaded region of Fig. 2(b). For each lattice depth U_0, an average image is generated from eight individual runs and then integrated along the transverse direction $\hat{y}$. Figure 3(a) is a stack of 55 such profiles. For sake of comparison, Fig. 3(b) is the result of a numerical simulation of the wave packet dynamics using the one-dimensional Schrödinger equation solved by the split-Fourier method; the initial condition is a Gaussian wave packet with the experimentally measured momentum and position dispersions [19]. There is no adjustable parameter and the overall agreement with experimental data means that our simple 1D model captures most of the physics involved.

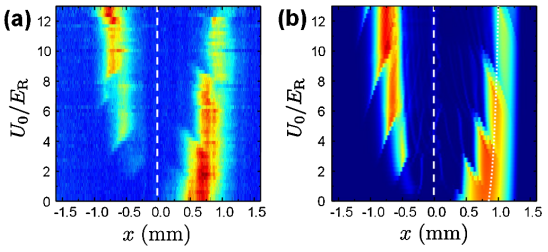

FIG. 3 (color online). (a) Measured density distribution of the wave packet (of initial mean velocity $\bar{v} = 11$ mm/s) after a propagation time $t_{\mathrm{prop}} = 100$ ms, for different lattice depths U_0. Each horizontal line is the average of typically eight absorption images integrated along the $\hat{y}$ direction. The vertical white dashed line shows the position of the center of the lattice. (b) Results of the simulation without any adjustable parameters. The finite resolution of the imaging system (~ 10 μm) is included. The dotted line is the expected position of the center of the wave packet according to classical dynamics (see text).

Let us concentrate first on the transmitted part of the wave packet ($x > 0$). If there were no lattice, the propagation time t_{prop} is long enough so that the initial size of the wave packet is negligible with respect to its size after propagation. The spatial distribution of the wave packet would then be a direct mapping of its initial velocity distribution $f(v)$: $n(x, t_{\mathrm{prop}}) \propto f[(x - x_0)/t_{\mathrm{prop}}]$.

One can then understand intuitively the main features of Fig. 3 for the scattering of a wave packet, from the transmission coefficients shown in Fig. 2(b) for a plane wave. In the background of the shaded area of Fig. 2(b) representing the wave packet one can see the transmitted and reflected components. In the presence of the lattice, the reflected part propagates backwards and is located, for the propagation time chosen here, at a symmetrical position. This explains why the transmitted and reflected wave packets appear like a complementary mirrored image of each other. The sawtoothlike boundary, reminiscent of the transmission diagram, is a fingerprint of the band structure inside the lattice. However, the effect of the lattice potential is not limited to the one of the sinusoidal component, responsible for the Bragg reflection described above. The spatially averaged attractive potential also accelerates the wave packet. The white dotted line in Fig. 3(b) shows the final position of a classical particle starting with velocity $\bar{v}$ from position x_0 and propagating for a time t_{prop}, taking into account its acceleration by the spatially averaged lattice potential. The fair agreement with the data indicates that the slight curvature in the position of the wave packet as a function of U_0 simply arises from this classical effect.

Beyond studying the asymptotic scattering states, it is also possible to visualize the dynamics of the interaction by varying t_{prop}. Figure 4(a) displays such a time sequence that fairly compares to the numerical simulation depicted in the same conditions in Fig. 4(b). One clearly observes the spreading of the incident wave packet over the whole lattice for $30 \lesssim t_{\mathrm{prop}} \lesssim 45$ ms and its subsequent splitting into a reflected and a transmitted one. Unfortunately, the details of the inner dynamics are washed out by the free expansion of the wave packet during the time-of-flight sequence and the finite resolution of the imaging system.

Numerical simulations, properly checked against the previous experimental results, are useful here. In Fig. 4(c) we have deliberately suppressed the time-of-flight period and enhanced the optical resolution and the contrast with respect to Fig. 4(b): one then clearly observes multiple reflections of some components of the wave packet at symmetric positions $\pm x_{\mathrm{refl}}$, with decreasing amplitude at

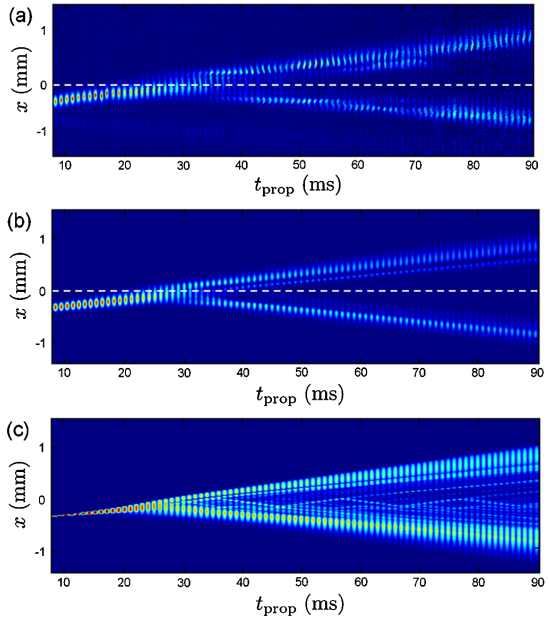

FIG. 4 (color online). Time sequence showing the scattering of a wave packet with mean velocity $\bar{v} \simeq 11$ mm/s on the optical lattice for $U_0 \simeq 11E_R$. The white dashed lines in (a) and (b) show the position of the center of the lattice. The time interval between successive images is 1 ms. (a) Experimental data. (b) Simulation, taking into account the finite imaging resolution as well as the time of flight (TOF) period. (c) Same as (b) but without TOF nor reduced resolution; the color scale is nonlinear in order to enhance contrast.

each bounce. This "cavity-ring-down" behavior explains the formation of structures in the transmitted and reflected wave packets as observed in Fig. 4(a) and especially visible as a parallel lower stripe in the transmitted wave packet for $50 \lesssim t_{\mathrm{prop}} \lesssim 75$ ms. However, experimentally, observing several bounces is not possible here due to the small number of atoms involved.

In the same way, in images such as Fig. 3 the reflected wave packet appears to be relatively smooth. It is actually not the case, as can be seen in simulations with full resolution (Fig. 5). The lattice acts as a matter wave interference filter with very narrow features due to the high number of lattice sites (foamy zones of Fig. 2).

Until now we have used a simple one-dimensional description of the system. However, the system is actually far from being one dimensional, since the transverse quantum of energy $\hbar\omega_\perp \simeq h \times 90$ Hz is much smaller than the typical longitudinal energy scales, typically by 2 orders of magnitude. Our simple one-dimensional model agrees well with the experimental results as shown above because couplings between longitudinal and transverse degrees of freedom are weak (they are due only to experimental

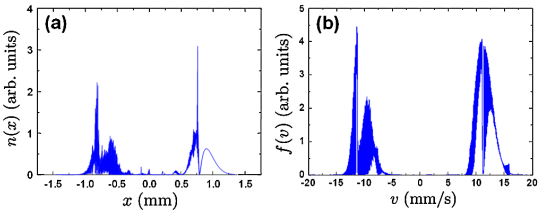

FIG. 5 (color online). (a) Calculated density and (b) velocity distribution of a wave packet of initial mean velocity $\bar{v} = 11$ mm/s after a propagation time $t_{\mathrm{prop}} = 100$ ms with full resolution. The lattice depth is $U_0 = 8E_R$.

imperfections such as misalignments of the lattice beams with respect to the guide, for instance); some transverse excitations can nevertheless be observed on our data [see, e.g., the long wavelength dipole oscillations in Fig. 4(a), especially for $t_{\mathrm{prop}} \gtrsim 30$ ms]. Stronger couplings would be expected to significantly alter the scattering properties of the structure [23,24].

In conclusion, we have studied in detail the scattering of a guided matter wave by a finite-length optical lattice in the slowly varying envelope limit. The experiments can be interpreted in the framework of a local band structure, and the whole lattice can be seen as a cavity based on Bragg mirrors.

Major improvements are expected with the use of high numerical aperture optics [25,26]. Drastically reducing the length $\tilde{w}$ of the lattice and thus generating a structure consisting of only a few sites, possibly with a shaped envelope, one could tailor almost arbitrarily the matter wave filter response. The latter can also be altered using a moving optical lattice [27,28]. The transmission band of the filter could then be adjusted at will. Such setups would prove useful in measuring, for instance, the coherence length [29] of guided atom lasers [30–32]. In a different direction, it would be appealing to study the effect of interatomic interactions [33] on the propagation of the wave packet, with the possible appearance of soliton trains [34] or atom-blockade effects [35]. This regime could be reached by using much higher transverse frequencies for the guide, in order to enhance the effects of nonlinearities.

We thank I. Carusotto for useful discussions, and acknowledge support from Agence Nationale de la Recherche (GALOP project), Région Midi-Pyrénées, and Institut Universitaire de France.

[1] B. E. A. Saleh and M. C. Teich, *Fundamentals of Photonics* (Wiley InterScience, New York, 2007).
[2] A. D. Cronin, J. Schmiedmayer, and D. E. Pritchard, Rev. Mod. Phys. **81**, 1051 (2009).
[3] D. E. Pritchard *et al.*, Ann. Phys. (Leipzig) **10**, 35 (2001).
[4] S. L. Rolston and W. D. Phillips, Nature (London) **416**, 219 (2002).

[5] L. Santos and L. Roso, J. Phys. B **30**, 5169 (1997).
[6] L. Santos and L. Roso, Phys. Rev. A **58**, 2407 (1998).
[7] N. Friedman, R. Ozeri, and N. Davidson, J. Opt. Soc. Am. B **15**, 1749 (1998).
[8] I. Carusotto, M. Artoni, and G. C. La Rocca, Phys. Rev. A **62**, 063606 (2000).
[9] T. Lauber *et al.*, J. Phys. B **44**, 065301 (2011).
[10] C. Cohen-Tannoudji, B. Diu, and F. Laloë, *Quantum Mechanics* (Wiley, New York, 1977).
[11] F. Shimizu, Phys. Rev. Lett. **86**, 987 (2001).
[12] T. A. Pasquini *et al.*, Phys. Rev. Lett. **93**, 223201 (2004).
[13] C. Kittel, *Introduction to Solid-State Physics* (Wiley, New York, 1953).
[14] N. W. Ashcroft and N. D. Mermin, *Solid State Physics* (Saunders, Philadelphia, PA, 1976).
[15] D. W. L. Sprung, H. Wu, and J. Martorell, Am. J. Phys. **61**, 1118 (1993).
[16] N. W. McLachlan, *Theory and Application of Mathieu Functions* (Oxford University Press, Oxford, 1947).
[17] See Supplemental Material at http://link.aps.org/supplemental/10.1103/PhysRevLett.107.230401 for more details.
[18] A. Couvert *et al.*, Europhys. Lett. **83**, 50001 (2008).
[19] Nonlinearities due to atom-atom interactions are negligible for the dilute wave packets studied here, and thus are not accounted for in the simulation (the chemical potential of the BEC when it reaches the lattice is on the order of $0.1E_R$, and thus negligible as compared to any longitudinal energy scale). The only effect of interactions is to set (in addition to the quantum pressure) the velocity dispersion of the wave packet in the initial stages of the expansion in the guide, by conversion of the interaction energy of the BEC into kinetic energy. For more details, see [20].
[20] F. Vermersch *et al.*, Phys. Rev. A **84**, 043618 (2011).
[21] B. Gadway *et al.*, Opt. Express **17**, 19173 (2009).
[22] J. H. Huckans *et al.*, Phys. Rev. A **80**, 043609 (2009).
[23] G. L. Gattobigio, A. Couvert, B. Georgeot, and D. Guéry-Odelin, New J. Phys. **12**, 085013 (2010).
[24] G. L. Gattobigio, A. Couvert, B. Georgeot, and D. Guéry-Odelin, arXiv:1105.1971.
[25] Y. R. P. Sortais *et al.*, Phys. Rev. A **75**, 013406 (2007).
[26] K. Henderson *et al.*, New J. Phys. **11**, 043030 (2009).
[27] L. Fallani *et al.*, Phys. Rev. Lett. **91**, 240405 (2003).
[28] B. Eiermann *et al.*, Phys. Rev. Lett. **91**, 060402 (2003).
[29] M. Köhl, T. W. Hänsch, and T. Esslinger, Phys. Rev. Lett. **87**, 160404 (2001).
[30] W. Guérin *et al.*, Phys. Rev. Lett. **97**, 200402 (2006).
[31] J. Billy *et al.*, Ann. Phys. (Paris) **32**, 17 (2007).
[32] A. Bernard *et al.*, New J. Phys. **13**, 065015 (2011).
[33] O. Morsch and M. K. Oberthaler, Rev. Mod. Phys. **78**, 179 (2006).
[34] I. Carusotto, D. Embriaco, and G. C. La Rocca, Phys. Rev. A **65**, 053611 (2002).
[35] I. Carusotto, Phys. Rev. A **63**, 023610 (2001).

A Zeeman slower design with permanent magnets in a Halbach configuration

P. Cheiney,[1,2] O. Carraz,[1,2] D. Bartoszek-Bober,[3] S. Faure,[1,2] F. Vermersch,[1,2]
C. M. Fabre,[1,2] G. L. Gattobigio,[1,2] T. Lahaye,[1,2] D. Guéry-Odelin,[1,2] and R. Mathevet[1,2,a)]
[1]*Université de Toulouse, UPS - 118 route de Narbonne, F-31062 Toulouse, France*
[2]*CNRS, UMR 5589, Laboratoire Collisions Agrégats Réactivité, IRSAMC - F-31062 Toulouse, France*
[3]*Marian Smoluchowski Institute of Physics, Jagiellonian University, Cracow, Poland*

(Received 13 January 2011; accepted 28 May 2011; published online 29 June 2011)

We describe a simple Zeeman slower design using permanent magnets. Contrary to common wire-wound setups, no electric power and water cooling are required. In addition, the whole system can be assembled and disassembled at will. The magnetic field is however transverse to the atomic motion and an extra repumper laser is necessary. A Halbach configuration of the magnets produces a high quality magnetic field and no further adjustment is needed. After optimization of the laser parameters, the apparatus produces an intense beam of slow and cold ^{87}Rb atoms. With typical fluxes of (1–5) $\times 10^{10}$ atoms/s at 30 m s^{-1}, our apparatus efficiently loads a large magneto-optical trap with more than 10^{10} atoms in 1 s, which is an ideal starting point for degenerate quantum gas experiments.
 [doi:10.1063/1.3600897]

I. INTRODUCTION

Nowadays, many atomic physics experiments study or use quantum degenerate gases for which a large initial sample of cold atoms is required. A wide variety of experimental techniques has been developed for slowing and cooling atoms. Many of them rely on the radiation pressure from quasi-resonant light. In particular, since their first realization,[1] Zeeman slowers have become very popular for loading magneto-optical traps (MOT). These cold atom reservoirs are then an ideal starting point to implement other techniques for further cooling.

Recently, several Zeeman slowers using permanent magnets have been built[2] following the proposal of Ref. 3 (see also Ref. 4 for a somewhat different approach formerly used). Here, we present an alternative design based on a Halbach configuration[5] of the magnets and demonstrate fully satisfactory operation. Before going into details, let us emphasize some advantages of the setup:

- simple machining and construction, compact, and light,[6]
- no electric power consumption nor water cooling,
- high fields with excellent transverse homogeneity,
- very smooth longitudinal profile and low stray magnetic fields,
- easy to assemble and disassemble without vacuum breaking, e.g., for high-temperature baking out.

This paper is organized as follows. In Sec. II, we first give the basics of the theoretical framework and then compare our permanent magnets approach with the usual wire-wound technique. Then we collect in Sec. III some information on magnets, shields, field calculations, and measurements useful to characterize our setup described in Sec. IV. We subsequently detail in Sec. V the whole experimental apparatus before we finally present the Zeeman slower performances in Sec. VI.

II. ZEEMAN SLOWERS DESIGNS

A. Notations and field specifications

In a Zeeman slower, atoms are decelerated by scattering photons from a near resonant counter propagating laser. Let Oz denote the mean atom and light propagation axis, Γ and μ the linewidth and magnetic moment of the atomic transition, $\boldsymbol{k}$ the light wave vector, m the atomic mass, and $v(z)$ the velocity at z of an atom entering the field at $z = 0$. To keep atoms on resonance, changes in the Doppler shift $kv(z)$ are compensated for by opposite changes of the Zeeman effect $\mu B(z)$ in an inhomogeneous magnetic field $B(z)$.[7] We use an *increasing field* configuration[8] for better performance with ^{87}Rb.

As the scattering rate cannot exceed $\Gamma/2$, the maximum achievable acceleration is

$$a_{\max} = \frac{\Gamma}{2}\frac{\hbar k}{m}. \tag{1}$$

To keep a safety margin, the ideal magnetic field profile $B_{\mathrm{id}}(z)$ is calculated for only a fraction $\eta = 0.75$ of $a_{\max}$. Energy conservation reads $v(z)^2 = v(0)^2 - 2\eta a_{\max} z$ so that

$$B_{\mathrm{id}}(z) = B_{\mathrm{bias}} + \Delta B(1 - \sqrt{1 - z/L}), \tag{2}$$

where the length of the apparatus is $L = v(0)^2/2\eta a_{\max}$ and $\mu\Delta B/\hbar = kv(0)$ assuming $v(L) \ll v(0)$. Here, $v(0)$ defines the capture velocity as, in principle, all velocity classes below $v(0)$ are slowed down to $v(L)$. A bias field B_{bias} is added for technical reasons discussed later on (Sec. IV C 1). To match the resonance condition, lasers must be detuned from the atomic transition by

$$\delta_0 \approx \mu(B_{\mathrm{bias}} + \Delta B)/h. \tag{3}$$

a)Electronic mail: renaud.mathevet@irsamc.ups-tlse.fr.

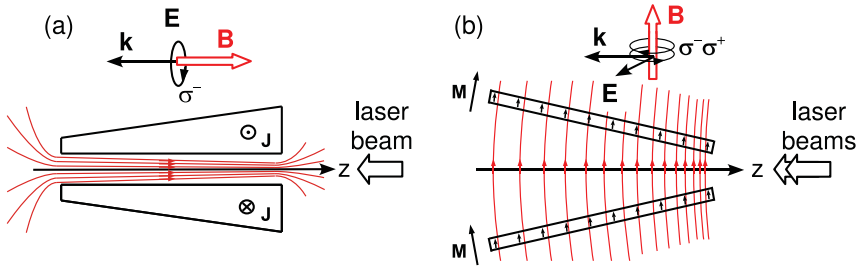

FIG. 1. (Color online) Zeeman slower configurations. (a) Conventional wire-wound tapered solenoid; magnetic field is longitudinal, σ^- light is used. $\boldsymbol{J}$ denotes the current density vector. (b) Use of long tilted permanent magnets; magnetic field is transverse. Light polarisation is decomposed in its $\sigma^\pm$ components and a repumper is needed. $\boldsymbol{M}$ denotes the magnetization of the material.

Finally, slowing must be efficient over the whole atomic beam diameter. A conservative estimate of the acceptable field variations in a cross section is $\delta B = h\Gamma/|\mu|$ which amounts to $\sim$4 G given the rubidium linewidth $\Gamma \approx 2\pi \times 6$ MHz. Here, such high transverse homogeneity, intrinsic to solenoids, is achieved using permanent magnets in a particular geometry inspired by Halbach cylinders. This represents a major improvement with respect to the original proposal[3] which the reader is also referred to for a more detailed theoretical analysis.

B. Different implementations

1. Wire-wound vs permanent magnets slowers

In most Zeeman slowers, the magnetic field is generated with current flowing in wires wound around the atomic beam. The ideal profile of Eq. (1) is commonly obtained varying the number of layers (Fig. 1(a)) or more recently the winding pitch.[9] The field is then essentially that of a solenoid: longitudinal and very homogeneous in a transverse plane. There are usually some drawbacks to this technique. Winding of up to several tens of layers has to be done with care to get a smooth longitudinal profile. It represents hundreds of meters and typically 10 kg of copper wire so the construction can be somewhat tedious. It is moreover done once for all and cannot be removed later on. As a result, only moderate baking out is possible which may limit vacuum quality. Finally, electric power consumption commonly amounts to hundreds of watts so water cooling can be necessary.

Of course, the use of permanent magnets circumvents these weak points. In the original proposal,[3] two rows of centimeter-sized magnets are positioned on both sides of the atomic beam. Contrary to wire-wound systems the field is thus transverse.[10] Fortunately, slowing in such a configuration is also possible.[11] Although this initial design is very simple, the field varies quickly off axis, typically several tens of Gauss over the beam diameter, which may reduce the slower efficiency.

2. Halbach configuration

A way to get a well controlled magnetic field in a transverse cross section is to distribute the magnetic material all around the atomic beam to make a so-called Halbach cylinder. In the context of atom physics, fields with a linear or quadratic dependence have been used to realize refractive atom-optical components.[12,13] Here a highly uniform field is required. Following Ref. 5 let us consider a magnetized rim such that the magnetization $\boldsymbol{M}$ at an angle θ from the y-axis makes an angle 2θ with respect to the same axis (Fig. 2(a)). Then, the magnetic field reads

$$\boldsymbol{B}_{\mathrm{Hal}}(\boldsymbol{r}) = \begin{cases} \boldsymbol{0}, & \text{for} \quad r > R_{\mathrm{ext}}, \\ B_{\mathrm{R}} \ln\left(\dfrac{R_{\mathrm{ext}}}{R_{\mathrm{int}}}\right) \hat{\boldsymbol{y}}, & \text{for} \quad r < R_{\mathrm{int}}, \end{cases}$$

where B_{R} is the remanent field of the magnetic material, commonly in the 10–15 kG range for modern rare-earth magnets. Numerical investigations (see Sec. III) indicate that a 8-pole Halbach-like configuration as depicted in Fig. 2(b) is able to produce fields on the order of 600 G with homogeneity better than 1 G on a 16 mm cross section. Higher field strength and/or beam diameters are easy to achieve if necessary.

More detailed studies demonstrate that deviations on a typical 600 G magnetic field stay below the $\pm$1 G limit for $\pm$0.2 mm mispositioning of the magnets, which is a common requirement on machining. Likewise, the same variations are observed for $\pm$2.5% dispersion in the strength of the magnets. This value is consistent with a rough statistical analysis we made on a sample of 25 magnets.

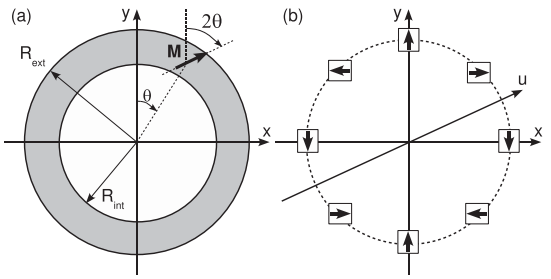

FIG. 2. (a) Notations for Halbach cylinder. (b) Transverse cross section showing a 8-pole Halbach configuration.

III. FIELD CALCULATIONS

A. Magnets modeling

1. Magnetic material

Our setup uses long $2a \times 2b \times 2c = 6 \times 6 \times 148$ mm^3 NdFeB magnets (HKCM, part number: Q148x06x06Zn-30SH). They are made from 30 SH grade which has a higher maximum operation temperature than other grades. Its remanent field $B_R = 10.8$ kG is also lower. The device is thus more compact and outer field extension is reduced. Such rare-earth material is very hard from a magnetic point of view so very little demagnetization occurs when placed in the field of other magnets, at least in our case where fields do not exceed the kilogauss range. This makes field calculations particularly simple and reliable. Even if an exact formula for the field of a cuboid magnet can be found,[14] in many cases, it can be replaced with an ease to handle dipole approximation.

2. Dipole approximation

In the proposed geometry described below, the magnets have a square cross section ($2b = 2a$) and the long magnets can be decomposed in a set of cubic magnets with side $2a$. Then, one easily checks numerically that when the distance to the magnet is larger than twice the side, the field of the associated dipole is an accurate approximation of that of the actual magnet to better than 2%.[15] It is not a very restrictive condition as in our case, $2a = 6$ mm and magnets cannot be located nearer than 11 mm from the beam axis.

A full vector expression of the field of a dipole can be found in any textbook. It is well adapted for computer implementation. Even if the full magnetic system is then represented by more than 1500 dipoles, calculations are still very fast: the simulations presented in Sec. IV take less than 1 s on a conventional personal computer.[14]

B. Magnets layout

In principle, the field magnitude can be adjusted varying the amount, the density and/or the position of the magnetic material. The availability of very elongated magnets ($c/a \approx 25$) directed us toward a simple layout. Only the distance to the axis $d(z)$ is varied. At first approximation, the magnets can be considered as infinite. The magnetic field strength then decreases as the inverse of the distance squared. So, to produce the field $B(z)$ a good ansatz for $d(z)$ is

$$d(z) = d(L)\sqrt{\frac{B(L)}{B(z)}}. \tag{4}$$

As a matter of fact, this guess turns out to be both very efficient and close to a linear function. Numerical calculations show (Fig. 3) that a linear approximation of Eq. (4) can be optimized to give a field within ± 3 G from the ideal one over the most part of the slower. Such deviations are completely irrelevant concerning the longitudinal motion. Magnets are then positioned on the generatrices of a cone and the mechanics is straightforward (Sec. IV A).

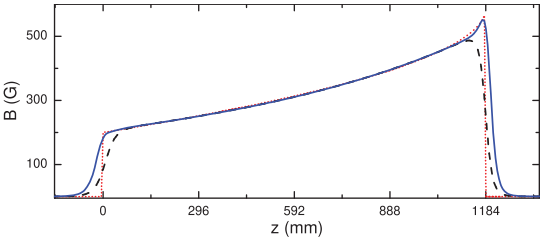

FIG. 3. (Color online) Ideal (red/dotted) and calculated profiles, without (black/dashed) and with (blue/solid) end caps.

Naturally, the agreement is not so good at both ends where the ideal profile has sharp edges, while the actual field spreads out and vanishes on distances comparable to the diameter on which magnets are distributed. The actual ΔB is reduced which lowers the capture velocity and thus the beam flux. We made additional sections of eight extra cubic magnets in a Halbach configuration designed to provide localized improvement on the field profile at both ends ("*end caps*"). As seen in Fig. 3, matching to the ideal profile is enhanced, especially at the high field side where the ideal profile exhibits a marked increase.

The length of the Zeeman slower is $L = 1184$ mm corresponding to eight sections of 148 mm-long magnets. The capture velocity is then $v(0) = (2\eta a_{\max} L)^{1/2} \approx 450$ m s^{-1} and $\Delta B = 388$ G. A bias field $B_{\text{bias}} = 200$ G is added to avoid low-field level crossings around 120 G. These field parameters together with the magnet size and properties determine the distance and angle from axis of the magnets. In our case, the best choice was a slope of -15.9 mm/m corresponding to $d(0) = 49.5$ mm and $d(L) = 30.7$ mm. Entrance and output end caps are both made of 10 mm-side cubic magnets of N35 grade ($B_R = 11.7$ kG). They are located on circles whose diameters are 94.0 mm and 66.0 mm, respectively.

IV. MECHANICS AND FIELD MEASUREMENTS

A. Mechanical design

The Zeeman slower consists in nine mounts supporting eight U-shaped aluminum profiles (Fig. 4). The U-shaped profiles go through the mounts by means of square holes evenly spaced on a circle whose diameter decreases from mount to mount according to Eq. (2) and Eq. (4) possibly linearized. Magnets are then inserted one after each other in the U-shaped profiles and clamped by a small plastic wedge. End caps are filled with the suitable block magnets and screwed together with their spacer in the first and last mount (see Fig. 4(a)). The whole setup is then rigid and all parts tightly positioned. Indeed, as said before, calculations are very reliable and Zeeman slower operation is known to be robust so there is no need for adjustment. Mounts are made of two parts screwed together. The Zeeman slower can then be assembled around the CF16 pipe without vacuum breaking, e.g., after baking out the UHV setup.[14]

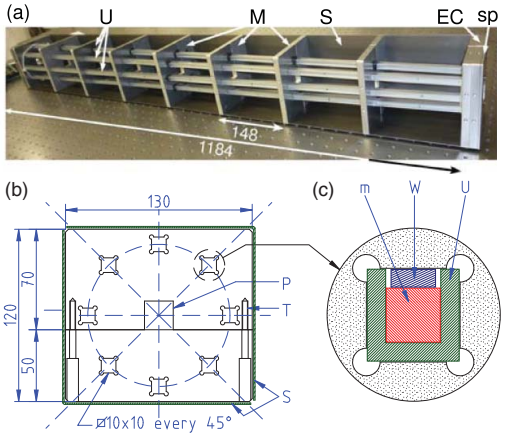

FIG. 4. (Color online) (a) Picture of the Zeeman slower: [M] mounts, [EC] output end cap screwed in last mount, [U] U-shaped profiles, [S] half part of the shield, [sp] 5 mm spacer between end cap and shield side. (b) Individual mount; [T] threading to screw the two parts of the mount together, [P] central square milling in which CF16 pipe goes through. (c) Detail of a square hole to show U-shaped profiles insertion, magnets [m], and plastic wedge [W]. Dimensions in mm.

B. Shielding

Stray magnetic fields might strongly affect atomic physics experiments. Actually, the 8-pole configuration produces very little field outside (see Fig. 6(a)), except of course, at both ends. However, to lower stray fields even further, we have made a rectangular single-layer shield from a 1 mm-thick soft iron sheet wrapped around the mounts. Besides, mechanical properties and protection are also improved. As seen in Fig. 5(a), the inner field is almost unaffected. On the contrary, the outer magnetic field falls down much quicker all the more since the plateau around 0.5 G in Fig. 5(b) is probably an artifact associated with the probe. In practice, no disturbance is detected on the MOT and even on optical molasses 125 mm downstream.[14]

C. Magnetic field and lasers characterization

1. Magnetic field

Magnetic field measurements are done with a home-made 3D probe using 3 Honeywell SS495 Hall effect

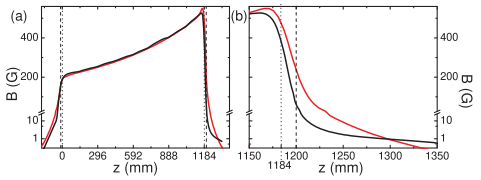

FIG. 5. (Color online) Calculated (red/gray) and measured (black) magnetic field profiles. (a) Scan along the beam axis. (b) Close up of the output region. In the calculation the shield is not taken into account. Dotted and dashed lines indicate the Zeeman slower and the shield physical ends. Log scale before break.

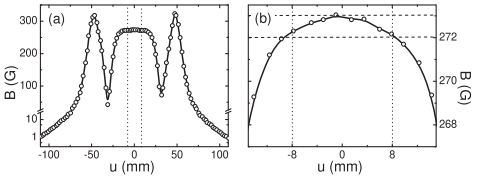

FIG. 6. (a) Measured magnetic field without shield across the beam axis at $z \sim 460$ mm along the u-direction of Fig. 2. (b) Close up of the central region. Dashed lines indicate the atom beam extension and a 1 G magnetic field span. Line to guide the eye. Log scale before break. The shield was removed to allow the probe to go through. With the shield, the inner field is almost unaffected and the outer field is below the probe sensitivity.

sensors.[14] Figure 5 displays a longitudinal scan of the magnetic field on the axis of the Zeeman slower with end caps and shield. It can be first noticed that the longitudinal profile is intrinsically very smooth as the magnets make a uniform magnetized medium throughout the Zeeman slower. After calibration of the magnetic material actual remanent field, deviations from the calculated profile are less than a few Gauss. Besides, one usually observes only localized mismatches attributed to the dispersion in the strength of the magnets. The shield input and output sides flatten the inner field at both ends. Of course the effect decreases when they get further apart but the Zeeman slower should not be lengthened too much. A 5 mm spacer (tag [sp] in Fig. 4) is a good trade-off. Then, the actual magnetic field measured parameters are $B_{\text{bias}} = 200$ G and $\Delta B = 350$ G only slightly smaller than the calculated value.

Figure 6 depicts a transverse cut of the magnetic field. It is realized along the u-direction of Fig. 2 near the middle of the Zeeman slower ($z \sim 460$ mm). The shield was removed to allow the probe to go through. It exhibits the two expected features: (i) little outer field and (ii) highly homogeneous inner field. In the vicinity of the axis, the measured profile is however less flat than expected. This is mainly due to the finite size of the probe. Anyway, magnetic field deviations stay within a Gauss or so in the region of interest. With the shield, the outer field is below probe sensitivity.

2. Lasers

The Zeeman slower operates between the $5^2S_{1/2}$ and $5^2P_{3/2}$ states of ^{87}Rb around $\lambda = 780$ nm (D2 line). For an increasing-field Zeeman slower, a closed σ^- transition is required,[8] $F = 2$, $m_F = -2 \leftrightarrow F' = 3$, $m_{F'} = -3$ in our case. However, the magnetic field is here perpendicular to the propagation axis. Thus, any incoming polarization state possesses *a priori* π and $\sigma^\pm$ components: it is not possible to create a pure σ^- polarization state (see Fig. 1 and Ref. 16). In addition to laser power losses, the π and σ^+ components excite the $m_{F'} = -2$ and -1 states from which spontaneous emission populates $F = 1$ ground state levels. Repumping light is thus necessary between the $F = 1$ and $F' = 2$ manifolds. The detrimental effect of the unwanted polarization components is minimized when the incoming polarization is perpendicular to the magnetic field since there is no π contribution in that case. We measured a 20° (FWHM) acceptance for the polarization alignment.

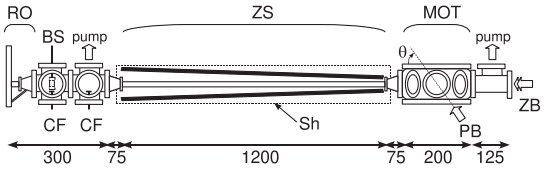

FIG. 7. Sketch of the overall experimental setup. [RO] recirculating oven, [BS] beam shutter, [CF] cold finger, [ZS] Zeeman slower, [MOT] MOT chamber, [ZB] Zeeman cycling and repumping beams, [PB] $\theta = 56°$ probe beam, and [Sh] magnetic shield. 45° and 90° probe beams are sent through the horizontal windows depicted on the MOT chamber. Dimensions in mm, not rigorously to scale.

Permanent magnets enable easily to reach magnetic fields on the order of $B_{\text{bias}} + \Delta B \approx 500 - 600$ G. As a consequence, detuning of the cycling light below the transition frequency amounts to $\delta_0 \approx -800$ MHz (Eq. (3)). Such high detunings are realized sending a master laser through two double pass 200 MHz AOMs before locking on a resonance line using saturation spectroscopy. The repumper is simply locked on the red-detuned side of the broad Doppler absorption profile.

The two master lasers are Sanyo DL7140-201S diodes having a small linewidth (∼5 MHz). We use them without external cavity feedback. Beams are recombined on a cube and pass through a polarizer. Then they are sent with the same polarization into a 1 W Tapered Amplifier (Sacher TEC-400-0780-1000). A total power of more than 250 mW is available on the atoms after fiber coupling. The beam is expanded to about 23 mm (full width at $1/e^2$) and focused in the vicinity of the oven output aperture for better transverse collimation of the atomic beam.

V. EXPERIMENTAL APPARATUS

A. Vacuum system

Figure 7 shows a sketch of the experimental setup. At one end, the MOT chamber is a spherical octagon from Kimball physics (MCF600-SO200800). It has two horizontal CF100 windows and eight CF40 ports. It is pumped by a 20 L/s ion pump. One CF40 port is connected to the 1200 mm-long CF16 pipe around which the Zeeman slower is set. At the other end, one finds a first six-way cross, used to connect a 40 L/s ion pump, a thermoelectrically cooled cold finger and two windows for beam diagnosis. It is preceded by a second six-way cross that holds another cold finger, a angle valve for initial evacuation of the chamber and a stepper-motor-actuated beam shutter. Finally, the in-line port holds the recirculating oven.[14]

B. Probe beams

Probe beams on the $F = 2 \leftrightarrow F' = 3$ transition can be sent in the chamber through the different windows and absorption is measured in this way at 45°, 56°, or 90° from the atomic beam. Absorption signals are used to calibrate fluorescence collected through a CF40 port by a large aperture condenser lens and focused on a 1 cm^2 PIN photodiode (Centronics OSD 100-6). Photocurrent is measured with a homemade transimpedance amplifier (typically 10 MΩ) and a low-noise amplifier (Stanford Research Systems SR560) used with a moderate gain ($G = 5$) and a 3 kHz low-pass filter. Frequency scans are recorded on a digital oscilloscope and averaged for 8–16 runs. During the measurements, a repumper beam on the $F = 1 \rightarrow F' = 2$ transition may be turned on.

VI. ZEEMAN SLOWER PERFORMANCES

A. Atom flux

Figure 8 displays typical fluorescence and absorption signals. The oven base temperature was set to $T_1 = 190\,°\text{C}$ so that fluorescence of the thermal unslowed beam is clearly visible. When Zeeman light is on, a sharp peak at low velocity appears both in the fluorescence and absorption spectra. Detuning of the cycling light in that experiment is such that the final velocity is about 25 m s^{-1}.

These signals are recorded scanning the frequency of a probe beam making an angle θ with the atomic beam. A given detuning Δ of the probe from resonance corresponds to the excitation of the velocity class $v = \lambda\Delta/\cos\theta$. The absorption signal $A(\Delta)$ is then converted into $A(v)$ as in Fig. 8 from which typical output velocity $\overline{v}$, velocity spread δv, and maximum absorption $A_{\max}$ can be estimated. The atom flux Φ then reads

$$\Phi = c \sin\theta \cos\theta D \frac{A_{\max}\overline{v}\delta v}{\lambda\Gamma\sigma_0}, \tag{5}$$

where c is a numerical parameter near unity;[14] Γ, σ_0, and D denote the transition decay rate, the resonant cross section, and atomic beam diameter.

On a separate experiment, we spatially scan a small probe beam across the atomic beam. The atom density exhibits a trapezoid shape. The measured length of the parallel sides are 20 and 30 mm so we take $D = 25$ mm. It corresponds well to the free expansion of the collimated beam from the CF16 output of the Zeeman slower. Then, the typical estimated flux for a maximum absorption $A_{\max} = 0.6\%$ is $\Phi = 4 \times 10^{10}$ atoms/s.

The flux increase with oven temperature is plotted in the inset of Fig. 8. Typical experiments are carried at $T_1 = 130\,°\text{C}$ for which we get an intense slow beam of 2×10^{10} atoms/s.

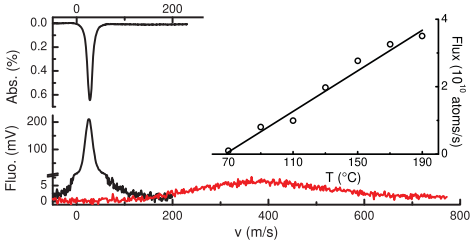

FIG. 8. (Color online) Red/gray: thermal beam fluorescence signal. Black: absorption and fluorescence signals of the slowed beam; axis break on fluorescence signal. Inset: temperature dependence of the atom flux; line to guide the eye.

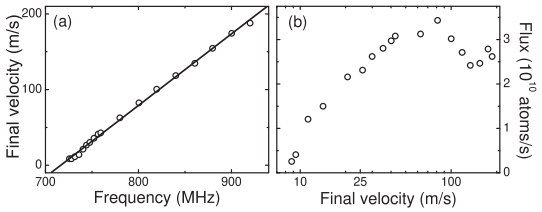

FIG. 9. (a) Final velocity as a function of Zeeman cycling light detuning ($I = 4.7\ \mathrm{mW\,cm^{-2}}$). Line: linear fit, the slope is $0.95\ \mathrm{m\,s^{-1}/MHz}$. (b) Atom flux as a function of final velocity.

Finally, we measured little influence of the entrance end cap on the atom flux and a moderate increase, $10 \pm 5\%$, with the output one.

B. Velocity distribution

Naturally, the Zeeman cycling light detuning strongly affects the atom beam velocity distribution (Fig. 9). A linear dependence of the final velocity in the detuning is observed. The actual slope is on the order of that expected from a simple model $\mathrm{d}v/\mathrm{d}\delta = 2\pi/k = 0.78\ \mathrm{m\,s^{-1}/MHz}$ but slightly higher and intensity-dependent.[17]

Besides, the atom flux is roughly constant for final velocities above $40\ \mathrm{m\,s^{-1}}$. Below this value, the flux measured in the chamber 125 mm downstream decreases. Indeed, the beam gets more divergent and atoms are lost in collisions with the walls of the vacuum chamber.

C. Needed laser powers

Figure 10 demonstrates that comparable amounts of cycling and repumper light are necessary. With a total power of 100 mW we get a non-critical operation of the Zeeman slower at its best flux and a final velocity of $30\ \mathrm{m\,s^{-1}}$, well suited for efficient MOT loading. The equivalent intensity is about $24\ \mathrm{mW\,cm^{-2}}$. However, as we shall see now, a lot of power can be saved with a more elaborate strategy.

D. Repumper

In the results reported until now, repumping and cycling light have the same polarization: linear and perpendicular to

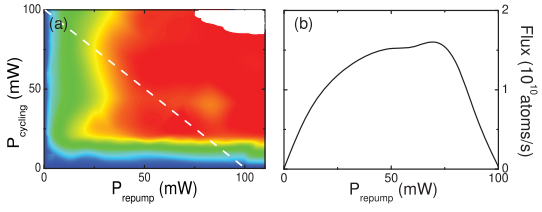

FIG. 10. (Color online) (a) Atom flux as a function of cycling and repumper beams powers. (b) Cross section along the white dotted line corresponding to a total available power of 100 mW. Power ratio is measured with a scanning Fabry-Perot interferometer.

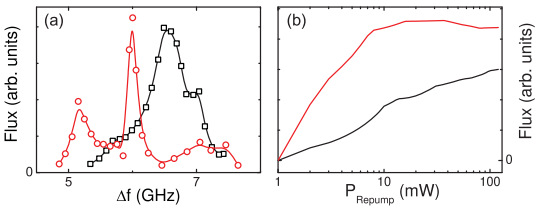

FIG. 11. (Color online) (a) Atom flux as a function of repumper frequency. Δf is the beat note frequency of the repumper with an auxiliary laser locked on the $F = 2 \rightarrow F' = 3$ resonance line; red/gray circles/black squares: repumper polarization perpendicular/parallel to the magnetic field. (b) Atom flux as a function of repumper power (log scale) when its frequency is fixed (black) or swept (red/gray) across the full spectrum of left panel.

the magnetic field, a state commonly referred to as *linear* σ recalling that it is a superposition of $\sigma^{\pm}$ states.[16] If no common amplification in a tapered amplifier is used, polarizations are likely to be orthogonal. The repumper polarization is then parallel to the magnetic field i.e., a π state. When the repumper frequency is varied as in Fig. 11(a) very different spectra for the two configurations are observed. Efficient repumping occurs with more or less well defined peaks spread over about 2 GHz and roughly centered around the $F = 1 \rightarrow F' = 2$ transition. This means that several depumping/repumping pathways are involved, probably occurring at localized places along the Zeeman slower.

It is not easy to get a simple picture of what is happening: a complete *ab initio* simulation of the internal dynamics is not simple due to the large number of Zeeman sublevels (24 in total for all the ground and excited states), the multiple level crossings occurring in the 50–200 G range, and high light intensities. However, one can overcome this intricate internal dynamics by sweeping quickly (typically around 8 kHz) the repumper frequency over all the observed peaks. With a low-pass filter, the central frequency remains locked on the side of the Doppler profile. Doing so, we get a slightly higher flux for significantly less repumper power, typically 10 mW (Fig. 11(b)).

E. MOT loading

A final demonstration of the Zeeman slower efficiency is given by monitoring the loading of a MOT. It is made from 3 retroreflected beams 28 mm in diameter (FW at $1/e^2$). We use 10–20 mW and 1–3 mW of cycling and repumper light per beam. When the Zeeman slower is on with a final velocity of $30\ \mathrm{m\,s^{-1}}$, a quasi-exponential loading is observed with characteristic time $\tau \sim 320$ ms for magnetic field gradients on the order of $15\text{–}20\ \mathrm{G\,cm^{-1}}$. After 1 s or so, the cloud growth is complete. From absorption spectroscopy, we deduce a density $n = 1.4 \times 10^{10}\ \mathrm{atoms\,cm^{-3}}$. The typical cloud size is 12 mm so we estimate the atom number to be on the order of $N = 2 \times 10^{10}$. These figures are consistent with the above measurements of an atom flux of several 10^{10} atoms/s and nearly unity capture efficiency. As expected, thanks to the high magnetic field in the slower, the Zeeman beams are far detuned and do not disturb the MOT.

VII. CONCLUSION

We have presented a simple and fast to build, robust Zeeman slower based on permanent magnets in a Halbach configuration. Detailed characterization shows it is an efficient and reliable source for loading a MOT with more than 10^{10} atoms in 1 s. Without power nor cooling water consumption, the apparatus produces homogeneous and smooth high fields over the whole beam diameter and low stray fields. It also simplifies high-temperature bakeout. We thus believe it to be a very attractive alternative to wire-wound systems.

ACKNOWLEDGMENTS

We thank J. M. Vogels for his major contribution to the design of the recirculation oven and D. Comparat for useful bibliography indications. This work was supported by the Agence Nationale pour la Recherche (ANR-09-BLAN-0134-01), the Région Midi-Pyrénées, and the Institut Universitaire de France.

[1] W. D. Phillips and H. Metcalf, Phys. Rev. Lett. **48**, 596 (1982).
[2] Y. Ovchinnikov, J. McCelland, D. Comparat, and G. Reinaudi, private communications (February 2011).
[3] Y. B. Ovchinnikov, Opt. Commun. **276**, 261 (2007).
[4] S. N. Bagayev, V. I. Baraulia, A. E. Bonert, A. N. Goncharov, M. R. Seydaliev, and A. S. Tychkov, Laser Phys. **11**, 1178 (2001).
[5] K. Halbach, Nucl. Instrum. Methods **169**, 1 (1980).
[6] 1200 mm long, 120 × 130 mm^2 cross section; dural holders, magnets and shield weights are, respectively, 5.0, 2.5, and 4.5 kg. It takes half a day of work to put parts together once machining is done.
[7] W. D. Phillips, Rev. Mod. Phys. **70**, 721 (1998).
[8] T. E. Barrett, S. W. Dapore-Schwartz, M. D. Ray, and G. P. Lafyatis, Phys. Rev. Lett. **67**, 3483 (1991).
[9] S. C. Bell, M. Junker, M. Jasperse, L. D. Turner, Y.-J. Lin, I. B. Spielman, and R. E. Scholten, Rev. Sci. Instrum. **81**, 013105 (2010).
[10] We could not find a configuration that produces a longitudinal magnetic field of several hundreds of Gauss with a reasonable amount of magnetic material.
[11] P. Melentiev, P. Borisov, and V. Balykin, JETP **98**, 667 (2004).
[12] W. G. Kaenders, F. Lison, I. Müller, A. Richter, R. Wynands, and D. Meschede, Phys. Rev. A **54**, 5067 (1996).
[13] D. Patterson and J. M. Doyle, J. Chem. Phys. **126**, 154307 (2007).
[14] See supplementary material at http://dx.doi.org/10.1063/1.3600897 for more information on the magnetic field for a cuboid calculation, the flux calculation, the oven design and for pictures of the setup. A movie of MOT loading, Mathematica programs for field calculations and technical drawings (.dxf) are available at http://www.coldatomsintoulouse.com/rm/.
[15] Convergence can be much slower for cuboids with different aspect ratios.
[16] G. Grynberg, A. Aspect, and C. Fabre, *Introduction to Quantum Optics, From the Semi-classical Approach to Quantized Light* (Cambridge University Press, Cambridge, England, 2010).
[17] V. S. Bagnato, C. Salomon, E. J. Marega, and S. C. Zilio, J. Opt. Soc. Am. B **8**, 497 (1991).

Chapter 3

Arrays of single Rydberg atoms

J'entrai pas au cri
d'« À nous deux Paris »
en Île-de-France...[1]

3.1 Introduction

Over the last thirty years, tremendous progress has been done in the manipulation of single quantum objects, such as single photons or single ions, allowing the actual realization in the lab of what was considered as *Gedankenexperimente* by the founding fathers of quantum mechanics. These remarkable achievements were honored by the award of the Nobel Prize in Physics in 2012 to Serge Haroche and David Wineland [51, 132]. The degree of control achieved nowadays, using a variety of different experimental platforms such as trapped ions, ultracold atoms, single photons, superconducting circuits, NV centers, quantum dots..., together with the motivation of applications such as quantum information processing [89], quantum metrology [42], and quantum simulation [39], has given birth to a whole new field that can be called *quantum engineering*. Among all the explored platforms, the ones using Rydberg atoms appear to be extremely promising.

Rydberg states of atoms correspond to highly excited atomic states, with a principal quantum number $n \gg 1$. This gives Rydberg atoms exaggerated properties. They have a size scaling as n^2 and thus a very large electric dipole moment: the matrix element of the dipole moment operator between two adjacent states is on the order of $n^2 e a_0$ where a_0 is the Bohr radius, and e the elementary charge. Moreover, they have long lifetimes (scaling as n^3 for low angular momentum states). Rydberg atoms, due to their similarities with hydrogen, have played a very important role in the early days of quantum mechanics and atomic physics. The advent of tunable lasers at the end of the seventies triggered a regain of interest in the physics of Rydberg atoms, which were an ideal testbed for studying coherent interactions between atoms and the electromagnetic field [32]. This second 'golden age' of Rydberg physics culminated in the cavity QED experiments by the

[1] Georges Brassens, *Les ricochets* (1976).

Haroche group [52], among others.

Due to their very strong electric dipoles, two Rydberg atoms separated by a distance R interact very strongly with each other via the dipolar interaction, either at first order (one then deals with a resonant dipole-dipole interaction $U = C_3/R^3$, where C_3 scales as n^4) or at second-order (in this case, one deals with the van der Waals interaction $U = C_6/R^6$ where C_6 scales as n^{11}). Figure 3.1a, taken from Ref. [111], shows that interactions between two Rydberg atoms with $n \sim 100$ and separated by a few microns are about twelve orders of magnitude higher than between ground-state atoms, reaching several MHz.

These exaggerated properties of Rydberg states are at the origin of the third 'golden age' of Rydberg physics, which started some fifteen years ago. Pioneering proposals [58, 77] were put forward in the early 2000s', following early experimental studies of interactions in cold Rydberg gases [4, 85], and suggested to use cold Rydberg atoms for quantum information processing. The basic mechanism at work is the *Rydberg blockade* (figure 3.1b). Consider that for a single atom, one couples, using a resonant laser, the ground state $|g\rangle$ to the Rydberg state $|r\rangle$ with a Rabi frequency Ω. Now suppose that two atoms are close to each other, such that, due to interactions, the collective state $|rr\rangle$ undergoes a shift $U \gg \hbar\Omega$. Then, when one shines the same resonant laser on the pair of atoms, the system can be resonantly excited from $|gg\rangle$ to $|rg\rangle$ or $|gr\rangle$, but a second excitation to $|rr\rangle$ is off-resonant and thus strongly suppressed: this is the essence of the Rydberg blockade. One readily shows that in this case, the system undergoes a collective Rabi oscillation, with an enhanced Rabi frequency $\Omega\sqrt{2}$, between $|gg\rangle$ and the entangled state $\left(|rg\rangle + \mathrm{e}^{i\phi}\,|gr\rangle\right)/\sqrt{2}$ (the phase ϕ has a well-defined value, that depends on the relative positions of the atoms and on the wavevectors of the lasers used for Rydberg excitation). This can be extended to N atoms: if all atoms are close enough such that the interaction between any two atoms exceeds the single-atom Rabi coupling Ω (i.e. the sample size is smaller than the so-called *blockade radius*), then the system oscillates at a frequency $\Omega\sqrt{N}$ between the collective ground state and a W-state where a single Rydberg excitation is delocalized over the N atoms.

Following these proposals, Rydberg blockade effects were experimentally observed in cold atomic ensembles, first in MOTs [124, 120] and then in BECs [55] and optical lattices [115] (for a more complete list of references, see e.g. Refs. [26, 68]). However, in such ensembles one deals in general with (i) a sample larger than the blockade radius, and (ii) with fluctuating atom numbers, which makes the observation of collective Rabi oscillations difficult. This was solved in 2009 by our group and by the group of Mark Saffman: using two individual atoms trapped by optical tweezers separated by a controlled distance, Rydberg blockade and collective enhancement were observed [38, 125]. These works were soon extended by using the blockade to create entanglement of two atoms in the ground state [131] and to realize a C–NOT gate [56].

Based on these successful demonstrations, it appeared very promising to try and extend those studies to a larger number of individual atoms held in arrays of optical microtraps, thus creating an appealing platform not only for quantum information processing [111],

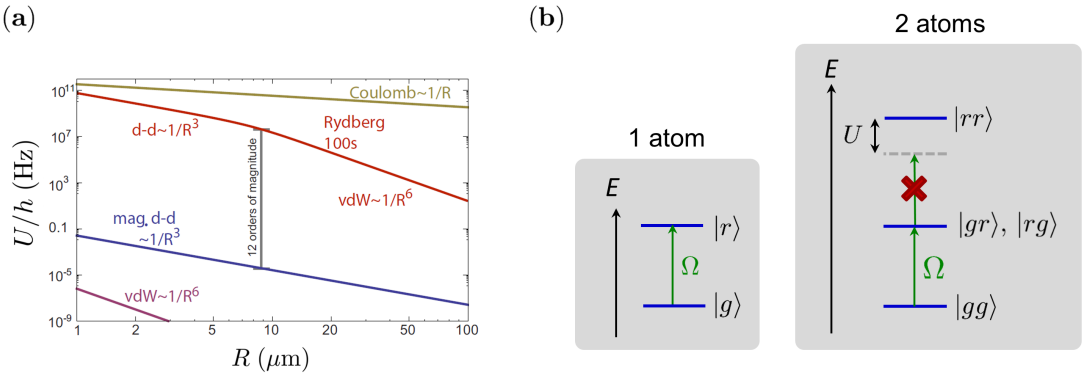

Figure 3.1: (a): Interactions between Rydberg atoms with $n \sim 100$ reach several MHz for distances as large as several micrometers. Figure taken from [111]. (b): Principle of the Rydberg blockade.

but more generally for quantum engineering. In particular, arrays of single atoms interacting via strong Rydberg dipolar interactions have strong assets to implement quantum simulation with neutral atoms, using a bottom-up approach similar to the one of trapped ions, complementary to the top-down approach using quantum gases loaded in optical lattices [16].

The Rydberg blockade experiment of Refs. [38, 131] were performed on the pioneering single-atom trapping setup built in the Quantum Optics group of LCF at the end of the 1990s', around a custom-made high numerical aperture objective (NA = 0.7) made of nine lenses [118]. The setup had not been designed in view of experiments with Rydberg atoms, and lacked, among other things, of any control of electric fields. In the meantime, the group had demonstrated that single-atom trapping, with similar performance, could be achieved using much simpler aspheric lenses [121] instead of a complicated objective.

Antoine Browaeys thus initiated in 2009 the construction of a whole new setup, dedicated to the creation of arrays of single atoms held in microtraps, and interacting when excited to Rydberg states. The project benefited from funding by the ERC, and started at the end of 2010 with a team composed of a PhD student, Lucas Béguin, and a post-doc, Aline Vernier. My arrival in the group in January 2012 coincided with the first signals of single atoms in the new setup[2], that I'll describe briefly in the next section. For an in-depth description, the reader is referred to the PhD theses of Lucas Béguin [8] and Sylvain Ravets [103].

3.2 Overview of the Chadoq experiment

Our setup combines essentially three techniques: the trapping of single ^{87}Rb atoms in optical tweezers, the creation of arrays of tweezers using a spatial light modulator, and the excitation of the atoms to Rydberg states.

[2]In the group, the experiment is known as *Chadoq*, for *Contrôle Holographique d'Atomes pour la Démonstration d'Opérations Quantiques.*

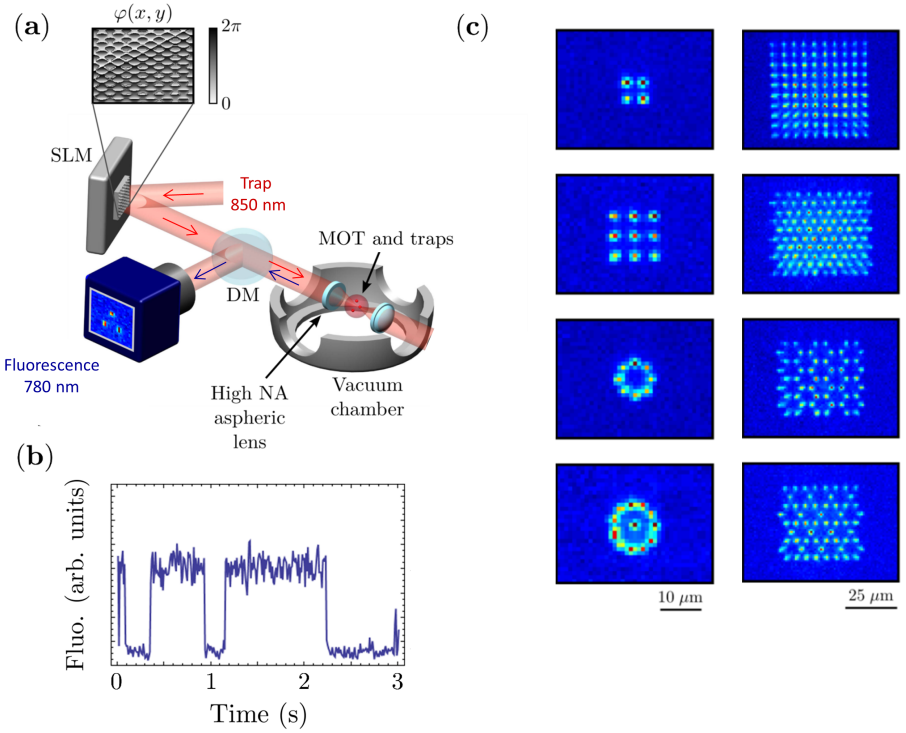

Figure 3.2: (a): Schematic view of the experimental setup. (b): The fluorescence signal of a single atom, showing a characteristic telegraph-like behavior. (c): A gallery of fluorescence signals corresponding to individual atoms trapped in arrays of optical tweezers created with the SLM.

Single-atom trapping

Figure 3.2(a) shows a schematic view of our experimental setup. The heart of the machine consists of two commercial aspheric lenses (N.A. = 0.5, focal length 10 mm, working distance 7 mm) that are facing each other inside the vacuum chamber, and with which we focus a laser beam at 850 nm down to a $1/e^2$ radius of about 1 μm. This creates an optical dipole trap, with a typical depth of about 1 mK for a power of about 3 mW. The transverse and longitudinal frequencies are about 80 kHz and 15 kHz respectively.

We load this conservative microtrap from a low-density optical molasses created around it. From time to time, an atom undergoing diffusion in the molasses enters the microtrap and is cooled down by the molasses beams while being captured in the tweezers, so that it remains trapped there. Now, if a second atom enters the trap, a light-assisted collision occurs and results in the loss of both atoms; due to the small volume of the trap, this occurs on a timescale of a few tens of microseconds, much faster than the rate of entry of atoms into the tweezers at low molasses density. Therefore, observed with a time resolution of several milliseconds, the trap occupation alternates randomly between zero and one: one obtains a single-atom source, albeit a non-deterministic one, the probability for the trap to contain a single atom being 50%. The rate at which the toggling occurs can be varied easily by varying the density of the optical molasses cloud (e.g. by adding a very weak

magnetic field gradient, turning the molasses into a low-density MOT).

We observe this loading dynamics by collecting, using the same aspheric lens, the fluorescence emitted at 780 nm by the atom, separating it from the trapping light with a dichroic mirror, and imaging it on a sensitive detector. Figure 3.2(b) shows a typical signal, obtained by collecting the emitted photons for 20 ms on a fiberized avalanche photodiode. One observes two well-defined fluorescence levels, a low one and a high one, corresponding respectively to the absence and to the presence of one atom in the microtrap. By defining a threshold, one thus unambiguously triggers an experimental sequence as soon as the trap is loaded.

Creating arrays of microtraps

In order to create arrays of optical tweezers, we use a spatial light modulator (SLM) to imprint an arbitrary phase on the trapping beam prior to focusing [92]. Despite the fact that the SLM only permits to manipulate the phase of the laser beam, and not its amplitude, the use of the Gershberg-Saxton (GS) algorithm [40] allows one to obtain a good approximation of any desired target intensity pattern in the focal plane of the lens. This allows us to create arbitrary, two-dimensional arrays of microtraps as shown in figure 3.2(c). The versatility of the SLM is also used for improving the quality of our arrays of traps [92]:

- Despite the care with which the optical setup was designed and built, we still have small residual optical aberrations, which degrade the quality of large arrays. By measuring them using a Shack-Hartman sensor, and adding to the SLM phase pattern the opposite of the measured wavefront distortion, we drastically improve the quality of the microtraps (in particular their depth).

- In large arrays, despite the fact that the target intensity corresponds to an array with all traps of the same intensity, the ones obtained in practice show a relatively large dispersion in the observed trap intensities (of up to a factor of two). This would prove detrimental for loading single atoms with 50% probability in the traps. We solve this problem by implementing an active improvement of the uniformity of the arrays of traps. For a given array, we first calculate an initial phase pattern for the SLM using the GS algorithm. We then measure, at the output of the vacuum chamber, the intensity of each tweezers on a CCD camera conjugated with the atoms' plane. Some traps are too dim, while others are too intense. We use this information to calculate a new target intensity, where the intensity of the traps that were previously too intense is reduced, and vice-versa. We use this new target intensity as an input for the GS algorithm, while keeping, as the initial guess for the phase, the previously calculated grating. Iterating this procedure for about 20 times allows us to obtain for instance arrays of 100 traps with an rms deviation of the intensities below 1.5%.

We thus have a very satisfactory way, using the SLM, to generate high quality, arbitrary 2D arrays of microtraps. However, the SLM refreshing rate being of only a few tens

of Hz at most, these arrays are, for all practical purposes, static on the timescales of the experiment. For many experiments however, it is desirable to have the possibility to single out temporarily at least one atom among all the ones confined in the array. For this purpose, we have included in our setup an extra *addressing beam* [66]. The principle is straightforward: we superimpose onto the trapping beam an extra beam at 850 nm (with a frequency shift of a few hundreds of MHz with respect to the trap beam), whose intensity and position can be controlled fast using two crossed AOMs, and which is focused to a $1/e^2$ radius of about 1.3 μm at the position of the atoms. This beam introduces an extra light shift on the selected atom when it is in the ground state, which can be used for many applications:

- We can selectively excite to Rydberg states either only the selected atom, either all of them but this one. In [66] we demonstrated this addressing, without any measurable cross-talk between atoms separated by 3 μm.

- We can manipulate collective quantum states. For instance, using the Rydberg blockade we first prepare two atoms in the 'super-radiant' state

$$\left|\psi^+\right\rangle = \frac{|gr\rangle + |rg\rangle}{\sqrt{2}}. \tag{3.1}$$

  We then illuminate the second atom with the addressing beam for a carefully chosen time so as it acquires a phase-shift of π when in $|g\rangle$ (the 850 nm beam induces a negligible light shift on the Rydberg state $|r\rangle$), and we thus obtain, again as shown in [66], the 'sub-radiant' state

$$\left|\psi^-\right\rangle = \frac{|gr\rangle - |rg\rangle}{\sqrt{2}}. \tag{3.2}$$

- Finally, we plan to use this addressing beam as a movable tweezers [11], that should allow us to drag atoms along in the array, for instance to sort out a disordered array.

Manipulating Rydberg atoms

For exciting the atoms to Rydberg states (figure 3.3(a)), we use a standard two-photon transition, with a first photon at 795 nm, detuned by $\Delta = 2\pi \times 740$ MHz above the $\left|5S_{1/2}, F = 2\right\rangle \leftrightarrow \left|5P_{1/2}, F = 2\right\rangle$ line, and a second photon in the blue, at 474 nm, to excite Rydberg states $\left|nD_{3/2}, m_j = 3/2\right\rangle$ (with $50 \leqslant n \leqslant 100$). Both lasers are stabilized using an ultrastable ULE cavity, resulting in a global linewidth that we estimate to be about 30 kHz. The Rabi frequencies Ω_{R} and Ω_{B} on those two transitions are typically of a few tens of MHz, resulting in an effective Rabi coupling $\Omega = \Omega_{\mathrm{R}}\Omega_{\mathrm{B}}/(2\Delta)$ of typically 1 MHz (beyond Rabi frequencies of 5 MHz, we start to suffer strongly from spontaneous emission from the intermediate $5P_{1/2}$ state).

We detect the successful Rydberg excitation of an atom in a rather crude, but actually quite effective, way: an atom excited to a Rydberg state with $n > 50$ has a radiative decay

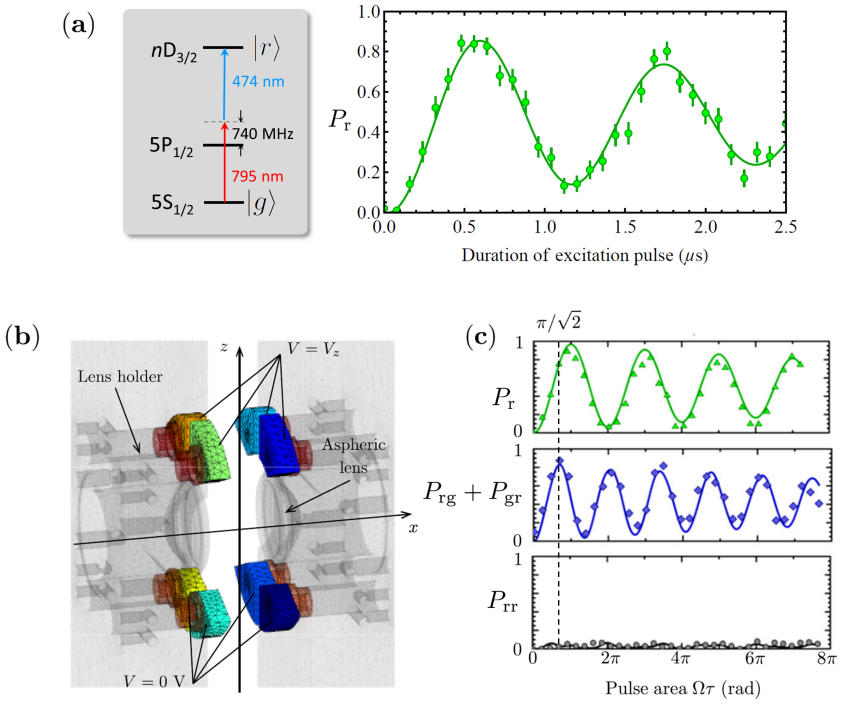

Figure 3.3: (a): The two-photon Rydberg excitation scheme and an example of a single-atom Rabi oscillation between the ground state and the Rydberg state $\left|82D_{3/2}, m_j = 3/2\right\rangle$. (b): Finite-element method simulation of the set of electrodes placed around the aspheric lenses. In the given configuration, we apply an electric field along the z-direction. (c): Rydberg blockade with two atoms separated by 4 μm and excited to $|r\rangle = \left|62D_{3/2}, m_j = 3/2\right\rangle$. The top panel shows a Rabi oscillation for a single atom, to calibrate the Rabi frequency Ω. The middle panel shows the probability $P_{\mathrm{gr}} + P_{\mathrm{rg}}$ to excite only one atom to the Rydberg state, clearly showing the collective enhancement of the Rabi frequency by a factor $\sqrt{2}$. Finally, the bottom panel showing the probability P_{rr} to excite both atoms to $|r\rangle$ illustrates strikingly the blockade. Figure adapted from [9].

time to the ground state in excess of 100 μs, and is not trapped (actually it is slightly repelled) by the optical tweezers. Due to its finite thermal velocity (about 70 nm/μs for our typical $T \simeq 50$ μK), it thus has ample time to escape the trapping region before decaying back to the ground state. This means that at the end of a sequence, when we switch on again the tweezers and the MOT beams to induce fluorescence, a Rydberg atom manifests itself as a missing atom in the trap. We repeat an excitation sequence for about 100 times and then reconstruct the various probabilities for each atom of the array to be either in $|g\rangle$ or in $|r\rangle$. An example of a Rabi oscillation between the ground state and the Rydberg state $\left|82D_{3/2}, m_j = 3/2\right\rangle$ is shown in Figure 3.3(a).

For a sequence without a Rydberg excitation pulse, a ground-state atom as a non-zero, but small, probability $\varepsilon \simeq 3\%$ to be lost (essentially due to collisions with the background gas), and thus to be mistakenly inferred to be in a Rydberg state. This distorts the measured populations, but this can be corrected for if needed, following the procedure

described in [119]. The converse detection error (i.e. recapturing an atom that actually was excited transiently to a Rydberg state) can be estimated to be well below 1%, and thus negligible at our level of accuracy.

Rydberg atoms are extremely sensitive to electric fields (their static polarizability scales as n^7 with the principal quantum number n). We have thus designed our setup to minimize stray fields, and to allow for compensating them: (i) the aspheric lenses are coated with transparent, conductive 200 nm-thick layer of indium-tin oxide (ITO); (ii) eight independent electrodes placed around the lenses allow for applying controlled fields pointing in any direction [figure 3.3(b)]. Using Stark spectroscopy on a single atom, we measured a residual field of about 150 mV/cm without compensation, that could be corrected to better than 5 mV/cm by applying appropriate voltages on the electrodes. We also used the electrodes to tune electrically the interactions between the atoms at a Förster resonance (see section 3.3 below).

A final, very useful tool to manipulate Rydberg atoms is microwave radiation, which couples together various Rydberg states. In [6] for instance, we used a microwave antenna placed outside the vacuum chamber, above the top viewport, to induce transitions at about 9.1 GHz between the states $62D_{3/2}$ and $63P_{1/2}$. More recently, we extended this to the 20.1 GHz transition $62D_{3/2} \leftrightarrow 64P_{1/2}$. This degree of freedom allows to tune the strength of the interactions (see 3.3). Moreover, due to the giant dipole matrix elements between Rydberg states, a very moderate microwave power is enough to drive fast Rabi oscillations, in the range of several MHz, between the chosen levels.

As a first test of our experimental setup, we performed two-atom blockade experiments, and observed the collective Rabi oscllations and the suppression of double excitations of an unprecedented quality, as can be seen on figure 3.3(c). However, in order to perform a more sensitive assessment of the quality of our apparatus, we embarked on detailed quantitative measurements of the different types of interactions existing between two atoms in Rydberg states.

3.3 Interactions between two single Rydberg atoms

At the large interatomic distances $R > 3$ μm and the principal quantum numbers $n < 100$ that are relevant for our experiments, the size $\sim n^2 a_0$ of the electronic wavefunction of Rydberg states is negligible as compared to R. Thus the interaction between atoms is essentially given by the dipole-dipole Hamiltonian

$$V_{\mathrm{ddi}} = \frac{1}{4\pi\varepsilon_0} \frac{\boldsymbol{d}_1 \cdot \boldsymbol{d}_2 - 3(\boldsymbol{d}_1 \cdot \boldsymbol{n})(\boldsymbol{d}_2 \cdot \boldsymbol{n})}{R^3}, \tag{3.3}$$

where $\boldsymbol{n}$ is the unit vector joining the positions of the two atoms, and $\boldsymbol{d}_i$ is the electric dipole moment operator of atom i. One can easily check that higher-order terms in the multipole expansion, such as dipole-quadrupole interactions, quadrupole-quadrupole interactions, and so on are completely negligible for our experimental parameters.

The perturbative effects of this interaction Hamiltonian on a pair of atoms depends on which Rydberg states the atoms are prepared in, and on the distance R between them. Let us assume first that both atoms are prepared in the same state, e.g. a D state; we shall denote this *pair state* as $|dd\rangle$ for short. As atomic eigenstates have a definite parity, the average value of the dipole moment (an odd-parity operator) in the state $|d\rangle$ vanishes. This means that (3.3) has no effect to first order of perturbation theory. Therefore, the dipolar interaction manifests itself only at second-order, giving rise to an energy shift of the level $|dd\rangle$ given by the usual expression

$$\Delta E = \sum_{\phi,\phi'} \frac{|\langle \phi\phi' | V_{\mathrm{ddi}} | dd\rangle|^2}{2E_d - E_\phi - E_{\phi'}}, \tag{3.4}$$

where $|\phi\rangle, |\phi'\rangle$ denote single-atom states that are dipole-coupled to $|d\rangle$. This shift, being second-order in (3.3), scales as C_6/R^6, and is nothing else but the van der Waals interaction. It is straightforward to evaluate how the C_6 coefficient scales with the principal quantum number n: the dipole matrix elements for an atom scale as n^2, whence a n^8 scaling of the numerators in (3.4); the energy denominators, on the other hand, scale as n^{-3}, and thus $C_6 \sim n^{11}$, an extraordinarily fast scaling.

This perturbative treatment fails when the interatomic distance R becomes too small, such that the couplings $\sim C_3/R^3$ between different pair states start to be on the same order as the energy difference between them. In this case, one generally needs to diagonalize numerically the full Hamiltonian. However, in some cases, a single pair state has an energy very close to the energy of the original $|dd\rangle$ state, and the situation becomes very simple as one deals with essentially two coupled levels. This phenomenon has been called in the Rydberg community a Förster resonance, due to its analogy with the phenomenon of fluorescence resonance energy transfer in photochemistry, that was understood quantitatively in 1948 by Theodor Förster [36, 25]. The two coupled pair states have in general different polarizabilities, and therefore, by applying a small electric field, one can tune them into exact resonance. The dipole-dipole interaction then leads to new eigenstates, that are symmetric and antisymmetric combinations of the initial pair states, and that are split by an interaction energy scaling as $1/R^3$.

Finally, another way to observe a resonant dipole-dipole interaction between two Rydberg atoms is to prepare them initially in two different, dipole-coupled states, for example a P and a D state. Then, the two pair states $|dp\rangle$ and $|pd\rangle$ are automatically always resonant, and the resonant dipole-dipole interaction scaling as C_3/R^3 is observed.

In a series of experiments aiming at benchmarking our experimental setup, we have measured quantitatively these different variants of the dipolar interaction between a pair of individual atoms located at controlled positions. As compared to studies using ensembles of atoms where interaction effects tend to be averaged over all the pairwise atomic separations (see [26] and references therein), we could (i) measure directly the scaling with distance and the angular dependence of the interaction, and (ii) observe its coherent character in time-resolved experiments. We have successively studied van der Waals interactions,

Förster resonances, and resonant dipole-dipole interaction between two different Rydberg states:

- In [9], we measured the van der Waals interaction between two atoms prepared in the state $\left|nD_{3/2}, m_j = 3/2\right\rangle$ (and with the internuclear axis aligned along the quantization axis) as a function of their distance R, for principal quantum numbers $n = 53, 62, 82$. For that, we worked in a *partial blockade* regime, where the single-atom Rabi frequency Ω is comparable to the interaction U. The dynamics of the populations of the four two-atom states $|gg\rangle, |rg\rangle, |gr\rangle, |rr\rangle$ then depends on both Ω (which is measured in a calibration experiment with only one atom) and on U. Fitting the observed dynamics with U as the only adjustable parameter allows one to extract an accurate value of the interaction. In [7], we studied the angular dependence of the van der Waals interaction, which is isotropic for S states but anisotropic for D states.

- In [105], we studied the $\left|59D_{3/2}, 59D_{3/2}\right\rangle \leftrightarrow \left|61P_{1/2}, 57F_{5/2}\right\rangle$ Förster resonance of ^{87}Rb, using our ability to apply arbitrary electric fields using our electrodes to tune the pair states into resonance. We first performed a spectroscopic study to determine the exact value of the electric field giving rise to the avoided crossing between the two pair states, and checked that the splitting at resonance indeed scales as $1/R^3$ with distance. In a second step, we studied the interaction in the time domain, by preparing first the system in $|dd\rangle$, and then switching abruptly (with a risetime of about 10 ns) the electric field to resonance, for an adjustable time T. A final optical readout pulse then allowed us to measure the probability for the pair of atoms to be in $|dd\rangle$, showing coherent oscillations between the two coupled pair states, at a frequency $\propto C_3/R^3$. In a subsequent experiment, we measured the angular dependence of the dipolar interaction at resonance, clearly observing the characteristic variation $1 - 3\cos^2\theta$ of the interaction with the angle θ between the internuclear axis and the quantization axis [104]. As compared to earlier studies of Förster resonances in disordered ensembles comprising a large number of atoms [112, 86, 128, 106, 107, 90, 91], our pristine system consisting of only two atoms at controlled positions makes it possible to study directly the spatial dependence of the interaction and to observe its coherent character.

- Finally, in [6] we studied the resonant dipole-dipole interaction between two atoms prepared in different Rydberg states, namely $|\uparrow\rangle \equiv \left|62D_{3/2}, m_j = 3/2\right\rangle$ and $|\downarrow\rangle \equiv \left|63P_{1/2}, m_j = 1/2\right\rangle$. The dipole-dipole interaction then couples the states $|\uparrow\downarrow\rangle$ and $|\downarrow\uparrow\rangle$, with a strength scaling as C_3/R^3. Here again, in contrast to experiments in disordered atomic ensembles [4, 85, 126, 48, 10], we could measure the R-dependence of the interaction. In this case, we extended our measurements all the way up to $R = 50$ μm, a very large distance on the atomic scale. When considering the two coupled Rydberg states as the two eigenstates of a pseudo-spin 1/2, the dipole-dipole Hamiltonian can be recast in the form of an XY spin Hamiltonian (i.e. a

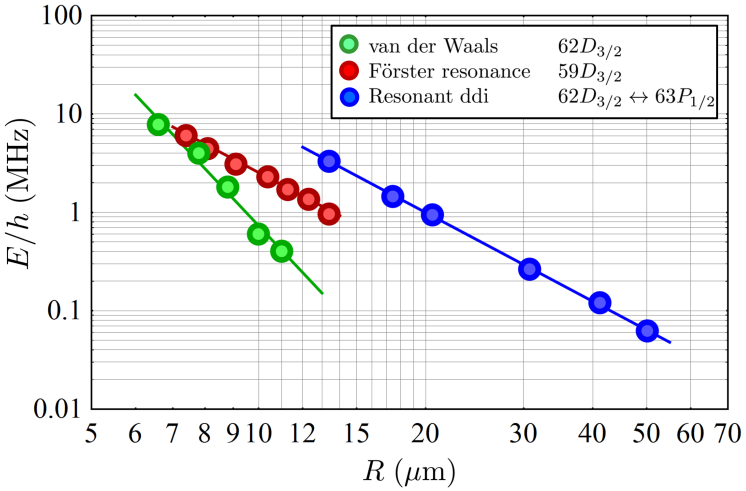

Figure 3.4: Log-log plot of the measured interactions energies E between two single Rydberg atoms separated by a distance R, in the van der Waals regime (green points, data taken from [9]), at a Förster resonance (red points, data taken from [105]), and for the resonant dipole-dipole interaction between two distinct Rydberg states (blue points, data taken from [6]). The solid lines are the theoretical values, without any adjustable parameters.

spin-exchange Hamiltonian), so this study can be considered as the demonstration of an elementary building block for the quantum simulation of spin Hamiltonians.

Figure 3.4 summarizes, on the same log-log plot, the distance dependence of the interaction energies we have measured for two Rydberg atoms with $n \simeq 60$, in the various cases of the van der Waals interactions (green), resonant dipolar interaction at a Förster resonance (red), and the resonant dipolar interaction between two different states (blue). The solid lines correspond to *ab-initio* calculations of the interactions, without any adjustable parameters. The excellent agreement between data and calculations shows that the level of control achieved with our setup is encouraging in view of experiments involving more atoms.

3.4 Prospects: towards many atoms

The next step is to extend our studies to many atoms, ideally several tens of particles. Over the last year, we have already made significant progress along those lines.

Understanding technical imperfections

We have first studied systems of three atoms, observing both van der Waals blockade [7] and resonant dipole-dipole interaction [6]. In the latter case, we studied the propagation of a single spin excitation in a three atom-chain initially prepared in $|\uparrow\downarrow\downarrow\rangle$, and obtained clear experimental evidence for long-range hopping of the excitation (see figure 3.5).

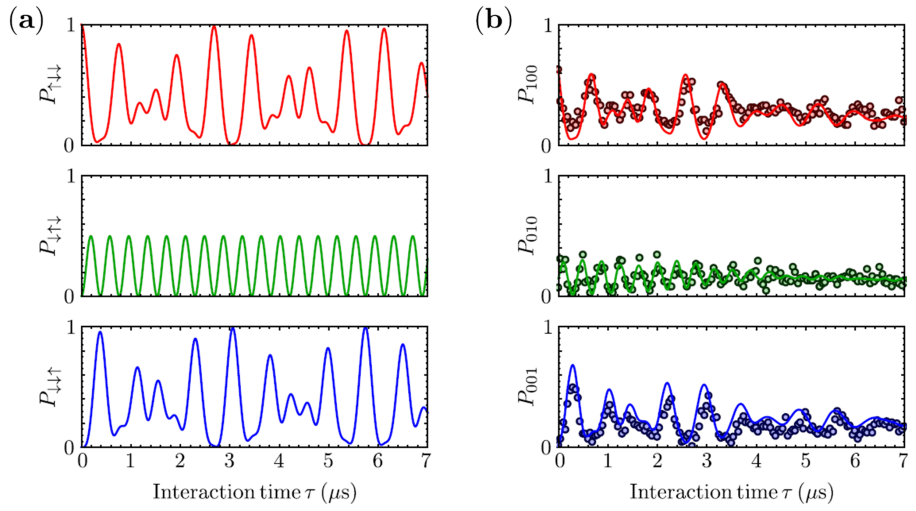

Figure 3.5: Long-range hopping of a spin excitation along a three-atom chain [6]. (a) Theoretical calculations for the ideal case where the system is initially in $|\uparrow\downarrow\downarrow\rangle$. (b) Experimental data (points) and solution of a model without any adjustable parameters, taking into account the independently measured experimental imperfections (solid line).

One of the main interest of those two studies was to understand quantitatively some of the technical limitations of our experimental approach. A first issue is the finite temperature of the atoms in the tweezers (around 50 μK), which leads to (i) shot-to-shot fluctuations in the distances between the particles, and therefore in their interactions, and (ii) to a residual motion of the atoms during the interaction time (which occurs in free flight). Both effects contribute to dephasing in the dynamics, and might be detrimental when the number of atoms scales up. Raman sideband cooling of neutral atoms held in optical tweezers similar to ours was demonstrated recently in [60, 123], which means that this limitation can be circumvented in principle. A second issue is related to the state detection, which shows small errors as described above, due to the probability $\varepsilon \neq 0$ to lose a ground-state atom during the sequence and thus to infer incorrectly that it was in a Rydberg state. Here again however, this can be corrected following the ideas of [119], which are routinely implemented in ion-trap based quantum simulations (see e.g. [57]).

Loading the microtrap arrays

One major limitation of our approach so far is that the loading of microtraps by single atoms is non-deterministic. The average time for an array of N traps to be fully loaded, starting from an empty array, increases exponentially with N, roughly as 2^N as $N \to \infty$. In practice, we could perform experiments with up to 9 atoms [65], but then the duty cycle of the experiment becomes very long, with a single shot every minute on average, which requires acquisition times of several hours to record the dynamics of the system with sufficient statistics. Except for some experiments in which one could content oneself with a sparse (50%) loading of the arrays, we will thus need to investigate quasi-deterministic

loading schemes in the near future. Several approaches have been suggested or even demonstrated at the level of a proof of principle:

- In [46], a blue-detuned 'collision beam' was used to ensure that in a tweezers loaded with several ^{85}Rb atoms, light-assisted collisions gave rise to the loss of only *one* atom out of the two involved in the collision. This allowed the authors to achieve single-atom loading probabilities in excess of 80% in a microtrap. It remains to be checked whether this approach works for ^{87}Rb, and for large arrays of tweezers.

- Another possibility is to use the Rydberg blockade itself, by loading initially each tweezers with a few atoms, exciting only one of them to a Rydberg state using the Rydberg blockade, and removing the remaining ground-state atoms with a push-out beam. Preliminary results by the Wisconsin group, reported in [31], achieved only a modest increase in the single-atom loading probability of the tweezers, which reached about 60%, too low for the method to be of a practical interest so far. The idea however probably deserves to be investigated further.

- Finally, a different approach to the loading of an array of N traps would consist in starting with a larger array containing $2N$ traps, loading it sparsely to have $\sim N$ single atoms, and then sorting the atoms, using a movable optical tweezers, to fully load the N traps of the array of interest. This is certainly quite challenging technically, but this type of approach has already been demonstrated in similar setups [82, 117].

Future experiments

With the current status of the setup, several appealing directions for future experiments become realistic.

A first one deals with basic demonstrations of building blocks for quantum information processing. Having already demonstrated Rydberg blockade with up to about ten atoms, a natural follow-up experiment will be to demonstrate the generation of entangled W states where the qubit is encoded in two hyperfine levels of the ground state of the atom, as was done for two atoms in [131]. In particular, what kind of fidelities can be achieved, and what limits it when we scale up the number of qubits, remains an open question. Such a study can then be generalized to the generation of other classes of entangled states, such as for instance GHZ states, still using the Rydberg blockade but with slightly more involved protocols that amount to implementing collective C-NOT gates [83, 87].

Another line of research deals with quantum simulation [129], in particular of spin Hamiltonians. A system of atoms interacting *via* van der Waals interactions when in the Rydberg state can be described by an Ising-type Hamiltonian

$$H_{\text{Ising}} = \sum_{i<j} \frac{C_6}{|\boldsymbol{r}_i - \boldsymbol{r}_j|^6} \sigma_z^{(i)} \sigma_z^{(j)} \tag{3.5}$$

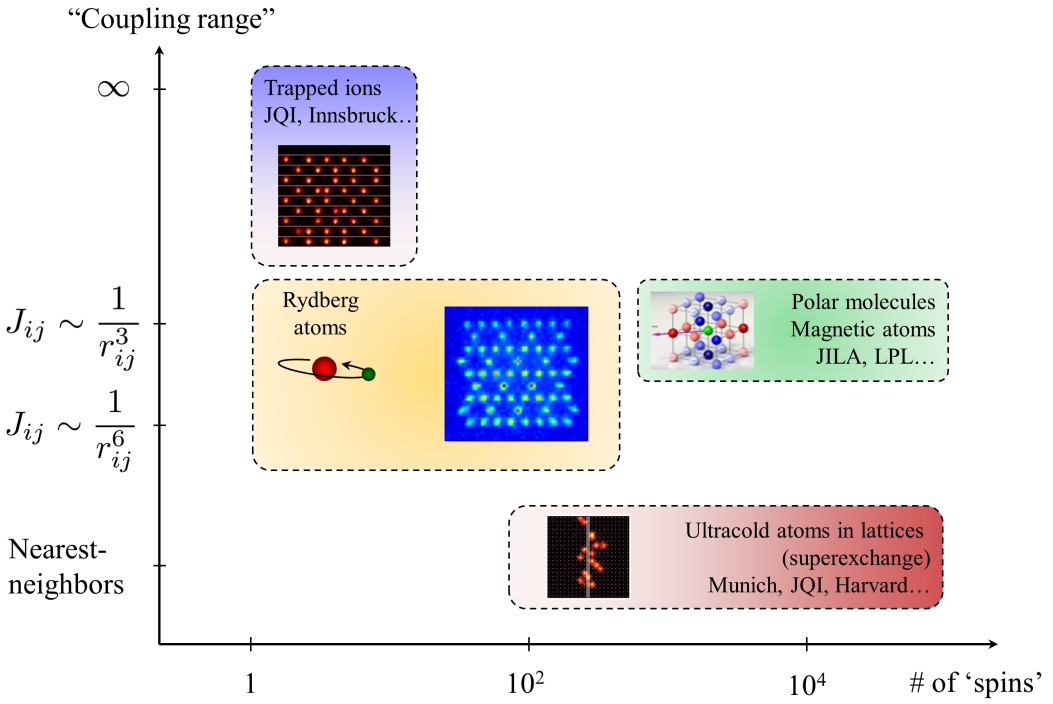

Figure 3.6: The various AMO platforms for quantum simulation of spin Hamiltonians: ultracold atoms in optical lattices, ultracold dipolar gases in lattices, trapped ions, and Rydberg atoms in arrays of tweezers. Here I have sorted them according to two important parameters for a quantum simulator (numbers of simulated spins and range of the couplings), but many other parameters could be listed (dimensionality, ease with which the geometry of the lattice can be changed, absolute strengths of the couplings...). Depending on the specific problem to be solved by quantum simulation, some platforms will presumably be more adapted than others, but the Rydberg one certainly has interesting assets: in particular, it is two-dimensional, the couplings are very large and extend beyond nearest-neighbors, the geometry of the system can be changed very easily...

where the pseudo-spin-1/2 states corresponds to the atom being in $|g\rangle$ or $|r\rangle$, and where single-particle terms (that can be absorbed in a 'longitudinal field' Hamiltonian) have been removed for simplicity. The term $\sim \sum_i \Omega \sigma_x^{(i)}$ describing the laser coupling is equivalent to a transverse magnetic field. This quantum Ising model in a transverse field is one of the most basic models displaying quantum phase transitions [109]. In [116], adiabatic sweeps of the laser detuning and Rabi frequency were used to map out the phase diagram of this model in 2D.

In contrast, the resonant dipole-dipole interaction between two different Rydberg states $|r_1\rangle$ and $|r_2\rangle$ can be recast in terms of a spin-exchange, or XY Hamiltonian:

$$H_{\mathrm{XY}} = \sum_{i<j} \frac{C_3}{|\boldsymbol{r}_i - \boldsymbol{r}_j|^3} \left(\sigma_+^{(i)} \sigma_-^{(j)} + \mathrm{h.c.}\right). \tag{3.6}$$

Here, the spin states correspond to the two Rydberg states $|r_{1,2}\rangle$. It is possible to map the spin excitations of this model onto hard-core bosons, the exchange of excitation between

two atoms corresponding to (long-range) hopping of the corresponding bosons. Our three-atom spin chain experiment [6] corresponds to the smallest non-trivial instance of this model. In future work, in collaboration with Thomas Pohl's group in Dresden, we plan to find pairs of states for which the resonant dipole-dipole interaction and the (always present) van der Waals interaction are comparable in strength. In this case, one realizes a XXZ Heisenberg Hamiltonian, with some couplings slowly decaying as $1/R^3$, which is expected to display new, exotic properties [53, 96].

I thus believe that our system will be an interesting platform for the simulation of spin Hamiltonians, complementary to the other approaches using the tools of atomic physics, namely ultracold atoms or molecules in optical lattices and trapped ions (see e.g. [54] and references therein), as illustrated on Figure 3.6.

In the long run, one can envision to use the rich internal structure of Rydberg states to implement more complex Hamiltonians. For instance one could use two types of excitations to implement the equivalent of a Hubbard model with two species of hard-core bosons. The dipole-dipole interaction then naturally introduces a spin-orbit coupling for the motion of these excitations, which opens interesting perspectives for the quantum simulation of topological matter displaying e.g. edge states, that we could image directly [98].

3.5 Published articles

Below is a list of the articles I have co-authored about our work on Rydberg atoms.

- L. Béguin *et al.*, Phys. Rev. Lett. **110**, 263201 (2013), reproduced on page 78.
- F. Nogrette *et al.*, Phys. Rev. X **4**, 021034 (2014), reproduced on page 83.
- D. Barredo *et al.*, Phys. Rev. Lett. **112**, 183002 (2014), reproduced on page 92.
- H. Labuhn *et al.*, Phys. Rev. A. **90**, 023415 (2014), reproduced on page 97.
- S. Ravets *et al.*, Nature Phys. **10**, 914 (2014), reproduced on page 101.
- D. Barredo *et al.*, Phys. Rev. Lett. **114**, 113002 (2015), reproduced on page 105.

Direct Measurement of the van der Waals Interaction between Two Rydberg Atoms

L. Béguin,[1] A. Vernier,[1] R. Chicireanu,[2] T. Lahaye,[1] and A. Browaeys[1]

[1]*Laboratoire Charles Fabry, Institut d'Optique, CNRS, Univ Paris Sud, 2 avenue Augustin Fresnel, 91127 Palaiseau cedex, France*
[2]*Laboratoire de Physique des Lasers, Atomes et Molécules, Université Lille 1, CNRS; 59655 Villeneuve d'Ascq cedex, France*

(Received 22 March 2013; published 24 June 2013)

We report the direct measurement of the van der Waals interaction between two isolated, single Rydberg atoms separated by a controlled distance of a few micrometers. Working in a regime where the single-atom Rabi frequency for excitation to the Rydberg state is comparable to the interaction, we observe partial Rydberg blockade, whereby the time-dependent populations of the various two-atom states exhibit coherent oscillations with several frequencies. Quantitative comparison of the data with a simple model based on the optical Bloch equations allows us to extract the van der Waals energy, and observe its characteristic C_6/R^6 dependence. The measured C_6 coefficients agree well with *ab initio* calculations, and we observe their dramatic increase with the principal quantum number n of the Rydberg state.

DOI: 10.1103/PhysRevLett.110.263201 PACS numbers: 34.20.Cf, 03.67.Bg, 32.80.Ee

The van der Waals–London interaction $U_{\mathrm{vdW}} = C_6/R^6$ between two neutral, polarizable particles separated by a distance R is ubiquitous in nature. It underlies many effects, from the condensation of nonpolar gases to the adhesion of gecko toes [1]. At a macroscopic scale, measuring thermodynamic quantities of a system gives indirect access to the van der Waals interaction between the constituent atoms or molecules [2]. Alternatively, one can directly measure the net force between macroscopic bodies resulting from the microscopic van der Waals forces. However, in this case, summing over the underlying C_6/R^6 interactions between individual particles results in a potential scaling as $1/L^\alpha$, where L is the separation between the bodies, and $\alpha < 6$ is a geometry-dependent exponent (e.g., $\alpha = 1$ for two spheres with a diameter $D \gg L$) [1,2].

At the level of individual particles, spectroscopy of the vibrational levels close to the dissociation limit of a diatomic molecule, analyzed semiclassically, allows one to infer the long-range interaction between atoms [3]. Progress in atomic physics has made it possible to measure van der Waals interactions between ground-state atoms and a surface (scaling as $1/L^3$, or even $1/L^4$ if retardation plays a role) with a variety of techniques [4]. However, directly measuring the van der Waals interaction between two ground-state atoms would be extremely challenging, due to their very small interaction. In contrast, Rydberg atoms (atoms with large principal quantum number n) exhibit very strong interactions that scale rapidly with n. Using this property, the interaction between Rydberg atoms and a surface has been measured at relatively large distances [5,6]. Here, we report on the measurement of the C_6/R^6 interaction between two isolated Rydberg atoms prepared in a well defined quantum state.

The principle of our experiment is the following. We irradiate the pair of atoms with lasers that couple the ground state $|g\rangle$ and the targeted Rydberg state $|r\rangle$ with Rabi frequency Ω. Depending on the relative strength of U_{vdW} and $\hbar\Omega$, two limiting cases can be identified. If $U_{\mathrm{vdW}} \ll \hbar\Omega$, the atoms behave independently and the doubly excited state $|rr\rangle$ can be fully populated. On the contrary, when $\hbar\Omega \ll U_{\mathrm{vdW}}$, the excitation of $|rr\rangle$ is off resonant and thus suppressed [see Fig. 1(a)], yielding Rydberg blockade [7–9]. This leads to the appearance of "blockade spheres" inside of which only one Rydberg excitation can be created. The blockade sphere picture gives an intuitive understanding of nontrivial many-body effects in driven systems. Rydberg blockade has been observed in recent years in extended cold atom ensembles [10–14] as well as between two atoms [15,16].

In the transition region $\hbar\Omega \sim U_{\mathrm{vdW}}$, i.e., in the partial blockade regime, the blockade sphere picture is too simplistic: the populations of the various many-atom states undergo coherent collective oscillations with several frequencies which depend on U_{vdW}. In our two-atom experiment, this allows us to extract the interaction strength. By measuring U_{vdW} for various R, we observe its characteristic $1/R^6$ dependence. The measured C_6 coefficients, which scale extremely fast with n, agree well with *ab initio* calculations. Our results prove that detailed control over the interactions between Rydberg atoms is possible; this is a prerequisite for applications to high-fidelity quantum information processing [17] and quantum simulation using long-range interatomic interactions [18].

We use two single ^{87}Rb atoms at a temperature of 50 μK, loaded in 1 mK-deep microscopic optical traps from a magneto-optical trap [see Fig. 1(b)] [19]. Our new setup is designed to overcome the limitations of the apparatus used in our early studies of Rydberg blockade [16] and entanglement [20]. We use an aspheric lens under vacuum [21] with numerical aperture 0.5 (focal length 10 mm, working distance 7 mm) to focus two 850 nm trapping beams down to 1.1 μm ($1/e^2$ radius). The distance R between the traps is varied by changing the

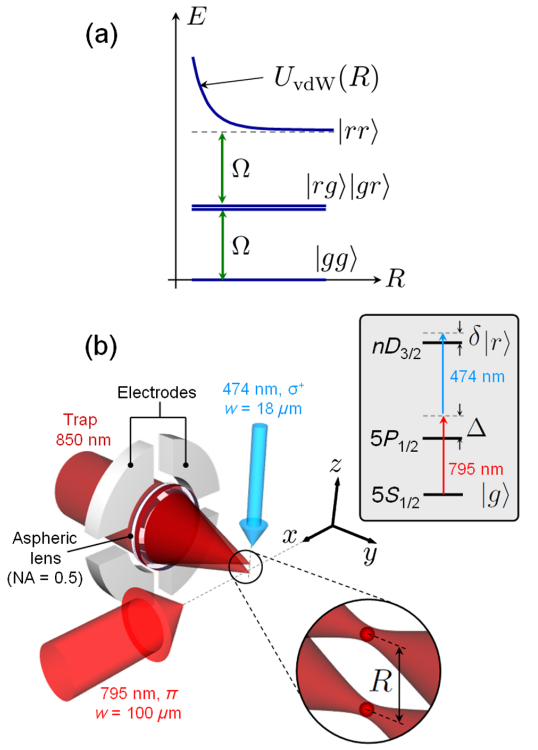

FIG. 1 (color online). (a) Principle of the Rydberg blockade. The single-atom Rabi frequency is Ω. (b) Experimental setup. Two single atoms are trapped in microscopic optical traps separated by R. Eight electrodes (four of which, facing the ones displayed here, are not shown) provide electric field control. Inset: two-photon excitation scheme (the intermediate-state detuning is $\Delta \simeq 2\pi \times 740$ MHz).

incidence angle of the beams on the lens. We calibrate R by measuring the displacement of an image of the trap when changing the incidence of the trapping beams. The resulting uncertainty is below 5% [22].

The aspheric lens used to focus the trapping beams also collects the atom fluorescence from each trap on separate photon counters. The two-photon excitation from $|g\rangle = |5S_{1/2}, F = 2, m_F = 2\rangle$ to the Rydberg state $|r\rangle = |nD_{3/2}, m_j = 3/2\rangle$ [see the inset of Fig. 1(b)], described in Ref. [23], yields coherent oscillations with single-atom Rabi frequencies $\Omega/(2\pi)$ in the range from 500 kHz to 5 MHz [see Fig. 2(a)]. The excitation pulse has a duration τ (during which the traps are off), and the laser frequencies are adjusted so that the (light-shift corrected) one-atom detuning is $\delta \simeq 0$. After excitation, we infer the state of each atom by detecting its presence or absence in its respective trap (atoms in $|r\rangle$ are slightly antitrapped by the optical potential, which results in their loss). We thus reconstruct the populations P_{ij} of the two-atom states $|ij\rangle$ (i, j taking the values g, r), by repeating each sequence about 100 times [23].

Our setup was designed to minimize residual electric fields detrimental to Rydberg state manipulations: (i) the aspheric lens surface facing the atoms is coated with a conductive 200 nm-thick indium-tin-oxide layer; (ii) eight independent electrodes allow us to apply electric fields along any direction [24]. Using Stark spectroscopy on the $|62D_{3/2}, m_j = 3/2\rangle$ state, we determine that with all electrodes grounded, a residual field of $\sim$150 mV/cm (pointing essentially along x) was present. After applying appropriate correction voltages, the residual field is below $\sim$5 mV/cm. This cancellation is critical to the success of the experiment: small (transverse) stray fields mix $|r\rangle$ with other Rydberg states not coupled to light, or exhibiting Förster zeros [25], thus degrading the blockade.

Figures 2(b)–2(e) shows the probabilities $P_{rg} + P_{gr}$ to excite only one atom, and P_{rr} to excite both, versus the area $\Omega\tau$ of the excitation pulse, for various R and Ω, in the case $n = 62$. In Fig. 2(b), the atoms are far apart ($R \simeq 15$ μm) and thus almost independent. Indeed, the probability P_{rr} of exciting both atoms is nearly equal to the product $P_{1,r}P_{2,r}$ [see Fig. 2(a)], where $P_{i,r}$ is the probability for atom i to be in $|r\rangle$, obtained in a control experiment with only trap i. In this case $P_{rg} + P_{gr}$ is expected to oscillate at frequency 2Ω between 0 and 1/2, close to what we observe. On the contrary, in Fig. 2(e), the atoms are close ($R \simeq 4.0$ μm) and $\Omega \simeq 2\pi \times 1.9$ MHz is small enough for almost perfect blockade to occur: at all times, P_{rr} is negligible ($P_{rr} < 0.06$, with an average of 0.036), and thus differs substantially from the product of the single-atom excitation probabilities expected for independent atoms. At the same time, $P_{rg} + P_{gr}$ oscillates at $(1.49 \pm 0.07)\Omega$, close to the expected collective frequency $\sqrt{2}\Omega$ [16].

In between those regimes [see Figs. 2(c) and 2(d)], blockade is only partial: $P_{rg} + P_{gr}$ and P_{rr} show a more complex behavior, revealing nontrivial two-atom states. We model this dynamics by solving the optical Bloch equations (OBEs) [26,27]. Each atom i ($i = 1, 2$) is considered as a two-level atom with ground state $|g\rangle_i$ and $nD_{3/2}$ Rydberg state $|r\rangle_i$, coupled by a near-resonant laser with Rabi frequency Ω (in practice, for our data, the atoms experience, within 5%, the same Ω). In the basis $\{|gg\rangle, |gr\rangle, |rg\rangle, |rr\rangle\}$, and using the rotating wave approximation, the Hamiltonian is

$$H = \begin{pmatrix} 0 & \hbar\Omega/2 & \hbar\Omega/2 & 0 \\ \hbar\Omega/2 & -\hbar\delta & 0 & \hbar\Omega/2 \\ \hbar\Omega/2 & 0 & -\hbar\delta & \hbar\Omega/2 \\ 0 & \hbar\Omega/2 & \hbar\Omega/2 & U_{\mathrm{vdW}} - 2\hbar\delta \end{pmatrix}. \quad (1)$$

We omit diagonal terms corresponding to interaction between ground-state atoms (for $R = 1$ μm the van der Waals interaction is in the 10^{-8} Hz range, and the

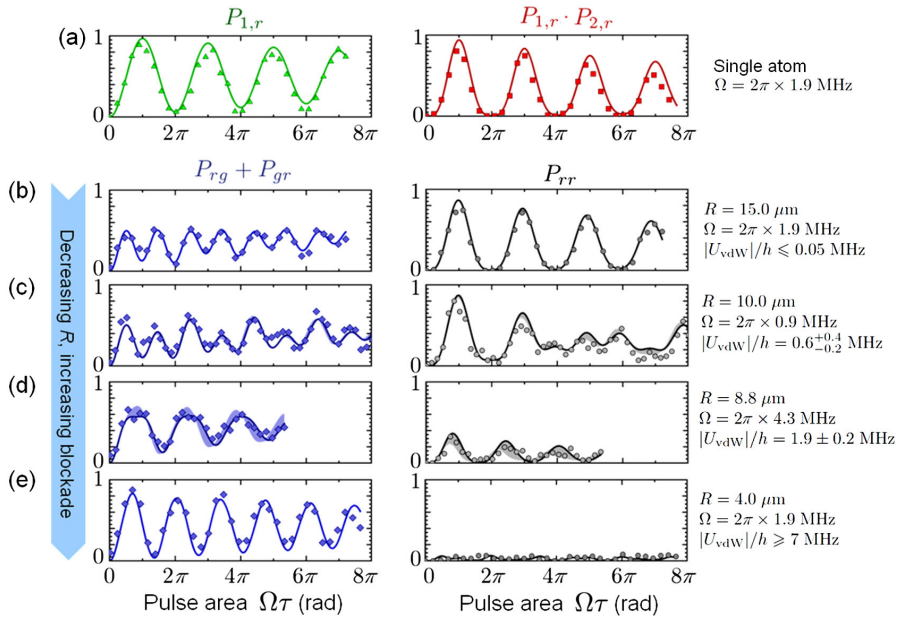

FIG. 2 (color online). From independent to blockaded atoms, via partial blockade, for $n = 62$. (a) Single-atom Rabi oscillation $P_{1,r}(\Omega\tau)$ between $|g\rangle$ and $|r\rangle$ (green triangles), and product of such excitation probabilities for single atoms in traps 1,2 with the other trap off (red squares). (b)–(e): Probability $P_{rg} + P_{gr}$ to excite one atom to the Rydberg state (blue diamonds), and double Rydberg excitation probability P_{rr} (black circles), versus excitation pulse area $\Omega\tau$. From (b) to (e), R decreases, yielding increasing blockade. Solid lines are fits of the data by the solution of the OBEs (see text). Shaded areas correspond to one standard deviation in determining $|U_{\rm vdW}|$ (statistical error bars on Ω, at the 1% level, are not shown).

magnetic dipole-dipole interaction in the mHz range) or between a ground-state and a Rydberg atom (in the 1 Hz range at $R = 1\ \mu$m), as they are negligible with respect to the relevant energy scales of the problem. Experimentally, we observe (especially for large Ω) a small damping of the oscillations, essentially due to off-resonant spontaneous emission via the $5P_{1/2}$ intermediate state. To take this into account, we solve the OBEs for the two-atom density matrix $\dot{\rho} = -i[H, \rho]/\hbar + \mathcal{L}$. We write the dissipative term as $\mathcal{L} = \mathcal{L}_1 \otimes \rho_2 + \rho_1 \otimes \mathcal{L}_2$, where

$$\mathcal{L}_i = \gamma \begin{pmatrix} \rho_{rr} & -\rho_{gr}/2 \\ -\rho_{rg}/2 & -\rho_{rr} \end{pmatrix}_i \qquad (2)$$

is the dissipator for atom i (neglecting dephasing), expressed in the basis $\{|g\rangle_i, |r\rangle_i\}$, and ρ_i the reduced density matrix of atom i. This phenomenological way to include dissipation is sufficient for the present data; a more exact way would include several levels (including the $5P_{1/2}$ state) for each atom, as was done in Refs. [23,27]. We neglect cooperative effects such as super radiance (this is legitimate as R is much larger than the wavelength $\lambda \simeq 795$ nm of the $5S$-$5P$ transition which dominates the dissipation via spontaneous emission) [26].

The parameters Ω and γ appearing in the model are obtained by fitting single-atom Rabi oscillation data [see the triangles in Fig. 2(a)]. The only remaining parameters in the model are $U_{\rm vdW}$ and δ. We treat $U_{\rm vdW}$ as an adjustable parameter to fit the solution of the OBEs to $P_{rg}(t) + P_{gr}(t)$ and $P_{rr}(t)$. Examples of such fits are presented as solid lines in Figs. 2(b)–2(e) (shaded areas show the confidence interval in $U_{\rm vdW}$). We also treat δ as a free parameter, to account for slow drifts of the lasers [28]. With this method, we obtain only $|U_{\rm vdW}|$, as for $\delta \simeq 0$ the sign of the interaction does not affect the dynamics. We have checked that deliberately setting $\delta = 0$ and $\gamma = 0$ in the fit (thus reducing our analysis to solving an effectively three-level Schrödinger equation), yields values of $|U_{\rm vdW}|$ departing by at most 20% from those above. We checked that the interaction energy yielded by the fits does not depend on the chosen Ω by doubling or halving it. We emphasize that the convergence of the fit is optimal when $U_{\rm vdW} \sim \hbar\Omega$. Combined with our range of accessible Ω, this means we can determine values of $|U_{\rm vdW}|/h$ in the range from 0.1 to 10 MHz.

Figure 3 shows $|U_{\rm vdW}|$ extracted from such fits versus R, for the Rydberg states $|r\rangle = |nD_{3/2}, m_j = 3/2\rangle$ with $n = 53$, $n = 62$, and $n = 82$. The data are consistent with a power law of exponent -6. Here, the determination of the exponent is much more direct than for interacting ultracold [11] or thermal [29] ensembles, in which the

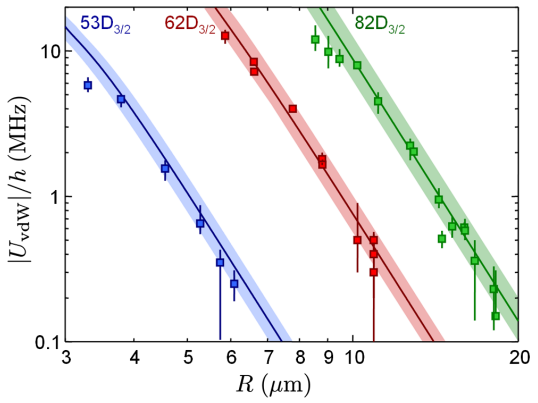

FIG. 3 (color online). Magnitude $|U_{\mathrm{vdW}}|$ of the interaction energy between atoms in $|nD_{3/2}, m_j = 3/2\rangle$, extracted from the fits of Fig. 2, versus R, for $n = 53$ (blue), $n = 62$ (red), and $n = 82$ (green). Error bars are one standard deviation in the fitted $|U_{\mathrm{vdW}}|$. Solid lines: *ab initio* theoretical expectations (see text) without any adjustable parameter. Shaded areas: 5% systematic uncertainty in R.

random distribution of atoms smears out the interaction R dependence. Our results illustrate the dramatic dependence of U_{vdW} with n: for instance, changing n from 53 to 62 at given R yields a fiftyfold increase in U_{vdW}. Fitting the data by $|U_{\mathrm{vdW}}| = |C_6|_{\mathrm{Expt.}}/R^6$ with $|C_6|_{\mathrm{Expt.}}$ as an adjustable parameter, we obtain the values of Table I.

To compare our measurements to the theoretical expressions of $|U_{\mathrm{vdW}}|$ (solid lines in Fig. 3), we diagonalize the interaction Hamiltonian, considering only the leading, electric dipole interaction term. From the quantum defects reported in Ref. [30], we compute radial wave functions using the Numerov algorithm [31]. We restrict the Hamiltonian to a two-atom basis $|n_1 l_1 j_1 m_{j1}, n_2 l_2 j_2 m_{j2}\rangle$ comprising only states close in energy (up to $\sim h \times 5\,\mathrm{GHz}$) from the $|nD_{3/2}, m_j = 3/2, nD_{3/2}, m_j = 3/2\rangle$ state, and satisfying $|n - n_{1,2}| \leq 4$. This corresponds to (sparse) matrices up to $\simeq 10^3 \times 10^3$ [32].

At the large distances relevant here, the dipole-dipole interaction simply shifts the two-atom levels by a quantity C_6/R^6 that can be obtained from second-order perturbation theory. At shorter distances, mixing between adjacent levels occurs [25], altering the $1/R^6$ character of the interaction (this can be seen for $n = 53$ when $R < 4$ μm). We obtain the $|C_6|_{\mathrm{Th.}}$ coefficients of Table I by fitting the numerically obtained interactions at distances $15 < R < 20$ μm. Our results are in good agreement with second-order perturbation theory calculations [33]. We get an estimate of the uncertainty in $|C_6|_{\mathrm{Th.}}$ by adding random, uniformly distributed relative errors of $\pm 0.5\%$ to radial matrix elements appearing in the Hamiltonian. The relative uncertainty is larger ($\sim 10\%$) for $n = 53$, due to cancellations of terms with opposite signs. Taking into account

TABLE I. Experimental and theoretical $|C_6|$ coefficients for $n = 53$, 62, and 82.

n	$\lvert C_6\rvert_{\mathrm{Expt}}(\mathrm{GHz}\cdot\mu\mathrm{m}^6)$	$\lvert C_6\rvert_{\mathrm{Th}}(\mathrm{GHz}\cdot\mu\mathrm{m}^6)$
53	13.7 ± 1.2	16.9 ± 1.7
62	730 ± 20	766 ± 15
82	8500 ± 300	8870 ± 150

error bars, the agreement between our measurement and the calculated C_6 is very good. It appears from Fig. 3 that for the largest values of U_{vdW}, our experimental determination systematically lies below the theory. An explanation might be that mechanical effects induced by interactions lead to a modification of the dynamics, as recently suggested [34]. Our present analysis neglects these effects and may lead to an underestimation of the actual interaction. Including these effects is left to future work.

In summary, we have directly measured the van der Waals interaction between two isolated Rydberg atoms. The level of control demonstrated here opens exciting perspectives in multiatom systems, for observing geometry-dependent effects due to the anisotropy of the dipolar interaction [35], or the nonadditivity of van der Waals interactions [36]. It is also a prerequisite for generating high-fidelity, many-atom entanglement using Rydberg blockade, as well as for quantum simulation of long-range interacting spin systems.

We thank A. Guilbaud, P. Roth, C. Beurthe, F. Moron, and F. Nogrette for technical assistance, C. Evellin for contributions at the early stage of this work, Y. R. P. Sortais for invaluable advice in the design of the setup, H. Labuhn and S. Ravets for a careful reading of the manuscript, and J. Vigué for useful discussions. L. B. is partially supported by the DGA. We acknowledge financial support by the EU (ERC Stg Grant ARENA, AQUTE Integrating Project, and Initial Training Network COHERENCE), and by Région Île-de-France (LUMAT and Triangle de la Physique).

[1] J. N. Israelachvili, *Intermolecular And Surface Forces* (Academic, New York, 2010).
[2] P. C. Hiemenz and R. Rajagopalan, *Principles of Colloid and Surface Chemistry* (Marcel Dekker, New York, 1997).
[3] R. J. Le Roy and R. B. Bernstein, J. Chem. Phys. **52**, 3869 (1970).
[4] See, e.g., A. Aspect and J. Dalibard, Séminaire Poincaré **1**, 67 (2002), and references therein.
[5] A. Anderson, S. Haroche, E. A. Hinds, W. Jhe, and D. Meschede, Phys. Rev. A **37**, 3594 (1988).
[6] V. Sandoghdar, C. I. Sukenik, E. A. Hinds, and S. Haroche, Phys. Rev. Lett. **68**, 3432 (1992).
[7] D. Jaksch, J. I. Cirac, P. Zoller, R. Côté, and M. D. Lukin, Phys. Rev. Lett. **85**, 2208 (2000).

[8] M. D. Lukin, M. Fleischhauer, and R. Cote, Phys. Rev. Lett. **87**, 037901 (2001).
[9] D. Comparat and P. Pillet, J. Opt. Soc. Am. B **27**, A208 (2010).
[10] K. Singer, M. Reetz-Lamour, T. Amthor, L. G. Marcassa, and M. Weidemüller, Phys. Rev. Lett. **93**, 163001 (2004).
[11] R. Heidemann, U. Raitzsch, V. Bendkowsky, B. Butscher, R. Löw, L. Santos, and T. Pfau, Phys. Rev. Lett. **99**, 163601 (2007).
[12] J. D. Pritchard, D. Maxwell, A. Gauguet, K. J. Weatherill, M. P. A. Jones, and C. S. Adams, Phys. Rev. Lett. **105**, 193603 (2010).
[13] Y. O. Dudin and A. Kuzmich, Science **336**, 887 (2012).
[14] P. Schauss, M. Cheneau, M. Endres, T. Fukuhara, S. Hild, A. Omran, T. Pohl, C. Gross, S. Kuhr, and I. Bloch, Nature (London) **491**, 87 (2012).
[15] E. Urban, T. A. Johnson, T. Henage, L. Isenhower, D. D. Yavuz, T. G. Walker, and M. Saffman, Nat. Phys. **5**, 110 (2009).
[16] A. Gaëtan, Y. Miroshnychenko, T. Wilk, A. Chotia, M. Viteau, D. Comparat, P. Pillet, A. Browaeys, and P. Grangier, Nat. Phys. **5**, 115 (2009).
[17] M. Saffman, T. G. Walker, and K. Mølmer, Rev. Mod. Phys. **82**, 2313 (2010).
[18] H. Weimer, M. Müller, I. Lesanovsky, P. Zoller, and H. P. Büchler, Nat. Phys. **6**, 382 (2010).
[19] N. Schlosser, G. Reymond, I. Protsenko, and P. Grangier, Nature (London) **411**, 1024 (2001).
[20] T. Wilk, A. Gaëtan, C. Evellin, J. Wolters, Y. Miroshnychenko, P. Grangier, and A. Browaeys, Phys. Rev. Lett. **104**, 010502 (2010).
[21] Y. R. P. Sortais *et al.*, Phys. Rev. A **75**, 013406 (2007).
[22] The dispersion in the interatomic distances due to the finite temperature has negligible effects. For $T = 50\,\mu$K, the transverse size in our traps (of radial frequency $\omega_r \sim 2\pi \times 100$ kHz) is $\sim$100 nm (longitudinal size only contributes to second order).
[23] Y. Miroshnychenko, A. Gaëtan, C. Evellin, P. Grangier, D. Comparat, P. Pillet, T. Wilk, and A. Browaeys, Phys. Rev. A **82**, 013405 (2010).
[24] R. Löw, H. Weimer, J. Nipper, J. B Balewski, B. Butscher, H. P. Büchler, and T. Pfau, J. Phys. B **45**, 113001 (2012).
[25] T. G. Walker and M. Saffman, Phys. Rev. A **77**, 032723 (2008).
[26] C. Ates, T. Pohl, T. Pattard, and J. M. Rost, Phys. Rev. A **76**, 013413 (2007).
[27] X. L. Zhang, A. T. Gill, L. Isenhower, T. G. Walker, and M. Saffman, Phys. Rev. A **85**, 042310 (2012).
[28] For our data, the best-fit value of $\delta/(2\pi)$ lies in the range $\pm$300 kHz, compatible with observed frequency drifts of the excitation lasers over the acquisition of a full data set (a few hours).
[29] T. Baluktsian, B. Huber, R. Löw and T. Pfau, Phys. Rev. Lett. **110**, 123001 (2013).
[30] W. Li, I. Mourachko, M. W. Noel, and T. F. Gallagher, Phys. Rev. A **67**, 052502 (2003).
[31] M. L. Zimmerman, M. G. Littman, M. M. Kash, and D. Kleppner, Phys. Rev. A **20**, 2251 (1979).
[32] At the large distances used to extract C_6, only a few tens of states contribute significantly. However, to obtain the correct short-distance behavior, $\sim 10^3$ states are necessary.
[33] A. Reinhard, T. C. Liebisch, B. Knuffman, and G. Raithel, Phys. Rev. A **75**, 032712 (2007).
[34] W. Li, C. Ates, and I. Lesanovsky, arXiv:1303.3212.
[35] T. J. Caroll, K. Claringbould, A. Goodsell, M. J. Lim, and M. W. Noel, Phys. Rev. Lett. **93**, 153001 (2004).
[36] D. Cano and J. Fortágh, Phys. Rev. A **86**, 043422 (2012).

Single-Atom Trapping in Holographic 2D Arrays of Microtraps with Arbitrary Geometries

F. Nogrette, H. Labuhn, S. Ravets, D. Barredo, L. Béguin, A. Vernier, T. Lahaye, and A. Browaeys

Laboratoire Charles Fabry, UMR 8501, Institut d'Optique, CNRS, Univ Paris Sud 11, 2 avenue Augustin Fresnel, 91127 Palaiseau cedex, France

(Received 21 February 2014; revised manuscript received 24 March 2014; published 23 May 2014)

We demonstrate single-atom trapping in two-dimensional arrays of microtraps with arbitrary geometries. We generate the arrays using a spatial light modulator, with which we imprint an appropriate phase pattern on an optical dipole-trap beam prior to focusing. We trap single ^{87}Rb atoms in the sites of arrays containing up to approximately 100 microtraps separated by distances as small as 3 μm, with complex structures such as triangular, honeycomb, or kagome lattices. Using a closed-loop optimization of the uniformity of the trap depths ensures that all trapping sites are equivalent. This versatile system opens appealing applications in quantum-information processing and quantum simulation, e.g., for simulating frustrated quantum magnetism using Rydberg atoms.

DOI: 10.1103/PhysRevX.4.021034 Subject Areas: Atomic and Molecular Physics, Optics

I. INTRODUCTION

The optical trapping of cold atoms [1] allows for a variety of applications, from the study of quantum gases [2] to the manipulation of single atoms [3]. Impressive achievements in the engineering of quantum systems have been obtained using relatively simple configurations of light fields, such as single-beam traps [4], crossed optical dipole traps [5], arrays of microtraps obtained by microlens arrays [6,7] or holographic plates [8], optical lattices [9,10], or speckle fields [11].

In the last few years, an interest in more advanced tailoring of optical potentials has arisen. Several technical approaches can be considered. A first solution consists of "painting" arbitrary patterns of light using a time-dependent light deflector [12,13], over time scales that are fast compared to the typical oscillation frequency in the trap. Ultracold atoms then experience an optical potential corresponding to the time-averaged light intensity. Another approach relies on the generation of reconfigurable light patterns using spatial light modulators (SLMs), either in amplitude or in phase [14–17].

Single atoms held in arrays of microtraps with a spacing of a few μm are a promising platform for quantum-information processing and quantum simulation with Rydberg atoms [18–22]. The realization of an array of approximately 50 microtraps for single atoms using an elegant combination of fixed diffractive optical elements and polarization optics was recently demonstrated in Ref. [23].

Here, we report on the trapping of single atoms in reconfigurable 2D arrays of microtraps, separated by distances down to 3 μm, with almost arbitrary geometries. We create not only mesoscopic arrays of a few traps but also regular 2D lattices with up to approximately 100 sites, with geometries ranging from simple square or triangular lattices to more advanced ones, such as kagome or honeycomb structures. Using a closed-loop optimization of the uniformity of the trap depths allows us to obtain very uniform lattices. As compared to previous approaches using SLMs, this novel feature opens appealing prospects for quantum simulation with neutral atoms [24] and eliminates a source of complication in the theoretical modeling of these systems. For that, we use a phase-modulating SLM, which has the advantage of being versatile and easily reconfigurable. Another major asset of the system lies in the fact that, in combination with wave-front analysis, the SLM can also be used to correct *a posteriori* for aberrations that are inevitably present in the optical setup, thus improving considerably the optical quality of the traps.

This article is organized as follows. After giving an overview of the principles behind our setup, we give a detailed account of the obtained results. We present a gallery of examples of microtrap arrays in which we trap single atoms, and we study the single-atom loading statistics of a 3×3 square array. In a second part, we give details about the implementation of the optical setup and the calculation of the phase holograms. We then explain how we optimize the obtained traps using a Shack-Hartmann (SH) wave-front sensor and present a closed-loop improvement of the uniformity of the trap intensities.

II. MAIN RESULTS

In this section, after briefly describing our experimental setup, we demonstrate the trapping of single atoms in microtrap arrays with various geometries.

A. Overview of the experimental setup

Figure 1 shows a sketch of the setup we use to trap single ^{87}Rb atoms [25]. It is based on a red-detuned dipole trap at a wavelength $\lambda = 850$ nm, with a $1/e^2$ radius $w_0 \simeq 1$ μm. For a power of 3 mW, the trap has a typical depth $U_0 = k_B \times 1$ mK, with radial (respectively, longitudinal) trapping frequencies around 100 kHz (respectively, 20 kHz). To load atoms into the microtrap, we produce a cloud of cold atoms at approximately 50 μK in a magneto-optical trap (MOT). The dipole-trap beam is focused in the cloud with a custom-made high-numerical-aperture (NA) aspheric lens with focal length $f_{\text{asph}} = 10$ mm [26]. We detect single atoms by measuring their fluorescence signal at 780 nm (collected by the same aspheric lens) using a cooled, 16-bit electron-multiplying CCD (EMCCD) camera [27]. We separate the fluorescence signal from the trapping beam with a dichroic mirror (DM). A second aspheric lens, facing the first one in a symmetrical configuration, is used to recollimate the trapping beam. An 8-bit CCD camera, placed after the vacuum chamber, is conjugated with the plane of the single atoms for diagnostic purposes.

We generate arrays of microtraps with arbitrary geometries using a phase-modulating SLM [28], which imprints a calculated phase pattern $\varphi(x, y)$ onto the trapping beam of initial Gaussian amplitude $A_0(x, y)$. The intensity distribution in the focal plane of the aspheric lens is then given by the squared modulus of the 2D Fourier transform of $A_0 \exp(i\varphi)$. The phase pattern φ needed to obtain the desired intensity distribution is determined by the iterative algorithm described in Sec. III B.

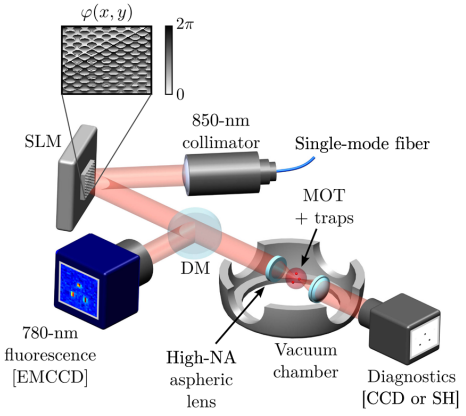

FIG. 1. Generation of an array of microtraps for single-atom trapping. The SLM imprints the calculated phase pattern $\varphi(x, y)$ on the 850-nm dipole-trap beam. A high-numerical-aperture aspheric lens under vacuum focuses it at the center of a MOT. The intensity distribution in the focal plane is $\propto |\text{FT}(A_0 e^{i\varphi})|^2$, where A_0 is the initial Gaussian amplitude profile of the 850-nm beam and FT stands for Fourier transform. The atomic fluorescence at 780 nm is reflected off a DM and detected using an EMCCD camera. A second aspheric lens (identical to the first one) recollimates the 850-nm beam. This transmitted beam is used for trap diagnostics (either with a diagnostics CCD camera or a SH wave-front sensor).

B. Gallery of microtrap arrays

Figure 2 presents a selection of 2D trap arrays that we have created with the setup described above. For each array, we show the phase pattern $\varphi(x, y)$ used to create it, an image of the array obtained with the diagnostics CCD camera behind the chamber, and the average of approximately 1000 images of the atomic fluorescence of single atoms in the traps (imaged with the EMCCD camera). The figure illustrates strikingly the versatility of the setup. We can create small clusters containing approximately 10 traps, useful for the study of mesoscopic systems [Figs. 2(a)–2(h)]. It is also possible to create larger, regular lattices of up to approximately 100 traps with varying degrees of complexity, from simple square [Fig. 2(i)] or triangular [Fig. 2(j)] lattices to honeycomb [Fig. 2(k)] or kagome [Fig. 2(l)] structures, which opens, for instance, the possibility to simulate frustrated quantum magnetism with Rydberg-interacting atoms. The typical nearest-neighbor distance a in those arrays is 4 to 5 μm. We have also created arrays with spacings as small as $a \simeq 3$ μm without observing a significant degradation in the quality of the arrays. Other configurations, e.g., aperiodic structures, can be generated easily.

The total power needed to create an array of N microtraps with a depth $U_0/k_B \simeq 1$ mK necessary for single-atom trapping is about $3N$ mW on the atoms. Because of the finite diffraction efficiency of the SLM and losses on various optical components, we find that this needed power requires us to have slightly below $5N$ mW at the output of the fiber guiding the 850-nm light to the experiment, which remains a very reasonable requirement even for $N = 100$ traps.

C. Single-atom trapping in the arrays

We now demonstrate directly single-atom trapping in a 3×3 square array [see Fig. 3(a)]. Figure 3(b) shows a series of snapshots obtained with the EMCCD camera (the exposure time being 50 ms), showing fluorescence images of single atoms. As each of the $N = 9$ traps has a probability $p \sim 1/2$ of containing one atom, we observe that most images correspond to a sparsely loaded array, with an average number of atoms present close to $Np = 9/2$ and fluctuations corresponding to atoms randomly entering and leaving each trap. To confirm that these images do correspond to single-atom trapping, we plot the photon counts per 50 ms in the pixels corresponding to the positions of each of the nine traps as a function of time [see Fig. 3(c)]. One observes the characteristic random telegraphlike signal, with only two fluorescence levels, which is the hallmark of single atoms loaded into the microtraps by the collisional blockade mechanism [3,25].

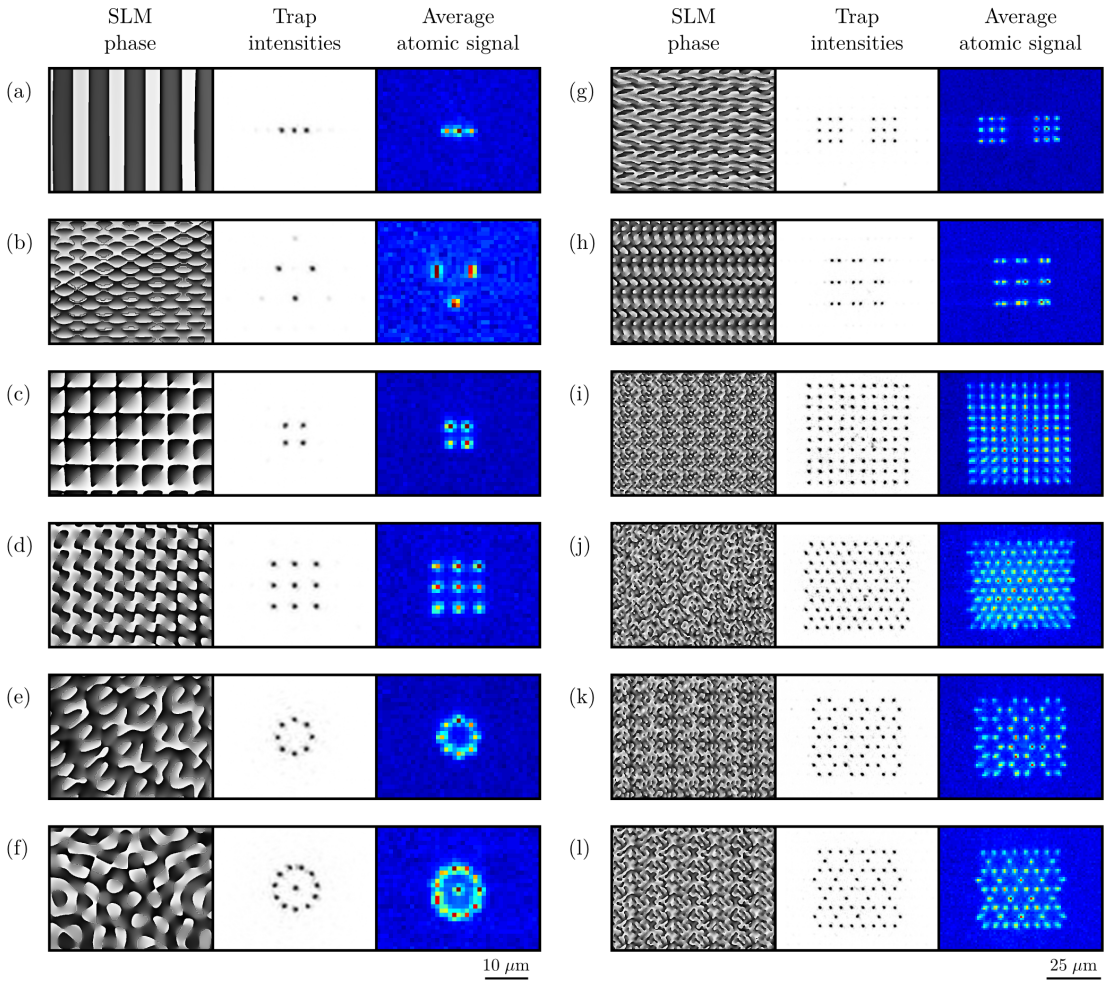

FIG. 2. A gallery of microtrap arrays with different geometries. For each panel, we show the calculated phase pattern φ used to create the array (left), an image of the resulting trap arrays taken with the diagnostics CCD (middle), and the average of approximately 1000 fluorescence images of single atoms loaded into the traps (right).

By analyzing each of the nine traces, we find that the occupation probability p_i of each trap i is close to $1/2$. (We find probabilities p_i ranging from 0.43 to 0.57, with an average $\bar{p} = 0.53$.)

Figure 3(d) is a histogram of the number of atoms trapped in the 3×3 array, obtained by analyzing approximately 2500 images [23]. For an array of N independent traps, if each trap has the same probability p to be filled, the probability P_n to have n atoms in the array is given by the binomial distribution

$$P_n = \frac{N!}{n!(N-n)!} p^n (1-p)^{N-n}. \quad (1)$$

The dots in Fig. 3(d) correspond to Eq. (1) with $N = 9$ and $p = \bar{p}$ and show good agreement with the data. Therefore, the assumption that all traps are loaded with the same probability is a good approximation for estimating the probability of a given configuration to occur.

III. DETAILED IMPLEMENTATION

In the preceding section, we focused on giving a detailed presentation of the results obtained. However, obtaining arrays of traps with as high a quality as what is demonstrated in Figs. 2 and 3 requires some care in the implementation of the setup. In this section, we detail the implementation of both the hardware and the software parts of the system.

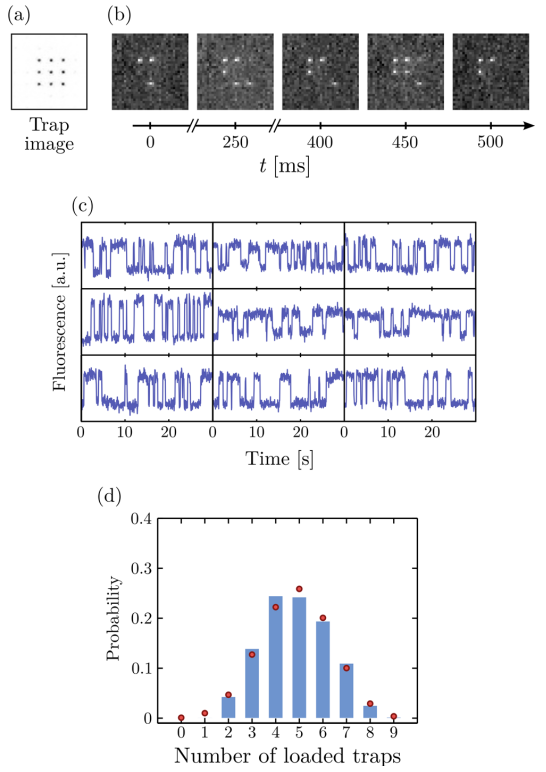

FIG. 3. Single-atom trapping in a 3×3 array. (a) Image of the traps, separated by 4 μm, obtained with the diagnostics CCD camera. (b) Sample fluorescence images of single atoms trapped in the array. The exposure time is 50 ms. (c) Photon counts per 50 ms at the pixels corresponding to each of the nine trap positions, as a function of time. The random, telegraphlike signal with only two fluorescence levels is the signature of single-atom trapping. (d) Histogram of the occurrences of images with n atoms trapped (with $0 \leq n \leq 9$) over a set of approximately 2500 images. The red dots correspond to the binomial distribution [Eq. (1)] with $p = 0.53$.

A. Optical layout

Our SLM has an active area of 12×18 mm^2, with a resolution of 600×800 pixels. It is illuminated by a collimated Gaussian beam with a 6.7-mm $1/e^2$ radius coming from a polarization-maintaining, single-mode fiber connected to a collimator with a focal length $f = 75$ mm. As diffraction-limited operation of the aspheric lens is obtained for an infinite-to-focus conjugation, with a pupil diameter $D = 10$ mm, we use an afocal telescope with a transverse magnification $m_y = -0.8$ to adapt the SLM active area to the aspheric lens aperture, while maintaining the collimation of the beam.

The implementation of the full system (vacuum chamber, dichroic mirror for fluorescence detection, components for generating the microtrap array) results in a relatively long distance ($\ell \simeq 500$ mm) between the SLM and the aspheric lens. This leads to the following problem [see Fig. 4(a)]: When generating off-axis traps, the beam diffracted by the SLM impinges on the lens off center, giving rise to clipping and field aberrations. These effects decrease the quality of arrays with a large number of microtraps. We circumvent this problem using pupil conjugation: We take advantage of the extra degree of freedom given by the position of the telescope to conjugate the plane of the SLM with the aspheric lens, as shown in Fig. 4(b).

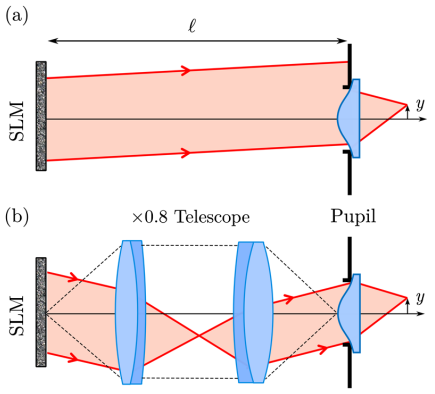

FIG. 4. Pupil conjugation. (a) Without a telescope, for a given field $y \neq 0$, the dipole-trap beam is clipped and not centered on the aspheric lens. (b) The implemented telescope adapts the size of the beam to the aspheric lens pupil; by conjugating the SLM aperture to the entrance pupil of the aspheric lens, the beam is well centered, whatever the field.

The optimization of the system is done with an optical design software. The simulation includes all the components from the optical fiber to the focal plane of the aspheric lens in the vacuum chamber. The lenses of the telescope and the lens of the collimator are near-infrared achromatic doublets used at low numerical aperture and small fields. The performance of the system over a field of 30×30 μm^2 in the microtrap plane is satisfactory: The Strehl ratio, i.e., the ratio of the actual peak intensity over the theoretical peak intensity for a diffraction-limited system [29], is predicted to be $S \geq 0.88$ by the calculation.

For the phase-pattern calculation described below, we replace the telescope and the aspheric lens by a single equivalent lens with an effective focal length $f_{\text{eff}} = f_{\text{asph}}/|m_y| = 12$ mm and an effective pupil in the SLM plane with diameter $D_{\text{eff}} = 12$ mm.

B. Gerchberg-Saxton algorithm

We use the Gerchberg-Saxton (GS) algorithm [30] to calculate the phase pattern $\varphi(x, y)$ required to obtain an intensity distribution in the lens focal plane close to a desired target intensity I_t. For the sake of completeness, we briefly recall below the essential steps of the algorithm (see Fig. 5).

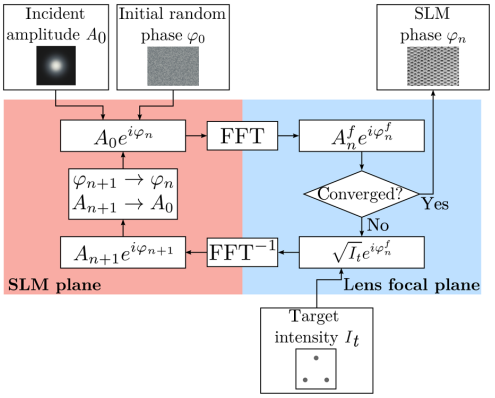

FIG. 5. The Gerchberg-Saxton algorithm. The field in the lens focal plane is calculated by the FFT of the complex field in the SLM plane. If the obtained intensity $|A_n^f|^2$ does not match the target intensity I_t, another iteration must be performed: The amplitude of the field in the focal plane is forced to the target amplitude $\sqrt{I_t}$, and this new field is propagated back to the pupil plane by the inverse FFT, resulting in a new amplitude and a new phase φ_{n+1}. This new phase is kept as the next SLM phase pattern, while the amplitude is forced to the incident one A_0, giving a new input field $A_0 e^{i\varphi_{n+1}}$ for the next iteration.

We initialize the algorithm using a random phase pattern φ_0 in which each pixel value is given by a uniformly distributed random variate in the range $(0, 0.2) \times 2\pi$. The target image I_t is a superposition of Gaussian peaks with $1/e^2$ radii $w = 1$ μm centered on the desired location of the microtraps. The amplitude of each Gaussian can be defined separately, which allows for correcting nonuniformities in the depths of the microtraps over the array (see Sec. III E).

The incident field on the SLM is modeled as having a uniform phase and an amplitude $A_0(x, y)$. At each iteration of the algorithm, we propagate the electric field in the SLM plane $A_0 e^{i\varphi_n}$ through the effective lens using a fast Fourier transform (FFT) to calculate the field $A_n^f e^{i\varphi_n^f}$ in the focal plane. If the difference between the calculated intensity $|A_n^f|^2$ and the desired target image I_t is small enough, the phase pattern φ_n is used to drive the SLM; otherwise, the amplitude of the field in the focal plane is replaced by the target amplitude $\sqrt{I_t}$. This new field $\sqrt{I_t} e^{i\varphi_n^f}$ is then propagated back to the SLM plane by an inverse FFT, giving the field $A_{n+1} e^{i\varphi_{n+1}}$ in the SLM plane. The calculated phase φ_{n+1} is kept as the new phase pattern in the SLM plane, while the amplitude is replaced by the incident one A_0, and another iteration is performed for the field $A_0 e^{i\varphi_{n+1}}$. For the patterns shown in Fig. 2, the algorithm converges (i.e., the calculated phase patterns do not evolve any more) toward an approximate solution, typically after a few tens of iterations [31]. The intensity distribution in the lens focal plane is then a good approximation of I_t. However, we can approach the target even closer, as described in Sec. III E.

C. Phase patterns displayed on the SLM

The phase pattern φ_{tot} used to drive the SLM includes several contributions beyond the calculated phase pattern φ and reads

$$\varphi_{\mathrm{tot}} = \varphi + \varphi_{\mathrm{blaze}} + \varphi_{\mathrm{Fresnel}} + \varphi_{\mathrm{factory}} + \varphi_{\mathrm{SH}}, \qquad (2)$$

where the sum is calculated modulo 2π. In this equation,

(i) φ_{blaze} is a blazed grating pattern, allowing us to block the zeroth-order reflection from the SLM arising from its nonperfect diffraction efficiency;

(ii) $\varphi_{\mathrm{Fresnel}}$ is a quadratic phase pattern acting as a Fresnel lens, which allows us to fine-tune the focusing of the microtraps;

(iii) $\varphi_{\mathrm{factory}}$ is the correction phase pattern provided by the SLM manufacturer to correct for the optical flatness defects of the SLM chip; and

(iv) φ_{SH} corrects for aberrations introduced by the setup and is obtained using a Shack-Hartmann wave-front sensor as described in Sec. III D below.

Figure 6 gives an example of the composition of the final phase pattern obtained by summing (modulo 2π) the various terms described above.

D. Improving the traps by analyzing the wave front and correcting for aberrations using the SLM

Without the last term of Eq. (2), we observe that the quality of the obtained microtrap arrays decreases when the number of traps increases. Indeed, the assumption of a perfect effective lens used in the calculation of the hologram is not valid. The imperfections of the optics (vacuum windows, aspheric lens, etc.) and the residual misalignments distort the wave front, thus reducing the depth of the microtraps.

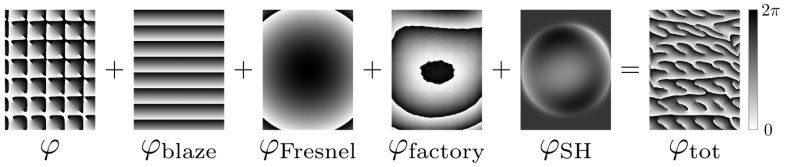

FIG. 6. Composition of the phase pattern φ_{tot} displayed on the SLM for generating the trap array of Fig. 2(c). The sum is calculated modulo 2π.

1. Wave-front measurement

In order to correct for the above-mentioned imperfections, we measure the wave front with a Shack-Hartmann sensor and use the resulting φ_{SH} to drive the SLM [32]. We perform this measurement at the exit of the vacuum chamber, where the trapping beam has been recollimated by the second aspheric lens (see Fig. 1). The wave-front sensor [33] analyzes the wave front corresponding to a single trap centered in the field where the phase pattern displayed on the SLM is $\varphi_{\mathrm{blaze}} + \varphi_{\mathrm{factory}}$. The measured rms deviation from a flat wave front is $\delta_{\mathrm{rms}} = 0.15\lambda$ (tilt and focus terms being removed). After applying the correction phase φ_{SH} to the SLM, we measure $\delta_{\mathrm{rms}} = 0.014\lambda$. Figure 7 illustrates the impact of the phase corrections on the trap pattern (as measured by the diagnostics CCD camera) for a 4×4 array: A comparison between Figs. 7(a) and 7(b) suggests that the correction increases the trap depth by a factor close to 2.

This wave-front measurement includes the aberrations induced by the recollimating aspheric lens and the second vacuum window (see Fig. 1). An independent wave-front measurement on the trapping beam before the chamber yields $\delta_{\mathrm{rms}} = 0.05\lambda$ without correction, showing that the optics of the vacuum chamber account for most of the wave-front aberrations. Applying directly the measured φ_{SH} on the SLM thus "overcorrects" aberrations, and one might fear that at the location of the atoms, the effect of the correction is actually detrimental. It is therefore desirable to check directly the actual effect of the correction on the atoms. For this purpose, we directly measure the trap depth and frequency with single atoms.

2. Impact on the trap depth

We measure the trap depth using light-shift spectroscopy with a single atom [34,35]. For that, we shine a σ^+-polarized probe that is quasiresonant with the transition $|5S_{1/2}, F = 2, m_F = 2\rangle \rightarrow |5P_{3/2}, F = 3, m_F = 3\rangle$ on the atom and we record the number of fluorescence photons scattered by the atom as a function of probe detuning. The shift of the resonance with respect to its free-space value gives directly the trap depth U_0 [36]. Figure 8(a), obtained on the central trap of a 3×1 array with a 4-μm separation, shows that including the Shack-Hartmann correction actually increases the trap depth by about 50%.

3. Impact on the trap frequency

Another important parameter of the trap is the trapping frequency. In order to determine the transverse trapping frequency seen by the atoms, we excite the breathing mode, as in Refs. [25,37]. For that purpose, the microtrap is switched off for a few microseconds, during which the atom leaves the center of the trap. When the trap is switched on again for a time ΔT_{hold}, the atom oscillates in the trap, with a radial frequency ω_r [38]. If the trap is then switched off again for a short time, the probability to recapture the atom afterward depends on its kinetic energy at the time of the last switch-off, and thus oscillates at $2\omega_r$.

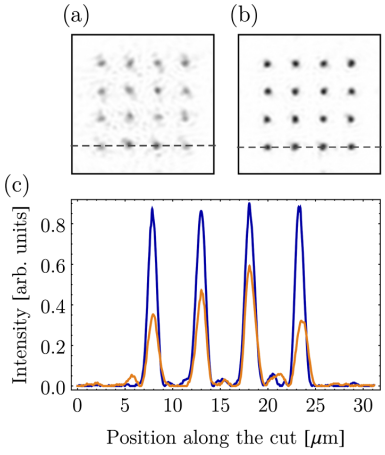

FIG. 7. Effect of the Shack-Hartmann correction pattern φ_{SH}. A CCD image of 4×4 microtraps is shown (a) only with the factory correction and (b) with both the factory and the Shack-Hartmann patterns applied. (c) Intensity profiles along the dashed lines on (a) and (b), with (blue curve) and without (orange curve) the correction φ_{SH}. The arrays are created with the same calculated phase φ. The laser power and the exposure time of the CCD camera are the same for both cases.

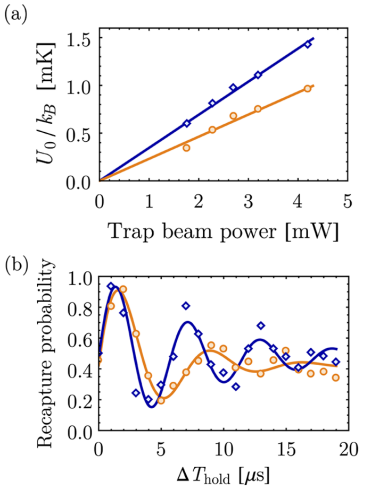

FIG. 8. (a) Trap depth U_0/k_B as a function of the trap power, with (blue diamonds) and without (orange disks) Shack-Hartmann correction. With the latter, the trap depth increases by about 50%. (b) Recapture probabilities for an atom oscillating in the trap as a function of the hold time ΔT_{hold}. The trap frequency increases by about 30% when the Shack-Hartmann correction pattern is added to the SLM.

Figure 8(b) shows the results of such a measurement, for a power of 2.8 mW per trap, again in the 3×1 array. The measured trap frequencies are $\omega_r = 2\pi \times 68.0$ kHz before correction and $\omega_r = 2\pi \times 86.5$ kHz with the Shack-Hartmann correction applied to the SLM. The increase in trapping frequency comes essentially from the increased depth of the corrected traps.

Using the single atom as a diagnostics tool, we could, in principle, test whether one can improve even further the trap quality by applying to the SLM a phase $\alpha\varphi_{\mathrm{SH}}$ (where $0 \leq \alpha \leq 1$ is an adjustable parameter), in the hope of correcting only the aberrations "seen" by the atom, i.e., not the aberrations induced by the second lens and the second viewport. A test for $\alpha = 1/2$ (which would yield the best correction if both lenses and windows introduce equal aberrations) gives results slightly worse than for $\alpha = 1$, and in the following, we thus keep this choice.

E. Closed-loop optimization of the uniformity of the trap depths in the array

An important figure of merit to assess the quality of the arrays is the uniformity of the trap depths. Figure 9(a) shows the distribution of the trap intensities, inferred from an analysis of an image of the array obtained with the diagnostics CCD camera, for a 10×10 square lattice with a spacing $a = 4$ μm. In this case, the phase applied to the SLM is obtained by running the GS algorithm with a target image I_t for which all traps have the same intensity. One observes a dispersion in the trap depths of $\pm 19\%$ rms (the minimal and maximal values being $I_{\mathrm{min}} = 61$ and $I_{\mathrm{max}} = 148$, where the average intensity of all traps is normalized to $\bar{I} = 100$). This variation in trap depths is detrimental for loading optimally the trap array with single atoms. Indeed, if the trap depth is too low, one still traps single atoms, but with a probability of occupancy significantly lower than $1/2$. Conversely, if the trap is too deep, one enters a regime in which the probability to have more than one atom is not negligible [36].

A way to compensate for this imperfection is to use the image of the trap array obtained with the diagnostics CCD to calculate a new target image where the new trap intensity I_i' of trap i is scaled according to the measured one I_i as

$$I_i' = \frac{\bar{I}}{1 - G(1 - I_i/\bar{I})}, \tag{3}$$

where $\bar{I}$ is the average intensity of all traps and G an adjustable "gain." In other words, traps that are too weak get enhanced in the new target image, while the brightest ones get dimmed. We then run again the GS algorithm with this new target image as an input and with the previously obtained phase pattern φ as the initial guess for the phase (see Fig. 10). We observe that the distribution of the trap intensities decreases quite drastically after a few iterations. Choosing $G \simeq 0.7$ gives the best performance. (Lower values decrease the convergence speed, while higher values yield overshoots in the correction.) Figure 9(b) shows the

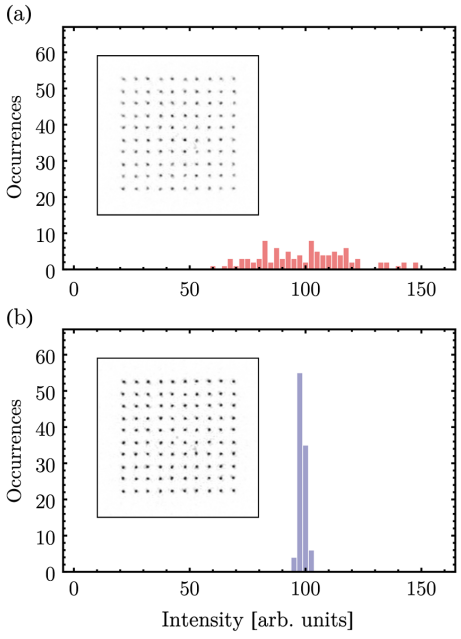

FIG. 9. Improving the uniformity of trap depths in a 10×10 square array. (a) Histogram of the maximal intensity levels of the microtraps I_i, measured with the diagnostics CCD camera (see the inset), for the trap array obtained after a single use of the GS algorithm and a target image where all traps have the same intensity. The standard deviation is 19%. (b) Same as (a) but after the closed-loop optimization of the uniformity of the trap intensities. The standard deviation is now 1.4%.

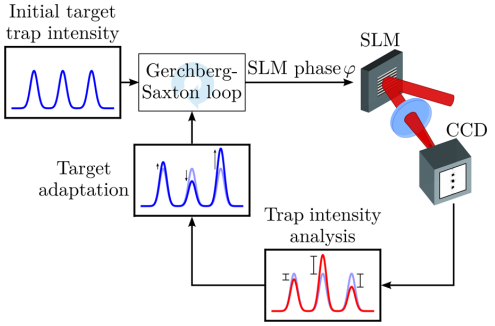

FIG. 10. Closed-loop algorithm used for improving the uniformity of trap depths. From the various trap intensities measured with the CCD camera (red profile), we calculate a new target intensity I_t following Eq. (3): The brightest traps are dimmed, while the dimmest ones are enhanced. We then use this adapted target as the input for a new iteration of the GS algorithm, with the previously calculated phase as the initial condition.

resulting histogram of trap intensities for the 10×10 square lattice, after 20 iterations. The array is now very uniform, with trap intensities varying between 96% and 103% of $\bar{I}$ (peak to peak). This improvement corresponds to a 15-fold reduction in the dispersion of the trap depths.

The single-atom trapping demonstrated in the arrays of Figs. 2 and 3 could be achieved only after this closed-loop optimization is implemented and illustrates strikingly the efficiency of the method. We believe that such an optimization, which takes full advantage of the reconfigurable character of the SLM, could prove useful in order to create very uniform lattices with arbitrary structures for quantum simulation with ultracold atoms.

IV. CONCLUSION AND OUTLOOK

The simple setup described above is a versatile tool for creating arrays of microtraps with almost arbitrary geometries. We have demonstrated single-atom loading in such arrays, which opens exciting possibilities to engineer interesting few-atom entangled states using, e.g., a Rydberg blockade [39], especially in combination with dynamical addressability using moving optical tweezers [40].

For arrays with a large number of traps, a current limitation of the system is the nondeterministic character of the single-atom loading of the microtraps: As each trap has a probability $1/2$ of being filled with an atom, an N-trap array has, at any given time, only an exponentially small probability $1/2^N$ to be fully loaded. Implementing quasi-deterministic loading schemes will thus be needed to take full advantage of the setup, which implies increasing the loading probability p per trap beyond $1/2$. A first approach toward this goal consists in using the Rydberg blockade: Loading probabilities of $p \sim 60\%$ have been recently demonstrated in a single microtrap [41]. Alternatively, using a blue-detuned "collision beam," relatively high loading probabilities, already in excess of 90%, have been achieved [42]. This scheme opens the possibility to fully load an array of 20 traps with a probability of more than 10%. Testing both approaches on our setup will be the subject of future work.

In combination with the recently demonstrated Raman-sideband cooling of single atoms trapped in optical tweezers [43,44], a similar system with smaller distances between microtraps—which could be achieved using high-numerical-aperture objectives such as the ones used in quantum-gas microscopes [45]—could then become an interesting alternative approach to study the many-body physics of ultracold atoms in engineered optical potentials, without using traditional optical lattices [46].

ACKNOWLEDGMENTS

We thank Yvan Sortais for invaluable advice about the optical design and for a careful reading of the manuscript, André Guilbaud for technical assistance, and Bruno Viaris, Laurence Pruvost, and Zoran Hadzibabic for fruitful discussions. We are grateful to Lionel Jacubowiez, Thierry Avignon, and Samuel Bucourt for the loan of Imagine Optic Shack-Hartmann wave-front sensors. This work was supported financially by the EU [ERC Stg Grant ARENA, AQUTE Integrating Project, FET-Open Xtrack Project HAIRS, and EU Marie-Curie Program ITN COHERENCE FP7-PEOPLE-2010-ITN-265031 (H. L.)], by the DGA (L. B.), and by Région Île-de-France (LUMAT and Triangle de la Physique, LAGON Project).

[1] R. Grimm, M. Weidemüller, and Yu. B. Ovchinnikov, *Optical Dipole Traps for Neutral Atoms*, Adv. At. Mol. Opt. Phys. **42**, 95 (2000).

[2] M. Lewenstein, A. Sampera, and V. Ahufinger, *Ultracold Atoms in Optical Lattices: Simulating Quantum Many-Body Systems* (Oxford University Press, Oxford, England, 2012).

[3] N. Schlosser, G. Reymond, I. Protsenko, and P. Grangier, *Sub-Poissonian Loading of Single Atoms in a Microscopic Dipole Trap*, Nature (London) **411**, 1024 (2001).

[4] G. Cennini, G. Ritt, C. Geckeler, and M. Weitz, *Bose-Einstein Condensation in a CO_2-Laser Optical Dipole Trap*, Appl. Phys. B **77**, 773 (2003).

[5] M. D. Barrett, J. A. Sauer, and M. S. Chapman, *All-Optical Formation of an Atomic Bose-Einstein Condensate*, Phys. Rev. Lett. **87**, 010404 (2001).

[6] R. Dumke, M. Volk, T. Müther, F. B. J. Buchkremer, G. Birkl, and W. Ertmer, *Micro-optical Realization of Arrays of Selectively Addressable Dipole Traps: A Scalable Configuration for Quantum Computation with Atomic Qubits*, Phys. Rev. Lett. **89**, 097903 (2002).

[7] M. Schlosser, S. Tichelmann, J. Kruse, and G. Birkl, *Scalable Architecture for Quantum Information Processing with Atoms in Optical Microstructures*, Quantum Inf. Process. **10**, 907 (2011).

[8] R. Newell, J. Sebby, and T. G. Walker, *Dense Atom Clouds in a Holographic Atom Trap*, Opt. Lett. **28**, 1266 (2003).

[9] I. Bloch, *Ultracold Quantum Gases in Optical Lattices*, Nat. Phys. **1**, 23 (2005).

[10] K. D. Nelson, X. Li, and D. S. Weiss, *Imaging Single Atoms in a Three-Dimensional Array*, Nat. Phys. **3**, 556 (2007).

[11] J. Billy, V. Josse, Z. Zuo, A. Bernard, B. Hambrecht, P. Lugan, D. Clément, L. Sanchez-Palencia, P. Bouyer, and A. Aspect, *Direct Observation of Anderson Localization of Matter Waves in a Controlled Disorder*, Nature (London) **453**, 891 (2008).

[12] F. K. Fatemi, M. Bashkansky, and Z. Dutton, *Dynamic High-Speed Spatial Manipulation of Cold Atoms Using Acousto-optic and Spatial Light Modulation*, Opt. Express **15**, 3589 (2007).

[13] K. Henderson, C. Ryu, C. MacCormick, and M. G. Boshier, *Experimental Demonstration of Painting Arbitrary and Dynamic Potentials for Bose-Einstein Condensates*, New J. Phys. **11**, 043030 (2009).

[14] A. L. Gaunt and Z. Hadzibabic, *Robust Digital Holography for Ultracold Atom Trapping*, Sci. Rep. **2**, 721 (2012).

[15] A. L. Gaunt, T. F. Schmidutz, I. Gotlibovych, R. P. Smith, and Z. Hadzibabic, *Bose-Einstein Condensation of Atoms in a Uniform Potential*, Phys. Rev. Lett. **110**, 200406 (2013).
[16] V. Boyer, C. M. Chandrashekar, C. J. Foot, and Z. J. Laczik, *Dynamic Optical Trap Generation Using FLC SLMs for the Manipulation of Cold Atoms*, J. Mod. Opt. **51**, 2235 (2004).
[17] S. Bergamini, B. Darquié, M. Jones, L. Jacubowiez, A. Browaeys, and P. Grangier, *Holographic Generation of Microtrap Array for Single Atoms by Use of a Programmable Phase Modulator*, J. Opt. Soc. Am. B **21**, 1889 (2004).
[18] M. Saffman, T. Walker, and K. Mølmer, *Quantum Information with Rydberg Atoms*, Rev. Mod. Phys. **82**, 2313 (2010).
[19] E. Urban, T. A. Johnson, T. Henage, L. Isenhower, D. D. Yavuz, T. G. Walker, and M. Saffman, *Observation of Rydberg Blockade between Two Atoms*, Nat. Phys. **5**, 110 (2009).
[20] A. Gaëtan, Y. Miroshnychenko, T. Wilk, A. Chotia, M. Viteau, D. Comparat, P. Pillet, A. Browaeys, and P. Grangier, *Observation of Collective Excitation of Two Individual Atoms in the Rydberg Blockade Regime*, Nat. Phys. **5**, 115 (2009).
[21] L. Béguin, A. Vernier, R. Chicireanu, T. Lahaye, and A. Browaeys, *Direct Measurement of the van der Waals Interaction between Two Rydberg Atoms*, Phys. Rev. Lett. **110**, 263201 (2013).
[22] D. Barredo, S. Ravets, H. Labuhn, L. Béguin, A. Vernier, F. Nogrette, T. Lahaye, and A. Browaeys, *Demonstration of Strong Rydberg Blockade in Three-Atom Systems with Anisotropic Interactions*, Phys. Rev. Lett. **112**, 183002 (2014).
[23] M. J. Piotrowicz, M. Lichtman, K. Maller, G. Li, S. Zhang, L. Isenhower, and M. Saffman, *Two-Dimensional Lattice of Blue-Detuned Atom Traps Using a Projected Gaussian Beam Array*, Phys. Rev. A **88**, 013420 (2013).
[24] I. Bloch, J. Dalibard, and S. Nascimbène, *Quantum Simulations with Ultracold Quantum Gases*, Nat. Phys. **8**, 267 (2012).
[25] Y. R. P. Sortais, H. Marion, C. Tuchendler, A. M. Lance, M. Lamare, P. Fournet, C. Armellin, R. Mercier, G. Messin, A. Browaeys, and P. Grangier, *Diffraction Limited Optics for Single Atom Manipulation*, Phys. Rev. A **75**, 013406 (2007).
[26] We use a D-ZLaF52LA aspheric lens from LightPath technologies. It is optimized at 780 nm for an infinite-to-focus conjugation with a numerical aperture NA = 0.54. When used at 850 nm, its performance is maintained for a reduced aperture NA = 0.44, i.e., $D = 10$ mm.
[27] We use a Andor iXon Ultra, which can be used in an EMCCD mode. However, due to the relatively high photon yield (approximately 300 photons per 50-ms time bin), here, we do not need to use the electron multiplier to detect single atoms.
[28] Reflective liquid crystal on silicon, Hamamatsu X10468-02.
[29] H. Gross, *Handbook of Optical Systems* (Wiley-VCH, Weinheim, 2007), Vol. 3.
[30] R. W. Gerchberg and W. O. Saxton, *A Practical Algorithm for the Determination of Phase from Image and Diffraction Plane Pictures*, Optik (Stuttgart) **35**, 237 (1972).
[31] We have implemented the algorithm using MATLAB. Without any attempt to optimize the code, convergence takes less than one minute on a personal computer.
[32] C. López-Quesada, J. Andilla, and E. Martín-Badosa, *Correction of Aberration in Holographic Optical Tweezers Using a Shack-Hartmann Sensor*, Appl. Opt. **48**, 1084 (2009).
[33] We use a HASO4 First from Imagine Optic.
[34] M. K. Tey, Z. Chen, S. A. Aljunid, B. Chng, F. Huber, G. Maslennikov, and C. Kurtsiefer, *Strong Interaction between Light and a Single Trapped Atom without the Need for a Cavity*, Nat. Phys. **4**, 924 (2008).
[35] C. Y. Shih and M. S. Chapman, *Nondestructive Light-Shift Measurements of Single Atoms in Optical Dipole Traps*, Phys. Rev. A **87**, 063408 (2013).
[36] L. Béguin, Ph.D. thesis, Institut d'Optique Graduate School, 2013.
[37] H. Engler, T. Weber, M. Mudrich, R. Grimm, and M. Weidemüller, *Very Long Storage Times and Evaporative Cooling of Cesium Atoms in a Quasielectrostatic Dipole Trap*, Phys. Rev. A **62**, 031402 (2000).
[38] The longitudinal confinement is much weaker than in the radial direction, so for short switch-off times, the longitudinal motion of the atom is only weakly excited.
[39] M. Müller, I. Lesanovsky, H. Weimer, H. P. Büchler, and P. Zoller, *Mesoscopic Rydberg Gate Based on Electromagnetically Induced Transparency*, Phys. Rev. Lett. **102**, 170502 (2009).
[40] J. Beugnon, C. Tuchendler, H. Marion, A. Gaëtan, Y. Miroshnychenko, Y. R. P. Sortais, A. M. Lance, M. P. A. Jones, G. Messin, A. Browaeys, and P. Grangier, *Two-Dimensional Transport and Transfer of a Single Atomic Qubit in Optical Tweezers*, Nat. Phys. **3**, 696 (2007).
[41] M. Ebert, A. Gill, M. Gibbons, X. Zhang, M. Saffman, and T. G. Walker, *Atomic Fock State Preparation Using Rydberg Blockade*, Phys. Rev. Lett. **112**, 043602 (2014).
[42] A. V. Carpentier, Y. H. Fung, P. Sompet, A. J. Hilliard, T. G. Walker, and M. F. Andersen, *Preparation of a Single Atom in an Optical Microtrap*, Laser Phys. Lett. **10**, 125501 (2013).
[43] A. M. Kaufman, B. J. Lester, and C. A. Regal, *Cooling a Single Atom in an Optical Tweezer to Its Quantum Ground State*, Phys. Rev. X **2**, 041014 (2012).
[44] J. D. Thompson, T. G. Tiecke, A. S. Zibrov, V. Vuletić, and M. D. Lukin, *Coherence and Raman Sideband Cooling of a Single Atom in an Optical Tweezer*, Phys. Rev. Lett. **110**, 133001 (2013).
[45] W. S. Bakr, J. I. Gillen, A. Peng, S. Foelling, and M. Greiner, *A Quantum Gas Microscope for Detecting Single Atoms in a Hubbard Regime Optical Lattice*, Nature (London) **462**, 74 (2009).
[46] A. M. Kaufman, B. J. Lester, C. M. Reynolds, M. L. Wall, M. Foss-Feig, K. R. A. Hazzard, A. M. Rey, and C. A. Regal, *Hong-Ou-Mandel Atom Interferometry in Tunnel-Coupled Optical Tweezers*, arXiv:1312.7182.

Demonstration of a Strong Rydberg Blockade in Three-Atom Systems with Anisotropic Interactions

D. Barredo, S. Ravets, H. Labuhn, L. Béguin, A. Vernier, F. Nogrette, T. Lahaye, and A. Browaeys
Laboratoire Charles Fabry, Institut d'Optique, CNRS, Univ Paris Sud,
2 avenue Augustin Fresnel, 91127 Palaiseau cedex, France
(Received 17 February 2014; published 8 May 2014)

We study the Rydberg blockade in a system of three atoms arranged in different two-dimensional geometries (linear and triangular configurations). In the strong blockade regime, we observe high-contrast, coherent collective oscillations of the single excitation probability and an almost perfect van der Waals blockade. Our data are consistent with a total population in doubly and triply excited states below 2%. In the partial blockade regime, we directly observe the anisotropy of the van der Waals interactions between $|nD\rangle$ Rydberg states in the triangular configuration. A simple model that only uses independently measured two-body van der Waals interactions fully reproduces the dynamics of the system without any adjustable parameter. These results are extremely promising for scalable quantum information processing and quantum simulation with neutral atoms.

DOI: 10.1103/PhysRevLett.112.183002 PACS numbers: 32.80.Ee, 03.67.Bg, 34.20.Cf

Engineering quantum many-body systems with a high degree of control and tunable interactions is an active field of research as it is a prerequisite for quantum information processing [1] and quantum simulation [2]. Recently, significant achievements have been obtained towards this goal, e.g., using trapped ions for simulating quantum magnetism [3–5]. Another platform considered for such tasks consists of systems of neutral Rydberg atoms interacting via the strong and controllable long-range dipole-dipole interaction, which is responsible for the Rydberg blockade [6–9]. Through this mechanism, multiple excitations with a resonant narrow-band laser are inhibited within a blockade sphere by Rydberg-Rydberg interactions. The dipole blockade provides a way to realize fast quantum gates and to entangle particles, as demonstrated for two atoms [10,11]. This mechanism can in principle be extended to an ensemble of N atoms, with fascinating applications in quantum state engineering [12].

Although the picture of a blockade sphere has been remarkably successful at describing many recent experiments [13–22], some theoretical works question this simple approach. Even for the case of $N = 3$, some situations have been identified where nearly resonant dipole-dipole interactions [23], the nonadditivity of the van der Waals potentials [24], or the anisotropy of the interactions [25] lead to the breakdown or reduction of the blockade.

In this Letter, we show that, for experimentally relevant parameters, the Rydberg blockade is robust in ensembles of three atoms. In particular, we consider two different arrangements, namely, a line and an equilateral triangle. We observe an almost perfect van der Waals blockade and the coherent collective behavior of Rydberg excitations in both configurations. To go beyond this observation and understand the dynamics of the system in detail, we measure the angular dependence of the effective interaction energy V_{eff} between two single-atoms excited to $|r\rangle \equiv |nD_{3/2}, m_j = 3/2\rangle$ Rydberg states. Using the measured two-body interaction strength we demonstrate that it is possible to fully reproduce the three-atom excitation dynamics in both the full and partial blockade regimes, with a model based on a master equation with no adjustable parameters. With the degree of experimental control demonstrated here, many theoretical proposals envisioning quantum simulation using Rydberg atoms become realistic.

We consider three atoms, with ground $|g_i\rangle$ and Rydberg $|r_i\rangle$ states coupled with Rabi frequencies Ω_i, and interacting via pairwise interactions V_{ij}. The system is thus described by the Hamiltonian [26]

$$\hat{H} = \sum_{i=1}^{3} \frac{\hbar\Omega_i}{2}(\hat{\sigma}_{rg}^{(i)} + \hat{\sigma}_{gr}^{(i)}) + \sum_{i<j} V_{ij}\hat{\sigma}_{rr}^{(i)}\hat{\sigma}_{rr}^{(j)}, \qquad (1)$$

where $\hat{\sigma}_{rg}^{(i)} = |r_i\rangle\langle g_i|$, $\hat{\sigma}_{gr}^{(i)} = |g_i\rangle\langle r_i|$, and $\hat{\sigma}_{rr}^{(i)} = |r_i\rangle\langle r_i|$. All parameters of the Hamiltonian can be tuned by a proper choice of the experimental settings. In particular, choosing $|r\rangle = |nD_{3/2}\rangle$ gives an extra degree of freedom to tune V_{ij} due to the anisotropy of the interaction. In what follows all Rabi couplings $\Omega_i \equiv \Omega$ are equal within 5%.

A strong blockade is obtained if the interaction strengths V_{ij} between atom pairs are much greater than the atom-light coupling $\hbar\Omega$ [Fig. 1(a)]. In this regime, the states carrying double and triple Rydberg excitations are off-resonant with the light field and the system can be described as a two-level model involving the collective states $|ggg\rangle$ and $|\Phi_{1r}\rangle = (|ggr\rangle + |grg\rangle + |rgg\rangle)/\sqrt{3}$, coupled by an effective Rabi frequency $\sqrt{3}\Omega$. Here, $|ijk\rangle \equiv |i_1\rangle|j_2\rangle|k_3\rangle$ stands

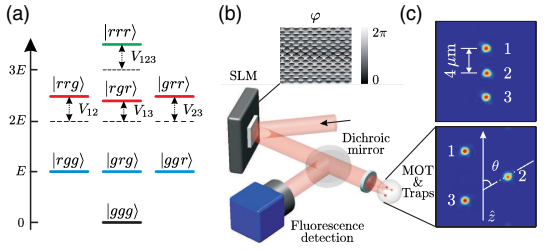

FIG. 1 (color online). (a) Relevant energy levels of a three-atom system with van der Waals interactions V_{ij}. In the blockade regime, the ground state $|ggg\rangle$ is resonantly coupled to the symmetric collective state $(|ggr\rangle+|grg\rangle+|rgg\rangle)/\sqrt{3}$. (b) Scheme of the experimental setup. Arbitrary geometries of two-dimensional arrays of dipole traps are obtained by imprinting a phase map φ with the SLM. (c) Trap geometry. Three single-atoms are trapped in microscopic optical tweezers separated by $R = 4$ μm in a linear (top) and by $R = 8$ μm in a triangular arrangement (bottom). The quantization axis $\hat{z}$ is set by a 3G external magnetic field.

for products of the single-atom ground $|g\rangle$, and Rydberg $|r\rangle$ states for atoms 1, 2, and 3.

Our apparatus, shown schematically in Fig. 1(b), was previously described in detail [27]. Three single ^{87}Rb atoms are loaded from a magneto-optical trap into three 1 mK-deep microscopic optical traps [28], formed by focusing down a 850 nm Gaussian beam to a waist of 1 μm ($1/e^2$ radius) using a high numerical aperture lens under vacuum [29]. Arbitrary patterns of traps are obtained by imprinting a calculated phase pattern on the beam with a spatial light modulator (SLM) [30]. CCD images of the two trap configurations used in this work are displayed in Fig. 1(c). In the first arrangement (top), the three traps are collinear (parallel to the quantization axis $\hat{z}$) and separated by $R = 4$ μm. In the second configuration (bottom), the traps form an equilateral triangle with 8 μm sides.

The same aspheric lens is used to collect the atom fluorescence from each trap. We trigger the experimental sequence as soon as one atom is detected in each of the three traps. The atoms are then optically pumped into $|g\rangle = |5S_{1/2}, F = 2, m_F = 2\rangle$. The quantization axis $\hat{z}$ is set by a 3G external magnetic field. For Rydberg excitation from $|g\rangle$ to $|nD_{3/2}, m_j = 3/2\rangle$, we use a two-photon process [31]: a π-polarized laser beam at 795 nm, detuned from the $|5P_{1/2}, F = 2, m_F = 2\rangle$ intermediate state by $2\pi \times 740$ MHz, and a σ^+-polarized 474 nm laser beam. Both excitation lasers are frequency locked using an ultrastable cavity providing laser linewidths $\sim$10 kHz. During the Rydberg excitation, the dipole traps are switched off to avoid light shifts. After excitation for a duration τ, we switch on again the dipole traps and we look for the fluorescence of the three atoms. Excitation of an atom to the Rydberg state is inferred from its loss from the corresponding trap (and thus the absence of fluorescence), as Rydberg states are not trapped. The eight different populations P_{ijk} of the three-atom states $|ijk\rangle$ are then reconstructed by repeating each sequence $\sim$150 times [31].

We first consider a one-dimensional array of three individual atoms aligned along the quantization axis [see Fig. 1(c) top] and separated by 4 μm. To obtain the single-atom Rabi frequencies Ω_i we measure the probability P_{r_i} to excite atom i to the Rydberg state, with the other two traps switched off, as a function of the excitation pulse area. We observe well-contrasted Rabi oscillations [Fig. 2(a)]. A fit of the data (solid line) gives the same Rabi frequencies $\Omega_i \simeq 2\pi \times 0.8$ MHz for the three atoms (within 5%), as well as small damping rates $\gamma_i \simeq 0.3$ μs^{-1} (see below). In Fig. 2(b) a single atom is loaded in each of the three traps. In this configuration we expect full blockade, as the single-atom Rabi frequencies are much smaller than van der Waals interactions: even for the $R = 8$ μm distance between the outermost atoms, extrapolation of the measurement of Ref. [27] gives $V_{13} \simeq h \times 32$ MHz. The three atoms are excited to the collective state $|\Phi_{1r}\rangle$ [Fig. 1(a)], and the single excitation probability $P_{1r} \equiv P_{rgg} + P_{grg} + P_{ggr}$ shows oscillations with a frequency of $(1.72 \pm 0.02)\Omega$, compatible with the expected $\sqrt{3}\Omega$. Clear blockade of multiple Rydberg

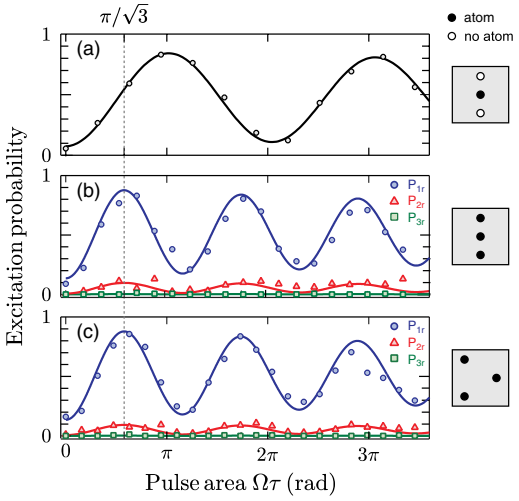

FIG. 2 (color online). (a) Representative single-atom Rabi flopping to the $|82D_{3/2}\rangle$ state for the central atom in the linear arrangement. Single-atom Rabi frequencies $\Omega \simeq 2\pi \times 0.8$ MHz, and damping rates $\gamma \simeq 0.3$ μs^{-1} for all three atoms are obtained from fits (solid lines) to the solution of the OBEs for a single two-level atom. (b) Probability of single (blue circles), double (red triangles), and triple (green squares) Rydberg excitation as a function of the excitation pulse area in the linear arrangement. The collective enhancement of the Rabi frequency by $\sqrt{3}$ clearly appears in the data. Solid lines are the result of the model described in the text without any adjustable parameter. (c) Same as (b) but for the triangular geometry.

excitations is observed in the data, as the populations $P_{2r} = P_{rrg} + P_{rgr} + P_{grr}$ ($P_{3r} = P_{rrr}$) of doubly (triply) excited states are almost totally suppressed in the system, with P_{2r} (P_{3r}) never exceeding 9% (1%).

We now show that the actual blockade is even better than suggested by these values. Indeed, each atom has a small probability ε to be lost during the sequence, independently of its internal state [32]. An independent measurement of the loss probability gives $\varepsilon = (5 \pm 1)\%$. Since in our detection scheme an atom loss is interpreted as an excitation to the Rydberg state, the *observed* double excitation P_{2r} differs from the *actual* one $\tilde{P}_{2r}$ and, to first order in ε, it reads [32]

$$P_{2r} = (1 - \varepsilon)\tilde{P}_{2r} + 2\varepsilon\tilde{P}_{1r}. \quad (2)$$

If the blockade were perfect, one would have $\tilde{P}_{2r} = 0$, and the measured P_{2r} would thus oscillate between 0 and 2ε, in phase with P_{1r}. From the data on Fig. 2(b) we can extract an upper bound of $\sim$2% on $\tilde{P}_{2r}$ [32].

To gain more insight into the quality of the blockade for our experimental parameters, we simulate the dynamics of the system with Hamiltonian (1). A sum of independent single atom dissipators,

$$L[\rho] = \sum_i \frac{\gamma_i}{2}(2\hat{\sigma}_{gr}^{(i)}\rho\hat{\sigma}_{rg}^{(i)} - \hat{\sigma}_{rr}^{(i)}\rho - \rho\hat{\sigma}_{rr}^{(i)}), \quad (3)$$

is used to account for a small experimental damping γ_i of the oscillations (mainly due to off-resonant spontaneous emission through the intermediate state $|5P_{1/2}\rangle$; all the γ_i are equal within 10%). The results of the simulation, with no adjustable parameter, are represented by solid lines in Fig. 2(b), where the loss-error correction (2) is included. The very good agreement with the data further supports the quality of the blockade. Our results are compatible with the prediction of the model of double excitation probability $\tilde{P}_{2r}^{(\mathrm{theo.})} \sim 10^{-3}$ for the same experimental parameters. Although proving experimentally that the double excitation is that low would require a more detailed study of systematic effects, this figure is very encouraging for high-fidelity generation of three-atom $|\mathrm{W}\rangle$ states.

In the results discussed so far, we only considered a one-dimensional configuration. For scalability to a large number of atoms, however, two-dimensional arrays of traps are preferable. In this case, some atom pairs necessarily have an internuclear axis not aligned along the quantization axis and the anisotropy of the interaction comes into play, which might eventually prevent a perfect blockade [23–25]. To investigate this effect we study the blockade in an equilateral triangle configuration. Here, the anisotropic character of the D-state orbital plays a role and the interaction energies between atom pairs $V_{12} \simeq V_{23}$ are weaker than V_{13}, although the atoms are equally separated. Despite this, Fig. 2(c) shows that the strength of the blockade is not reduced in the triangular geometry. Double and triple excitation probabilities are inhibited and the single excitation probability oscillates at $\sim\sqrt{3}\Omega$. This result opens encouraging prospects for achieving strong blockade over two-dimensional arrays of atoms.

In order to observe directly the anisotropy of the interaction [33] we measured the interaction energy between atom pairs separated by $R = 12$ μm as a function of the angle θ between the internuclear axis and the quantization axis $\hat{z}$. The procedure to extract the effective interaction energy V_{eff} is similar to the one introduced in Ref. [27]. Working in the partial blockade regime ($\hbar\Omega \sim V_{\mathrm{eff}}$), we model the excitation dynamics through the solution of the optical Bloch equations (OBE) involving two-level atoms. Strictly speaking, to model two atoms in the $|nD_{3/2}\rangle$ state and $\theta \neq 0$, one would need to consider all 49 Zeeman sublevels with their different van der Waals couplings [34]. So as to keep the model tractable, even for large number of atoms, we model the system in the simplest nontrivial way, retaining only one single doubly excited state $|rr\rangle$ with an effective energy shift $V_{\mathrm{eff}}(\theta)$. All input parameters are obtained from single-atom Rabi oscillation experiments. The measured dynamics of the two-atom system are then fitted with the solution of the OBEs with V_{eff} as the only fitting parameter. A more detailed study of the angular dependence of the van der Waals interaction, taking into account the full Zeeman structure of the atom pair, is beyond the scope of this Letter and will be the subject of future work.

The result of this approach is shown in Fig. 3 for the $|82D_{3/2}\rangle$ state. The anisotropy of the effective interaction is evident. The energy shift shows a maximum around $\theta = 0$

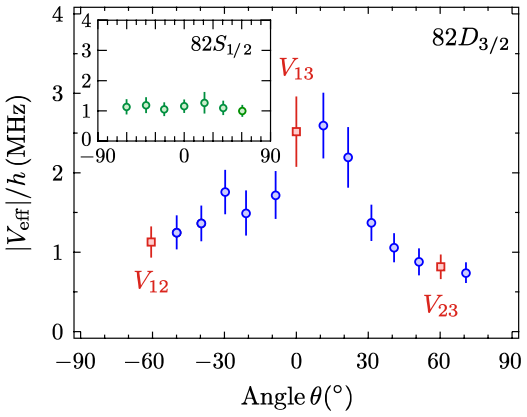

FIG. 3 (color online). Angular dependence of the effective interaction energy V_{eff} for two atoms in $|82D_{3/2}\rangle$ at $R = 12$ μm, with θ the angle between the internuclear axis and the quantization axis $\hat{z}$. Red squares indicate the measured energy shifts V_{13}, V_{23}, and V_{12} used for the simulation of three-atom dynamics in the partial blockade regime (see Fig. 4). In the inset, the angular dependence of the interaction for the spherically symmetric $|82S_{1/2}\rangle$ state is shown for comparison. Error bars represent one standard deviation confidence intervals in the fits.

and decreases for larger angles. A relative change of interaction strength by a factor ~3 is measured when θ varies from $\theta = 0$ to $\theta = 60°$. In contrast, for a spherically symmetric S-Rydberg state, the interaction energy is isotropic (see inset of Fig. 3) [35] . For the D state, we observe an unexpected, slight asymmetry in the angular dependence of V_{eff}, probably due to small systematic effects [36] .

The angular dependence of V_{eff} manifests itself in the interaction dynamics of the three atoms in the triangular configuration. By increasing the sides of the triangle to $R = 12$ μm, the effective interaction energies become $(V_{12}, V_{23}, V_{13}) \simeq h \times (0.9, 1.1, 2.6)$ MHz (see red squares in Fig. 3), and the blockade is only partial for our chosen Rabi frequency Ω. In Fig. 4 we show the populations of doubly (P_{rrg}, P_{rgr}, P_{grr}) and triply (P_{rrr}) excited states for two different Rabi frequencies. In the first data set [Fig. 4(a)], $\Omega = 2\pi \times 0.8$ MHz and the anisotropy in the binary interaction ($V_{12} \neq V_{13}$) is directly observed in the dynamics: the probability P_{rgr} to detect double excitation of atoms 1 and 3 is almost totally suppressed, while it is appreciable for P_{rrg} and P_{grr}. Those two curves show almost the same dynamics, as expected. Triple excitations are totally blocked in this regime. For comparison, we show also the dynamics when a slightly higher Rabi frequency $\Omega = 2\pi \times 1.6$ MHz is used [Fig. 4(b)]. This corresponds to a partial blockade regime where $V_{13} > \hbar\Omega > V_{12}$. In this case, even triple excitations are not completely blockaded. P_{rrg} and P_{grr} also exhibit similar behavior, while P_{rgr} shows different dynamics. The populations of states carrying only single excitations also show the anisotropy [32].

Many-body effects have largely been recognized to play a key role in the modeling of systems in physics and chemistry [37]. In the case of Rydberg atoms they have been invoked to explain anomalous broadenings of Förster resonances [38,39]. To understand the evolution of the population of the states during excitation and to investigate to what extent few-atom many-body physics can be described from pairwise interactions we perform again a simulation using the OBEs for the three-atom system. In the model, with no adjustable parameters, the measured interaction energies at $\theta = 0$ and $\theta = 60°$ (red squares in Fig. 3) are introduced. As shown by the solid lines in Fig. 4, the simulation (where atom loss correction is included) fully reproduces the experimental data. The fact that the simulation can accurately describe the evolution of the triply excited state P_{rrr} suggests that, for our choice of parameters, the pairwise addition of van der Waals level shifts $V_{123} = V_{12} + V_{13} + V_{23}$ is valid to a very good approximation. However, this additivity of the potential may not hold in the case of resonant dipole-dipole interactions. There, quantum interference between different many-body interaction channels can influence the dynamics [23]. All these processes can be studied for Rydberg atoms close to Förster resonance and will be the subject of future work. Another interesting line of research will consist in studying the recently predicted Borromean trimers bound by the dipole-dipole interaction [40].

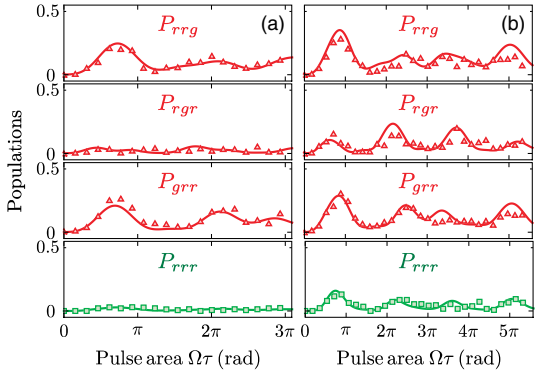

FIG. 4 (color online). Probabilities of detection of double Rydberg excitation P_{rrg}, P_{rgr}, P_{grr}, and triple excitation P_{rrr} versus excitation pulse area $\Omega\tau$ for driving Rabi frequencies $\Omega = 2\pi \times 0.8$ MHz (a), and $\Omega = 2\pi \times 1.6$ MHz (b) in the triangular configuration. The distance between the traps is $R = 12$ μm. The ratio between effective pairwise interaction energies is $V_{13}/V_{12} \sim 3$ for $\theta = 60°$. Solid lines are the solution of the OBEs without any adjustable parameter.

In summary, we have investigated the dynamics of a system of three Rydberg atoms in both full and partial blockade regimes. We observe a strong van der Waals blockade of the excitations and coherent Rabi oscillations for two different spatial configurations. For the same experimental parameters in the equilateral triangle arrangement, the anisotropy of the interaction potential between $|nD\rangle$ states does not prevent the observation of a strong van der Waals blockade, which is a prerequisite for the scalability of quantum information processing proposals using two-dimensional arrays of dipole traps. The strong blockade achieved and the small damping of the oscillations pave the way for the generation of many-atom entanglement with high fidelity through the Rydberg blockade [12]. In the partial blockade regime, the angular dependence of the interaction energy shift between two atoms has been measured for the $|82D_{3/2}\rangle$ and $|82S_{1/2}\rangle$ Rydberg states. Furthermore, we have shown that with the measured effective energy shifts it is possible to reproduce the three-atom dynamics with high accuracy. This result demonstrates that one can confidently scale those studies for two-dimensional arrays of more than a few atoms, enabling the quantum simulation of large-size, long-range interacting spin systems.

We thank Daniel Cano for interesting discussions. This work was supported financially by the EU [ERC Stg Grant ARENA, AQUTE Integrating project, FET-Open Xtrack project HAIRS, EU Marie-Curie program ITN COHERENCE FP7-PEOPLE-2010-ITN-265031 (H.L.)], by the DGA (L.B.), and by Région Île-de-France (LUMAT and Triangle de la Physique, LAGON project).

[1] M. A. Nielsen, I. L. Chuang, *Quantum Computation and Quantum Information* (Cambridge University Press, Cambridge, England, 2000).
[2] R. Feynman, Int. J. Theor. Phys. **21**, 467 (1982).
[3] B. P. Lanyon *et al.*, Science **334**, 57 (2011).
[4] J. W. Britton, B. C. Sawyer, A. C. Keith, C.-C. Joseph Wang, J. K. Freericks, H. Uys, M. J. Biercuk, and J. J. Bollinger, Nature (London) **484**, 489 (2012).
[5] R. Islam, C. Senko, W. C. Campbell, S. Korenblit, J. Smith, A. Lee, E. E. Edwards, C.-C. J. Wang, J. K. Freericks, and C. Monroe, Science **340**, 583 (2013).
[6] H. Weimer, M. Müller, I. Lesanovsky, P. Zoller and H. P. Büchler, Nat. Phys. **6**, 382 (2010).
[7] D. Jaksch, J. I. Cirac, P. Zoller, S. L. Rolston, R. Côté, and M. D. Lukin, Phys. Rev. Lett. **85**, 2208 (2000).
[8] M. D. Lukin, M. Fleischhauer, R. Cote, L. M. Duan, D. Jaksch, J. I. Cirac, and P. Zoller, Phys. Rev. Lett. **87**, 037901 (2001).
[9] D. Comparat and P. Pillet, J. Opt. Soc. Am. B **27**, A208 (2010).
[10] T. Wilk, A. Gaëtan, C. Evellin, J. Wolters, Y. Miroshnychenko, P. Grangier, and A. Browaeys, Phys. Rev. Lett. **104**, 010502 (2010).
[11] L. Isenhower, E. Urban, X. L. Zhang, A. T. Gill, T. Henage, T. A. Johnson, T. G. Walker, and M. Saffman, Phys. Rev. Lett. **104**, 010503 (2010).
[12] M. Saffman, T. G. Walker, and K. Mølmer, Rev. Mod. Phys. **82**, 2313 (2010).
[13] K. Singer, M. Reetz-Lamour, T. Amthor, L. G. Marcassa, and M. Weidemüller, Phys. Rev. Lett. **93** 163001 (2004).
[14] R. Heidemann, U. Raitzsch, V. Bendkowsky, B. Butscher, R. Löw, L. Santos, and T. Pfau, Phys. Rev. Lett. **99**, 163601 (2007).
[15] J. D. Pritchard, D. Maxwell, A. Gauguet, K. J. Weatherill, M. P. A. Jones, and C. S. Adams, Phys. Rev. Lett. **105**, 193603 (2010).
[16] Y. O. Dudin and A. Kuzmich, Science **336**, 887 (2012).
[17] Y. O. Dudin, L. Li, F. Bariani, and A. Kuzmich, Nat. Phys. **8**, 790 (2012).
[18] P. Schauss, M. Cheneau, M. Endres, T. Fukuhara, S. Hild, A. Omran, T. Pohl, C. Gross, S. Kuhr, and I. Bloch, Nature (London) **491**, 87 (2012).
[19] E. Urban, T. A. Johnson, T. Henage, L. Isenhower, D. D. Yavuz, T. G. Walker, and M. Saffman, Nat. Phys. **5**, 110 (2009).
[20] A. Gaëtan, Y. Miroshnychenko, T. Wilk, A. Chotia, M. Viteau, D. Comparat, P. Pillet, A. Browaeys, and P. Grangier, Nat. Phys. **5**, 115 (2009).
[21] G. Günter, H. Schempp, M. Robert-de-Saint-Vincent, V. Gavryusev, S. Helmrich, C. S. Hofmann, S. Whitlock, and M. Weidemuller, Science **342**, 954 (2013).
[22] A. M. Hankin, Y.-Y. Jau, L. P. Parazzoli, C. W. Chou, D. J. Armstrong, A. J. Landahl, and G. W. Biedermann, Phys. Rev. A **89**, 033416 (2014).
[23] T. Pohl and P. R. Berman, Phys. Rev. Lett. **102**, 013004 (2009).
[24] D. Cano and J. Fortágh, Phys. Rev. A **86**, 043422 (2012).
[25] J. Qian, X.-D. Zhao, L. Zhou, and W. Zhang, Phys. Rev. A **88**, 033422 (2013).
[26] I. Lesanovsky, Phys. Rev. Lett. **106**, 025301 (2011).
[27] L. Béguin, A. Vernier, R. Chicireanu, T. Lahaye, and A. Browaeys, Phys. Rev. Lett. **110**, 263201 (2013).
[28] N. Schlosser, G. Reymond, I. Protsenko and P. Grangier, Nature (London) **411**, 1024 (2001).
[29] Y. R. P. Sortais *et al.*, Phys. Rev. A **75**, 013406 (2007).
[30] F. Nogrette *et al.*, arXiv:1402.5329 [Phys. Rev. X (to be published)].
[31] Y. Miroshnychenko, A. Gaëtan, C. Evellin, P. Grangier, D. Comparat, P. Pillet, T. Wilk, and A. Browaeys, Phys. Rev. A **82**, 013405 (2010).
[32] See Supplemental Material at http://link.aps.org/supplemental/10.1103/PhysRevLett.112.183002 for detailed error-loss analysis and full system dynamics.
[33] T. J. Carroll, K. Claringbould, A. Goodsell, M. J. Lim, and M. W. Noel, Phys. Rev. Lett. **93**, 153001 (2004).
[34] A. Reinhard, T. C. Liebisch, B. Knuffman, and G. Raithel, Phys. Rev. A **75**, 032712 (2007).
[35] For excitation to the S state, the polarizations of the 795 nm (474 nm) lasers are π (σ^-).
[36] However, the observed asymmetry has a negligible impact on the three-atom dynamics that we study in the rest of the Letter.
[37] R. A. DiStasio, O. A. von Lilienfeld, and A. Tkatchenko, Proc. Natl. Acad. Sci. U.S.A. **109**, 14791 (2012).
[38] W. R. Anderson, J. R. Veale, T. F. Gallagher, Phys. Rev. Lett. **80**, 249 (1998).
[39] I. Mourachko, D. Comparat, F. de Tomasi, A. Fioretti, P. Nosbaum, V. Akulin, and P. Pillet, Phys. Rev. Lett. **80**, 253 (1998).
[40] M. Kiffner, W. Li, and D. Jaksch, Phys. Rev. Lett. **111**, 233003 (2013).

Single-atom addressing in microtraps for quantum-state engineering using Rydberg atoms

Henning Labuhn, Sylvain Ravets, Daniel Barredo, Lucas Béguin, Florence Nogrette, Thierry Lahaye, and Antoine Browaeys
Laboratoire Charles Fabry, UMR 8501, Institut d'Optique, CNRS, Univ Paris Sud 11,
2 avenue Augustin Fresnel, 91127 Palaiseau cedex, France
(Received 19 June 2014; published 22 August 2014)

We report on the selective addressing of an individual atom in a pair of single-atom microtraps separated by 3 μm. Using a tunable light shift, we render the selected atom off-resonant with a global Rydberg excitation laser which is resonant with the other atom, making it possible to selectively block this atom from being excited to the Rydberg state. Furthermore we demonstrate the controlled manipulation of a two-atom entangled state by using the addressing beam to induce a phase shift onto one component of the wave function of the system, transferring it to a dark state for the Rydberg excitation light. Our results are an important step towards implementing quantum information processing and quantum simulation with large arrays of Rydberg atoms.

DOI: 10.1103/PhysRevA.90.023415 PACS number(s): 37.10.Gh, 32.80.Ee, 03.67.Bg

Cold neutral atoms are a promising platform for quantum computation and quantum simulation [1]. Their weak interactions in the ground state lead to long coherence times. Using highly excited Rydberg states allows one to switch on and off the strong interactions that are necessary for engineering many-body quantum states [2]. For many of those experiments it is desirable to confine single atoms at well-defined positions separated by a few micrometers, which can be achieved, e.g., using arrays of optical tweezers [3]. Another requirement is the selective manipulation of individual atoms in the ensemble. This can be done by applying static field gradients, or a laser beam focused to one single trap site, which induces a frequency shift at the targeted site. Such techniques have been demonstrated with trapped ions [4–6] and neutral atoms in optical lattices [7–13].

In previous work [14,15], we have demonstrated quantum-state engineering with single atoms held in two and three optical microtraps, by using the Rydberg blockade mechanism with global excitation of the atoms. Extending these studies to a larger number of atoms and to wider classes of quantum states requires extra tools. A step towards this goal was our recent demonstration of single-atom trapping in large arrays of optical microtraps with arbitrary geometries [3]. Combined with global excitation, this already opens the possibility to generate interesting multiatom entangled states, such as the W state $|W\rangle = (|rgg\cdots g\rangle + |grg\cdots g\rangle + \cdots + |ggg\cdots r\rangle)/\sqrt{N}$, where $|g\rangle$ ($|r\rangle$) corresponds to the ground (Rydberg) state. However, single-site addressing is needed to engineer other classes of quantum states. For instance, the realization of the collective controlled-NOT (CNOT) gate of Ref. [16] that can be used to create the Greenberger-Horne-Zeilinger state $|\mathrm{GHZ}\rangle = (|gg\cdots g\rangle + |rr\cdots r\rangle)/\sqrt{2}$, requires the singling out of one control atom whose state determines the state of the remaining, target, atoms.

Here we demonstrate the selective addressing of one single ^{87}Rb atom among two atoms held in microtraps separated by 3 μm, by shining a tightly focused, red-detuned 850-nm laser beam on it. This addressing beam induces a frequency shift on the ground state of the atom, while leaving its Rydberg states nearly unaffected. This differential light shift thus makes the addressed atom off-resonant with the Rydberg excitation laser, which is resonant for the other atom. This article is organized as follows. We first briefly describe the implementation of the addressing beam, and characterize its size and depth *in situ* using a single atom. We then perform a global Rydberg excitation in the presence of the addressing beam, and observe nearly perfect suppression of excitations for the addressed atom. Finally, we use the addressing beam to perform a controlled local operation on one atom, coherently transferring the symmetric entangled state $(|rg\rangle + |gr\rangle)/\sqrt{2}$ to the antisymmetric, dark state $(|rg\rangle - |gr\rangle)/\sqrt{2}$.

Our experimental setup, schematically shown in Fig. 1(a), has been described previously [3,14,15]. We use a spatial light modulator (SLM) to create two microtraps, separated by a distance of 3 μm in the focal plane of a high-numerical-aperture (NA) aspherical lens. The traps, each with a $1/e^2$ radius of about 1 μm and a depth of $U_0 \approx h\times 20$ MHz, are focused in an ^{87}Rb magneto-optical trap (MOT). Due to fast light-assisted collisions, we trap only either zero or one atom per trap [17], and trigger the experiment on the presence of one atom in each trap. The temperature of the atoms in the traps is approximately 50 μK. We coherently couple the ground state $|g\rangle = |5S_{1/2}, F = 2, m_f = 2\rangle$ to the Rydberg state $|r\rangle = |nD_{3/2}, m_j = 3/2\rangle$ (with n in the range 50–100) via a two-photon transition, with the wavelengths of the excitation lasers being 795 and 474 nm. During the excitation, of duration τ, the traps are switched off to avoid extra broadening arising from the shot-to-shot fluctuations of the light shift due to the random positions of the atoms in the traps. The detuning from the intermediate state $|5P_{1/2}, F = 2, m_f = 2\rangle$ is $2\pi\times 740$ MHz. After the excitation pulse, we measure the states of both atoms. Repeating the experiment about 100 times, we reconstruct the populations P_{ij} of the two-atom states $|ij\rangle$, where i and j can take the values g and r.

The $1/e^2$ radii of the lasers used for Rydberg excitation are 100 μm for the 795-nm beam, and 18 μm for the 474-nm beam. This configuration prevents the direct addressing of a single trap. To achieve single-site addressability, we thus induce an extra light shift on the ground state of the atom at the targeted site, to selectively control the Rydberg excitation. As a fast (i.e., on microsecond time scales) reconfiguration cannot be achieved with the SLM, we superimpose a second, independently controlled 850-nm laser beam onto the trapping beam. Orthogonal polarizations and a frequency difference of

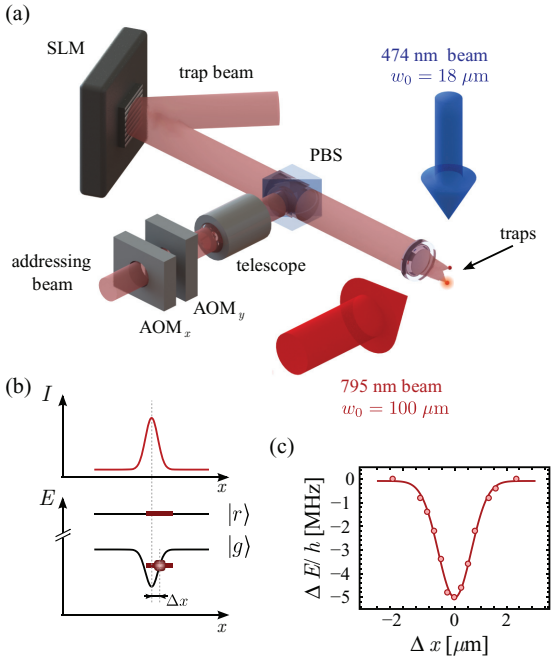

FIG. 1. (Color online) (a) Sketch of the experimental setup. The two microtraps are created by a red-detuned 850-nm laser beam on which an appropriate phase is imprinted using a spatial light modulator (SLM), and focused by a high-NA aspheric lens in a MOT. The addressing beam is superimposed onto the trap beam by a polarizing beam-splitter cube (PBS), and focused down on the targeted atom by the same aspheric lens. The two perpendicular AOMs can be used for precise dynamical x-y positioning of the addressing beam. A telescope is used to conjugate the AOM plane with the aspheric lens, to avoid clipping when the addressing beam is deflected. (b) The light shift ΔE of the ground state of the targeted single atom is directly proportional to the intensity I of the addressing beam at the position x of the atom. (c) Measured light shift ΔE as a function of the distance Δx between the addressing beam and the targeted trap, yielding a $1/e^2$ radius of the addressing beam of $w_0 \simeq 1.3\ \mu$m.

about 200 MHz prevent interference between the trapping and addressing beams. The addressing beam has a $1/e^2$ radius of $w_0 \simeq 1.3\ \mu$m in the focus, slightly larger than the trap size. This choice results from a trade-off between two opposite requirements, namely, minimizing alignment sensitivity and inhomogeneous light shifts (which favors a large w_0) and minimizing cross-talk (which implies choosing a small w_0). For a perfectly Gaussian beam with $w_0 \simeq 1.3\ \mu$m, one expects theoretically that if one atom is addressed by a light shift of 10 MHz, the second atom 3 μm away experiences a light shift of only 0.2 kHz, which is negligible as compared to the other relevant frequencies in the experiment. An electro-optic modulator enables fast (about 10 ns) switching of the addressing beam. In addition, two acousto-optic modulators (AOMs) can be used for dynamical x-y positioning of the addressing beam with respect to the targeted trap.

In a first experiment, we measure the intensity profile of the addressing beam *in situ* by performing Rydberg spectroscopy on a single atom. For different positions Δx of the addressing beam with respect to the targeted atom, we scan the frequency of the Rydberg excitation lasers. As mainly the ground state experiences a light shift ΔE proportional to the addressing beam intensity, the resonance frequency for Rydberg excitation is shifted by ΔE [see Fig. 1(b)]. Figure 1(c) shows the measured light shift as a function of Δx. A Gaussian fit gives a $1/e^2$ radius $w_0 = 1.3 \pm 0.1\mu$m. The residual light shift experienced by the nearby atom 3 μm away is below the resolution of our experiment.

We observe that for large light shifts, the probability of losing an atom during the sequence increases. We attribute this effect to the following: due to the finite temperature, the atom never sits exactly at the intensity maximum of the addressing beam. The fast switching on and off of the addressing beam thus imparts kinetic energy to the atom. This increase in kinetic energy becomes more and more important as the intensity of the addressing beam gets larger. For large enough intensities in the addressing beam, this effect thus increases the probability for the atom to leave the trapping region during the experiment. However, for light shifts below 40 MHz, this loss probability remains below 1%, and is thus negligible.

We now perform a Rydberg blockade experiment with two single atoms in order to demonstrate single-site addressability (Fig. 2). In Ref. [18], site-resolving excitation beams were used to demonstrate blockade with two atoms separated by 10 μm. Here, we use a global excitation scheme in combination with the addressing beam, and obtain similar results, albeit with a distance between the atoms of only 3 μm. For both atoms, the ground state $|g\rangle$ is coupled to the Rydberg state $|r\rangle = |59D_{3/2}\rangle$ with a Rabi frequency $\Omega \simeq 2\pi \times 1$ MHz [Fig. 2(a)]. If the atoms were independent, they would both undergo Rabi oscillations between $|g\rangle$ and $|r\rangle$ with the Rabi frequency Ω. The strong dipole-dipole interaction $U_{\rm dd}$ between the Rydberg states forbids a double excitation of the atoms if $U_{\rm dd} \gg \hbar\Omega$. This condition is largely fulfilled for the parameters chosen here: the interaction energy of two atoms in $|59D_{3/2}\rangle$, separated by 3 μm, is approximately $h \times 300$ MHz. We thus excite only the superposition state $|s\rangle = (|rg\rangle + e^{i\boldsymbol{k}\cdot\boldsymbol{r}}|gr\rangle)/\sqrt{2}$, whose coupling to the two-atom ground state $|gg\rangle$ is $\sqrt{2}\Omega$ [18,19] (here, $\boldsymbol{k}$ is the vector sum of the wave vectors of the excitation lasers, and $\boldsymbol{r}$ is the position of atom 2 with respect to atom 1). This results in P_{rg} and P_{gr} oscillating between 0 and 1/2 with a frequency $\sqrt{2}\Omega$, as can be seen in Fig. 2(b). Another signature of the blockade is the suppression of double excitation $P_{rr} \simeq 0$ [see bottom panel in Fig 2(b)].

If we shine the addressing beam on atom 2, we observe a strong suppression of the excitation probability for the states $|gr\rangle$ and $|rr\rangle$ [see Fig. 2(c)], as atom 2 is never excited to the Rydberg state $|r\rangle$. At the same time, atom 1 shows Rabi oscillations between $|g\rangle$ and $|r\rangle$ with the single-atom Rabi frequency Ω. The small residual excitation probability of atom 2 that we observe is fully accounted for by the errors in our state detection [15], meaning that cross-talk between the two traps is negligible.

Finally, we show that we can also use the addressing beam to directly manipulate a two-atom quantum state. Without any addressing, the excitation to the state $|rr\rangle$ is completely

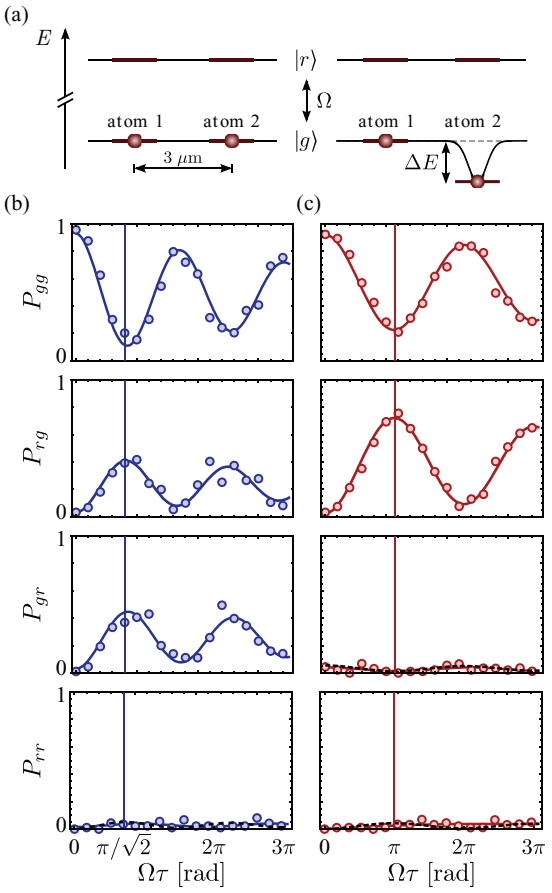

FIG. 2. (Color online) (a) Two atoms, separated by 3 μm, are illuminated by light that resonantly couples the ground state $|g\rangle$ to $|r\rangle = |59D_{3/2}\rangle$ with the single-atom Rabi frequency Ω. The time evolution of the populations of the two-atom states $|gg\rangle$, $|gr\rangle$, $|rg\rangle$, and $|rr\rangle$ are shown, (b) without any addressing and (c) with atom 2 addressed with a light shift of $\Delta E \simeq h\times 10$ MHz. Solid lines are fits by damped sine curves. The vertical solid lines mark the pulse areas $\Omega\tau$ corresponding to a π pulse for the nonaddressed case (blue) and the addressed case (red). The black dashed lines show the expected measured populations for a perfect blockade of atom 2, taking into account state-detection errors.

suppressed in the Rydberg blockade regime ($U_{\rm dd} \gg \hbar\Omega$). By applying an excitation pulse of duration $\pi/(\sqrt{2}\Omega)$ we thus prepare the atoms in the state $|\psi(0)\rangle = (|gr\rangle + e^{i\boldsymbol{k}\cdot\boldsymbol{r}}|rg\rangle)/\sqrt{2}$. We then illuminate atom 2 with the addressing beam [Fig. 3(a)]. Its energy is shifted by ΔE when in the ground state, while its Rydberg state remains unaffected [see Fig. 2(a)]. After a time T the state of the system has therefore evolved to

$$|\psi(T)\rangle = \frac{1}{\sqrt{2}}\left(|gr\rangle + e^{-i\Delta E\,T/\hbar}e^{i\boldsymbol{k}\cdot\boldsymbol{r}}|rg\rangle\right). \qquad (1)$$

The antisymmetric dark state $|\psi(T_\pi)\rangle = (|gr\rangle - e^{i\boldsymbol{k}\cdot\boldsymbol{r}}|rg\rangle)/\sqrt{2}$ (with $T_\pi = \pi\hbar/\Delta E$) is not coupled to the ground state

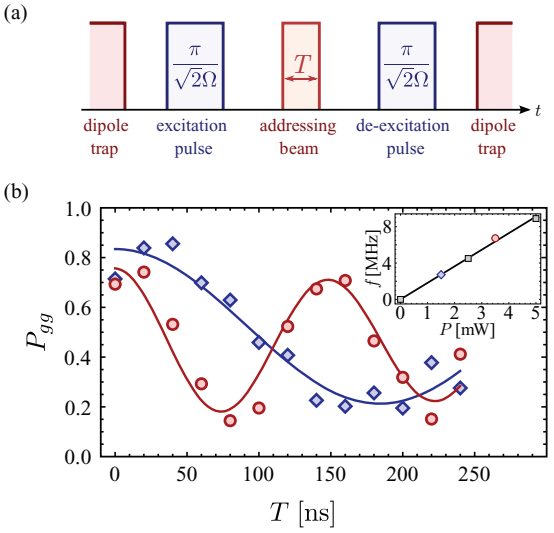

FIG. 3. (Color online) (a) Pulse sequence for the phase manipulation: while the dipole trap is switched off, the atoms are excited to the state $|s\rangle = (|gr\rangle + e^{i\boldsymbol{k}\cdot\boldsymbol{r}}|rg\rangle)/\sqrt{2}$. The addressing beam induces a light shift ΔE on the ground state of atom 2, thus changing the relative phase evolution between $|gr\rangle$ and $|rg\rangle$. This is followed by a global deexcitation pulse. (b) Population of the two-atom ground state $|gg\rangle$ after the deexcitation pulse, as a function of the addressing pulse length T, for a laser power in the addressing beam $P =$ 1.5 mW (blue diamonds) and $P = 3.5$ mW (red circles). Solid lines are fits by damped sine curves of frequency f. Inset: oscillation frequency f as a function of the power P of the addressing beam, showing the expected linear dependence. For this experiment we use the Rydberg state $|82D_{3/2}\rangle$.

$|gg\rangle$. The probability of deexciting the atoms to $|gg\rangle$ is thus expected to oscillate between 0 and 1 with a frequency $f = \Delta E/h$.

Figure 3(b) shows the probability P_{gg} of deexciting the atoms back to $|gg\rangle$ versus the duration T of the addressing pulse. We observe the expected oscillation of the final ground-state population P_{gg}. Due to the finite Rydberg excitation efficiency (about 90% for our parameters), we measure a contrast of the oscillations that is lower than 1. In addition, the finite temperature of the atoms in the experiment leads to a small motion of the atoms during the sequence, implying that (i) the phase $\boldsymbol{k}\cdot\boldsymbol{r}$ imprinted by the excitation pulse is not exactly canceled out by the deexcitation pulse [20]; and (ii) the light shift ΔE experienced by atom 2 fluctuates from shot to shot. Averaged over many runs, both effects lead to a decreased contrast and a finite damping of the observed oscillations. To take these effects into account, we fitted the data with a damped sine curve of the form $P_{gg}(T) = A + B\exp(-\gamma t)\cos(2\pi f T)$, with the oscillation frequency f and the damping rate γ as adjustable parameters. Repeating the experiment for different powers of the addressing beam, we obtain the expected linear dependence of f with the applied light shift on the atom [see inset of Fig. 3(b)]. This demonstrates our ability to perform some controlled local operations on qubits in a quantum register.

In conclusion, we have shown that we can selectively prevent one single atom in a pair of single-atom traps from being resonant with Rydberg excitation lasers, with no measurable cross-talk with a neighboring atom as close as 3 μm. We also demonstrated the use of the addressing beam to perform a local operation in a system of two atoms. Our scheme is easily scalable to a larger number of traps. These techniques will prove useful for a variety of applications in quantum simulation and quantum information processing with Rydberg atoms. For instance, they open the possibility of selectively addressing a single qubit in a larger ensemble, e.g., as a control atom for realizing collective quantum gates [16], or to excite a single atom to a different Rydberg state, allowing the study of the transfer of excitations along a Rydberg chain [21].

We thank Yvan Sortais for helpful advice about the optical design. We acknowledge financial support by the EU [ERC Stg Grant ARENA, AQUTE Integrating Project, FET-Open Xtrack Project HAIRS, and EU Marie-Curie Program ITN COHERENCE Grant No. FP7-PEOPLE-2010-ITN-265031 (H.L.)], by DGA (L.B.), and by Région Île-de-France (LUMAT and Triangle de la Physique, LAGON Project).

[1] I. Bloch, J. Dalibard, and S. Nascimbène, Nat. Phys. **8**, 267 (2012).
[2] M. Saffman, T. G. Walker, and K. Mølmer, Rev. Mod. Phys. **82**, 2313 (2010).
[3] F. Nogrette, H. Labuhn, S. Ravets, D. Barredo, L. Béguin, A. Vernier, T. Lahaye, and A. Browaeys, Phys. Rev. X **4**, 021034 (2014).
[4] H. C. Nägerl, D. Leibfried, H. Rohde, G. Thalhammer, J. Eschner, F. Schmidt-Kaler, and R. Blatt, Phys. Rev. A **60**, 145 (1999).
[5] H. Häffner, W. Hänsel, C. F. Roos, J. Benhelm, D. Chek-al-kar, M. Chwalla, T. Körber, U. D. Rapol, M. Riebe, P. O. Schmidt, C. Becher, O. Gühne, W. Dür, and R. Blatt, Nature **438**, 643 (2005).
[6] C. Monroe and J. Kim, Science **339**, 1164 (2013).
[7] R. Dumke, M. Volk, T. Müther, F. B. J. Buchkremer, G. Birkl, and W. Ertmer, Phys. Rev. Lett. **89**, 097903 (2002).
[8] M. Saffman, Opt. Lett. **29**, 1016 (2004).
[9] M. Karski, L. Förster, J.-M. Choi, A. Steffen, N. Belmechri, W. Alt, D. Meschede, and A. Widera, New J. Phys. **12**, 065027 (2010).
[10] C. Weitenberg, M. Endres, J. F. Sherson, M. Cheneau, P. Schauß, T. Fukuhara, I. Bloch, and S. Kuhr, Nature (London) **471**, 319 (2011).
[11] M. Schlosser, S. Tichelmann, J. Kruse, and G. Birkl, Quantum Inf. Process. **10**, 907 (2011).
[12] T. Fukuhara, A. Kantian, M. Endres, M. Cheneau, P. Schauß, S. Hild, D. Bellem, U. Schollwöck, T. Giamarchi, C. Gross, I. Bloch, and S. Kuhr, Nat. Phys. **9**, 235 (2013).
[13] J. H. Lee, E. Montano, I. H. Deutsch, and P. S. Jessen, Nat. Commun. **4**, 2027 (2013).
[14] L. Béguin, A. Vernier, R. Chicireanu, T. Lahaye, and A. Browaeys, Phys. Rev. Lett. **110**, 263201 (2013).
[15] D. Barredo, S. Ravets, H. Labuhn, L. Béguin, A. Vernier, F. Nogrette, T. Lahaye, and A. Browaeys, Phys. Rev. Lett. **112**, 183002 (2014).
[16] M. Müller, I. Lesanovsky, H. Weimer, H. P. Büchler, and P. Zoller, Phys. Rev. Lett. **102**, 170502 (2009).
[17] Y. R. P. Sortais, H. Marion, C. Tuchendler, A. M. Lance, M. Lamare, P. Fournet, C. Armellin, R. Mercier, G. Messin, A. Browaeys, and P. Grangier, Phys. Rev. A **75**, 013406 (2007).
[18] E. Urban, T. A. Johnson, T. Henage, L. Isenhower, D. D. Yavuz, T. G. Walker, and M. Saffman, Nat. Phys. **5**, 110 (2009).
[19] A. Gaëtan, Y. Miroshnychenko, T. Wilk, A. Chotia, M. Viteau, D. Comparat, P. Pillet, A. Browaeys, and P. Grangier, Nat. Phys. **5**, 115 (2009).
[20] T. Wilk, A. Gaëtan, C. Evellin, J. Wolters, Y. Miroshnychenko, P. Grangier, and A. Browaeys, Phys. Rev. Lett. **104**, 010502 (2010).
[21] S. Wüster, C. Ates, A. Eisfeld, and J. M. Rost, Phys. Rev. Lett. **105**, 053004 (2010).

LETTERS
PUBLISHED ONLINE: 26 OCTOBER 2014 | DOI: 10.1038/NPHYS3119
nature physics

Coherent dipole–dipole coupling between two single Rydberg atoms at an electrically-tuned Förster resonance

Sylvain Ravets, Henning Labuhn, Daniel Barredo, Lucas Béguin, Thierry Lahaye and Antoine Browaeys*

Resonant energy transfers, the non-radiative redistribution of an electronic excitation between two particles coupled by the dipole–dipole interaction, lie at the heart of a variety of phenomena[1], notably photosynthesis. In 1948, Förster established the theory of fluorescence resonant energy transfer (FRET) between broadband, nearly-resonant donors and acceptors[2]. The $1/R^6$ scaling of the energy transfer rate, where R is the distance between particles, enabled widespread use of FRET as a 'spectroscopic ruler' for determining nanometric distances in biomolecules[3]. The underlying mechanism is a coherent dipolar coupling between particles, as recognized in the early days of quantum mechanics[4], but this coherence has not been directly observed so far. Here we study, spectroscopically and in the time domain, the coherent, dipolar-induced exchange of excitations between two Rydberg atoms separated by up to 15 μm, and brought into resonance by applying an electric field. Coherent oscillation of the system between two degenerate pair states then occurs at a frequency scaling as $1/R^3$, the hallmark of resonant dipole–dipole interactions[5]. Our results not only demonstrate, at the fundamental level of two atoms, the basic mechanism underlying FRET, but also open exciting prospects for active tuning of strong, coherent interactions in quantum many-body systems.

The possibility to tune at will coherent interactions in many-body systems by changing external parameters is one of the key tools enabling quantum simulation. For instance, in ultracold quantum gases, such tuning can be achieved by magnetically-induced Feshbach resonances[6,7]. Rydberg atoms are another promising platform for the quantum simulation of complex many-body problems, owing to the strong interactions associated with their large principal quantum numbers[8]. They have proved to be an efficient tool for characterizing non-radiative exchange of energy in resonant collisional processes[9], studying collective effects[10] and engineering quantum states of matter[11]. The observation of Rydberg blockade between individual atoms[12,13], where the strong interaction between Rydberg states inhibits multiple excitations within a blockade sphere, opens the way towards the development of Rydberg quantum simulators[14]. An appealing tool for those applications is the possibility to tune the strength of the interactions by external electric fields using Förster resonances[15–23]. So far, owing to inhomogeneities in the atomic ensembles used in experiments, only indirect evidence for the coherent character of the interaction has been obtained[24,25].

Here, we study a system of two single atoms at a Förster resonance. We first perform a spectroscopic measurement of the energies of the two-atom states as a function of the applied electric field, and observe directly the avoided crossing between pair states induced by the dipole–dipole interaction. The splitting at resonance is observed to scale as $1/R^3$ as a function of the distance R between the atoms. In a second experiment, we prepare the system in a given pair state away from resonance, and switch to resonance for a controlled time, revealing the coherent oscillation between the two degenerate pair states induced by the dipolar interaction. These results open the way to real-time tuning of interactions for quantum simulation with Rydberg atoms[11,14].

Two atoms located at positions $\mathbf{R}_1$ and $\mathbf{R}_2$ interact through the dipole–dipole interaction

$$\hat{V}_{\mathrm{dip}} = \frac{1}{4\pi\varepsilon_0}\left(\frac{\hat{\boldsymbol{\mu}}_1\cdot\hat{\boldsymbol{\mu}}_2 - 3(\hat{\boldsymbol{\mu}}_1\cdot\mathbf{n})(\hat{\boldsymbol{\mu}}_2\cdot\mathbf{n})}{R^3}\right)$$

where $\hat{\boldsymbol{\mu}}_i$ is the electric dipole moment of atom i ($i = 1, 2$), $\mathbf{R} = \mathbf{R}_2 - \mathbf{R}_1$ and $\mathbf{n} = \mathbf{R}/R$. When the two atoms are prepared in the same state, $\hat{V}_{\mathrm{dip}}$ usually has no effect to first order, as the average value of the dipole moment vanishes in an atomic eigenstate. Second-order perturbation theory gives rise to an energy shift of the atom pair, which results in the van der Waals interaction[26] $U_{\mathrm{vdW}} \propto R^{-6}$. However, resonance effects between two Rydberg atoms can occur when two pair states are degenerate[5], and in this case the dipolar interaction manifests itself at first order. Such a resonance, called a 'Förster resonance' in analogy with the FRET mechanism at work in photochemistry, can be achieved using small electric fields to Stark-tune the energy of the pair states.

In this work, we use the states $|p\rangle = |61P_{1/2}, m_J = 1/2\rangle$, $|d\rangle = |59D_{3/2}, m_J = 3/2\rangle$ and $|f\rangle = |57F_{5/2}, m_J = 5/2\rangle$ of ^{87}Rb. The pair states $|dd\rangle$, $|pf\rangle$ and $|fp\rangle$ are almost degenerate (Fig. 1a): their Förster defect $\Delta_0 = (E_{pf} - E_{dd})/h$, in the absence of an electric field, is only 8.5 MHz (h is Planck's constant). Using the differential Stark effect between $|dd\rangle$ and $|pf\rangle$, they can be brought to exact resonance by applying an electric field $F_{\mathrm{res}} \simeq 32\,\mathrm{mV\,cm^{-1}}$ (Fig. 1b). The small electric fields at play ensure that we work in a regime of induced dipoles (even for the highly polarizable f state), as opposed to the rigid dipoles obtained for larger electric fields. At resonance, the eigenstates of the interacting system are $|\pm\rangle = (|dd\rangle \pm |\widetilde{pf}\rangle)/\sqrt{2}$, where $|\widetilde{pf}\rangle = (|pf\rangle + |fp\rangle)/\sqrt{2}$. If the system is initially prepared in $|dd\rangle$, it thus oscillates between the two degenerate electronic

Laboratoire Charles Fabry, UMR 8501, Institut d'Optique, CNRS, Univ Paris Sud 11, 2 avenue Augustin Fresnel, 91127 Palaiseau Cedex, France.
*e-mail: antoine.browaeys@institutoptique.fr

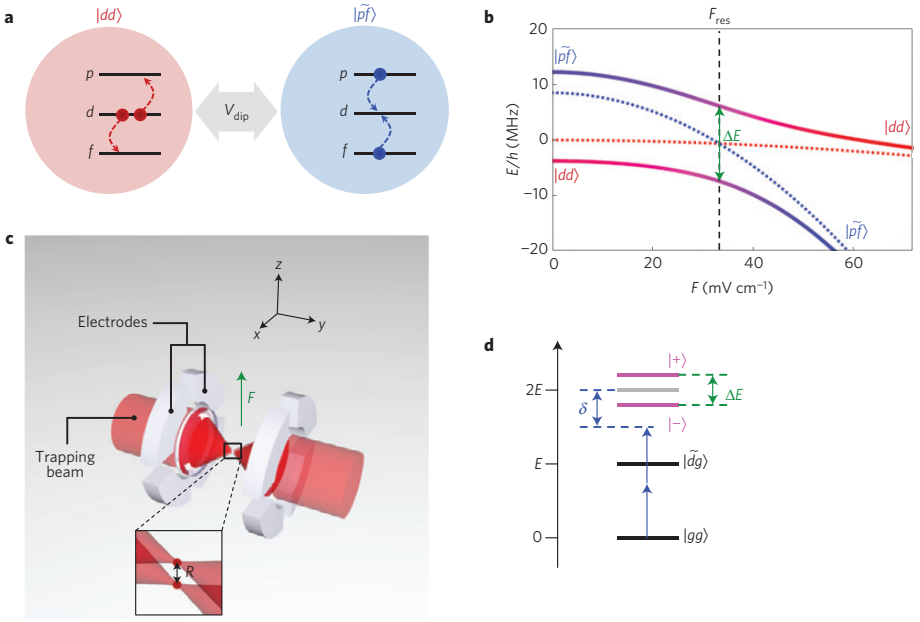

Figure 1 | Principle of the experiment. a, The pair states $|dd\rangle$ and $|\widetilde{pf}\rangle$ are coupled by the dipolar interaction at a Förster resonance. **b**, Stark effect of the pair states. In the absence of coupling, the two pair-state energy levels (dotted lines) vary when an external electric field F is applied, and cross each other for $F = F_{res}$. The coupled system (solid lines) undergoes an avoided crossing at resonance (vertical dashed line). **c**, Experimental set-up. Two individual ^{87}Rb atoms are trapped in microscopic optical tweezers separated by a distance R. Eight independent electrodes allow the application of a tunable electric field F along the internuclear axis z. **d**, Structure of the coupled levels at resonance. We scan the excitation laser (blue arrow) to perform a two-atom excitation from $|gg\rangle$ to $|dd\rangle$ via the intermediate, one-excitation state $|\widetilde{dg}\rangle = (|dg\rangle + |gd\rangle)/\sqrt{2}$. The detuning between the laser frequency and the position of $|dd\rangle$ in the absence of interactions (grey horizontal line) is denoted by δ.

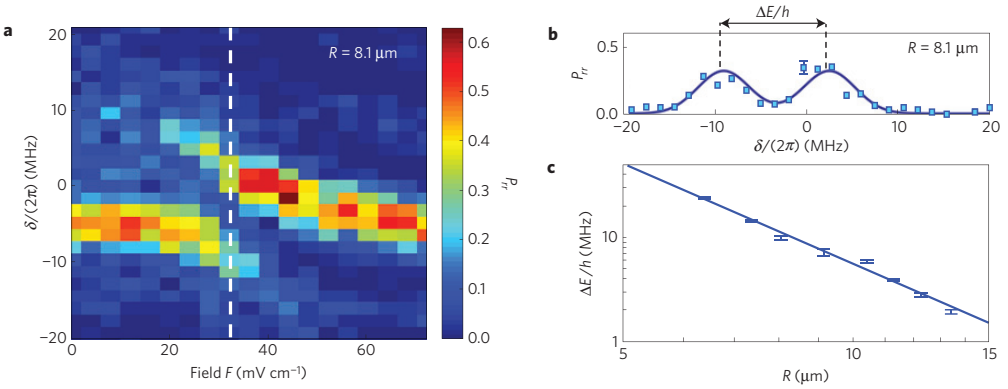

Figure 2 | Spectroscopy at the Förster resonance. a, Two-atom excitation spectrum where the population of doubly-Rydberg-excited states, P_{rr}, is plotted as a function of δ and F, showing the avoided crossing between the resonant pair states. The white dashed line indicates the position of the Förster resonance. **b**, Spectrum $P_{rr}(\delta)$ at resonance for $R = 8.1\,\mu$m. A representative error bar (one standard error in the measurement of P_{rr}) is shown. A double Gaussian (solid line) is fit to the data. **c**, Double-logarithmic plot of the splitting ΔE between the peaks, at resonance, as a function of R. Error bars are one standard deviation in the determination of ΔE in the fit by a double Gaussian. The solid line shows a fit by a power law, giving an exponent -3.2 ± 0.2.

configurations with a frequency given by the dipolar coupling $2\sqrt{2}C_3/R^3$ (where $C_3\sqrt{2}/R^3 = \langle dd|\hat{V}_{dip}|\widetilde{pf}\rangle$). In particular, after half a period of interaction, the system has evolved to the entangled state $|\widetilde{pf}\rangle$.

Our experimental set-up has been described previously[26,27]. We trap two single laser-cooled atoms in optical tweezers separated by a controlled distance R of a few micrometres (Fig. 1c). A set of eight independent electrodes allows us to apply a controlled electric field F aligned with the internuclear axis[28]. A 3 G magnetic field, also aligned along z, is used to split the Zeeman sublevels. We optically pump the atoms in the ground state $|g\rangle = |5S_{1/2}, F = 2, m_F = 2\rangle$ (with an efficiency >90%), which we couple, with an effective Rabi frequency Ω, to the Rydberg state $|d\rangle$ using a two-photon transition (using two lasers of wavelengths 795 nm and 474 nm, with π and σ^+

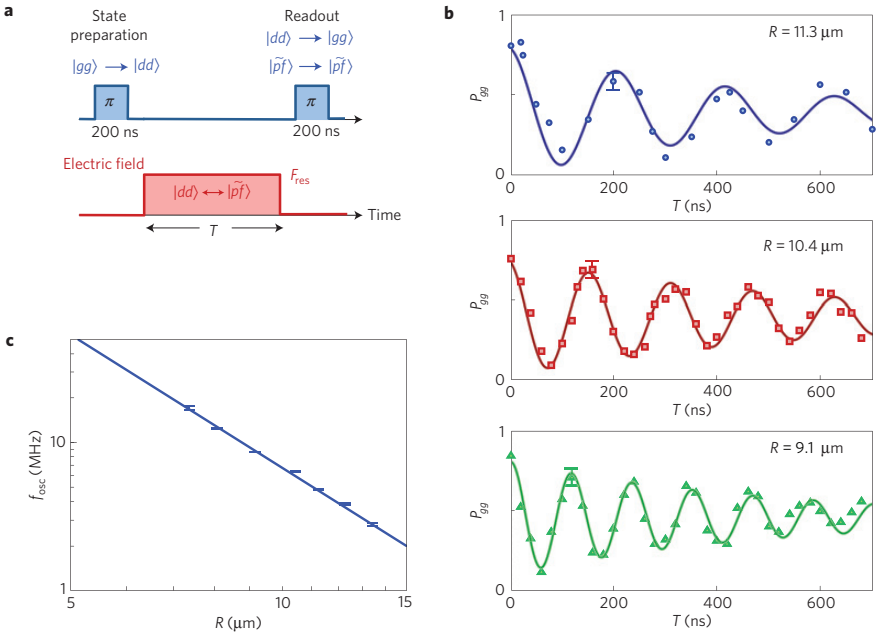

Figure 3 | Observation of the oscillation between the two pair states. a, Experimental sequence. After exciting the atoms to $|dd\rangle$ (first π-pulse, of duration 200 ns), we switch on the resonant interaction for a variable amount of time T by tuning the electric field to F_{res}. The system oscillates back and forth between the two pair states $|dd\rangle$ and $|\widetilde{pf}\rangle$ for the duration T. A deexcitation pulse (second π-pulse) couples back the $|dd\rangle$ part of the resulting state to $|gg\rangle$. **b**, Evolution of P_{gg} as a function of the interaction time for several values of R. P_{gg} oscillates at a frequency f_{osc} which depends on R. A representative error bar (one standard error in the measurement of P_{gg}) is shown. The solid lines are fits by a damped sine wave with frequency f_{osc}. **c**, Double-logarithmic plot of the oscillation frequency f_{osc} as a function of R. Error bars correspond to one standard deviation in the determination of f_{osc}. The solid line shows a fit by a power law, giving an exponent -3.0 ± 0.1.

polarizations, respectively). The readout of the states of the atoms is performed by shining resonant light at 780 nm on the atoms, giving a fluorescence signal only if the atom is in $|g\rangle$ (an atom in a Rydberg state, be it $|p\rangle$, $|d\rangle$, or $|f\rangle$, is lost from the trap during the sequence). Repeating the same sequence ~100 times allows us to reconstruct the four populations P_{gg}, P_{gr}, P_{rg} and P_{rr} (where r stands for any of the Rydberg states p, d and f, which we cannot discriminate directly with our loss-based detection scheme), with a typical uncertainty in the measurement of P_{ij} on the order of ± 0.05 (see representative error bars in Figs 2b and 3b).

We first fix $R = 8.1$ μm and perform a spectroscopic measurement to find the electric field F_{res} corresponding to the Förster resonance. Our laser system couples $|gg\rangle$ to $|dd\rangle$ (but not to $|pf\rangle$ or $|fp\rangle$), via the states $|dg\rangle$ and $|gd\rangle$. Thus $|gg\rangle$ is partially coupled to the states $|+\rangle$ and $|-\rangle$ at resonance. For increasing values of F, we scan the laser detuning δ (defined with respect to the transition $|gg\rangle$ to $|dd\rangle$, see Fig. 1d) and measure the probability P_{rr} for both atoms to be in a Rydberg state (Fig. 2a). For $F = 0$, we observe a single line centred at $\delta/(2\pi) \approx -5$ MHz, corresponding to the attractive van der Waals interaction between the two atoms out of resonance. For $F \approx 20$ mV cm^{-1}, a repulsive branch appears in the spectrum, a signature of the interaction between $|dd\rangle$ and $|\widetilde{pf}\rangle$. Increasing the field even further allows scanning across the avoided crossing until only one peak is visible again. We reach the Förster resonance (smallest splitting between the two peaks) at $F_{res} = 32 \pm 4$ mV cm^{-1}, where we observe two symmetric peaks corresponding to $|\pm\rangle$. The spectra also show further small structures in addition to the two main peaks. However, to extract the interaction energy in a simple way, we fit the spectra by two Gaussians with a splitting ΔE between the two peaks (Fig. 2b).

We then measure the evolution of the spectra at resonance when varying the distance R. When R increases, the splitting between the peaks decreases. Figure 2c is a double-logarithmic plot of ΔE versus R. The data show a power-law behaviour of exponent -3.2 ± 0.2, consistent with the expected C_3/R^3 law. We measure $C_3 = 2.1 \pm 0.1$ GHz μm^3, where the error is statistical. Systematic effects are an overall ~5% uncertainty in our calibration of R, a small bias in the determination of ΔE due to the choice of double Gaussian functions to fit the data and possible residual light-shifts in the two-photon spectroscopy. (To estimate the bias introduced by our choice of fit function, we fitted simulated spectra, obtained by solving the optical Bloch equations, by double Gaussians. The extracted splitting underestimates by ≃10% the actual splitting ΔE.) Theoretical calculations[29] give $C_{3,th} \simeq 2.54$ GHz μm^3.

We now study the coherence properties of the system at resonance using a sequence (Fig. 3a) reminiscent of pump–probe spectroscopy. We prepare the system in the state $|dd\rangle$ using a π-pulse of 200 ns, which transfers each atom from $|g\rangle$ to $|d\rangle$. To start in a pure $|dd\rangle$ state, we perform the excitation in the van der Waals regime above resonance ($F \approx 64$ mV cm^{-1}), where the Förster defect is $\Delta(F) \geq h \times 100$ MHz and where interactions are weak. We then turn on the resonant interaction for a variable duration T, by rapidly switching (risetime below 10 ns) the field to F_{res}. During this time, the two-atom system oscillates between $|dd\rangle$ and the entangled state $|\widetilde{pf}\rangle$, with a frequency $f_{osc} = \Delta E/h = 2\sqrt{2}C_3/(hR^3)$ given by the dipolar coupling. We then apply a deexcitation π-pulse identical to the first one to read out the state of the system. The deexcitation pulse couples the $|dd\rangle$ component of the system back to $|gg\rangle$. At the end of the sequence we measure the probability P_{gg} to be back in $|gg\rangle$, thus indirectly measuring the population left in $|dd\rangle$ after the pulse

of electric field. We observe highly contrasted oscillations between $|dd\rangle$ and $|\widetilde{pf}\rangle$, with a frequency depending on R (Fig. 3b).

The oscillations between two states are a direct proof of the coherent nature of the coupling underlying Förster energy transfer, and also allow a more accurate determination of the interaction energy than the spectroscopic method described above. We fit the oscillation by a damped sine wave to extract the oscillation frequency $f_{\rm osc}$. Figure 3c shows a double-logarithmic plot of the values of $f_{\rm osc}$ as a function of R. The data shows a power-law behaviour of exponent -3.0 ± 0.1, again in excellent agreement with the expected R^{-3} behaviour. The measured $C_3 = 2.39 \pm 0.03\,\mathrm{GHz\,\mu m^3}$ is also close to the theoretical value.

The observed damping of the oscillations comes mainly from dephasing, arising from two effects. First, shot-to-shot fluctuations in the distance R (on the order of $\delta R \simeq 170\,\mathrm{nm}$), due to the finite temperature of the atoms in the tweezers, give rise to dephasing, as the oscillation frequency $f_{\rm osc} \propto 1/R^3$ is slightly different for each realization. This effect dominates at short distances: for instance, for $R \simeq 9\,\mu\mathrm{m}$, the corresponding spread $\delta f_{\rm osc}/f_{\rm osc} = 3\delta R/R$ in relative frequencies reaches ∼6%, which is enough to reduce the contrast of the oscillations by more than a factor of two after only four oscillation periods. Second, the voltages applied to the electrodes also fluctuate from shot to shot by a few mV, inducing fluctuations in F and thus in the detuning $\Delta(F)$ from resonance (by a fraction of a MHz for our parameters). This has negligible impact for small R, but appreciably contributes to the damping for large R, where the dipolar interaction is weaker. In principle, both sources of damping can be strongly decreased by technical improvements in the set-up, using colder atoms as demonstrated recently[30,31] and more stable voltage sources.

Our results open exciting prospects for real-time tuning of interactions in systems of Rydberg atoms, in particular to switch on and off Ryberg blockade on nanosecond timescales. As an illustration, in the above experiment, when switching F from $64\,\mathrm{mV\,cm^{-1}}$ (away from resonance) to $32\,\mathrm{mV\,cm^{-1}}$ (right on resonance), the blockade shift between two atoms separated by $R = 10\,\mu\mathrm{m}$ varies from $U = U_{\rm vdW} \sim h \times 0.2\,\mathrm{MHz}$ (van der Waals regime) up to $U = \Delta E/2 \sim h \times 4\,\mathrm{MHz}$ (C_3/R^3 regime). If the pair of atoms initially in $|gg\rangle$ were driven with a Rabi frequency $\Omega/(2\pi) \sim 1\,\mathrm{MHz}$, one would observe a strong blockade in the second case, whereas blockade would be almost totally suppressed in the first situation. This means that, simply by changing the value of the electric field by a few $\mathrm{mV\,cm^{-1}}$, we obtain a twenty-fold enhancement of the interaction, and the blockade radius is increased by a factor ∼2 in real time, a feature hard to achieve by other means.

A natural extension of this work will consist in measuring the angular dependence of resonant interactions[29], in view of tailoring even further the interactions between two particles. Extending our results beyond two particles, to few-body[32] and many-body systems[15,16,23], will enable the study of transport of excitations and generation of entanglement in fully controlled many-body systems.

Received 30 May 2014; accepted 8 September 2014; published online 26 October 2014

References

1. Andrews, D. L. & Demidov, A. A. *Resonance Energy Transfer* (Wiley, 1999).
2. Förster, T. Zwischenmolekulare Energiewanderung und Fluoreszenz. *Ann. Phys.* **437,** 55–75 (1948).
3. Stryer, L. & Haugland, R. P. Energy transfer: A spectroscopic ruler. *Proc. Natl Acad. Sci. USA* **58,** 719–726 (1967).
4. Clegg, R. M. *Reviews in Fluorescence 2006* 1–45 (Springer, 2006).
5. Walker, T. G. & Saffman, M. Zeros of Rydberg–Rydberg Föster interactions. *J. Phys. B* **38,** S309–S319 (2005).
6. Inouye, S. *et al.* Observation of Feshbach resonances in a Bose–Einstein condensate. *Nature* **392,** 151–154 (1998).
7. Chin, C., Grimm, R., Julienne, P. & Tiesinga, E. Feshbach resonances in ultracold gases. *Rev. Mod. Phys.* **82,** 1225–1286 (2010).
8. Gallagher, T. F. *Rydberg Atoms* (Cambridge Univ. Press, 2005).
9. Safinya, K. A., Delpech, J. F., Gounand, F., Sandner, W. & Gallagher, T. F. Resonant Rydberg-atom–Rydberg-atom collisions. *Phys. Rev. Lett.* **47,** 405–408 (1981).
10. Comparat, D. & Pillet, P. Dipole blockade in a cold Rydberg atomic sample. *J. Opt. Soc. Am. B* **27,** A208–A232 (2010).
11. Saffman, M., Walker, T. G. & Mølmer, K. Quantum information with Rydberg atoms. *Rev. Mod. Phys.* **82,** 2313–2363 (2010).
12. Urban, E. *et al.* Observation of Rydberg blockade between two atoms. *Nature Phys.* **5,** 110–114 (2009).
13. Gaëtan, A. *et al.* Observation of collective excitation of two individual atoms in the Rydberg blockade regime. *Nature Phys.* **5,** 115–118 (2009).
14. Weimer, H., Müller, M., Lesanovsky, I., Zoller, P. & Büchler, H. P. A Rydberg quantum simulator. *Nature Phys.* **6,** 382–388 (2010).
15. Anderson, W. R., Veale, J. R. & Gallagher, T. F. Resonant dipole–dipole energy transfer in a nearly frozen Rydberg gas. *Phys. Rev. Lett.* **80,** 249–252 (1998).
16. Mourachko, I. *et al.* Many-body effects in a frozen Rydberg gas. *Phys. Rev. Lett.* **80,** 253–256 (1998).
17. Anderson, W. R., Robinson, M. P., Martin, J. D. D. & Gallagher, T. F. Dephasing of resonant energy transfer in a cold Rydberg gas. *Phys. Rev. A* **65,** 063404 (2002).
18. Mudrich, M., Zahzam, N., Vogt, T., Comparat, D. & Pillet, P. Back and forth transfer and coherent coupling in a cold Rydberg dipole gas. *Phys. Rev. Lett.* **95,** 233002 (2005).
19. Vogt, T. *et al.* Electric-field induced dipole blockade with Rydberg atoms. *Phys. Rev. Lett.* **99,** 073002 (2007).
20. Reinhard, A., Younge, K. C. & Raithel, G. Effect of Förster resonances on the excitation statistics of many-body Rydberg systems. *Phys. Rev. A* **78,** 060702(R) (2008).
21. Van Ditzhuijzen, C. S. E. *et al.* Spatially resolved observation of dipole–dipole interaction between Rydberg atoms. *Phys. Rev. Lett.* **100,** 243201 (2008).
22. Ryabtsev, I. I., Tretyakov, D. B., Beterov, I. I. & Entin, V. M. Observation of the Stark-tuned Förster resonance between two Rydberg atoms. *Phys. Rev. Lett.* **104,** 073003 (2010).
23. Günter, G. *et al.* Observing the dynamics of dipole-mediated energy transport by interaction-enhanced imaging. *Science* **342,** 954–956 (2013).
24. Nipper, J. *et al.* Highly resolved measurements of Stark-tuned Förster resonances between Rydberg atoms. *Phys. Rev. Lett.* **108,** 113001 (2012).
25. Nipper, J. *et al.* Atomic pair-state interferometer: Controlling and measuring an interaction-induced phase shift in Rydberg-atom pairs. *Phys. Rev. X* **2,** 031011 (2012).
26. Béguin, L., Vernier, A., Chicireanu, R., Lahaye, T. & Browaeys, A. Direct measurement of the van der Waals interaction between two Rydberg atoms. *Phys. Rev. Lett.* **110,** 263201 (2013).
27. Nogrette, F. *et al.* Single-atom trapping in holographic 2D arrays of microtraps with arbitrary geometries. *Phys. Rev. X* **4,** 021034 (2014).
28. Löw, R. *et al.* An experimental and theoretical guide to strongly interacting Rydberg gases. *J. Phys. B* **45,** 113001 (2012).
29. Reinhard, A., Cubel Liebisch, T., Knuffman, B. & Raithel, G. Level shifts of rubidium Rydberg states due to binary interactions. *Phys. Rev. A* **75,** 032712 (2007).
30. Kaufman, A. M., Lester, B. J. & Regal, C. A. Cooling a single atom in an optical tweezer to its quantum ground state. *Phys. Rev. X* **2,** 041014 (2012).
31. Thompson, J. D., Tiecke, T. G., Zibrov, A. S., Vuletić, V. & Lukin, M. D. Coherence and Raman sideband cooling of a single atom in an optical tweezer. *Phys. Rev. Lett.* **110,** 133001 (2013).
32. Gurian, J. H. *et al.* Observation of a resonant four-body interaction in cold cesium Rydberg atoms. *Phys. Rev. Lett.* **108,** 023005 (2012).

Acknowledgements

We thank C. S. Adams for enlightening discussions, F. Nogrette for technical assistance and M. Besbes for finite-element calculations of the electric field configuration. This work was supported financially by the EU (ERC Stg Grant ARENA, FET-Open Xtrack project HAIRS, EU Marie-Curie program ITN COHERENCE FP7-PEOPLE-2010-ITN-265031 (H.L.)), by the DGA (L.B.), and by Région Île-de-France (LUMAT and Triangle de la Physique, LAGON project).

Author contributions

All authors contributed extensively to the work presented in this paper.

Additional information

Reprints and permissions information is available online at www.nature.com/reprints. Correspondence and requests for materials should be addressed to A.B.

Competing financial interests

The authors declare no competing financial interests.

Coherent Excitation Transfer in a Spin Chain of Three Rydberg Atoms

Daniel Barredo, Henning Labuhn, Sylvain Ravets, Thierry Lahaye, and Antoine Browaeys
Laboratoire Charles Fabry, UMR 8501, Institut d'Optique, CNRS, Université Paris Sud 11, 2 avenue Augustin Fresnel, 91127 Palaiseau cedex, France

Charles S. Adams
Joint Quantum Centre (JQC) Durham-Newcastle, Department of Physics, Durham University, Durham DH1 3LE, United Kingdom

(Received 23 September 2014; revised manuscript received 21 November 2014; published 19 March 2015)

We study coherent excitation hopping in a spin chain realized using highly excited individually addressable Rydberg atoms. The dynamics are fully described in terms of an XY spin Hamiltonian with a long range resonant dipole-dipole coupling that scales as the inverse third power of the lattice spacing, C_3/R^3. The experimental data demonstrate the importance of next neighbor interactions which are manifest as revivals in the excitation dynamics. The results suggest that arrays of Rydberg atoms are ideally suited to large scale, high-fidelity quantum simulation of spin dynamics.

DOI: 10.1103/PhysRevLett.114.113002 PACS numbers: 32.80.Ee, 03.67.Bg, 05.50.+q

Spin Hamiltonians, introduced in the early days of quantum mechanics to explain ferromagnetism, are widely used to study quantum magnetism [1]. Assemblies of interacting, localized spins are a paradigm of quantum many-body systems, where the interplay between interactions and geometry-induced frustration creates a wealth of intriguing quantum phases. Many other phenomena, such as coherent energy transfer, photochemistry, or photosynthesis [2], can also be described using spin Hamiltonians. However, despite this fundamental significance, exact analytical solutions are known only for the simplest cases, and numerical simulations of strongly correlated spin systems are notoriously difficult.

For those reasons, quantum simulation of spin Hamiltonians by controllable systems raises great interest. Recently, various approaches were followed to simulate spin systems using tools of atomic physics [3], such as cold atoms [4–6] or polar molecules [7] in optical lattices, interacting via weak exchange or dipole-dipole interactions, or trapped ions with engineered effective interactions [8–10]. As compared to their condensed-matter counterparts, the spin couplings can be long range, which gives rise to new properties [11–14].

Rydberg atoms are a promising alternative platform for quantum simulation [15,16]. In particular, they allow implementing various spin-1/2 Hamiltonians on two-dimensional lattices with strong couplings, in the MHz range [17,18]. Rydberg systems interacting through van der Waals interactions can be described by Ising-type Hamiltonians $H = \sum_{ij} V_{ij} \sigma_i^z \sigma_j^z$ where σ^z is the z-Pauli matrix acting in the (pseudo-) spin Hilbert space, and $V_{ij} \sim |\boldsymbol{r}_i - \boldsymbol{r}_j|^{-6}$, where $\boldsymbol{r}_i$ denotes the position of atom i [17–21]. On the other hand, spin-exchange, or XY, spin Hamiltonians of the form $H = \sum_{ij} V_{ij} (\sigma_i^+ \sigma_j^- + \sigma_i^- \sigma_j^+)$, where $\sigma^\pm = \sigma^x \pm i\sigma^y$ are spin-flip operators and $V_{ij} \sim |\boldsymbol{r}_i - \boldsymbol{r}_j|^{-3}$, can be realized by using two different Rydberg states, interacting directly via the resonant dipole-dipole interaction. However, in this case, only incoherent transfer of excitations has been observed so far, due to the random atomic positions in the ensembles used in experiments [22–27].

In this Letter, we study the coherent dynamics of a spin excitation in a chain of three Rydberg atoms. The dipole-dipole interaction between atoms is given by the XY Hamiltonian [28]

$$H = \frac{1}{2} \sum_{i \neq j} \frac{C_3}{R_{ij}^3} (\sigma_i^+ \sigma_j^- + \sigma_i^- \sigma_j^+), \tag{1}$$

where $R_{ij} = |\boldsymbol{r}_i - \boldsymbol{r}_j|$ is the distance between atoms i and j. We calibrate the spin-spin coupling between two Rydberg atoms by investigating the temporal evolution of two Rydberg atoms prepared in the state $|\uparrow\downarrow\rangle$, as a function of distance R between the atoms, up to $R \simeq 50\ \mu$m. We then use three Rydberg atoms prepared in $|\uparrow\downarrow\downarrow\rangle$ and study the propagation of the excitation through this minimalistic spin chain, observing the effect of long-range hopping of the excitation. The agreement between experimental data and the XY model without adjustable parameters validates our setup as a future quantum simulator for systems of many spins in arbitrary two-dimensional arrays.

The experimental setup, shown in Fig. 1(a), is detailed in Ref. [30]. Briefly, we focus a red-detuned trapping beam

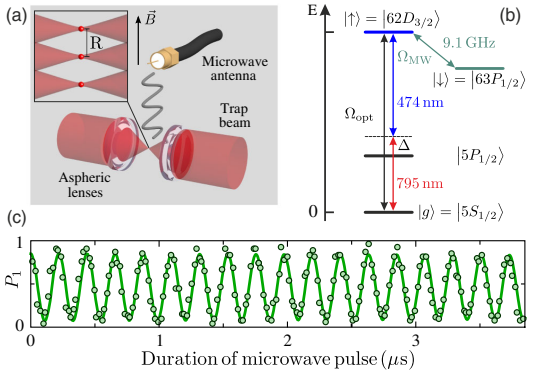

FIG. 1 (color online). (a) Individual ^{87}Rb atoms in microtraps aligned along the quantization axis, defined by a $B = 6$ G magnetic field. (b) Excitation lasers couple the ground state $|g\rangle = |5S_{1/2}, F = 2, m_F = 2\rangle$ and the Rydberg state $|\uparrow\rangle = |62D_{3/2}, m_J = 3/2\rangle$ with an effective Rabi frequency Ω_{opt}. Microwaves couple $|\uparrow\rangle$ to $|\downarrow\rangle = |63P_{1/2}, m_J = 1/2\rangle$, with Rabi frequency Ω_{MW}. (c) Microwave-driven Rabi oscillation of a single atom between $|\uparrow\rangle$ and $|\downarrow\rangle$, yielding $\Omega_{MW} = 2\pi \times 4.6$ MHz.

with an aspheric lens into a magneto-optical trap of ^{87}Rb, to a waist $\simeq 1$ μm. Multiple traps at arbitrary distances are created by imprinting an appropriate phase on the trapping beam with a spatial light modulator [31]. Because of fast light-assisted collisions in the small trapping volume, at most one atom is present in each trap. The temperature of the trapped atoms is approximately 50 μK. A 6 G magnetic field defines the quantization axis [32].

We encode the two spin states in the Rydberg states $|\uparrow\rangle = |62D_{3/2}, m_j = 3/2\rangle$ and $|\downarrow\rangle = |63P_{1/2}, m_j = 1/2\rangle$ [see Fig. 1(b)]. We trigger an experiment when an atom is detected in each trap. To prepare the atoms in a desired spin state, we first optically pump them in $|g\rangle = |5S_{1/2}, F = 2, m_F = 2\rangle$. We then switch off the traps to avoid inhomogeneous light shifts, and excite the atoms to $|\uparrow\rangle = |62D_{3/2}, m_J = 3/2\rangle$ via a two-photon transition (wavelengths 795 and 474 nm, with polarizations π and σ^+, respectively), detuned from the intermediate state $|5P_{1/2}, F = 2, m_F = 2\rangle$ by $\Delta \simeq 2\pi \times 740$ MHz. From the $|\uparrow\rangle$ state the atom can be transferred to $|\downarrow\rangle = |63P_{1/2}, m_j = 1/2\rangle$ using resonant microwaves at $\simeq$9.131 GHz, emitted by an antenna outside the vacuum chamber.

To read out the state of an atom at the end of a sequence, we switch on the excitation lasers, coupling only $|\uparrow\rangle$ back to the ground state. We then turn on the dipole traps to recapture ground-state atoms, while atoms in Rydberg states remain untrapped, and detect atoms in $|g\rangle$ by fluorescence. Therefore if we detect an atom in its trap at the end of a sequence, we assume it was in $|\uparrow\rangle$, while a loss corresponds to the $|\downarrow\rangle$ state. We reconstruct all the 2^N probabilities $P_{i_1 \ldots i_k \ldots i_N}$ of having i_k atom in trap k, with $i_k = 0$ or 1, for our N-trap system (with $N = 1, 2$, or 3) by repeating the experiment typically 100 times. For instance for $N = 3$, P_{100} is the probability to recapture an atom in trap 1, while recapturing none in traps 2 and 3. The statistical error on the determination of the probabilities is below 5%. Figure 1(c) illustrates the coherent spin manipulation for a single atom, by showing Rabi oscillations between $|\uparrow\rangle$ and $|\downarrow\rangle$: the probability P_1 to recapture the atom oscillates with a frequency $\Omega_{MW} \simeq 2\pi \times 4.6$ MHz. In 4 μs, we induce more than 35 spin flips without observing noticeable damping.

We first use two atoms, aligned along the quantization axis, to directly measure the coupling between two spins as a function of their distance. The sequence is shown in Fig. 2(a). We illuminate atom 1 with an addressing beam [33] which induces a 20 MHz light shift, making it off resonant to the global Rydberg excitation. Atom 2 is excited to $|\uparrow\rangle$, and then transferred to $|\downarrow\rangle$ using microwaves. Subsequently, atom 1 is optically excited to the $|\uparrow\rangle$ state with the addressing beam switched off (atom 2 in $|\downarrow\rangle$ is not affected by the Rydberg excitation pulse). We let the system evolve for an adjustable time τ and read out the

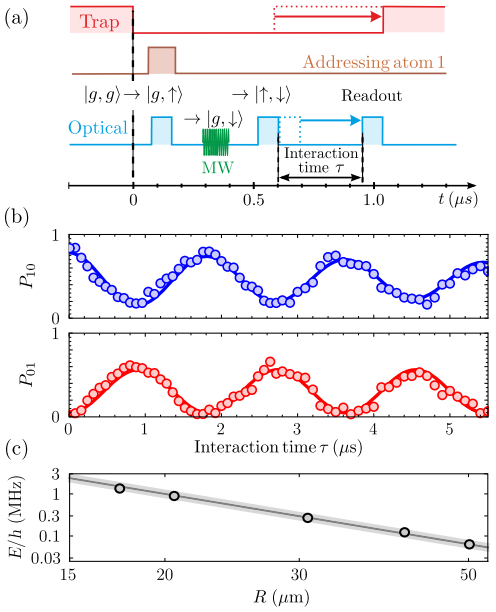

FIG. 2 (color online). (a) Sequence to observe spin exchange between two atoms. (b) Excitation hopping between states $|\uparrow\downarrow\rangle$ (blue disks) and $|\downarrow\uparrow\rangle$ (red disks) of two atoms separated by $R = 30$ μm. Solid lines are sinusoidal fits, with frequency $2E/h$. (c) Interaction energy E (circles) versus R. Error bars are smaller than the symbols size. The line shows the theoretical prediction C_3/R^3 with $C_3^{th} = 7965$ MHz μm^3. The shaded area corresponds to our systematic 5% uncertainty in the calibration of R.

final state by deexciting $|\uparrow\rangle$ back to $|g\rangle$. In the absence of experimental imperfections (see [28], Sec. S.3), P_{10} (respectively, P_{01}) would give the population of $|\uparrow\downarrow\rangle$ (respectively, $|\downarrow\uparrow\rangle$).

The evolution of $P_{10}(\tau)$ and $P_{01}(\tau)$ for two atoms prepared in $|\uparrow\downarrow\rangle$ separated by 30 μm is shown in Fig. 2(b). The spin excitation oscillates back and forth between the two atoms, with a frequency $2E/h \approx$ 0.52 MHz. The finite contrast is essentially due to spontaneous emission via the intermediate $|5P_{1/2}\rangle$ state during preparation and readout, which limits the oscillation amplitude to about 60%, and, to a lesser extent, to the onset of dipolar interactions during the second excitation pulse [28]. We then repeat the same experiment for several values of the distance R between the atoms, and observe spin-exchange oscillations for distances as large as 50 μm. Figure 2(c) shows the measured interaction energies as a function of R, together with the expected C_3/R^3 behavior (solid line) for the theoretical value $C_3^{\rm th} = 7965$ MHz μm^3 of the C_3 coefficient, calculated from the dipole matrix elements $\langle\uparrow|\hat{d}_{\pm1}|\downarrow\rangle$ [30,34]. A power-law fit to the data (not shown) gives an exponent -2.93 ± 0.20. Fixing the exponent to -3 gives $C_3^{\rm exp} = 7950 \pm 130$ MHz μm^3. The agreement between data and theory is excellent.

We now extend the system to a three-spin chain, with a distance $R = 20$ μm between the atoms. The sequence is similar to that in Fig. 2(a) for two atoms, except that we now use microwave transfer for atoms 2 and 3 to prepare $|g\downarrow\downarrow\rangle$. Here, the van der Waals interaction between the two atoms in $|\uparrow\rangle$ is only $\sim$10 kHz for $R = 20$ μm, and thus no blockade effect arises during excitation. We then excite atom 1 to prepare $|\uparrow\downarrow\downarrow\rangle$.

We first analyze theoretically the evolution of the system. Assuming that the initial state is $|\psi(0)\rangle = |\uparrow\downarrow\downarrow\rangle$, the dynamics induced by the XY Hamiltonian (1), which conserves the total magnetization $\sum_i \sigma_i^z$, occurs within the subspace spanned by $\{|\uparrow\downarrow\downarrow\rangle, |\downarrow\uparrow\downarrow\rangle, |\downarrow\downarrow\uparrow\rangle\}$. Figures 3(a) and 3(b) show the calculated dynamics of the spin excitation, which moves back and forth between the extreme sites. Figure 3(a) corresponds to the case where only nearest-neighbor interactions are retained in (1). Periodic, fully contrasted oscillations at a frequency $\sqrt{2}C_3/R^3$ are expected for the population of the extreme sites, while the population of $|\downarrow\uparrow\downarrow\rangle$ oscillates twice as fast between 0 and 1/2. In contrast, in Fig. 3(b), the full Hamiltonian (1) is simulated, including the interaction between extreme sites. One observes a clear signature of this long-range coupling, as the dynamics now becomes aperiodic for the populations of $|\uparrow\downarrow\downarrow\rangle$ and $|\downarrow\downarrow\uparrow\rangle$. The interplay of the couplings C_3/R^3 and $C_3/(8R^3)$ between nearest- and next-nearest neighbors makes the eigenvalues of (1) incommensurate. The back-and-forth exchange of excitation is thus modulated by a slowly varying envelope due to the beating of these frequencies.

Figure 3(c) shows the experimental results for P_{100}, P_{010}, and P_{001} (symbols). We observe qualitative agreement with Fig. 3(b), in particular the "collapse and revival" in the dynamics showing the effects of the long-range coupling. However, one notices differences with the ideal case: (i) the preparation is imperfect, as one starts with a significant population in $|\downarrow\uparrow\downarrow\rangle$, (ii) this, together with imperfect readout [28], reduces the overall amplitude of the oscillations, and (iii) the oscillations show some damping, which becomes significant for $\tau \geq 4$ μs.

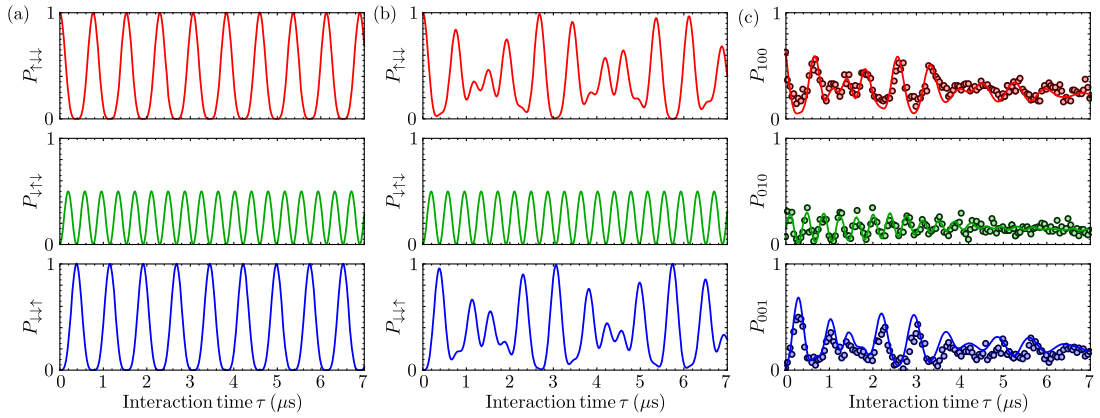

FIG. 3 (color online). Spin excitation transfer along a chain of three Rydberg atoms with nearest-neighbor separation of 20 μm. (a) Theoretical dynamics for a system initially prepared in $|\uparrow\downarrow\downarrow\rangle$, and evolving under a Hamiltonian similar to (1), but with only nearest-neighbor interactions. (b) The same as (a), but for the full Hamiltonian (1), including long-range interactions. (c) Experimental data (points) and prediction of the model taking into account experimental imperfections (see text), with no adjustable parameters. For perfect preparation and readout, the probabilities $P_{\uparrow\downarrow\downarrow}$ (respectively, $P_{\downarrow\uparrow\downarrow}$, $P_{\downarrow\downarrow\uparrow}$) and P_{100} (respectively, P_{010}, P_{001}) would coincide.

Imperfect preparation and readout stem from the fact that, in addition to the spontaneous emission via the intermediate state during the optical pulses, the Rabi frequency for optical excitation ($\simeq$5.3 MHz) of atom 1 from $|g\rangle$ to $|\uparrow\rangle$ is not much higher than the interaction ($\simeq$0.92 MHz for $R = 20$ μm). Thus, during the excitation of atom 1, the spin excitation already has a significant probability to hop to atom 2. The damping essentially arises from the finite temperature of the atoms, which leads to changes in the interatomic distances, and thus in the couplings.

To go beyond this qualitative understanding of the limitations of our "quantum simulator," we add all known experimental imperfections to the XY model [28]. The result, shown by solid lines on Fig. 3(c) accurately reproduces the data with no free parameters. To obtain these curves, we simulate the full sequence, i.e., all three optical (de-) excitation pulses with or without the addressing beam, the microwave pulse, and evolution time, by solving the optical Bloch equations describing the dynamics of the internal states of the atoms, restricted to three states: $|g\rangle$, $|\uparrow\rangle$, and $|\downarrow\rangle$. Dissipation comes from both off-resonant excitation of the intermediate $|5P_{1/2}\rangle$ state during the optical excitation pulse, and from the finite lifetimes of the Rydberg states (101 and 135 μs for $|\uparrow\rangle$ and $|\downarrow\rangle$, respectively [35]). The former effect is treated as an effective damping of the $|g\rangle \leftrightarrow |\uparrow\rangle$ transition, present only during the optical pulses, and with a damping rate chosen to match the damping of single-atom Rabi oscillations performed to calibrate the excitation Rabi frequency $\Omega_{\rm opt}$ [17].

We then account for the thermal motion of the atoms. A first consequence of the finite temperature ($T \simeq 50$ μK) is that at the beginning of the sequence, the atoms have random positions (the transverse rms extension of the thermal motion in each microtrap, of radial frequency 90 kHz, is about 120 nm) and random velocities (70 nm/μs rms). During the sequence, the traps are switched off and the atoms are thus in free flight with their initial velocity. When solving the optical Bloch equations, we thus first draw the initial positions $\boldsymbol{r}_i^0$ and velocities $\boldsymbol{v}_i^0$ of each atom i according to a thermal distribution, and use time-dependent dipolar couplings $C_3/|(\boldsymbol{r}_i^0 + \boldsymbol{v}_i^0 t) - (\boldsymbol{r}_j^0 + \boldsymbol{v}_j^0 t)|^3$ in Eq. (1) [36]. We then average the results over 100 realizations. This yields a dephasing of the oscillations, resulting in a significant contrast reduction at long times.

A second effect of the temperature is that an atom has a small probability $\varepsilon(t)$ to leave the trap region during the experiment. In this case, we mistakenly infer that it was in a Rydberg state at the end of the sequence. This leads to a small distortion of the measured populations P_{ijk} $(i, j, k = 0, 1)$ [37], that we compute from the actual ones as described in [17]. We measure $\varepsilon(t)$ (which increases with the duration t of the sequence, from $\sim$1% at $t = 0$ up to $\sim$20% for $t = 7$ μs) in a calibration experiment, and then use it to calculate the expected populations from the simulated ones [28].

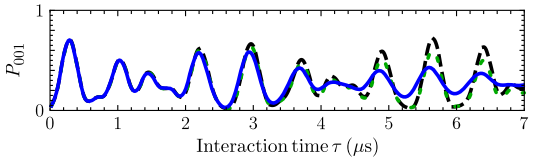

FIG. 4 (color online). Influence of the temperature on $P_{001}(\tau)$: simulated dynamics at zero temperature (black dashed line), and adding either only atom loss (green dotted line), or only atomic motion (blue solid line).

Figure 4 shows how those two consequences of the finite temperature contribute to the observed damping in the dynamics of P_{001}: both have sizable effects, but the dephasing due to fluctuations in the coupling dominates at long times. Reducing the atomic temperature using, e.g., Raman cooling [38,39] would render those effects negligible for our time scales, and allow the realization of a nearly ideal quantum simulator of spin dynamics.

In summary, we have measured the dynamics of a spin excitation in a minimal spin chain of three Rydberg atoms. The evolution of the system is accurately described by an XY Hamiltonian without any adjustable parameters. The obtained results are encouraging in view of scaling up the system to a larger number of spins. In particular, the residual motion of the atoms and the level of detection errors would already allow us to observe unambiguously the back-and-forth propagation of an excitation over a chain of $\sim$20 atoms [28]. However, so far, experiments with more than $\sim$5 atoms are hampered by the stochastic loading of the traps by single atoms [31]. In future work, we will thus explore various quasideterministic loading schemes that have been demonstrated at the level of a single [40,41] or a few [42,43] traps. Once this is achieved, our system will allow us to study the equivalent of an assembly of hard-core bosons on a 2D lattice with long-range, anisotropic hopping. We will also study dipolar interactions involving more than only two Rydberg states at an electrically tuned Förster resonance [44]. Our system will be ideal to study exotic phases and frustration in quantum magnetism, excitation hopping in complex networks [45,46], or quantum walks with long-range hopping [47].

We acknowledge financial support by the EU [ERC Stg. Grant ARENA, AQUTE Integrating Project, FET-Open Xtrack Project HAIRS, and EU Marie-Curie Program ITN COHERENCE FP7-PEOPLE-2010-ITN-265031 (H. L.)], and by Région Île-de-France (LUMAT and Triangle de la Physique, projects LAGON and COLISCINA during the stay of C. S. A. at LCF). C. S. A. also acknowledges support from the U.K. EPSRC and Durham University.

[1] A. Auerbach, *Interacting Electrons and Quantum Magnetism* (Springer-Verlag, New York, 1994).
[2] E. Collini, Chem. Soc. Rev. **42**, 4932 (2013).
[3] M. Lewenstein, A. Sanpera, and V. Ahufinger, *Ultracold Atoms in Optical Lattices: Simulating Quantum Many-Body Systems* (Oxford University Press, Oxford, U.K, 2012).
[4] J. Simon, W. S. Bakr, R. Ma, M. E. Tai, P. M. Preiss, and M. Greiner, Nature (London) **472**, 307 (2011).
[5] T. Fukuhara, P. Schauß, M. Endres, S. Hild, M. Cheneau, I. Bloch, and C. Gross, Nature (London) **502**, 76 (2013).
[6] A. de Paz, A. Sharma, A. Chotia, E. Maréchal, J. H. Huckans, P. Pedri, L. Santos, O. Gorceix, L. Vernac, and B. Laburthe-Tolra, Phys. Rev. Lett. **111**, 185305 (2013).
[7] B. Yan, S. A. Moses, B. Gadway, J. P. Covey, K. R. A. Hazzard, A. M. Rey, D. S. Jin, and J. Ye, Nature (London) **501**, 521 (2013).
[8] K. Kim, M. S. Chang, S. Korenblit, R. Islam, E. E. Edwards, J. K. Freericks, G. D. Lin, L. M. Duan, and C. Monroe, Nature (London) **465**, 590 (2010).
[9] P. Richerme, Z.-X. Gong, A. Lee, C. Senko, J. Smith, M. Foss-Feig, S. Michalakis, A. V. Gorshkov, and C. Monroe, Nature (London) **511**, 198 (2014).
[10] P. Jurcevic, B. P. Lanyon, P. Hauke, C. Hempel, P. Zoller, R. Blatt, and C. F. Roos, Nature (London) **511**, 202 (2014).
[11] P. Hauke, F. M. Cucchietti, A. Müller-Hermes, M.-C. Bañuls, J. I. Cirac, and M. Lewenstein, New J. Phys. **12**, 113037 (2010).
[12] D. Peter, S. Müller, S. Wessel, and H. P. Büchler, Phys. Rev. Lett. **109**, 025303 (2012).
[13] K. R. A. Hazzard, M. van den Worm, M. Foss-Feig, S. R. Manmana, E. Dalla Torre, T. Pfau, M. Kastner, and A. M. Rey, Phys. Rev. A **90**, 063622 (2014).
[14] M. Avellino, A. J. Fisher, and S. Bose, Phys. Rev. A **74**, 012321 (2006).
[15] M. Saffman, T. G. Walker, and K. Mølmer, Rev. Mod. Phys. **82**, 2313 (2010).
[16] H. Weimer, M. Müller, I. Lesanovsky, P. Zoller, and H.-P. Büchler, Nat. Phys. **6**, 382 (2010).
[17] D. Barredo, S. Ravets, H. Labuhn, L. Béguin, A. Vernier, F. Nogrette, T. Lahaye, and A. Browaeys, Phys. Rev. Lett. **112**, 183002 (2014).
[18] P. Schauß, J. Zeiher, T. Fukuhara, S. Hild, M. Cheneau, T. Macrì, T. Pohl, I. Bloch, and C. Gross, arXiv:1404.0980.
[19] H. Weimer, R. Löw, T. Pfau, and H. P. Büchler, Phys. Rev. Lett. **101**, 250601 (2008).
[20] T. Pohl, E. Demler, and M. D. Lukin, Phys. Rev. Lett. **104**, 043002 (2010).
[21] I. Lesanovsky, Phys. Rev. Lett. **106**, 025301 (2011).
[22] I. Mourachko, D. Comparat, F. de Tomasi, A. Fioretti, P. Nosbaum, V. M. Akulin, and P. Pillet, Phys. Rev. Lett. **80**, 253 (1998).
[23] W. R. Anderson, J. R. Veale, and T. F. Gallagher, Phys. Rev. Lett. **80**, 249 (1998).
[24] C. S. E. van Ditzhuijzen, A. F. Koenderink, J. V. Hernández, F. Robicheaux, L. D. Noordam, and H. B. van Linden van den Heuvell, Phys. Rev. Lett. **100**, 243201 (2008).
[25] G. Günter, H. Schempp, M. Robert-de-Saint-Vincent, V. Gavryusev, S. Helmrich, C. S. Hofmann, S. Whitlock, and M. Weidemüller, Science **342**, 954 (2013).
[26] S. Bettelli, D. Maxwell, T. Fernholz, C. S. Adams, I. Lesanovsky, and C. Ates, Phys. Rev. A **88**, 043436 (2013).
[27] D. Maxwell, D. J. Szwer, D. Paredes-Barato, H. Busche, J. D. Pritchard, A. Gauguet, K. J. Weatherill, M. P. A. Jones, and C. S. Adams, Phys. Rev. Lett. **110**, 103001 (2013).
[28] See Supplemental Material at http://link.aps.org/supplemental/10.1103/PhysRevLett.114.113002, which includes Ref. [29], for extra details about the simulation of the spin chain dynamics.
[29] C. Tuchendler, A. M. Lance, A. Browaeys, Y. R. P. Sortais, and P. Grangier, Phys. Rev. A **78**, 033425 (2008).
[30] L. Béguin, A. Vernier, R. Chicireanu, T. Lahaye, and A. Browaeys, Phys. Rev. Lett. **110**, 263201 (2013).
[31] F. Nogrette, H. Labuhn, S. Ravets, D. Barredo, L. Béguin, A. Vernier, T. Lahaye, and A. Browaeys, Phys. Rev. X **4**, 021034 (2014).
[32] The stray electric field is below 5 mV/cm. Note that as (1) conserves the excitation number, the system is quite immune to decoherence due to global fluctuations in electric or magnetic fields.
[33] H. Labuhn, S. Ravets, D. Barredo, L. Béguin, F. Nogrette, T. Lahaye, and A. Browaeys, Phys. Rev. A **90**, 023415 (2014).
[34] A. Reinhard, T. C. Liebisch, B. Knuffman, and G. Raithel, Phys. Rev. A **75**, 032712 (2007).
[35] I. I. Beterov, I. I. Ryabtsev, D. B. Tretyakov, and V. M. Entin, Phys. Rev. A **79**, 052504 (2009).
[36] Here, we neglect mechanical effects due to the interactions between Rydberg atoms during the interaction time. Using a classical model we estimate that these induce a displacement in R below 30 nm for $\tau \leq 7$ μs and are therefore negligible.
[37] C. Shen and L.-M. Duan, New J. Phys. **14**, 053053 (2012).
[38] A. M. Kaufman, B. J. Lester, and C. A. Regal, Phys. Rev. X **2**, 041014 (2012).
[39] J. D. Thompson, T. G. Tiecke, A. S. Zibrov, V. Vuletić, and M. D. Lukin, Phys. Rev. Lett. **110**, 133001 (2013).
[40] T. Grünzweig, A. Hilliard, M. McGovern, and M. F. Andersen, Nat. Phys. **6**, 951 (2010).
[41] M. Ebert, A. Gill, M. Gibbons, X. Zhang, M. Saffman, and T. G. Walker, Phys. Rev. Lett. **112**, 043602 (2014).
[42] Y. Miroshnychenko, W. Alt, I. Dotsenko, L. Förster, M. Khudaverdyan, D. Meschede, D. Schrader, and A. Rauschenbeutel, Nature (London) **442**, 151 (2006).
[43] M. Schlosser, J. Kruse, C. Gierl, S. Teichmann, S. Tichelmann, and G. Birkl, New J. Phys. **14**, 123034 (2012).
[44] S. Ravets, H. Labuhn, D. Barredo, L. Béguin, T. Lahaye, and A. Browaeys, Nat. Phys. **10**, 914 (2014).
[45] S. Wüster, C. Ates, A. Eisfeld, and J. M. Rost, Phys. Rev. Lett. **105**, 053004 (2010).
[46] S. Mostarda, F. Levi, D. Prada-Gracia, F. Mintert, and F. Rao, arXiv:1312.1833.
[47] R. Côté, A. Russell, E. E. Eyler, and P. L. Gould, New J. Phys. **8**, 156 (2006).

Chapter 4

Administrative data

In this last chapter, I first give a detailed CV, and then list my publications and my contributions in conferences.

4.1 Curriculum vitæ

Personal data

Born 14 September 1979 in Toulouse.
Married, one child.
French nationality.

Career

Oct. 2012–present: Researcher (CR1) at CNRS, Laboratoire Charles Fabry, UMR 8501, Palaiseau.
Jan. 2012–Oct. 2012: Researcher (CR2) at CNRS, Laboratoire Charles Fabry, UMR 8501, Palaiseau.
Oct. 2008– Dec. 2011: Researcher (CR2) at CNRS, LCAR, UMR 5589, Toulouse.
2006–2008: Post-doctoral researcher, University of Stuttgart (Germany), in Tilman Pfau's group.
2003–2005: Teaching assistant (allocataire-moniteur), Université Paris 6.
1999–2003: Student at École Normale Supérieure, Paris.

Education

2002–2005: PhD thesis in the Cold Atom group of Laboratoire Kastler Brossel, ENS, Paris, under the supervision of D. Guéry-Odelin and J. Dalibard, with honors (*Mention Très Honorable*). Title of the thesis: *Evaporative cooling of a mgnetically guided atomic beam.*

2001–2002: DEA of quantum physics, ENS, Paris: with honors ("mention TB"), rank joint 1st.
1999–2001: studies in Physics at ENS, Paris [2000: "Licence", with honors ("mention TB"); 2001: "Maîtrise", with honors ("mention TB")].
1999: Admitted at École Polytechnique (ranked 1) and ENS Paris (ranked 4).
1997–1999: Classes préparatoires PCSI–PC⋆, Lycée Pierre de Fermat, Toulouse.
1997: Baccalauréat S, with honors ("félicitations du jury").

Awards

2009: Louis Armand Prize of the French Academy of Sciences "for the realization of the first purely dipolar quantum gas".
2006: Individual Marie Curie EU fellowship.

Teaching experience

2012–: Lectures on Quantum mechanics at the "Préparation à l'Agrégation de Physique", ENS Cachan.
2008–2010: Teaching assistant for the lecture "Photons and Atoms" by Claude Fabre, at the Master 2 of Quantum Physics, ENS Paris.
2006–2007: Advanced Physical Laboratory, international master programme, University of Stuttgart.
2005–2006: Oral exams ("colles") in Physics, MPSI, Lycée Louis-le-Grand, Paris.
2003–2006: Teaching assistant ("moniteur"), University Paris 6.

Co-supervision of PhD students

Jan. 2013–now: Co-supervision of the PhD thesis of Henning Labuhn. Defense planned for December 2015.
Jan. 2013–now: Co-supervision of the PhD thesis of Sylvain Ravets, *Development of tools for quantum engineering using individual atoms: optical nanofibers and controlled Rydberg interactions*, defended on 16 December 2014. S. Ravets is now pursuing a six-month post-doctoral stay in our group.
Jan. 2012–Dec. 2013: Co-supervision of the PhD thesis of Lucas Béguin, *Measurement of the van der Waals interaction between two Rydberg atoms*, defended on 13 December 2013. Lucas Béguin is now a postdoctoral researcher in Philip Treutlein's group (Basel, Switzerland).
Sept. 2010–Dec. 2011: Co-supervision of the PhD thesis of Pierrick Cheiney, *Diffusion d'ondes de matière sur des potentiels complexes.* Pierrick Cheiney is now a postdoctoral researcher in Leticia Tarruell's group (ICFO, Spain).
Sept. 2009–Dec. 2011: Co-supervision of the PhD thesis of Charlotte Fabre, *Miroirs de Bragg pour ondes de matière et apport de la supersymétrie aux potentiels exponentiels.*

Charlotte Fabre is now a *professeur agrégée* in classes préparatoires.

Co-supervision of post-docs

May 2013–now: co-supervision of the post-doc of Daniel Barredo.
Jan. 2012–may 2013: co-supervision of the post-doc of Aline Vernier, who is now *Ingénieur de Recherche* at LOA, ENSTA, Palaiseau.

Supervision of undergraduate students

June 2014: Supervision of the L3 internship of Kevin Roux (IOGS).
June 2013: Supervision of the L3 internship of Vincent Lienhard (ENS Cachan).
July 2012: Supervision of the L3 internship of Pierre-Yves Perrin (IOGS).
July 2010: Supervision of the L3 internship of Clement Lao-Thiane (IOGS).
Jan.–March 2010: Co-supervision of the M2 internship of Pierrick Cheiney (M2 *Mécanique quantique*, ENS Ulm).
July 2009: Supervision of the L3 internship of Sebastien Garcia (ENS Ulm).
May–June 2009: Co-supervision of the M1 internship of Sven Badoux (Université Paul Sabatier).
April–June 2009: Co-supervision of the M2 internship of Charlotte Fabre (M2 *Sciences de la matière*, Université Paul Sabatier).
Oct 2007–July 2008: Supervision of the master thesis of Alaksei Charnukha (Universität Stuttgart).
July 2007–July 2008: Supervision of the *diplomarbeit* of Maximilian Meister (Universität Stuttgart).
July 2006–July 2007: Supervision of the *diplomarbeit* of Bernd Fröhlich (Universität Stuttgart).
Jan.–march 2006: Co-supervision of the M2 internship of Antoine Couvert (M2 *Mécanique quantique*, ENS Ulm).

Tasks of general interest

- 2015—: *Membre nommé* of the *Conseil de laboratoire* of LCF.
- Referee for Physical Review Letters, Physical Review A, EuroPhysics Letters, Optics Express, Journal of Physics B, New Journal of Physics.
- Referee for the IFRAF (Institut Francilien de Recherche sur les Atomes Froids), for the French Agency of Research (ANR), for the Austrian Science Fund.
- Organizer of the weekly colloquium of LCAR (september 2010–september 2011).
- Co-organizer of a parallel session *Condensed-matter with cold atoms* at the *Congrès Généeral de la Societe Française de Physique* (Bordeaux, France, 4–8 july 2011).

- Co-organizer, with A. Browaeys, C. S. Adams, and J. V. Porto, of a Les Houches summer school entitled "Current trends in atomic physics", in July 2016.
- *Webmaster* of the website of the cold atom group LCAR (2008–2011).
- Outreach: editions 2009 to 2013 of *Fête de la Science* at LCAR and then LCF, 50$^{\text{th}}$ anniversary of the laser in Toulouse, supervision of CPGE students for their TIPE...

4.2 Publications and conferences

4.2.1 Publication list

Refereed publications

1. D. Barredo, H. Labuhn, S. Ravets, T. Lahaye, A. Browaeys, and C. S. Adams, *Coherent Excitation Transfer in a "Spin Chain" of Three Rydberg Atoms* Phys. Rev. Lett. **114**, 113002 (2015).

2. S. Ravets, H. Labuhn, D. Barredo, L. Béguin, T. Lahaye, and A. Browaeys, *Coherent dipole–dipole coupling between two single Rydberg atoms at an electrically-tuned Förster resonance* Nature Phys. **10**, 914 (2014).

3. H. Labuhn, S. Ravets, D. Barredo, L. Béguin, F. Nogrette, T. Lahaye, and A. Browaeys, *Single-atom addressing in microtraps for quantum-state engineering using Rydberg atoms* Phys. Rev. A **90**, 023415 (2014).

4. F. Nogrette, H. Labuhn, S. Ravets, D. Barredo, L. Béguin, A. Vernier, T. Lahaye, and A. Browaeys, *Single-Atom Trapping in Holographic 2D Arrays of Microtraps with Arbitrary Geometries* Phys. Rev. X **4**, 021034 (2014).

5. D. Barredo, S. Ravets, H. Labuhn, L. Béguin, A. Vernier, F. Nogrette, T. Lahaye, and A. Browaeys, *Demonstration of a Strong Rydberg Blockade in Three-Atom Systems with Anisotropic Interactions* Phys. Rev. Lett. **112**, 183002 (2014).

6. L. Béguin, A. Vernier, R. Chicireanu, T. Lahaye and A. Browaeys, *Direct measurement of the van der Waals interaction between two Rydberg atoms* Phys. Rev. Lett **110**, 263201 (2013).

7. P. Cheiney, C. M. Fabre, F. Vermersch, G. L. Gattobigio, R. Mathevet, T. Lahaye and D. Guéry-Odelin
Matter wave scattering on an amplitude-modulated optical lattice
Phys. Rev. A. **87**, 013623 (2013).

8. T. Lahaye
Measuring the eccentricity of the Earth's orbit with a nail and a piece of plywood
Eur. J. Phys. **33** 1167 (2012).

9. T. Lahaye, P. Labastie and R. Mathevet
Fizeau's "aether-drag" experiment in the undergraduate laboratory
Am. J. Phys. **80** 497 (2012).

10. C.M. Fabre, P. Cheiney, G.L. Gattobigio, F. Vermersch, S. Faure, R. Mathevet, T. Lahaye and D. Guéry-Odelin
Realization of a distributed Bragg reflector for propagating guided matter waves
Phys. Rev. Lett. **107**, 230401 (2011).

11. P. Cheiney, O. Carraz, D. Bartoszek-Bober, S. Faure, F. Vermersch, C.M. Fabre, G.L. Gattobigio, T. Lahaye, D. Guéry-Odelin, and R. Mathevet
Zeeman slowers made simple with permanent magnets in a Halbach configuration
Rev. Sci. Inst. **82** 063115 (2011).

12. T. Lahaye, T. Pfau, and L. Santos
Mesoscopic ensembles of polar bosons in triple-well potentials
Phys. Rev. Lett. **104**, 170404 (2010) ; Erratum, Phys. Rev. Lett. **105**, 239904 (2010).

13. T. Lahaye, C. Menotti, L. Santos, M. Lewenstein and T. Pfau
The physics of dipolar bosonic quantum gases
Rep. Prog. Phys. **72**, 126401 (2009).

14. J. Metz, T. Lahaye, B. Fröhlich, A. Griesmaier, T. Pfau, H. Saito, Y. Kawaguchi and M. Ueda
Coherent collapses of dipolar Bose-Einstein condensates for different trap geometries
New J. Phys. **11**, 055032 (2009).

15. T. Lahaye, J. Metz, B. Fröhlich, T. Koch, M. Meister, A. Griesmaier, T. Pfau, H. Saito, Y. Kawaguchi and M. Ueda
d-wave collapse and explosion of a dipolar Bose-Einstein condensate
Phys. Rev. Lett. **101**, 080401 (2008).

16. T. Koch, T. Lahaye, J. Metz, B. Fröhlich, A. Griesmaier and T. Pfau
Stabilization of a purely dipolar quantum gas against collapse
Nature Phys. **4**, 218 (2008).

17. G. Reinaudi, T. Lahaye, Z. Wang, and D. Guéry-Odelin
Strong saturation absorption imaging of dense clouds of ultracold atoms
Opt. Lett. **32**, 3143 (2007).

18. T. Lahaye, T. Koch, B. Fröhlich, M. Fattori, J. Metz, A. Griesmaier, S. Giovanazzi and T. Pfau
Strong dipolar effects in a quantum ferrofluid
Nature **448**, 672 (2007).

19. B. Fröhlich, T. Lahaye, B. Kaltenhäuser, H. Kübler, S. Müller, T. Koch, M. Fattori and T. Pfau
Two-frequency acousto-optic modulator driver to improve the beam-pointing stability during intensity ramps
Rev. Sci. Instrum. **78**, 043101 (2007).

20. T. Lahaye
Refroidissement par évaporation d'un jet atomique guidé magnétiquement
Ann. Phys. Fr. **31-1**, 1 (2006).

21. G. Reinaudi, Z. Wang, A. Couvert, T. Lahaye and D. Guéry-Odelin
A moving magnetic mirror to slow down a bunch of atoms
Eur. Phys. J. D **40**, 405 (2006).

22. T. Lahaye, G. Reinaudi, Z. Wang, A. Couvert, and D. Guéry-Odelin
Transport of atom packets in a train of Ioffe-Pritchard traps
Phys. Rev. A **74**, 033622 (2006).

23. T. Lahaye and D. Guéry-Odelin
Kinetics of the evaporative cooling of an atomic beam
Phys. Rev. A. **73**, 063622 (2006).

24. G. Reinaudi, T. Lahaye, A. Couvert, Z. Wang and D. Guéry-Odelin
Evaporation of an atomic beam on a material surface
Phys. Rev. A **73**, 035402 (2006).

25. T. Lahaye, Z. Wang, G. Reinaudi, S. P. Rath, J. Dalibard and D. Guéry-Odelin
Evaporative cooling of a Rubidium atomic beam
Phys. Rev. A **72**, 033411 (2005).

26. T. Lahaye and D. Guéry-Odelin
Discrete-step evaporation of an atomic beam
Eur. Phys. J. D **33**, 67 (2005).

27. T. Lahaye, J. M. Vogels, K. Guenter, Z. Wang, J. Dalibard, and D. Guéry-Odelin
Realization of a magnetically guided atomic beam in the collisional regime
Phys. Rev. Lett. **93**, 093003 (2004).

28. D. Guéry-Odelin and T. Lahaye
Dynamics of a trapped ultracold two-dimensional atomic gas
Comptes Rendus Physique **5**, 55 (2004).

29. J. M. Vogels, T. Lahaye, C. Roos, J. Dalibard, and D. Guéry-Odelin
How to reach the collisional regime on a magnetically guided atomic beam?
J. Phys. IV France **116**, 259 (2004).

30. C. F. Roos, P. Cren, T. Lahaye, J. Dalibard, and D. Guéry-Odelin
Injection of a cold atomic beam into a magnetic guide
Laser Physics **13**, 607 (2003).

31. T. Lahaye, P. Cren, C. Roos, and D. Guéry-Odelin
Propagation of guided cold atoms
Commun. Nonlinear Sci. **8**, 315 (2003).

32. D. Egorov, T. Lahaye, W. Schöllkopf, B. Friedrich, and J. M. Doyle
Buffer-gas cooling of atomic and molecular beams
Phys. Rev. A **66**, 043401 (2002).

33. R. Delhuille, C. Champenois, M. Büchner, L. Jozefowski, T. Lahaye, R. Mathevet, A. Miffre, C. Rizzo, C. Robillard, G. Trénec, and J. Vigué
Some theoretical and experimental aspects of three-gratings Mach-Zehnder atom interferometers
C. R. Acad. Sci. Paris **2 IV**, 587 (2001).

Books

1. D. Guéry-Odelin and T. Lahaye
Classical mechanics illustrated by modern physics, 42 problems with solutions
English translation of 2., Imperial College Press (december 2010).

2. D. Guéry-Odelin and T. Lahaye
La mécanique classique illustrée par la physique contemporaine, 42 exercices and problèmes corrigés
Foreword by Jean Dalibard. Éditions Ellipses (september 2008).

Book chapters

1. A. Browaeys and T. Lahaye
Interacting Cold Rydberg Atoms: a Toy Many-Body System,
In Niels Bohr 1913–2013, Séminaire Poincaré **XVII**, 125 (2013).

2. D. Guéry-Odelin and T. Lahaye
Basics on Bose-Einstein condensation
In K. L. Chuan *et al.*, "Ultracold gases and quantum information", Proceedings of

Les Houches in Singapore 2009 summer school, 70 pages, Oxford University Press (2011).

3. T. Lahaye, J. Metz, T. Koch, B. Fröhlich, A. Griesmaier and T. Pfau
   A purely dipolar quantum gas
   In ATOMIC PHYSICS 21, proceedings of ICAP 2008, arXiv:0808.3876.

4. C. Menotti, M. Lewenstein, T. Lahaye and T. Pfau,
   Dipolar interaction in ultra-cold atomic gases
   Chapter of the volume "Dynamics and Thermodynamics of systems with long range interactions: theory and experiments", A. Campa, A. Giansanti, G. Morigi, F. Sylos Labini Eds., AIP Conference proceedings **970** (2008).

4.2.2 Conferences

1. IARPA's workshop on *Multi-Qubit Coherent Operations*, New-York City, NY, USA, 3–6 February 2015: invited talk *Quantum engineering in arrays of single Rydberg atoms.*

2. Workshop *Second International Workshop on Ultracold Rydberg Physics* Recife, Brazil, 5–8 October 2014: invited talk *Small systems of interacting Rydberg atoms.*

3. Workshop *Long-range interactions in quantum systems*, Palaiseau, France, 23–26 September 2014: invited talk *Resonant dipole-dipole interactions in systems of single Rydberg atoms.*

4. Workshop of the ITN Coherence, Granada, Spain, 10–12 September 2014: invited talk *Small systems of interacting Rydberg atoms.*

5. Workshop *Networks of Rydberg atoms*, Oxford, UK, 9–10 January 2014: invited talk *Rydberg blockade experiments in small arrays of single atoms.*

6. Invited talk in the company *ImagineOptic*, Orsay, France, 5 December 2013: *Arrays of microtraps for single-atom trapping.*

7. Workshop *Façonner la lumière*, ENS Ulm, Paris, France, 7 November 2013: invited talk *Arrays of microtraps for quantum information processing using the Rydberg blockade.*

8. QuPa workshop, Institut Henri Poincaré, Paris, France, 19 September 2013: invited talk *Rydberg atoms for quantum information processing.*

9. ICQT 2013, Moscow, Russia, 20–24 July 2013: poster *Direct measurement of the van der Waals interaction between two Rydberg atoms.*

10. DAMOP 2013, Quebec City, Canada, 3–7 June 2013: invited talk ('Hot Topics session') *Direct measurement of the van der Waals interaction between two Rydberg atoms.*

11. Invited talk at the seminar of the students of the Solid-state physics Master 2 program, LPS, Orsay, 28 November 2012: *Entangling Neutral Atoms using the Rydberg Blockade.*

12. First workshop of the GDR *Information Quantique, Fondements et Applications*, 23–25 March 2011, Nice, France: poster *Mesoscopic ensembles of polar bosons in triple-well potentials.*

13. Conference *Atom Lasers*, 4–9 April 2010, Les Houches, France: invited talk *Towards CW atom lasers by evaporation of guided beams: a review.*

14. Workshop *Dipolar quantum gases*, 30 September–2 October 2009, Stuttgart, Germany: invited talk *Mesoscopic dipolar BECs in triple well potentials.*

15. Conference *Bose-Einstein Condensation 2009*, 5–11 September 2009, San Feliu de Guixols, Spain: poster *All-optical guided atom lasers.*

16. Workshop *Control of quantum correlations in tailored matter: Common perspectives of mesoscopic systems and quantum gases*, 3–6 December 2008, Reisensburg, Germany: invited talk *Experiments with dipolar BECs.*

17. Workshop *Dipolar gases*, 25 june 2008, Villetaneuse, France: invited talk *Recent experiments with a dipolar BEC.*

18. Conference *Theory of Quantum Gases and Quantum Coherence*, 3–7 June 2008, Grenoble, France: invited talk *Experiments with dipolar BECs.*

19. Conference *Nonlinear phenomena in quantum degenerate gases*, 1–5 April 2008, Toledo, Spain: invited talk *Nonlinear dynamics of a dipolar BEC.*

20. Joint International Conference IFRAF–CO.CO.MAT *Control of quantum correlations in tailored matter: Common perspectives of mesoscopic systems and quantum gases*, 3–7 October 2007, Reisensburg, Germany. Invited talk *Strong dipolar interactions in a BEC.*

21. Summer school *Novel Quantum Phases and Non-equilibrium Phenomena in Cold Atom Gases*, 27 August–7 September 2007, International Centre for Theoretical Physics, Trieste, Italy: invited talk *Experiments with dipolar quantum gases.*

22. Annual DPG meeting, 19–23 March 2007, Düsseldorf, Germany. Talk *Strong dipolar effects in a Chromium BEC close to a Feshbach resonance.*

23. Conference *Quo vadis BEC?*, 27–29 October 2006, Berlin, Germany. Poster *Chromium BEC: a dipolar quantum gas.*

24. 38^{th} EGAS Conference (European Group on Atomic Systems) 7–10 June 2006, Ischia, Italy. Contributed talk *Evaporative cooling of a magnetically guided atomic beam.*

25. First IFRAF Workshop (Institut Francilien de Recherche sur les Atomes Froids), IHP, Paris, France, 4 May 2006: invited talk *Evaporative cooling of a magnetically guided atomic beam: the prospects of using a conveyor belt for atoms.*

26. VIIth Workshop on Quantum Optics and Foundations of Quantum Mechanics, Bilbao, Spain, 14 December 2005: invited talk *Evaporative cooling of a magnetically guided atomic beam: towards a cw coherent source for atom optics.*

27. Group seminar in Prof. Tilman Pfau's group, Stuttgart, Germany, 26 October 2005: *Evaporative cooling of a magnetically guided atomic beam.*

28. Group seminar in Prof. Markus Oberthaler's group, Heidelberg, Germany, 24 October 2005: *Evaporative cooling of a magnetically guided atomic beam.*

29. Group seminar in Prof. Rudi Grimm's group, Innsbruck, Austria, 22 September 2005: *Evaporative cooling of a magnetically guided atomic beam: towards a cw atom laser.*

30. Mesoscopic Phenomena in Ultracold Matter: From Single Atoms to Coherent Ensembles, 11–15 October 2004, Dresden, Germany. Poster *Realization of a magnetically guided beam in the collisional regime.*

31. Young Atom Opticians Conference, 3–8 June 2003, Amsterdam, the Netherlands. Poster *Magnetically guided beams: a first step towards a cw atom laser.*

32. Atomic Physics Gordon Conference, 17–22 June 2001, Williamstown, MA, USA. Poster *Buffer-gas cooling of a rubidium atomic beam.*

Appendix A

Outreach

Il s'enfermait tout' la journée
Au fond d'son atelier
Pour fair' des expériences[1]

A.1 Introduction

In this chapter, I give a brief description of the outreach activities I have been involved with since I was hired at CNRS, which consisted essentially in the realization of demonstration experiments, either for the general public or for undergraduate students. I personally find this "popularization" of physics extremely enriching, and even though I devote only a very small part of my time to such work, I decided, essentially for my own personal records, to include a short description of it in this *Mémoire d'habilitation*. The work described here was performed at LCAR, most notably because there I benefited from extremely enriching interactions with two passionate popularizers of physics: Béatrice Chatel and Renaud Mathevet. Without them, most of what is described below would not have been done.

This chapter is organized as follows. I first describe two realizations directed towards the general public: a "laser fountain", made for the celebration of the 50^{th} anniversary of the laser that B. Chatel organized during the 2010 science festival *La Novela* in Toulouse, and a small video of the operation of a Rb magneto-optical trap, that was posted on Youtube. The rest of the chapter is devoted to the realization of experiments triggered by undergraduate students working on their TIPE[2]. I first describe the construction and operation of a Paul trap for small anthracene particles, then I report on a replication of the famous "æther-drag" experiment performed by Fizeau in 1851, and finally I show that one can measure the eccentricity of the Earth orbit with very modest equipment. The last two experiments gave rise to a publication in the American Journal of Physics [70] and

[1] Boris Vian, *La Java des bombes atomiques* (1955).

[2] Travaux d'Initiative Personnelle Encadrés: a small research project by students of *Classes préparatoires*, on a theme chosen by themselves, and that can include the realization of experiments.

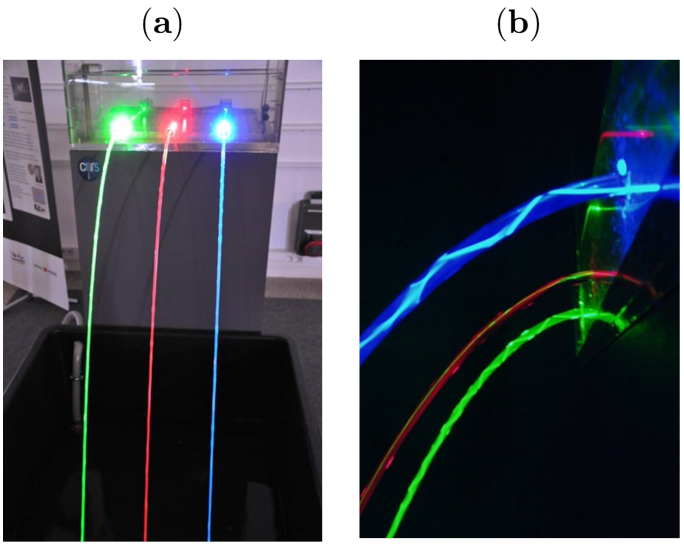

Figure A.1: (a): General view of the laser fountain. (b): Close-up on the total internal reflection of the maser beams inside the water jets.

in the European Journal of Physics [67], respectively, and the corresponding articles are reproduced at the end of this chapter.

A.2 A "laser fountain" for the 50^{th} anniversary of the laser

The year 2010 marked the fiftieth anniversary of invention of the laser by Maiman in 1960, and many outreach activities were organized worldwide to celebrate this landmark and increase the awareness of the general public about the importance of laser technology in our everyday life. In Toulouse, it was thus decided to include, in the yearly science festival *La Novela*, an ambitious exhibition about lasers. The project was lead by Béatrice Chatel from LCAR, and consisted in creating an temporary museum about the principles and applications of lasers, from basic research to industry, including not only static exhibitions (with holograms, laser-welded and laser-cut aircraft parts, artwork using lasers...) but also active workshops with live experiments performed and commented by researchers. Among those workshops, one was devoted to fiber-optics communication, and it naturally included a brief discussion of total internal reflection.

Based on earlier work done at the LPL in Villetaneuse, I decided to build a "laser fountain" that demonstrates total internal reflection in a very appealing way, by guiding a laser beam inside a jet of water, to serve as an introduction to the workshop. The resulting fountain is shown in Fig. A.1(a). An upper tank made of plexiglass, with a height of about 60 cm, contains some 20 L of water. Close to the bottom of the tank, 3 holes with a diameter of 8 mm are drilled in the side panel, and give birth to three parallel, parabolic water jets, which are collected in a lower tank on the floor, about 1 m below. Through the back panel of the upper tank, a laser beam is injected in each of the water

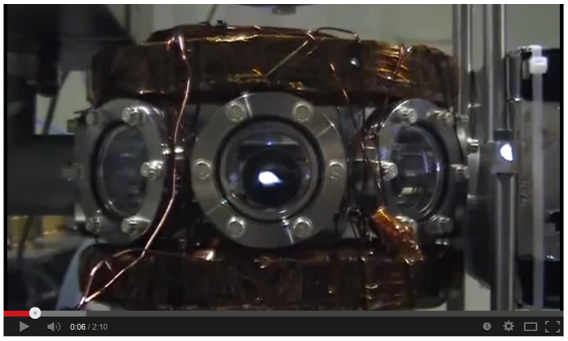

Figure A.2: A screen capture of the MOT video on Youtube.

jets[3], and undergoes several total internal reflections at the water/air interface, as can be seen in Fig. A.1(b).

The upper tank gets empty in a few minutes. In order for the fountain to run continuously, a pump was switched on automatically when the water level was below a preset value, and pumped back the water to the upper tank until it was almost full. At this point, the pump turned off again. The turbulence created in the tank by the pump died out in a few tens of seconds. This, in combination with the great care taken in machining the orifices to make them very smooth, allowed for water jets without any roughness, and made it possible to observe many total internal reflections. The fountain encountered big success among the public, from toddlers to adults...

This fountain was reused several times at LCAR for the *Fête de la Science*. I later built a smaller version, working on similar principles, for the entrance hall of the institute.

A.3 Yet another MOT video on Youtube

During the process of testing the permanent-magnet Zeeman slower described in section 2.2, we used a ^{87}Rb magneto-optical trap that was loaded by the slowed beam. I took a movie of the corresponding MOT dynamics, showing a few typical phenomena that one can observe visually with a MOT: loading it, turning the MOT into an optical molasses when switching off the magnetic field gradient, moving the zero of magnetic field using shim coils, observing the MOT decay due to background-gas collisions. We decided to share the video on Youtube[4] with a short text describing the various phases of the movie (see Fig. A.2). Four years later, the video has been viewed some 3,700 times. This video also proved to be very useful in talks for the general public, as a means to show how a cloud of cold atoms actually looks like in the lab, making the subject less abstract.

[3] I used three relatively cheap, 20 mW diode-pumped solid-state lasers from SDL, one red, one green, and one blue.

[4] https://www.youtube.com/watch?v=eAIDL_2xN8M.

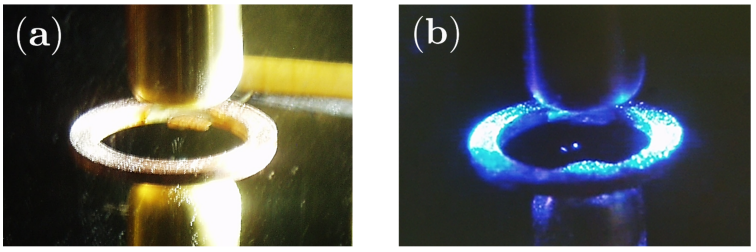

Figure A.3: (a): A view of a few anthracene particles confined in the Paul trap. Due to the gravitational sag in the trap, the particles are displaced downwards from the quadrupole center, and thus experience a micromotion along the vertical direction, which makes them appear as vertical filaments. (b): Two trapped anthracene particles seen under stroboscopic illumination at 50 Hz (using a UV LED), and that thus seem to be stationary.

A.4 A Paul trap for small particles

In 2010, I was contacted by students who looked for help in setting up a Paul trap for their TIPE. Paul traps are extensively used for the manipulation of charged particles, not only to realize ion traps, but also in quadrupole mass spectrometry. The basic mechanism consists in driving a set of electrodes creating a quadrupolar electric field by AC voltages. The configuration would be unstable if DC fields were used, but with a high enough driving frequency the motion can become stable, as the micromotion due to the fast driving acts as a potential energy term for the slow motion.

Several realizations of Paul traps used to demonstrate the capture and storing of small "dust" particles have been reported. In my case, I followed closely the work described in [133]. The particles to be trapped are small anthracene crystals, charged by friction with the plastic syringe that is used for injecting them into the trap. Damping by the viscous friction of air allows to damp the motion of the particles, and to load them into the (otherwise conservative) trap.

The quadrupole field was created using a ring electrode (in practice, a CF–16 copper gasket) and two connected endcaps (in a first version, these were machined brass spheres, but in a second version a simple pair of teaspoons worked just as well). They were held in place using wooden spacers. For simplicity, the trap was driven at 50 Hz from the mains, with voltages up to 10 to 15 kV. For that, a variable autotransformer fed a high-voltage transformer[5]. The assembly was fitted into a plexiglass enclosure, not only for obvious safety reasons, but also in order to shield the trapped particles from unwanted air currents. A side hole close to the ring electrode allowed for the injection of anthracene particles.

The anthracene powder, contained in a plastic syringe, was rapidly fed into the trap. The triboelectric effect ensured charging of the particles, and the viscous damping by air allowed to trap the dust particles having the appropriate charge to mass ratio. Figure

[5]Of the type used for ignition of a central-heating boiler; it was generously provided by Jacques Vigué who had saved it for another project.

A.3(a) shows the trapping of about five anthracene particles, which appear as vertical filaments. This is due to the due to the gravitational sag experienced by the particles in the trap: the particles are displaced downwards from the center of the quadrupole field, and thus experience a micromotion along the vertical axis. Figure A.3(b) shows two particles illuminated by a UV[6] LED fed by short current pulses with a repetition rate of 50 Hz, allowing the stroboscopic observation of the particles, which appear motionless in this case. Using the measured value of the gravitational sag and knowing the parameters of the trap, a semi-quantitative measurement of the charge-to-mass ratio of the anthracene particles could be performed by the students.

A.5 Fizeau's "æther-drag" experiment made simple

This work was also triggered by students who contacted Pierre Labastie, asking for help in setting up a replication of Fizeau's 1851 "æther-drag" experiment for their TIPE. A quick description of this famous experiment often occurs in textbooks on special relativity, as it is a nice way to illustrate the relativistic addition of velocities. Of course, Fizeau's motivation in 1851 was different: his work was a test of an hypothesis made in 1818 by Fresnel to "explain" the negative result of experiments performed by Arago with the goal to observe the dependence of the speed of light on the motion of the observer.

Fresnel's "partial æther-drag" formula gives, in the lab frame, the velocity V of light propagating in a transparent medium with refractive index n, which is itself moving with a velocity v in the lab frame:

$$V = \frac{c}{n} + \left(1 - \frac{1}{n^2}\right) v. \tag{A.1}$$

In contrast, a naive application of the usual (Galilean) addition of velocities ("total drag") would give $V = c/n + v$. In the limit of a medium becoming extremely dilute, such as in a gas whose pressure vanishes, the latter formula would give $V = c + v$, while Fresnel's equation predicts $V = c$, a much more reasonable result as in this case one expects no effect of such a dilute gas on the propagation of light. The experiment by Fizeau confirmed the validity of Fresnel's formula, and played a role in later developments of the electrodynamics of moving media, that finally culminated with the birth of special relativity.

Fizeau's extremely clever idea is to use an interferometer (which is actually a Sagnac-type interferometer), inside which a U-shaped tube with flowing water is inserted (see Figs. 1 and 2 of the article [70] reproduced below on page 128). The two paths of the interferometer are the same, but in one of them the light co-propagates with the water flow, while, in the other, light and water are counter-propagating. This clever trick allows one to reject common-mode phase-shifts due to turbulent flow in the tubes[7]. The position of the interference fringes that are observed at the output of the interferometer then depend linearly on the velocity of the water flow, and on the length of the interferometer. For

[6] When irradiated by UV light, anthracene particles fluoresce in the blue.

[7] In many textbooks, this crucial point is overlooked, and the interferometric arrangements that are shown would not allow for the observation of the effect.

reasonable water velocities of a few meters per second, a fringe displacement of about one fringe requires an interaction length of a few meters.

The difficulty of the experiment thus lies in the realization of a water circulation system compatible with the observation of interference fringes. Together with Renaud Mathevet, we built an inexpensive but robust setup, based on standard plumbing hardware. We used initially a green solid-state laser as a light source, but, for the fun of it, we also used white light as in the original experiments. We found good agreement with theory, discarding the Galilean addition of velocities. We finally decided to publish a detailed description of our setup in the American Journal of Physics.

A.6 Measuring the eccentricity of the Earth orbit with a nail

In this last section, I briefly describe an experiment which somehow departs from my field of optics or particle trapping, and rather deals with astronomy. It also originated from discussions with students about possible subjects for a TIPE, but finally I did it to entertain myself, essentially at home (as the reader will see, little equipment is needed). In the end I also published a paper about it, this time in the European Journal of Physics, and so, for completeness, I include a brief description of this work here.

It is well-known that the Sun's maximal altitude in the sky (reached at noon) displays strong seasonal variations, due to the obliquity of the Earth's rotation axis. However, it is less known that the exact time at which this maximum occurs also varies during the year, by a few minutes. The difference between the *true local noon* and the official noon given by clocks is called the *equation of time*. This difference is due to the combination of two effects :

- the obliquity on the ecliptic makes the projection of the Sun on the celestial equator move non-uniformly;
- the eccentricity of the Earth orbit gives rise, *via* Kepler's second law, to a non-uniform apparent motion of the Sun on the celestial equator.

Huyghens was the first to give correct expressions for the equation of time in the seventeenth century, although the irregularity of the apparent motion of the Sun had been known since Antiquity.

What I reported on in [67] was a very basic way to measure the equation of time, using an elementary homemade sundial consisting of a nail protruding from a plywood base. The length of the shadow of the nail when placed in the sunlight allows one to compute the elevation of the Sun. One then just needs to plot the altitude of the Sun over time during the the course of a day, and extract from this data the maximal altitude and the time at which this maximum is reached. Repeating this every few days over a full year gives a good determination of the variation of the equation of time during the year, which

in turns allows for determining the eccentricity of the Earth orbit. I obtained a value of $(1.7 \pm 0.1)\,\%$, to be compared to the published value $1.6711\,\%$. Besides being a lot of fun, performing this work was also a good reminder about the fact that one does not always need fancy equipment to measure something with a reasonable accuracy.

A.7 Published articles

Here, I list the two peer-reviewed educational articles I have co-authored:

- T. Lahaye, P. Labastie, and R. Mathevet, Am. J. Phys **80**, 497 (2012), reproduced on page 128. I should point out here a few typos introduced in the copy-editing process, and that we unfortunately did not spot when proofreading the paper. On page 498, in the denominator of the first fraction of Eq. (1), a factor c is missing. On page 499, in the second column, the numerical values of the velocities disappeared in two instances. They should read 4 and 6 m/s, respectively.

- T. Lahaye, Eur. J. Phys **33**, 1167 (2012) reproduced on page 137.

Fizeau's "aether-drag" experiment in the undergraduate laboratory

Thierry Lahaye and Pierre Labastie
Université de Toulouse, UPS, Laboratoire Collisions Agrégats Réactivité, IRSAMC; F-31062 Toulouse, France and CNRS, UMR 5589, F-31062 Toulouse, France

Renaud Mathevet
Université de Toulouse, UPS, Laboratoire Collisions Agrégats Réactivité, IRSAMC; F-31062 Toulouse, France; CNRS, UMR 5589, F-31062 Toulouse, France; and Laboratoire National des Champs Magntiques Intenses, UPR3228 CNRS/INSA/UJF/UPS, F-31400, Toulouse, France

(Received 16 December 2011; accepted 10 February 2012)

We describe a simple realization of Fizeau's "aether-drag" experiment. Using an inexpensive setup, we measure the phase shift induced by moving water in a laser interferometer and find good agreement with the relativistic prediction or, in the terms of 19th century physics, with Fresnel's partial-drag theory. This appealing experiment, particularly suited for an undergraduate laboratory project, not only allows a quantitative measurement of a relativistic effect on a macroscopic system but also constitutes a practical application of important concepts of optics, data acquisition and processing, and fluid mechanics.
[http://dx.doi.org/10.1119/1.3690117]

I. INTRODUCTION

In introductory courses and textbooks dealing with special relativity, Fizeau's "aether-drag" experiment often appears simply as an application of the law of composition of velocities, sometimes in the form of an exercise.[1] However, Albert Einstein himself declared that Fizeau's measurement of the speed of light in moving water was, together with stellar aberration, one of the experimental results that had influenced him most in the development of relativity.[2] In spite of this high praise, introductory expositions of Fizeau's experiment, including a discussion of its historical development and the details of the experimental setup, are often lacking. Moreover, many textbooks actually show incorrect experimental arrangements that would not allow for the observation of the effect in practice. Here, we show that one can actually perform Fizeau's experiment with rather modest equipment, and that such a project illustrates in an appealing way not only relativistic kinematics but also interesting aspects of wave optics, data acquisition and processing, and even fluid mechanics.

This article is organized as follows. We first review briefly the historical background of Fizeau's experiment, a "test" of special relativity carried out more than half a century before relativity was born! For completeness, we recall in Sec. III the derivation of the expected fringe shift in both the relativistic and non-relativistic frameworks, following the usual textbook treatment of the problem. We then turn to the main point of the paper, namely, how to reproduce the experiment in an undergraduate laboratory. Section IV is devoted to the description of our apparatus, starting with an emphasis on the experimental trade-offs one needs to address in the design phase. Finally, we discuss in Sec. V the results obtained, first with water as a moving medium and then with air, in order to discriminate between relativistic and non-relativistic predictions. The use of a white-light source instead of a laser is presented in Appendix A, with a discussion of the possible advantages and drawbacks. Appendix B establishes a useful fluid mechanics formula using dimensional analysis.

II. HISTORICAL BACKGROUND

Since Fizeau's aether-drag experiment is a landmark among the various experimental and theoretical developments leading to special relativity, it is worthwhile to recall briefly the history of these developments. An extensive historical study of the subject is beyond the scope of this paper. Here, we merely recall the main steps that led to Fizeau's aether drag experiment, as well as the major subsequent developments.[3]

We begin our reminder in the 17th century, at a time when the nature of light was a matter of harsh debate, as evidenced by the famous controversy between Christiaan Huygens and Isaac Newton. The speed of light in a vacuum c was known to be finite since the work of Ole Römer in 1676.[4] However, the measurement of the speed of light in a material medium of refractive index n was considered a crucial test because Huygens' wave theory implies that the speed of light in the medium is c/n, while Newton's corpuscular theory predicts it to be nc. Newton's views prevailed until the beginning of the 19th century, when interference experiments by Thomas Young and polarization experiments by Étienne Malus firmly established the wave theory.

An important event was the measurement by François Arago of the deviation of light from a distant star by a prism in 1810.[5] The idea of Arago is that if the speed of the light coming from distant stars is increased or decreased by the Earth's velocity, Newton's theory predicts that the deviation by a prism should be different from what would be observed if the source was terrestrial. He, therefore, tried to detect this difference and found a null result. This experiment seems to be the first in a long series that showed the impossibility of detecting the relative motion of light with respect to the Earth.[6]

Arago soon became friends with Augustin Fresnel, who had a mathematically sound theory of light waves, and asked him if the wave theory could explain the null result he had found. Fresnel's answer came a few years later.[7] His demonstration is based on the hypothesis of an absolute aether as a support of light waves, associated with a partial drag by transparent media. That is, if the medium of index n moves with speed $\boldsymbol{v}$, the aether inside the medium moves only at speed $(1-n^{-2})\,\boldsymbol{v}$. The value of Fresnel's drag coefficient $1-n^{-2}$ precisely gives a null result for the Arago experiment. However, his demonstration, using some supposed elastic properties of the aether, is not so convincing by modern standards.[6]

The first Earth-based direct measurement of the speed of light was realized by Hippolyte Fizeau in 1849, by means of a rotating cogwheel. This kind of time-of-flight technique was soon improved by Léon Foucault who, using a rotating mirror, succeeded in showing that the speed of light is lower in water than in air.[8,9] Nevertheless, such *absolute* measurements were far from accurate enough to measure the small change of the speed of light in moving media.

This is where Fizeau's aether-drag experiment enters the scene. As we shall see, this experiment is based on a much more sensitive *differential* measurement using the interferometric arrangement shown in Fig. 1. The experiment was performed in 1851 and almost immediately reported to the French academy of science, and then translated into English.[10] Fizeau measured an effect in agreement with Fresnel's theory to within a few percent, which unambiguously ruled out concurrent theories postulating total aether drag.

Many experiments of increasing precision were then undertaken to try to demonstrate the influence of Earth's motion on light propagation, but all gave null results. It soon became apparent that Fresnel's partial drag did not allow the measurement of any absolute motion of Earth to first order in v/c. In what would now be called a review paper,[11] Éleuthère Mascart concludes in 1874 (our translation): "the general conclusion of this memoir would be […] that the translation motion of the Earth is of no appreciable consequence on optical phenomena produced with terrestrial sources or solar light, that those phenomena do not allow to appreciate the *absolute* motion of a body and that only *relative* motions can be attained."

In 1881 Albert Michelson designed a new interferometer, which, according to existing theories, could detect Earth's displacement respective to aether because the expected effect was proportional to $(v/c)^2$. His first measurement was at most half of the expected fringe shift. He then improved the apparatus with Edward Morley. The two physicists gradually became convinced of a null result. In 1886 they decided to redo Fizeau's experiment—the only experiment with a positive result, and one that had yet to be reproduced. With a careful design of the hydraulics and an improved design for the interferometer,[12] they confirmed Fizeau's result, and Fresnel's aether drag, with much higher precision. However, in their celebrated experiment of 1887,[13] the measured shift was at most 0.01 fringe instead of an expected 0.4. The two experiments were thus incompatible according to existing theories, Fizeau's needing a partial drag and Michelson-Morley's needing a total drag of aether.

History then accelerated. In the late 1880 s, George Fitzgerald proposed the concept of length contraction. In 1895, Hendrick Lorentz published his theory of electromagnetic media, in which he derived Fresnel's formula from first principles. At the beginning of the 20th century, it became evident that time dilation was also necessary to account for all electromagnetic phenomena. After Albert Einstein published the theory of special relativity in 1905, Max Laue, in 1907, derived Fresnel's drag coefficient from the relativistic addition of velocities.[14] All experiments, being either of first (Fizeau) or second (Michelson-Morley) order in v/c, were then explained by a single theory with no need for an aether with such special properties.

In the relativistic framework, one can also account for the effects of dispersion, already predicted by Lorentz in 1895. Although the supplementary term makes only a few percent correction, Pieter Zeeman, in his 1914–1927 experiments, succeeded in measuring it.[15,16] More recently, this experiment was performed in liquids, solids, and gases using ring lasers[17] and confirmed the value of the dispersion term to within 15%.[18] Fizeau's experiment has also been successfully transposed to neutron matter waves.[19]

Thus, as may not be commonly understood, Fizeau's aether-drag experiment was a crucial turning point between old and modern conceptions of light and space-time. We believe this makes its replication particularly valuable from a pedagogical point of view.

III. THEORETICAL BACKGROUND

In this section, we recall the derivation of the phase difference $\Delta\varphi$ induced by the motion, with velocity v, of the medium of refractive index n in the interferometric arrangement shown in Fig. 2, which is essentially the one used by Michelson and Morley in 1886.[12] Let us consider first the case where water and monochromatic light of vacuum wavelength λ propagate in the same direction [shown as light gray (green online) in Fig. 2]. In the reference frame where water is at rest, the phase velocity of light is c/n. In the laboratory frame, using the relativistic composition of velocities, the phase velocity of light is

$$v_+ = \frac{c/n + v}{1 + (v/n)/c^2} = \frac{c/n + v}{1 + v/(nc)}. \tag{1}$$

The phase accumulated by light over the propagation distance of 2ℓ is thus

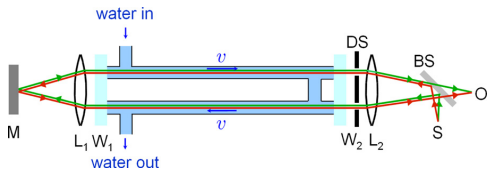

Fig. 1. (Color online) Sketch of the interferometer used by Fizeau (adapted from Michelson, Studies in Optics. Copyright © 1995 by Dover). For the sake of clarity, the two counter-propagating beams are drawn in different gray levels (colors). *S*: source; *O*: observer; *M*: mirror; W_i: windows; L_i: lenses; *BS*: beam splitter; *DS*: double slit.

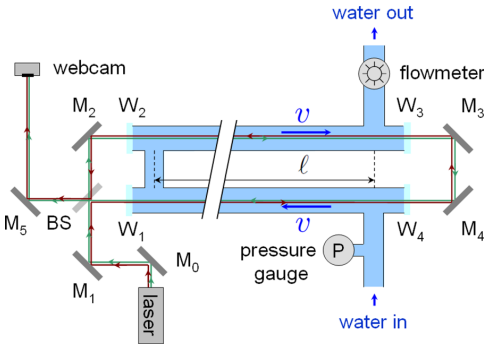

Fig. 2. (Color online) Sketch of the experimental setup (see text for details). M_i: mirror; W_i: windows; *BS*: beam splitter. The two counter-propagating beams are drawn in different gray levels (colors) for clarity.

$$\varphi_+ = \frac{2\pi c}{\lambda}\frac{2\ell}{v_+}. \tag{2}$$

Where light and water propagate in opposite directions [shown as dark gray in Fig. 2], the corresponding phase φ_- is obtained by replacing v by $-v$ in Eq. (1). The phase difference between the two arms of the interferometer thus reads

$$\Delta\varphi = \varphi_- - \varphi_+ \tag{3}$$

$$= 2\pi\frac{2\ell c}{\lambda}\left(\frac{1 - v/(nc)}{c/n - v} - \frac{1 + v/(nc)}{c/n + v}\right). \tag{4}$$

Expanding the above result to first order in v/c, we find

$$\Delta\varphi_{\text{rel.}} = 2\pi\frac{v}{c}\frac{4\ell}{\lambda}\left(n^2 - 1\right). \tag{5}$$

It is not difficult to perform the same calculation using the non-relativistic addition of velocities, i.e., by replacing $v_\pm$ by $c/n \pm v$. One then finds

$$\Delta\varphi_{\text{non-rel.}} = 2\pi\frac{v}{c}\frac{4\ell}{\lambda}n^2, \tag{6}$$

which has the same functional form except for a coefficient n^2 in place of $n^2 - 1$. In Fresnel's language, this would correspond to a complete aether-drag. The ratio of the predictions [Eqs. (6) and (5)] is about 2.3 for water ($n \simeq 1.33$) and approximately 1700 for air ($n \simeq 1.0003$), whence the interest in performing the experiment with air in addition to water (see Sec. V E).

As previously mentioned, the above derivation was first carried out by Laue in 1907[14] and is the one found in most textbooks. It has been pointed out[16] that such an approach is not strictly valid because the relativistic composition of velocities applies to point-like particles, and not to the phase velocity of waves. However, a more rigorous derivation, based on the Lorentz transformation of the four-vector $k^\mu = (\omega/c, \boldsymbol{k})$ associated with light, gives the same result provided the light and the medium propagate along the same axis.[16]

Up until now, we have neglected dispersion, i.e., the variation of the refractive index of the moving medium with the frequency of light ω. But the frequency of light in a moving frame is shifted by the Doppler effect. These shifts are opposite for the counterpropagating beams in the interferometer. They are then subjected to slightly different refraction indices due to dispersion. Taking this into account, the factor $n^2 - 1$ in Eq. (5) must to be replaced by[20]

$$n^2 - 1 + n\omega\frac{\mathrm{d}n}{\mathrm{d}\omega}. \tag{7}$$

Using the wavelength-dependent refractive index of water found in tables,[21] a simple calculation shows that for water at $\lambda = 532\,\text{nm}$, the fringe shift is actually 3.8% greater than what Eq. (5) predicts.

IV. EXPERIMENTAL SETUP: FIZEAU'S EXPERIMENT MADE EASY

A. Requirements

Fizeau's experiment was a real tour de force made possible by the very clever design of the experiment (see Fig. 1). The improvement by Michelson and Morley essentially transforms the original wavefront-division setup into a much brighter amplitude-division setup. In both arrangements, which we would now call Sagnac interferometers,[22] the two interfering beams follow almost exactly the same path (see Fig. 2). This not only doubles the interaction length with the moving medium, but more importantly, rejects common-mode phase fluctuations due, for example, to turbulence. This arrangement also ensures that the optical path length difference between the two interfering arms is zero when the interferometer is perfectly aligned.

Equation (5) shows that the expected fringe shift is enhanced by using a short wavelength λ and a large product ℓv. Let us estimate the requirements of the water velocity. We first set $\ell \sim 2\,\text{m}$ to make the size of the apparatus reasonable. Next, we choose $\lambda = 532\,\text{nm}$ to correspond to inexpensive diode-pumped solid-state lasers. We then see that achieving a phase shift on the order of 1 rad using water ($n \simeq 1.33$) requires velocities on the order of 4 m/s. The experimental setup thus requires that we can detect a phase shift of a fraction of a fringe and to produce a water flow of several meters per second.

The key to the success of the experiment is the care taken when setting up the plumbing. We thus describe in detail the various components of our experimental setup and refer the reader to the pictures shown in Fig. 3.

B. Hydraulics

For simplicity and to keep costs low, we built our system from standard piping materials available in any hardware store, and such that a regular tap can be used for the water source. Ideally, a large diameter d of the pipes is desirable because it simplifies the alignment of the interferometer beams and improves the velocity profile flatness over the beam section. However, the volumetric flow rate $Q = \pi d^2 v/4$ increases rapidly with d (for fixed v). The typical maximal flow rates available at the water outlets of a laboratory are on the order of 10–20 l/min. To achieve a velocity of $v \sim \text{m/s}$ thus requires $d \lesssim 10$ mm. Although using smaller-diameter pipes will lead to a higher flow velocity, it becomes impractical for the alignment of the laser beams and leads to increased head loss. The flow rate is, therefore, limited by the pressure available from the water distribution system. Unfortunately, the use of a pump to increase the inlet pressure is of little help because in the turbulent regime, which is relevant here, the flow rate increases only as the square root of the pressure (see Fig. 4 and Appendix B). In our experiment, we use 8-mm inner diameter copper tubing, allowing us to reach $v \sim \text{m/s}$.

The water pressure ΔP is varied using the tap valve and measured with a pressure gauge connected to the inlet port (see Fig. 2). We get a continuous measurement of the flow rate Q using a paddlewheel flowmeter[23] that delivers a square electric signal, whose frequency depends linearly on the flow rate. Flowmeter calibration, reported in the inset of Fig. 4, was realized by measuring the volumetric flow rate Q of water through the system with a graduated bucket and a stopwatch. We estimate the accuracy of our crude flow rate calibration to be on the order of 5%. With moderate effort, a calibration at the percent level or better could certainly be achieved. Note that the velocity $v_{\text{meas}} = 4Q/(\pi d^2)$ measured in this way is the mean velocity averaged over the radial velocity profile inside the pipes, and *not* the velocity v

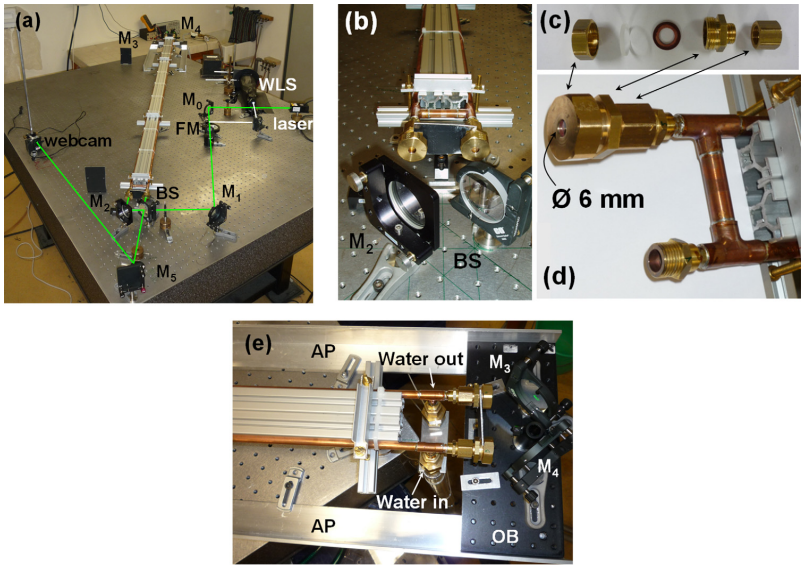

Fig. 3. (Color online) (a) General view of the experimental setup. WLS: white-light source; FM: flipping mirror. (b) Close-up of one end of the interferometer. (c) The various parts for connecting a window, from left to right: drilled brass BSP blank, BK7 25-mm diameter window, gasket, BSP reducer, BSP adapter. (d) Close-up of the interferometer end shown in (b), with one window disconnected. (e) The other end of the interferometer, showing the water connections and the optical breadboard (OB) supporting mirrors M_3 and M_4. AP: aluminum profiles.

appearing in Eq. (5) that occurs at the position of the beam. We will discuss this point in more detail below.

C. Mechanics

The two 2-m long copper pipes are relatively flexible and soft. Their straightness and parallelism are ensured by fastening them on a slotted, 30×60 mm^2 cross-section aluminum profile by means of cable ties [see Fig. 3(b)]. The T-shaped connections at their ends [see Figs. 3(d) and 3(e)] are made with low melting point tin solder and a heat gun. On the four ends where the windows need to be installed, male 3/8 in. British Standard Pipe (BSP) adapters are soldered.

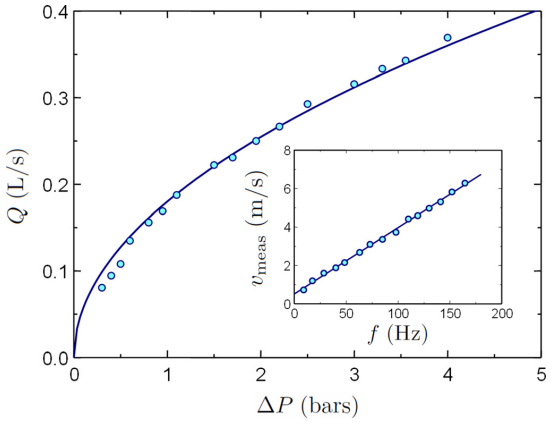

Fig. 4. (Color online) Flow rate Q through the apparatus as a function of the head loss ΔP. The solid line is a fit by the function $Q = a\sqrt{\Delta P}$ with a as an adjustable parameter; the best fit gives $a \simeq 0.18\,\mathrm{L}/(\mathrm{sbar}^{1/2})$. Inset: calibration curve of the flowmeter allowing one to infer the water speed v_{meas} from the frequency f of the signal it delivers. The solid line is the result of a linear fit.

The windows themselves are 3.3-mm thick, 25-mm diameter uncoated borosilicate glass substrates.[24] They are attached to the pipes via the system shown in Figs. 3(c) and 3(d). The window is pressed against a brass female 3/4 in. BSP cap at the center of which a 6-mm diameter hole is drilled. The inner threads were slightly altered with a lathe to fit the window outer diameter. The cap and window are then tightened with a fiber gasket onto a male–male BSP 3/4 in. to 3/8 in. adapter which is itself connected to the male BSP adapter soldered to the pipe via a female–female 3/8 in. BSP adapter.

The end with hoses connected to the water inlet and outlet in the laboratory sink is extended over the side of the table [see Fig. 3(e)]. Two L-shaped aluminum profiles mounted on the table support a small piece of optical breadboard on which we mount the two mirrors M_3 and M_4. In a preliminary set of experiments, we tried a configuration in which the water pipes were supported independently from the optical table (and thus from the interferometer) in order to avoid possible detrimental vibrations. However, this turned out to be cumbersome, and the much simpler solution of clamping the pipes tightly to the optical table, by means of four regularly spaced post-holders, does not yield any degradation of the measurements.

D. Optics and alignment

As a light source, we use an inexpensive diode-pumped, solid-state laser delivering a quasi-collimated beam with several milliwatts of light at $\lambda = 532$ nm.[25] The metallic mirrors (M_{0-4}) and the dielectric beamsplitter are all mounted on kinematic optical mounts. We found it convenient to draw the light path directly on the optical table [see Fig. 3(b)]

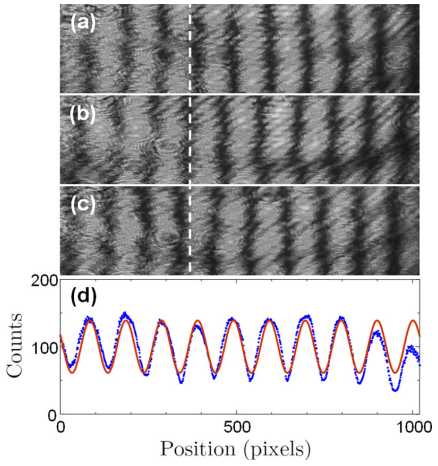

Fig. 5. (Color online) Sample images of the fringe pattern obtained from the camera for (a) $v = -5.7$ m/s, (b) $v = 0.8$ m/s, and (c) $v = 5.7$ m/s. The white dashed line shows the position x_0 of the central fringe for $v = 0$. (d) Processing of the image shown in (c)—the dots are the vertically integrated intensities and the (red) solid curve is the best fit to Eq. (8).

before mounting the mirrors and the beamsplitter, as this considerably simplifies the alignment of the interferometer.

To align the interferometer, we begin with four small diaphragms (diameter ~2 mm) positioned just in front of the centers of the windows W_{1-4}. The tubing system is then removed, and one walks the beam using M_1, BS, and M_2 so that beams W_1W_4 and W_2W_3 pass through the diaphragms. Using M_3 and/or M_4, one then aligns the returning beam onto the incoming one. After a few iterations, one obtains a quasi-perfect superposition of the beams and observes an almost flat intensity profile in the interference field. When tilting slightly one of the mirrors (e.g., M_3), nice straight parallel fringes appear.

Now the pipes can be repositioned and clamped onto the table. Water is set to flow, and one makes sure that no air bubbles are trapped inside the pipes, especially close to the windows where the diameter is larger. If so, they can be removed by loosening the cap while the water is flowing.

Instead of the expected fringe pattern, one usually observes caustics and diffuse reflections on the inner sides of the pipes. Indeed, due to the soldering, the parallelism of the windows cannot be ensured. When a beam strikes the window at a small angle from the normal, its path is slightly deviated. This deviation is only partially compensated at the inner glass/water interface, so the interferometer must be realigned. After a few iterations, the fringes return (see Fig. 5).

V. EXPERIMENTAL RESULTS

A. Data acquisition

For quantitative measurements of the fringe shift, we use an inexpensive webcam,[26] whose objective lens and IR filter have been removed in order to directly expose the CMOS detector chip to the fringe pattern. Using the micrometer screws of mirror M_2, for instance, the fringes are set parallel to one of the axes of the camera chip. From the webcam software, the gamma correction is adjusted to get a linear response of the detector.[27] The integration time and light intensity are adjusted to use the full dynamic range of the webcam, taking care not to saturate any pixels.

An important point for later data processing is that, prior to acquiring a series of images, one needs to locate the position of the central fringe on the camera. For this, it is convenient to wobble mirror M_2, for example. The fringe spacing varies, and the fringes move symmetrically away from the central one which is dark and does not move. Once the position x_0 of the central fringe has been located, the webcam is roughly centered on it to limit systematic errors due to changes in the fringe spacing. The fringe spacing is then adjusted to get about ten fringes on the detector chip. Too few fringes will not allow for an accurate measurement of the fringe position offset and period. On the other hand, if the fringes are too narrow, the resolution of the camera will limit accuracy.

B. Data processing

We process the images in the following way. We sum up the values of all pixels in a column, and thus obtain a one-dimensional intensity distribution $I(x)$, where x (in pixels) denotes the position along an axis perpendicular to the fringes (see Fig. 5). We then fit the data using

$$I(x) = I_0 + I_1 \sin\left(\frac{2\pi(x - x_0)}{\Lambda} + \Delta\varphi\right), \tag{8}$$

where I_0, I_1, Λ, and $\Delta\varphi$ are adjustable parameters, and x_0 is the (fixed) position of the central fringe, determined as explained above.

C. Experimental results with water

Acquisition and processing are repeated for various water velocities. Figure 6 shows the experimentally measured phase difference $\Delta\varphi$ as a function of the measured water velocity v_{meas}. The origin of phases has been chosen to vanish at zero velocity. As can be seen in the figure, we take five measurements for each velocity to improve the statistics and to get an estimate of the variance. Negative velocities were

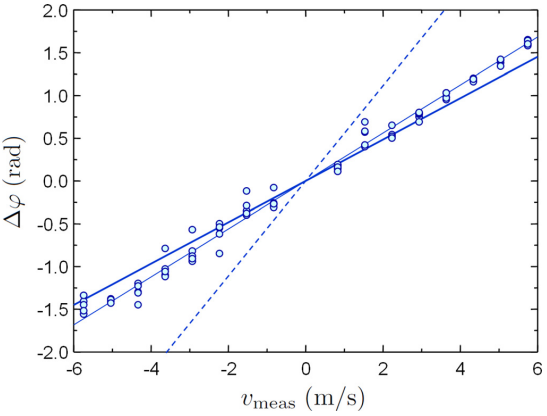

Fig. 6. (Color online) Experimental results using water as the moving medium. Circles: data; thin solid line: linear fit, giving a slope of 0.274 ± 0.003 rad s/m; thick solid line: relativistic prediction from Eq. (5); dashed line: non-relativistic prediction from Eq. (6).

obtained simply by exchanging the inlet and outlet ports of the tubing system. No data could be recorded for velocities below 1 m/s. Indeed, when the velocity is low, turbulence in the pipes is not fully developed, which leads to low spatial and temporal frequency fluctuations and very unstable pictures. We also could not take data for zero velocity because in this case the inlet or outlet valve must be closed; such a situation produces undue stress on the tubing system so that light can no longer properly exit the system. For this reason, the alignment procedure must be performed with water flowing in the pipes.

We observe a clear linear dependence of $\Delta\varphi$ on v_{meas}. A linear fit (thin solid line) gives a slope of 0.274 ± 0.003 rad s/m. The non-relativistic prediction of Eq. (6) (dashed line) has slope 0.563 rad s/m, which does not match the experimental results at all. The relativistic prediction given by Eq. (5) (thick solid line) has slope 0.248 rad s/m and is in much better agreement with the experimental data. However, there appears to be a slight systematic error in the data compared with the prediction. As stated earlier, this comes from the fact that we measure the mean velocity v_{meas} averaged over the velocity profile inside the pipes, whereas the velocity v appearing in Eq. (5) is the velocity at the position of the beam, i.e., on the axis of the pipes.

To understand how v_{meas} is related to v, let $v(r)$ denote the radial dependence of the velocity in the pipes of radius R and let $v_{\text{max}} = v(0)$. Because the beam is well centered on the pipe by construction, we can safely assume that $v = v_{\text{max}}$. We must therefore multiply the theoretical prediction by the correction factor

$$\frac{v_{\text{max}}}{v_{\text{meas}}} = \frac{\pi R^2 v_{\text{max}}}{\int_0^R 2\pi r v(r)\mathrm{d}r}. \tag{9}$$

A theoretical model for the radial dependence $v(r)$ is thus required. In the laminar regime (Poiseuille flow), $v(r)$ would have the parabolic shape shown as the dashed curve in Fig. 7, which, using Eq. (9), gives a correction factor equal to 2. However, for $v \gtrsim 1$ m/s, one can check that the Reynolds number $\mathrm{Re} = vd/\nu \gtrsim 10^4$, making the flow turbulent. Here, $\nu \sim 10^{-6}\mathrm{m}^2/\mathrm{s}$ denotes the kinematic viscosity of water. Under these conditions, there is no simple rigorous analytic expression for the velocity profile. However, for the range of Reynolds numbers used here, experimentally measured flow profiles are well reproduced[12] by the empirical law $v(r) = v_{\text{max}}(1 - r^2/R^2)^{1/6}$, corresponding to the much flatter velocity profile shown as the solid curve in Fig. 7. In the turbulent regime, Eq. (9) then gives a correction factor of 1.16. The relativistic prediction (5) multiplied by this correction factor, and including the 3.8% correction due to dispersion, yields a slope of 0.299 rad s/m (not shown in Fig. 6). The agreement between the experimental and theoretical values is thus at the level of 8%.

D. Discussion

Based on our data, we conclude that the non-relativistic prediction is clearly ruled out by our measurements. Nevertheless, the rather good agreement with the relativistic prediction must not be over interpreted. Indeed, it is difficult to put an accurate error bar on the result, as several systematic effects should be studied carefully for such a purpose. First, the systematic errors are dominated by our flowrate measurement. A more careful calibration should thus be performed in order to improve the accuracy. Second, the factor of 1.16 due to the shape of the velocity profile should be measured specifically for our system. A final source of uncertainty is the determination of the actual length ℓ appearing in Eq. (5). In practice, the flow makes a right-angle turn at each end of the pipes, so the velocity will presumably be affected up and downstream on length scales on the order of the pipe diameter d. This implies a correction of order d/ℓ (on the percent level), but again, an accurate estimation is difficult.

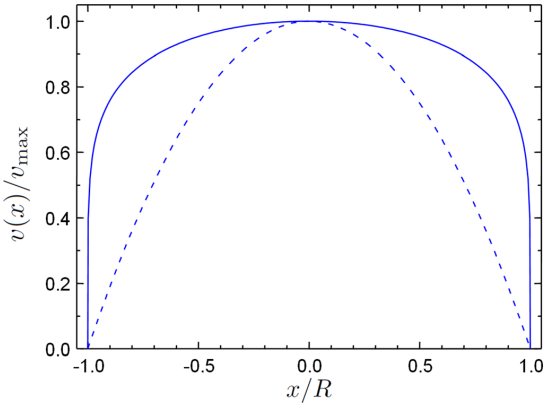

Fig. 7. (Color online) Dashed curve: Poiseuille's velocity profile for laminar flow given by $v(r) = v_{\text{max}}(1 - r^2/R^2)$. Solid curve: velocity profile for turbulent flow, modeled here by the empirical form $v(r) = v_{\text{max}}(1 - r^2/R^2)^{1/6}$.

In the end, due to a slight distortion of the tubing when the velocity (and thus the pressure) is varied, the fringe spacing changes by a small amount. As mentioned, an important feature of the Sagnac-like interferometric arrangement used here is that it operates at low interference order p. This is crucial in order to be sure that when the water is flowing inside the pipes, the observed shift of the fringes does arise from the aether drag effect and not from a slight change in the fringe spacing. As an example, let us assume that using a different interferometric setup, one observes an interference pattern with ten fringes, corresponding to interference orders, say $p_1 = 10^4$ to $p_2 = p_1 + 10$. If, as is likely, the fringe spacing changes by a quantity as small as 10^{-4} in relative value when the water velocity varies, one would observe that our ten fringes would shift, almost as a whole, by as much as one full fringe! For the data presented in the paper, we have measured that the fringe period Λ does not vary by more than 5% over the full range of velocities, yielding negligible errors due to the low interference orders used here.

E. Experimental results with air

In his original paper,[10] Fizeau states that he performed the experiment with air as a moving medium and that "the motion of the air does not produce any sensible displacement of the fringes," in agreement with the partial drag prediction (5). On the contrary, the non-relativistic prediction (6) predicts a measurable shift.

It is thus interesting to repeat the experiment using air instead of water. We do so by using a standard compressed air outlet, as available in most laboratories. One actually needs very moderate pressures in order to achieve relatively

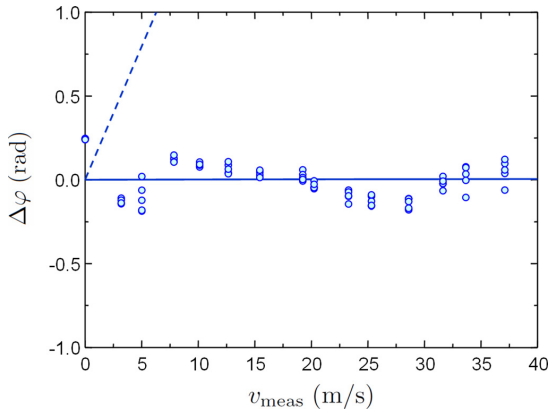

Fig. 8. (Color online) Experimental results using air as the moving medium. Circles: data; solid line: relativistic prediction from Eq. (5); dashed line: non-relativistic prediction from Eq. (6).

high velocities for the air flow in the 8-mm diameter pipes: only 0.2 bar typically yields $v_{\mathrm{meas}} \simeq 35\mathrm{m/s}$. Measuring the air velocity is not as straightforward as with water; we found it convenient to use a hot-wire anemometer[28] placed in a $D = 18$ mm inner-diameter pipe at the outlet of the $d = 8$ mm pipes. The velocity v_{meas} in the interaction region of the interferometer is then deduced from the measured velocity v_{anem} at the anemometer position via volumetric flow conservation $v_{\mathrm{meas}} = v_{\mathrm{anem}}(D/d)^2$. This assumes incompressible flow, which is valid since the air velocity is much smaller here than the speed of sound.[29]

Figure 8 shows the measured phase shifts (circles) along with the predictions of Eqs. (5) and (6). We cannot clearly identify the reason(s) behind the seemingly oscillatory behavior of the measured fringe shift with velocity. In any case, the non-relativistic prediction is clearly ruled out by the measurements, which are clearly compatible with the relativistic calculation.

VI. CONCLUSION AND OUTLOOK

Using rather modest equipment, we have shown that Fizeau's "aether-drag" experiment can be reproduced in the undergraduate laboratory at a quantitative level. It not only makes a nice practical introduction to the sometimes abstract concepts of special relativity but also constitutes an interesting application of several branches of experimental physics.

Immediate improvements of the setup described in this paper would consist of (i) calibrating the flowrate more carefully and (ii) increasing the stiffness of the tubing system. A natural extension of this work, suitable for a long-term student project, would consist of trying to study the systematic effects in detail—for example, the determination of the effective length ℓ. One way to measure this effect would be to start from the full pipe length and then repeat the experiment for shorter and shorter pipe lengths. The effect can then be evaluated by measuring the dependence of the slope $\Delta\varphi/v$ on the pipe length.

A more ambitious extension, suitable for advanced undergraduates, would illustrate more modern optical techniques. For instance, one may use a ring cavity of moderately high finesse (say $\mathcal{F} \sim 100$ –1000) and measure the variation of the resonance frequencies of the two counterpropagating modes when the velocity of the medium is varied. A gain in sensitivity by a factor $\mathcal{F}$ is then expected. Such techniques, with ultra-high finesse cavities, are currently used to measure, for example, non-reciprocity effects in the propagation of light with amazing sensitivities.[30]

ACKNOWLEDGMENTS

The authors thank Éric Desmeules for instigating this project and his students Mélodie Andrieu and Laurane Boulanger for help in setting up a preliminary version of the apparatus during their "TIPE" project (the data shown in Figs. 4 and 6 were essentially acquired by them). The authors thank Jacques Vigué for useful discussions. David Guéry-Odelin created the conditions that made this project possible. R.M. dedicates his contribution to José-Philippe Pérez for inspiring discussions over the years. Funding by CNRS is acknowledged.

APPENDIX A: USING A WHITE-LIGHT SOURCE INSTEAD OF A LASER

We have also performed this experiment using a white-light source instead of a laser. The source is a 1-mm diameter iris illuminated by a 55-W halogen lamp (the type used for car headlights) and a condenser lens. The resulting diverging beam is collimated by a 100-mm focal length lens and superimposed onto the path of the laser beam using two mirrors. The second mirror, located between M_0 and M_1, is a flipping mirror so that one can switch easily between the laser and the white light sources [see Fig. 3(a)]. Once the interferometer has been aligned with the laser, white-light fringes are readily observed. Naturally, if the iris is opened the luminosity is increased at the expense of spatial coherence, and the contrast in the picture is lost. The fringes are then localized in the vicinity of mirror M_3. A color image as in Fig. 9(a) is then recovered using a converging lens that conjugates M_3 and the detector plane.

The advantages of using a white source is that (i) the position of the dark central fringe can be found without ambiguity as the contrast of the colored fringes vanishes rapidly away from the zero path-length difference and (ii) compared to using a laser, unwanted interference fringes (due to scattering on dust particles for example) as well as speckle, are suppressed. There are,

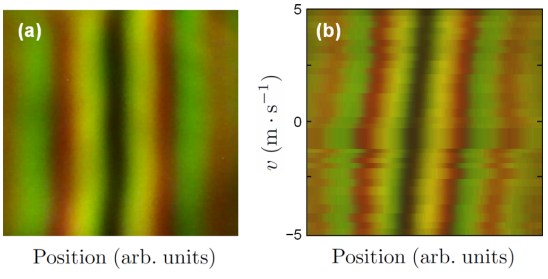

Fig. 9. (Color online) (a) A sample white-light fringe pattern. (b) Composite image of 22 fringe patterns obtained for different water velocities v. One clearly observes the linear shift of the central fringe position as a function of v.

however, a certain number of drawbacks. Besides the reduced luminosity, making quantitative comparisons with theory is obviously much more difficult than in the monochromatic case. Indeed, one would need to measure the light spectrum, as well as the wavelength-dependent reflectivity (including phaseshifts) introduced by the beamsplitter in order to model quantitatively the fringe pattern. For instance, we have observed that using a metallic beamsplitter instead of the dielectric one significantly alters the colors and the contrast of the fringe pattern obtained in white light.

We made a composite of 22 images taken for various water velocities v. The result, shown in Fig. 9(b), clearly shows that the fringe positions shift linearly with velocity. However, a quantitative analysis of such an image is not easy, and the motivation behind this figure is mainly for aesthetics.

APPENDIX B: TURBULENT HEAD LOSS IN A CIRCULAR PIPE: DIMENSIONAL ANALYSIS APPROACH

In the standard introductory physics curriculum, the computation of the head loss in a circular pipe is done using Poiseuille's equation, valid for laminar flow. It is much less common to present the case of turbulent flow to undergraduate students. Reference to the Moody diagram, giving the so-called *friction factor* as a function of Reynolds number and pipe roughness, can be found in engineering-oriented textbooks, but may appear as quite involved to beginning physics students. In this appendix, we show how dimensional analysis can be used to infer a plausible expression for the turbulent head loss, at least for its dependence on flow rate and pipe diameter, two parameters that are crucial for the design of our experimental setup.

We consider the head loss ΔP for the flow of a fluid of density ρ and kinematic viscosity ν in a circular pipe of diameter d and length l, flowing with a volumetric flow rate Q. Let us make two assumptions. First, for an infinitely long pipe, only the pressure gradient $\Delta P/l$ is physically relevant. And second, the limit of very large Reynolds number corresponds formally to the limit $\nu \to 0$. In this case, the viscosity ν should not appear explicitly in the expression for the head loss. Under these conditions, we expect the functional form for the head loss to be

$$\frac{\Delta P}{l} = A\rho^{\alpha}Q^{\beta}D^{\gamma}, \tag{B1}$$

where A is a dimensionless constant and (α, β, γ) the exponents to be determined. Equating the dimensions on both sides of this equation yields three equations for the exponents, which can be solved to give

$$\frac{\Delta P}{l} = A\frac{\rho Q^2}{D^5}. \tag{B2}$$

This expression agrees well with empirical formulae used in an engineering context if one chooses $A \sim 3 \times 10^{-2}$, and this is typically what one would find using the friction factor obtained in a Moody diagram[31,32] for our Reynolds numbers. For example, the value of the coefficient a obtained when fitting the flow rate data of Fig. 4 yields $A \simeq 2.5 \times 10^{-2}$, in good agreement with the previous estimate.

[1]E. F. Taylor and J. A. Wheeler, *Spacetime Physics: Introduction to Special Relativity*, 2nd ed. (W. H. Freeman & Company, New York, 1992).
[2]R. S. Shankland, "Conversations with Albert Einstein," Am. J. Phys. **31**, 47–57 (1963).
[3]For a detailed account, see O. Darrigol, "The genesis of the Theory of Relativity," Séminaire Poincaré, **1**, 1–22 (2005), available online at www.bourbaphy.fr/darrigol2.pdf, and references therein.
[4]O. Römer, "Démonstration touchant le mouvement de la lumière trouvé par M. Romer de l'Académie Royale des Sciences," J. des Sçavans, 233–236 (1676). An English translation appeared quickly in Philos. Trans. **12**, 893–894 (1677), available online at http://dx.doi.org/10.1098/rstl.1677.0024.
[5]Arago gave an account of the results to the French Academy of Sciences, but the text was not published until 1853, in F. Arago, "Mémoire sur la vitesse de la lumière," C. R. Acad. Sci. **36**, 38–49 (1853), available online at http://gallica.bnf.fr/ark:/12148/bpt6k2993z/f42.image.
[6]For a modern account see R. Ferraro and D. M. Sforza, "Arago (1810): The first experimental result against the ether," Eur. J. Phys. **26**, 195–204 (2005).
[7]A. Fresnel, "Lettre de M. Fresnel à M. Arago, sur l'influence du mouvement terrestre dans quelques phénomènes d'optique," Ann. Chim. Phys. **9**, 57–66 (1818), available online at http://www.google.com/books?id=nZc5AAAAcAAJ.
[8]L. Foucault, *Sur les vitesses relatives de la lumière dans l'air et dans l'eau* (Bachelier, Paris, 1853), available online at http://www.bibnum.education.fr/files/foucault-texte.pdf.
[9]A. A. Michelson, *Studies in Optics* (Dover, New York, 1995).
[10]H. Fizeau, "Sur les hypothèses relatives à l'éther lumineux, et sur une expérience qui paraît démontrer que le mouvement des corps change la vitesse avec laquelle la lumière se propage dans leur intérieur," C. R. Acad. Sci. **33**, 349–355 (1851); translated into English in H. Fizeau, "On the effect of the motion of a body upon the velocity with which it is traversed by light," Philos. Mag. 4th series **2**, 568–571 (1851). A longer account, with the same title, was published in H. Fizeau, Ann. Chim. Phys. **57**, 385–404 (1859), and translated in H. Fizeau, Philos. Mag. 4 th series **19**, 245–260 (1860).
[11]É. Mascart, "Sur les modifications qu'éprouve la lumière par suite du mouvement de la source lumineuse et du mouvement de l'observateur," Ann. Sci. Ec. Normale Super. (2 nd series) **3**, 363–420 (1874), available online at http://www.numdam.org/numdam-bin/feuilleter?j=asens.
[12]A. A. Michelson and E. W. Morley, "Influence of Motion of the Medium on the Velocity of Light," Am. J. Sci. **31**, 377–386 (1886).
[13]A. A. Michelson and W. Morley, "On the relative motion of the Earth and the luminiferous ether," Am. J. Sci. **34**, 333–345 (1887).
[14]M. Laue, "Die Mitführung des Lichtes durch bewegte Körper nach dem Relativitätsprinzip," Ann. Phys. **328**, 989–990 (1907).
[15]P. Zeeman, "Fresnel's coefficient for light of different colors (first part)," Proc. Roy. Acad. Sci. Amsterdam **17**, 445–451 (1914); "Fresnel's coefficient for light of different colours (second part)," *ibid.* **18**, 398–408 (1915). This experiment was recently revisited by Lerche who claims, on the basis of ignored systematic effects, that Zeeman's experiments are inconclusive.[16]
[16]I. Lerche, "The Fizeau effect: Theory, experiment, and Zeeman's measurements," Am. J. Phys. **45**, 1154–1164 (1977).
[17]W. M. Macek, J. R. Schneider, and R. M. Salamon, "Measurement of Fresnel Drag with the Ring Laser," J. Appl. Phys. **35**, 2556–2557 (1964).
[18]H. R. Bilger and A. T. Zavodny, "Fresnel Drag in a Ring Laser: Measurement of the Dispersive Term," Phys. Rev. A **5**, 591–599 (1972).
[19]A. Klein et al., "Neutron Propagation in Moving Matter: The Fizeau Experiment with Massive Particles," Phys. Rev. Lett. **46**, 1551–1554 (1981).
[20]J. D. Jackson, *Classical Electrodynamics*, 3rd ed. (Wiley, New-York, 1998), chap. 11.
[21]P. Schiebener, J. Straub, J. M. H. Levelt Sengers, and J. S. Gallagher, "Refractive index of water and steam as function of wavelength, temperature and density," J. Phys. Chem. Ref. Data **19**, 677–717 (1990).
[22]E. Hecht, *Optics*, 4th ed. (Addison-Wesley, San Franciso, 2002), pp. 412–413.
[23]Gems sensors rotoflow 155421 BSPP-RS.
[24]Edmund Optics, model 43892.
[25]Shangai Dream Lasers SDL-532-005T.
[26]Philips SPZ5000 webcam.
[27]This linearity can be checked by using a powermeter (or a calibrated photodiode) and a set of neutral density filters to attenuate the laser beam.

One then readily verifies that for a proper setting of the webcam's *gamma*, the pixel counts are proportional to the light intensity on the detector.

[28]Testo 425 hot-wire anemometer.

[29]Corrections due to the compressibility of air are on the order of $(v/v_s)^2$, where v is the flow velocity and $v_s \simeq 340$ m/s the speed of sound in air. For our parameters, compressibility thus amounts to an error of about 1% at most, and is completely negligible with respect to other sources of uncertainty.

[30]B. Pelle, H. Bitard, G. Bailly, and C. Robilliard, "Magnetoelectric directional nonreciprocity in gas-phase molecular nitrogen," Phys. Rev. Lett. **106**, 193003 (2011).

[31]É. Guyon, J.-P. Hulin, L. Petit, C. D. Mitescu, *Physical Hydrodynamics* (Oxford U.P., Oxford, 2001).

[32]T. E. Faber, *Fluid Dynamics for Physicists* (Cambridge U.P., Cambridge, 1995).

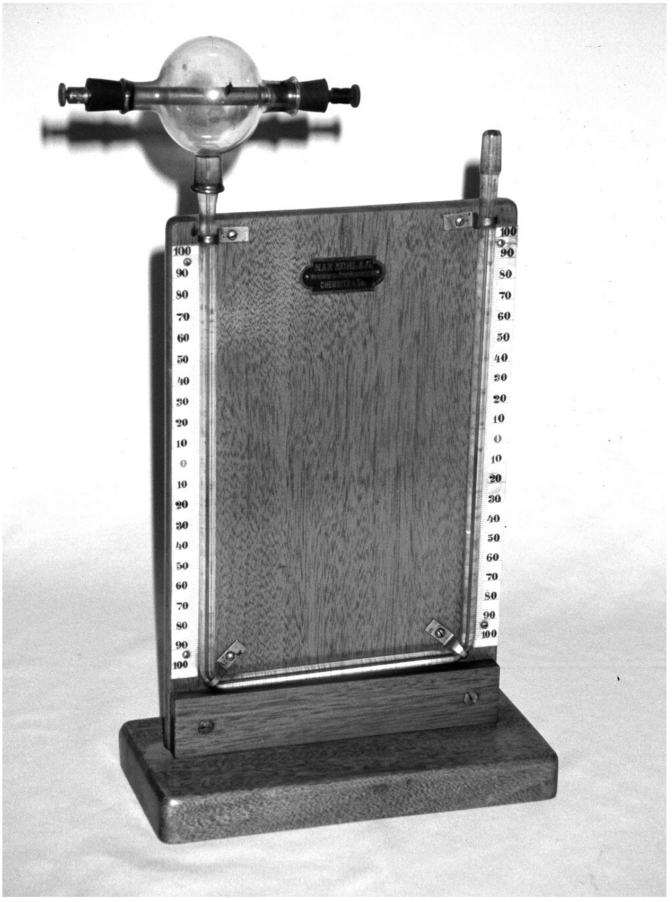

Heating Effects of an Electric Current. This piece of apparatus is at Case Western Reserve University in Cleveland, Ohio, and was made by Max Kohl of Chemnitz, Germany. It was used to demonstrate the heating effects of the electric current that passed through the conductor in the sealed glass bulb. The air in the bulb expanded, thus pushing the oil in the manometer down on the left-hand side. (Notes and photograph by Thomas B. Greenslade, Jr., Kenyon College)

IOP PUBLISHING EUROPEAN JOURNAL OF PHYSICS

Eur. J. Phys. **33** (2012) 1167–1178 doi:10.1088/0143-0807/33/5/1167

Measuring the eccentricity of the Earth's orbit with a nail and a piece of plywood

Thierry Lahaye[1]

Laboratoire Collisions Agrégats Réactivité, Université de Toulouse, UPS, IRSAMC, F-31062 Toulouse, France
CNRS, UMR 5589, F-31062 Toulouse, France

E-mail: thierry.lahaye@institutoptique.fr

Received 17 April 2012
Published 3 July 2012
Online at stacks.iop.org/EJP/33/1167

Abstract

I describe how to obtain a rather good experimental determination of the eccentricity of the Earth's orbit, as well as the obliquity of the Earth's rotation axis, by measuring, over the course of a year, the elevation of the Sun as a function of time during a day. With a very simple 'instrument' consisting of an elementary sundial, first-year students can carry out an appealing measurement programme, learn important concepts in experimental physics, see concrete applications of kinematics and changes of reference frames, and benefit from a hands-on introduction to astronomy.

(Some figures may appear in colour only in the online journal)

1. Introduction

One of the cornerstones of introductory courses in classical mechanics is the derivation of Kepler's laws. In particular, the derivation of Kepler's first law, stating that the trajectory of a planet is an ellipse with the Sun located at one of the foci, is an important application of Newton's laws to a multidimensional problem. However, very few students are aware of the fact that the eccentricities of the planets of the solar system are actually quite small, with trajectories very close to a circle, which makes Kepler's achievement (based on Tycho Brahe's measurements) even more remarkable.

Here, I describe a simple measurement programme, suitable for first-year university students, consisting in measuring the elevation of the Sun as a function of time during a day, and in repeating this typically once a week over a full year. By measuring the maximal elevation $h_{\max}$ of the Sun, and the time $t_{\max}$ at which this maximum occurs (i.e. the *true local noon*), students can readily check that these quantities vary a lot over the year. The change in

[1] Present address: Laboratoire Charles Fabry, CNRS UMR 8501, Institut d'Optique, F-91127 Palaiseau cedex, France.

0143-0807/12/051167+12$33.00

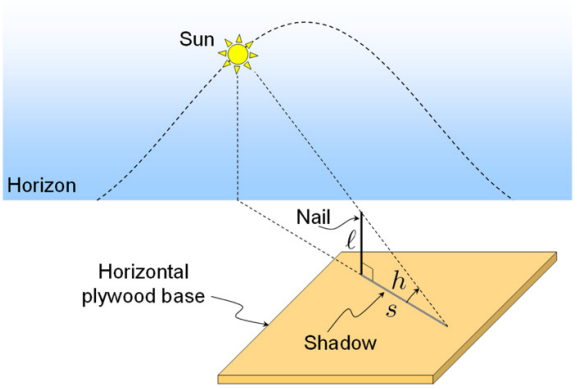

Figure 1. Schematic view of the elementary sundial.

$h_{\max}$ is essentially related to the obliquity ε of the Earth over the ecliptic, and thus allows for quite an accurate determination of ε (as well as that of the latitude of observation). The change of $t_{\max}$ over a year gives an experimental determination of the *equation of time* $E(t)$, i.e. the difference between the mean local noon and the true local noon, and allows for a determination of the eccentricity e of the Earth's orbit [1]. This is a rewarding result for students to realize that with such simple measurements, they can obtain good experimental values for the above quantities, and that with careful observations one can perform 'science without instruments' as did the astronomers of various antique civilizations [2, 3].

I have organized this paper as follows. I first describe how to measure in a simple way the elevation of the Sun versus time over a day, with an accuracy of about 1°. Then I give the results I obtained for $h_{\max}(t)$ and $E(t)$ by repeating the measurement about once a week for one year, starting in August 2010. I show how one can extract the obliquity ε of the Earth's axis and the eccentricity e of its orbit by fitting the experimental data with simple, analytic expressions. Finally, possible extensions of the work are proposed. Appendix A contains a brief reminder on basic notions of spherical astronomy, and should be read first by readers not familiar with these notions. In the remaining appendices, the derivation of the analytic expressions used for fitting the data is given, so that the paper is self-contained.

2. Measurements

We are interested in studying the motion of the Earth around the Sun. Using the relativity of motion, we can thus simply measure the apparent motion of the Sun on the celestial sphere, i.e. the time dependence of two angles that define the position of the Sun in the sky.

As we shall see, for our purpose, it is sufficient to measure the elevation of the Sun (also called *altitude*, or *height*) above the horizon, i.e. the angle h shown in figure 1. This can be done very simply by measuring the length s of the shadow of a vertical *gnomon* (i.e. a rod with a sharp point) of length ℓ. Then the elevation of the Sun is given by $h = \arctan(\ell/s)$.

Contrary to the case where one would measure also the azimuthal position of the Sun, here, the orientation of the horizontal base does not need to be fixed. One of the advantages of

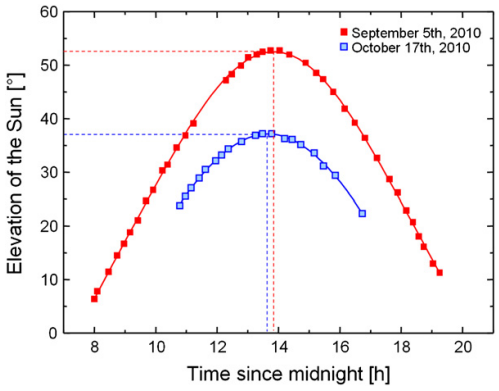

Figure 2. Measured elevation of the Sun over the course of a day, for two different dates. The solid lines are fits by a polynomial (see the text). The dashed lines display the values of $h_{\max}$ and $t_{\max}$.

using such a simple setup is therefore that one can change the position of the sundial over the course of the day, e.g. in order to operate indoor.

2.1. Construction and use of an elementary sundial

In practice, I used as a gnomon a steel nail protruding from a plywood base of size $20 \times 20\ \mathrm{cm}^2$. In order to have the nail as orthogonal to the base as possible, a hole with a diameter slightly less than that of the nail was first drilled into the plate using a drill press. The nail I used had a length $\ell = 69$ mm above the plate. To measure h, one simply installs this elementary sundial on a horizontal surface in the sunlight, and measures with a ruler the length of the shadow. Two effects limit the accuracy of the measurement: first, due to the finite angular diameter of the Sun, the shadow is slightly blurred; second, the horizontality of the base when installed on the floor of a room, or on a table, is not perfect[2]. In practice, an accuracy of typically one degree is easily obtained. (This can be estimated quantitatively by repeating the measurement several times with the sundial in different positions, in a short interval over which h barely varies, and observing the dispersion of the results.)

Concerning the determination of the time t at which $h(t)$ is measured, an accuracy of 1 min is sufficient for our purpose, and thus a simple wristwatch can be used. However, it is wise to check that the watch indicates the correct time before starting a series of measurements. Nowadays, this can be done very easily using the websites of national time agencies[3] that give access to the legal time with an accuracy of 1 s or better.

2.2. Measuring the altitude of the Sun over a day

Figure 2 shows two measurements of $h(t)$, where t is the legal time, performed in Toulouse, France (latitude $\varphi = 43.60^\circ$ N, longitude $\lambda = 1.45^\circ$ E) at two different dates. It is very clear from the data that the maximal height $h_{\max}$ of the Sun depends on the date; this is in general well known as it is related to the cycle of seasons.

[2] This could be improved easily, e.g. by using bubble levels to adjust the horizontality of the base.
[3] See for instance, www.time.gov in the US or www.syrte.fr in France.

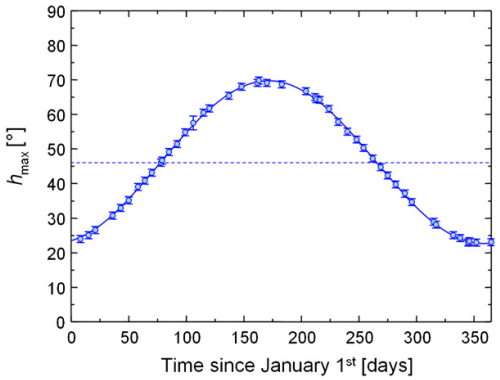

Figure 3. Measured maximal elevation of the Sun (points with error bars). We observe a sinusoidal variation around $\pi/2 - \varphi$, with an amplitude of 2ε. The solid line is a fit to the simple model discussed in the text.

However, what appears also clearly in figure 2 is that the time t_{max} at which this maximum occurs also depends on the date; this however is not widely known by students, nor even by some physicists, probably because the effect is relatively small (a few minutes) though perfectly measurable even with our crude setup.

In order to proceed, we need to extract from $h(t)$ the two quantities h_{max} and t_{max}. The theoretical expression of $h(t)$ is derived in appendix B; however, we can at this stage keep an empiric approach and just fit the data with a simple function. As $h(t)$ is symmetric about $t = t_{max}$ (provided one neglects the motion of the Sun with respect to the fixed stars over a few hours, which is reasonable given the accuracy of our measurements), I chose to fit the data with the following polynomial:

$$h(t) = h_{max} + \sum_{i=1}^{3} h_{2i}(t - t_{max})^{2i}, \tag{1}$$

where the five adjustable parameters are h_{max}, t_{max} and the coefficients $h_{2,4,6}$. I chose to go up to sixth order in order to get a nicer fit at small elevations (in the mornings and evenings), but if the data are taken only for a few hours around t_{max} (± 3 to 4 h around t_{max} are enough to determine the quantities of interest), one can use only a fourth-order polynomial without affecting the results. Such fits are shown as solid lines in figure 2. The accuracy in the determination of h_{max} and t_{max} obviously depends on the number of measurement points; for the data presented in figure 2, they are respectively of about 0.2° and 1 min, as data points were collected for several hours before and after t_{max}, at a rate of four points per hour typically. When the weather is partly cloudy, one sometimes has to stop taking data for a while, and the accuracy in the determination of h_{max} and t_{max} is thus not as good.

2.3. Annual variation of h_{max}: determination of φ and ε

By repeating the above measurements typically once per week for a year, the annual variations of h_{max} and t_{max} can be obtained. Figure 3 shows the maximal elevation h_{max} of the Sun as a function of time. One observes a quasi-sinusoidal variation with a period of one year.

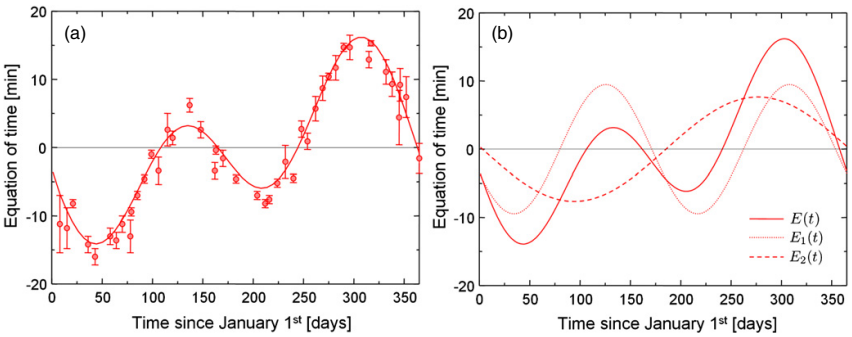

Figure 4. (a) Measured equation of time E (points with error bars). The solid line is a fit to the simple model of the equation of time given in the appendix. (b) Combining the effects of the Earth's obliquity ($E_1(t)$, dotted line) and of the eccentricity of the Earth's orbit ($E_2(t)$, dashed line) gives the full expression of the equation of time $E(t)$ (solid line).

The qualitative explanation for this phenomenon is simple, and is usually part of geography courses in elementary education, but I repeat it here for completeness. Due to the obliquity ε of the Earth's rotation axis, the angle between the Earth's axis and the line joining the centre of the Earth to the Sun varies between $\pi/2-\varepsilon$ (at the summer solstice, when the Earth's axis leans towards the Sun) and $\pi/2+\varepsilon$ (at the winter solstice). Correspondingly, the angular distance between the Sun and the celestial pole varies with a period of one year and an amplitude of ε. This induces a similar variation of $h_{\max}$, around a mean value which depends on the observer's latitude. For a quantitative treatment, the reader is referred to appendix C.

2.4. Annual variation of $t_{\max}$: determination of e

We now turn to a more subtle measurement concerning the variation of $t_{\max}$, which defines the true local noon. It is convenient to convert the measured values into a quantity called the *equation of time*, that we shall denote by E, defined as the difference between the mean local noon and the true local noon (our measured $t_{\max}$). The former is obtained from the legal noon, given by clocks (corrected if necessary by 1 h in summer due to daylight saving time) by adding (subtracting) 4 min for each degree of longitude west (east) from the reference meridian of the corresponding time zone. For instance, in Toulouse (longitude $\lambda = 1.45^\circ$ E), one needs to subtract $t_{\max}$ from 13.00 h in winter time and 14.00 h in summer time, and then subtract another 5.8 min to correct for the longitude, to obtain the equation of time E. For instance, on 17 October (see figure 2), we have $t_{\max} = 13.66$ h, thus giving $E = 60(14 - 13.66) - 5.8 = 14.6$ min.

Figure 4 gives the results obtained by measuring $E(t)$ over a year. One observes a non-trivial behaviour, the equation of time varying between a maximum of about 16 min in autumn and a minimum of about -15 min in winter, and vanishing at four different dates.

Physically, the origin of the equation of time lies in the fact that the duration of the true solar day, i.e. the time elapsed between two successive transits of the Sun across the observer's meridian, is not constant over a year. The solar day would have a constant duration if, along the year, the Sun moved on the celestial sphere (i) at constant angular velocity and (ii) along the celestial equator (this defines the so-called *mean Sun*; the time between two transits of the mean Sun defines the mean solar day of 86 400 s). However, these two assumptions are both

wrong: since the Sun moves along the ecliptic, which is inclined with respect to the equator due to the obliquity ε of the Earth's axis, the motion of its projection on the equator is irregular. (It coincides with the mean Sun at the time of the equinox, then lags behind the mean Sun for a quarter of the year, catches up at the solstice and then is ahead of the mean Sun for another three months.) This contribution E_1 to the equation of time thus has a six month period. Moreover, via Kepler's second law of areal velocity (see appendix D) the angular velocity of the apparent motion of the Sun is not constant over the year due to the fact that the Earth's orbit is not circular: for instance, when the Earth–Sun distance is smaller (in January), the Sun moves faster along the ecliptic. This contribution E_2 to $E(t)$ has obviously a one-year period. Combining these two contributions explains the temporal variation of the equation of time (see figure 4(b); appendix D gives the derivation of the analytical expressions of E_1 and E_2).

3. Exploiting the data

3.1. Obliquity of the Earth

It is easy to show (see appendix C) that to a very good approximation, one has

$$h_{\max} = \frac{\pi}{2} - \varphi + \varepsilon \sin\left(\frac{2\pi}{T}(t - t_0)\right), \tag{2}$$

where φ is the latitude of the place of observation, ε is the obliquity of the Earth's axis, T is the duration of the year and t_0 is the date of the vernal equinox. When fitting the data by equation (2) with the four previous quantities as adjustable parameters, we obtain

$$\begin{cases} \varphi = 43.8 \pm 0.2^\circ, \\ \varepsilon = 23.5 \pm 0.1^\circ, \\ T = 374 \pm 6 \text{ d}, \\ t_0 = 78 \pm 1 \text{ d}, \text{ i.e. 19 March}, \end{cases} \tag{3}$$

which is close to the accepted values (respectively, 43.60°, 23.44°, 365.25 d and 20 March.) Note that by repeating the measurements over the course of several years, a much more accurate determination of the duration T of the year could be achieved.

3.2. Eccentricity of the Earth's orbit

We show in appendix D that a good approximation of the equation of time is given by

$$E(t) = \frac{d}{2\pi}\left[\frac{1 - \cos\varepsilon}{2} \sin\left(\frac{4\pi}{T}(t - t_0)\right) - 2e \sin\left(\frac{2\pi}{T}(t - t_1)\right)\right] \tag{4}$$

where d is the duration of a day (i.e. 1440 min), e is the eccentricity of the Earth's orbit and t_1 is the date of perihelion passage.

Fitting the data shown in figure 4 by equation (4) with e and t_1 as adjustable parameters (and using the values determined above for ε, T and t_0), we obtain

$$\begin{cases} e = 0.017 \pm 0.001, \\ t_1 = 1 \pm 5 \text{ d}, \text{ i.e. 1 January}, \end{cases} \tag{5}$$

again in relatively good agreement with the values $e = 0.0167$ and $t_1 = 3$ d found in the literature.

4. Conclusion and outlook

I have shown that with very modest equipment, one can measure with reasonable accuracy some of the orbital elements of the Earth, and in particular its eccentricity, despite its relatively

small value. The above measurements can be the basis of further activities for students. Among them, one can list the following ones, given here under the form of exercises:

- Use equation (B.4) of appendix B to calculate the length of daytime as a function of the latitude along the year and compare it to the one obtained from the ephemerides given in calendars.
- Show that the duration of a solar day is $(1 + \mathrm{d}E/\mathrm{d}t) \times 86\,400$ s. What are its minimal and maximal values?
- Using a sundial with a fixed base, check experimentally that the azimuthal position of the Sun when it reaches its highest elevation is always the same (i.e. South) throughout the year[4].
- Still with a fixed-base sundial, plot experimentally the curve traced out over the year by the end of the shadow at the *mean* local noon. This eight-shaped curve is called an *analema* and is sometimes encountered on sundials in order to allow for a computation of the legal time from the measured solar time.

Acknowledgments

I thank Maxime Lahaye and Irina Lahaye for help in taking the data, Giovanni Luca Gattobigio for discussions, and Lucas Béguin, Antoine Browaeys and Renaud Mathevet for useful suggestions that helped me improve the manuscript.

Appendix A. A quick reminder on spherical astronomy

This section consists in a minimalist reminder about basic terms and notions of spherical astronomy needed for the understanding of the paper. The reader is referred to the first sections of [2] for a similar but more exhaustive reminder. A very detailed and accessible introduction to spherical astronomy can be found online in the celestial mechanics lecture notes of [4], or in standard textbooks about spherical astronomy [5].

To an Earth-bound observer O (that we assume, for definiteness, located in the northern hemisphere), celestial bodies appear to move on a sphere centred on himself, the *celestial sphere* (figure A1(a)). The local vertical points towards the *zenith* Z; the great circle perpendicular to the vertical is the *horizon*. Over a day, 'fixed' stars appear to rotate around the *north celestial pole* P (close to the star *Polaris*). The great circle going through Z and P crosses the horizon in two points defining the South S and the North N; the two other cardinal points on the horizon (East E and West W) are deduced from S and N by a 90° rotation around the vertical axis.

The position of celestial bodies can be specified in spherical coordinates by two angles, once a reference system has been chosen. Two reference systems are particularly useful: the *horizon system*, in which measurements are made in practice, and which is dependent on the observer's location on Earth, and the *equatorial system*, which is defined by the directions of 'fixed' stars.

- In the horizon system (figure A1(b)), the local vertical, pointing towards the *zenith*, is chosen as the z-axis. The position of a point on the celestial sphere is specified using the

[4] Note that with a fixed-base sundial, the determination of the equation of time can be much more accurate than with the method used in this paper. Indeed, in that case one needs to determine the time $t_{\max}$ at which the solar azimuth $\psi_\odot$ vanishes (i.e. when the Sun is South and crosses the observer's meridian), which can be done with a high precision as it varies linearly in time: the determination of such a zero-crossing is much more accurate than that of the position of a maximum.

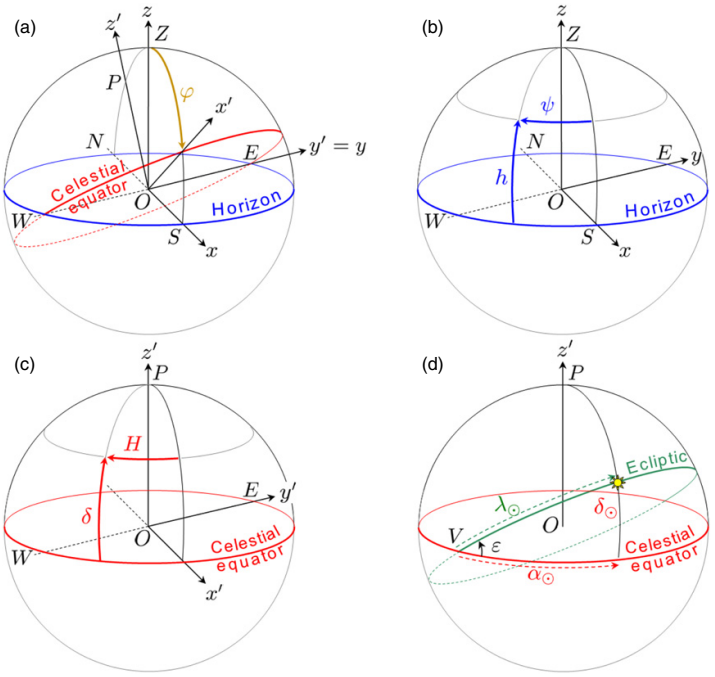

Figure A1. Geometry of the celestial sphere. (a) Important points, axes and circles on the celestial sphere. (b) Definition of the coordinates in the horizon system. (c) Definition of the coordinates in the equatorial system. (d) Definition of the coordinates of the Sun ⊙ in the equatorial system during its motion along the ecliptic.

altitude (or *elevation*) h (angle between the radius vector of the point and the horizon), and the *azimuth* ψ, counted along the horizon, starting from the South and counted positive towards the West (note that other conventions exist for the choice of the azimuth origin).

- In the equatorial system (figure A1(c)), OP is chosen as the polar axis. The intersection of the plane perpendicular to OP with the celestial sphere defines the *celestial equator*. The position of a point on the celestial sphere is given by the declination δ (angle from the celestial equator to the body) and the *hour angle* H (counted along the celestial equator, from the south to the equatorial projection of the body).

The equatorial system is obtained by rotating the horizon system around OE by an angle $\pi/2 - \varphi$, where φ is the (geographical) latitude of the point of observation; for instance, at the North pole ($\varphi = \pi/2$) the equatorial and horizon systems coincide.

Finally, the *ecliptic* is the great circle along which the apparent annual motion of the Sun (traditionally denoted by the astronomical symbol ⊙) takes place on the celestial sphere. It is inclined on the celestial equator by the obliquity ε of the Earth's axis.

The angular position of the Sun along the ecliptic is given by the ecliptic longitude $\lambda_\odot$, whose origin is taken at the vernal point V (the point where the ecliptic crosses the celestial equator, and where the Sun is located at the time of the spring equinox in the Northern

hemisphere). The angular distance on the celestial equator between V and the projection of the Sun on the equator is the Sun's *right ascension* $\alpha_\odot$.

Appendix B. Expression of $h(t)$ over a day

From the definitions given above, in the equatorial coordinate system (x', y', z'), the coordinates of the Sun read

$$S' = \begin{pmatrix} x' = \cos\delta\ \cos H \\ y' = -\cos\delta\ \sin H \\ z' = \sin\delta \end{pmatrix}, \tag{B.1}$$

with δ being the declination and H the hour angle of the Sun. In the horizon system (x, y, z), they read

$$S = \begin{pmatrix} x = \cos h\ \cos\psi \\ y = -\cos h\ \sin\psi \\ z = \sin h \end{pmatrix}, \tag{B.2}$$

where h is the altitude of the Sun and ψ is its azimuth. Since the equatorial system is deduced from the horizon system by a rotation of angle $\pi/2 - \varphi$ around the $(Oy) = (Oy')$ axis, the (x, y, z) coordinates are obtained by multiplying the (x', y', z') ones by the following rotation matrix:

$$R = \begin{pmatrix} \sin\varphi & 0 & -\cos\varphi \\ 0 & 1 & 0 \\ \cos\varphi & 0 & \sin\varphi \end{pmatrix}. \tag{B.3}$$

From the last component of the relation $S = RS'$ we obtain

$$\sin h = \cos\varphi\ \cos\delta\ \cos H + \sin\varphi\ \sin\delta \tag{B.4}$$

which gives the elevation of the Sun as a function of time (i.e. the hour angle H) for the given location and declination of the Sun.

Appendix C. A simple model for $h_{\max}(t)$

From equation (B.4) above, we find immediately that the elevation of the Sun becomes maximal when $\cos H = 1$ and reaches the value $h_{\max}$ fulfilling

$$\sin h_{\max} = \cos\varphi\ \cos\delta + \sin\varphi\ \sin\delta = \cos(\varphi - \delta), \tag{C.1}$$

whence

$$h_{\max} = \frac{\pi}{2} - \varphi + \delta. \tag{C.2}$$

We now need to express the time dependence of the declination of the Sun. Using figure A1, one can show (see equation (D.5) below) that $\sin\delta_\odot = \sin\varepsilon\,\sin\lambda_\odot$, which can be simplified to $\delta_\odot \simeq \varepsilon\,\sin\lambda_\odot$ to a very good approximation (even though $\varepsilon \simeq 23^\circ$, the maximal error due to this approximation is smaller than 0.3°, i.e. negligible as compared with our experimental uncertainties). Making further simplification that the solar ecliptic longitude $\lambda_\odot$ increases linearly in time (i.e. assuming here that the eccentricity of the Earth's orbit is $e = 0$), we have $\lambda_\odot = 2\pi\,(t - t_0)/T$, with t_0 being the date of the spring equinox. Combining this simple sinusoidal approximation for $\delta_\odot(t)$ and equation (C.2) finally yields equation (2) of the main text.

Appendix D. A simple model for the equation of time

Following e.g. [1], a good approximation of the theoretical expression of the equation of time can be obtained in the following way. If the eccentricity of the Earth's orbit were $e = 0$, and if the obliquity of the Earth were $\varepsilon = 0$, one would have $E = 0$. We can thus expect that by calculating separately the small contributions E_1 and E_2 of both the obliquity and of the eccentricity, and adding them, a good approximation of E is obtained: one basically expands E to the lowest orders in e and ε.

We first calculate the contribution E_1 to E arising from the nonzero value of the obliquity. Here, we can neglect the ellipticity of the Earth's orbit, and assume that the motion of the Sun around the Earth takes place on a circle, and thus, using Kepler's second law, at a constant angular velocity. The longitude $\lambda_\odot$ of the Sun along the ecliptic (see figure A1(d)) thus increases linearly in time as

$$\lambda_\odot = \frac{2\pi}{T}(t - t_0), \tag{D.1}$$

where T is the length of a year and t_0 is the date of the vernal (i.e. spring) equinox. However the mean Sun is a fictitious body that moves at constant angular velocity along the *celestial equator*, not the ecliptic. The difference between $\lambda_\odot$ and $\alpha_\odot$, once converted to time via the correspondence $1^\circ \leftrightarrow 4$ min, thus gives the obliquity contribution to the equation of time:

$$E_1 = (4\ \text{min}/^\circ) \times (\lambda_\odot - \alpha_\odot) \tag{D.2}$$

(for readability, from now on I shall drop the subscript $\odot$). We thus have to express α as a function of λ, and then use (D.1) to obtain $E_1(t)$. To find the relation between α and λ, we introduce the *equatorial* frame with the origin at the centre of the celestial sphere, the z-axis pointing towards the celestial pole, and the x-axis towards the vernal point V, and another, *ecliptic* frame obtained from the former by a rotation of the angle ε around Ox (see figure A1(d)). The coordinates of the Sun in the equatorial frame are $(\cos\delta\cos\alpha, \cos\delta\sin\alpha, \sin\delta)$, and in the ecliptic frame $(\cos\lambda, \sin\lambda, 0)$. Since the rotation matrix from the equatorial to the ecliptic frame reads

$$\begin{pmatrix} 1 & 0 & 0 \\ 0 & \cos\varepsilon & \sin\varepsilon \\ 0 & -\sin\varepsilon & \cos\varepsilon \end{pmatrix}, \tag{D.3}$$

one can relate (α, δ) to λ, and we obtain

$$\tan\alpha = \tan\lambda\cos\varepsilon, \tag{D.4}$$

$$\sin\delta = \sin\varepsilon\sin\lambda. \tag{D.5}$$

Therefore, using (D.4)

$$\lambda - \alpha = \lambda - \arctan(\cos\varepsilon\tan\lambda). \tag{D.6}$$

From this expression it may not be obvious to see the time dependence (in particular the periodicity) of E_1. We can obtain a better understanding (and a convenient expression) by noting that $\cos\varepsilon$ is actually close to 1 (for $\varepsilon = 23.44^\circ$, we have $\cos\varepsilon \simeq 0.9174$). If one Taylor expands $f(x, A) = x - \arctan(A\tan x)$ around $A = 1$, one obtains $f(x, A) \simeq (1-A)\sin(2x)/2$, and thus, putting everything together, we obtain our final expression for E_1:

$$E_1(t) \simeq \frac{d}{2\pi}\frac{1-\cos\varepsilon}{2}\sin\left(\frac{4\pi}{T}(t - t_0)\right). \tag{D.7}$$

where d is the duration of a day. The dotted line in figure 4(b) shows $E_1(t)$.

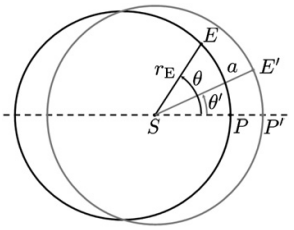

Figure D1. Circular (grey) and elliptical (black) orbits around the Sun S with the same semi-major axis a. The ellipticity of the ellipse is $e = 0.3$ for clarity.

We now turn to the calculation of E_2, the contribution of the eccentricity of the Earth's orbit: since its orbit is elliptic, the Earth does not move at constant angular velocity along its orbit, and the difference in the angular position between the Earth and a fictitious body moving at a constant speed with the same period gives the contribution E_2 to the equation of time. Figure D1 shows the trajectory of the Earth E (black ellipse with the Sun S at one focus) and of the fictitious Earth E' having a circular orbit centred on S, with the same orbital period as E. From Kepler's third law $T^2/a^3 = 4\pi^2/(GM_{\rm Sun})$, the radius r of the circular orbit is thus equal to the semi-major axis a of the elliptical orbit of E. Using the perihelia P, P' as the origins of angles, the polar angles defining the positions of P and P' are θ and θ', respectively. We are interested in finding the difference in angular positions $\vartheta \equiv \theta' - \theta$, as a function of θ, and then as a function of time. We will perform the calculation by keeping only first-order terms in the eccentricity e.

The equation of the elliptical orbit of E reads [6]

$$r_{\rm E} = \frac{a(1-e^2)}{1+e\cos\theta}. \tag{D.8}$$

Moreover, Kepler's second law about the areal velocity implies that

$$\frac{1}{2}a^2\dot{\theta}' = \frac{\pi a^2}{T} \tag{D.9}$$

for the circular orbit and

$$\frac{1}{2}r_{\rm E}^2\dot{\theta}' = \frac{S_{\rm ellipse}}{T} = \frac{\pi a^2\sqrt{1-e^2}}{T} \tag{D.10}$$

for the elliptical orbit, where we have used $S_{\rm ellipse} = \pi ab$ with $b = a\sqrt{1-e^2}$ being the semi-minor axis.

Thus we obtain

$$\frac{\dot{\theta}'}{\dot{\theta}} = \frac{r_{\rm E}^2}{a^2}\frac{1}{\sqrt{1-e^2}} = \frac{(1-e^2)^{3/2}}{(1+e\cos\theta)^2} \simeq 1 - 2e\cos\theta, \tag{D.11}$$

where the last approximation is valid to first order in e. Now, we have

$$\frac{{\rm d}\vartheta}{{\rm d}\theta} = \frac{{\rm d}\theta'}{{\rm d}\theta} - 1 = \frac{\dot{\theta}'}{\dot{\theta}} - 1 \simeq -2e\cos\theta \tag{D.12}$$

and therefore

$$\vartheta = -2e\sin\theta. \tag{D.13}$$

Since we are keeping only the first-order terms in e, we can replace θ by $\theta' = 2\pi\,(t - t_1)/T$ in the above equation, where t_1 is the time of perihelion passage. We finally obtain the following expression for E_2:

$$E_2(t) \simeq -\frac{\mathrm{d}e}{\pi} \sin\left(\frac{2\pi}{T}\,(t - t_1)\right). \tag{D.14}$$

The dashed line in figure 4(b) shows $E_2(t)$. Combining (D.7) and (D.14), we find expression (4) given in the text (solid line in figure 4(b)).

References

[1] Rees W G 1991 *Eur. J. Phys.* **12** 96
[2] Gutzwiller M C 1998 *Rev. Mod. Phys.* **70** 589
[3] Krisciunas K 2010 *Am. J. Phys.* **78** 834
[4] Tatum J B 2012 *Celestial Mechanics (Lecture Notes)* http://orca.phys.uvic.ca/~tatum
[5] See e.g. Woolard E W and Clemence G M 1966 *Spherical Astronomy* (New York: Academic)
[6] Goldstein H 1950 *Classical Mechanics* (Reading, MA: Addison Wesley)

Bibliography

[1] K. Aikawa, A. Frisch, M. Mark, S. Baier, R. Grimm, and F. Ferlaino. Reaching Fermi degeneracy via universal dipolar scattering. *Phys. Rev. Lett.*, 112:010404, 2014.

[2] K. Aikawa, A. Frisch, M. Mark, S. Baier, A. Rietzler, R. Grimm, and F. Ferlaino. Bose–Einstein condensation of Erbium. *Phys. Rev. Lett.*, 108:210401, 2012.

[3] B. P. Anderson and M. A. Kasevitch. Macroscopic quantum interference from atomic tunnel array. *Science*, 282:1686, 1998.

[4] W. R. Anderson, J. R. Veale, and T. F. Gallagher. Resonant dipole-dipole energy transfer in a nearly frozen Rydberg gas. *Phys. Rev. Lett.*, 80:249, 1998.

[5] J. B. Balewski, A. T. Krupp, A. Gaj, S. Hofferberth, R. Löw, and T. Pfau. Rydberg dressing: understanding of collective many-body effects and implications for experiments. *New J. Phys.*, 16:063012, 2014.

[6] D. Barredo, H. Labuhn, S. Ravets, T. Lahaye, A. Browaeys, and C. S. Adams. Coherent excitation transfer in a "spin chain" of three Rydberg atoms. *arXiv:1408.1055*, 2014.

[7] D. Barredo, S. Ravets, H. Labuhn, L. Béguin, A. Vernier, F. Nogrette, T. Lahaye, and A. Browaeys. Demonstration of a strong Rydberg blockade in three-atom systems with anisotropic interactions. *Phys. Rev. Lett.*, 112:183002, 2014.

[8] L. Béguin. *Measurement of the van der Waals interaction between two Rydberg atoms*. PhD thesis, University Paris 11, 2013.

[9] L. Béguin, A. Vernier, R. Chicireanu, T. Lahaye, and A. Browaeys. Direct measurement of the van der Waals interaction between two Rydberg atoms. *Phys. Rev. Lett.*, 110:263201, 2013.

[10] S. Bettelli, D. Maxwell, T. Fernholz, C. S. Adams, I. Lesanovsky, and C. Ates. Exciton dynamics in emergent Rydberg lattices. *Phys. Rev. A*, 88:043436, 2013.

[11] J. Beugnon, C. Tuchendler, H. Marion, A. Gaëtan, Y. Miroshnychenko, Y. R. P. Sortais, A. M. Lance, M. P. A. Jones, G. Messin, A. Browaeys, and P. Grangier.

Two-dimensional transport and transfer of a single atomic qubit in optical tweezers. *Nature Phys.*, 3:696, 2007.

[12] J. Billy. Private communication, 2013.

[13] J. Billy, E. A. L. Henn, S. Müller, T. Maier, H. Kadau, A. Griesmaier, M. Jona-Lasinio, L. Santos, and T. Pfau. Deconfinement-induced collapse of a coherent array of dipolar Bose–Einstein condensates. *Phys. Rev. A*, 86:051603, 2012.

[14] G. Bismut, B. Laburthe-Tolra, E. Maréchal, P. Pedri, O. Gorceix, and L. Vernac. Anisotropic excitation spectrum of a dipolar quantum Bose gas. *Phys. Rev. Lett.*, 109:155302, 2012.

[15] G. Bismut, B. Pasquiou, E. Maréchal, P. Pedri, L. Vernac, O. Gorceix, and B. Laburthe-Tolra. Collective excitations of a dipolar Bose–Einstein condensate. *Phys. Rev. Lett.*, 105:040404, 2010.

[16] I. Bloch, J. Dalibard, and W. Zwerger. Many-body physics with ultracold gases. *Rev. Mod. Phys.*, 80:885, 2008.

[17] I. Bloch, T. W. Hänsch, and T. Esslinger. Atom laser with a CW output coupler. *Phys. Rev. Lett.*, 82:3008, 1999.

[18] J. L. Bohn, R. M. Wilson, and S. Ronen. How does a dipolar Bose–Einstein condensate collapse? *Las. Phys.*, 19:547, 2009.

[19] C. C. Bradley, C. A. Sackett, and R. G. Hulet. Bose–Einstein condensation of lithium: Observation of limited condensate number. *Phys. Rev. Lett.*, 78:985, 1997.

[20] Y. Castin and R. Dum. Bose–Einstein condensates in time-dependent traps. *Phys. Rev. Lett.*, 77:5315, 1996.

[21] P. Cheiney. *Matter wave scattering on complex potentials.* PhD thesis, University Paul Sabatier, Toulouse, 2013.

[22] P. Cheiney, O. Carraz, D. Bartoszek-Bober, S. Faure, F. Vermersch, C. M. Fabre, G. L. Gattobigio, T. Lahaye, D. Guéry-Odelin, and R. Mathevet. A Zeeman slower design with permanent magnets in a Halbach configuration. *Rev. Sci. Instr.*, 82:063115, 2011.

[23] P. Cheiney, F. Damon, G. Condon, B. Georgeot, and D. Guéry-Odelin. Realization of tunnel barriers for matter waves using spatial gaps. *EPL*, 103:50006, 2013.

[24] P. Cheiney, C. M. Fabre, F. Vermersch, G. L. Gattobigio, R. Mathevet, T. Lahaye, and D. Guéry-Odelin. Matter-wave scattering on an amplitude-modulated optical lattice. *Phys. Rev. A*, 87:013623, 2013.

[25] R. M. Clegg. The history of FRET. *Reviews in Fluorescence*, 2006:1, 2006.

[26] D. Comparat and P. Pillet. Dipole blockade in a cold rydberg atomic sample. *J. Opt. Soc. Am. B*, 27:A208, 2010.

[27] A. Couvert. *Production et étude de lasers à atomes guidés, et de leur interaction avec des défauts contrôlés.* PhD thesis, University Paris 6, 2010.

[28] A. Couvert, M. Jeppesen, T. Kawalec, G. Reinaudi, R. Mathevet, and D. Guéry-Odelin. A quasi-monomode guided atom laser from an all-optical Bose–Einstein condensate. *EPL*, 83:50001, 2008.

[29] A. de Paz, A. Sharma, A. Chotia, E. Maréchal, J. H. Huckans, P. Pedri, L. Santos, O. Gorceix, L. Vernac, and B. Laburthe-Tolra. Nonequilibrium quantum magnetism in a dipolar lattice gas. *Phys. Rev. Lett.*, 111:185305, 2013.

[30] E. A. Donley, N. R. Claussen, S. L. Cornish, J. L. Roberts, E. A. Cornell, and C. E. Wieman. Dynamics of collapsing and exploding Bose–Einstein condensates. *Nature*, 412:295, 2001.

[31] M. Ebert, A. Gill, M. Gibbons, X. Zhang, M. Saffman, and T. G. Walker. Atomic Fock state preparation using Rydberg blockade. *Phys. Rev. Lett.*, 112:043602, 2014.

[32] C. Fabre. *Etude théorique et expérimentale de l'interaction d'un atome très excité avec le rayonnement. Application à la spectroscopie des états de Rydberg du sodium.* PhD thesis, Université Pierre et Marie Curie - Paris VI, 1980.

[33] C. M. Fabre. *Miroirs de Bragg pour ondes de matière et apport de la supersymétrie aux potentiels exponentiels.* PhD thesis, University Paul Sabatier, Toulouse, 2012.

[34] C. M. Fabre, P. Cheiney, G. L. Gattobigio, F. Vermersch, S. Faure, R. Mathevet, T. Lahaye, and D. Guéry-Odelin. Realization of a distributed Bragg reflector for propagating guided matter waves. *Phys. Rev. Lett.*, 107:230401, 2011.

[35] M. Fattori, C. D'Errico, G. Roati, M. Zaccanti, M. Jona-Lasinio, M. Modugno, M. Inguscio, and G. Modugno. Atom interferometry with a weakly interacting Bose–Einstein condensate. *Phys. Rev. Lett.*, 100:080405, 2008.

[36] T. Förster. Zwischenmolekulare Energiewanderung und Fluoreszenz. *Ann. Phys.*, 437:55, 1948.

[37] B. Fröhlich. Strong dipolar effects in a chromium Bose–Einstein condensate. Diplomarbeit, Universität Stuttgart, 2007.

[38] A. Gaetan, Y. Miroshnychenko, T. Wilk, A. Chotia, M. Viteau, D. Comparat, P. Pillet, A. Browaeys, and P. Grangier. Observation of collective excitation of two individual atoms in the Rydberg blockade regime. *Nat. Phys.*, 5:115, 2009.

[39] M. Georgescu, I. S. Ashhab, and F. Nori. Quantum simulation. *Rev. Mod. Phys.*, 86:153, 2014.

[40] R.W. Gerchberg and W. O. Saxton. A practical algorithm for the determination of phase from image and diffraction plane pictures. *Optik*, 35:237, 1972.

[41] J. M. Gerton, D. Strekalov, I. Prodan, and R. G. Hulet. Direct observation of growth and collapse of a Bose–Einstein condensate with attractive interactions. *Nature*, 408:692, 2000.

[42] V. Giovannetti, S. Lloyd, and L. Maccone. Advances in quantum metrology. *Nature Phot.*, 5:222, 2011.

[43] K. Góral, K. Rzazewski, and T. Pfau. Bose–Einstein condensation with magnetic dipole-dipole forces. *Phys. Rev. A*, 61:051601, 2000.

[44] K. Góral, L. Santos, and M. Lewenstein. Quantum phases of dipolar bosons in optical lattices. *Phys. Rev. Lett.*, 88:170406, 2002.

[45] A. Griesmaier, J. Werner, S. Hensler, J. Stuhler, and T. Pfau. Bose–Einstein condensation of Chromium. *Phys. Rev. Lett.*, 94:160401, 2005.

[46] T. Grünzweig, A. Hilliard, M. McGovern, and M. F. Andersen. Near-deterministic preparation of a single atom in an optical microtrap. *Nature Phys.*, 6:951, 2010.

[47] W. Guerin, J.-F. Riou, J. P. Gaebler, V. Josse, P. Bouyer, and A. Aspect. Guided quasicontinuous atom laser. *Phys. Rev. Lett.*, 97:200402, 2006.

[48] G. Günter, H. Schempp, M. Robert-de Saint-Vincent, V. Gavryusev, S. Helmrich, C.S. Hofmann, S. Whitlock, and M. Weidemll̈er. Observing the dynamics of dipole-mediated energy transport by interaction-enhanced imaging. *Science*, 342:954, 2013.

[49] E. W. Hagley, L. Deng, M. Kozuma, J. Wen, K. Helmerson, S. L. Rolston, and W. D. Phillips. A well-collimated quasi-continuous atom laser. *Science*, 283:1706, 1999.

[50] K. Halbach. Design of permanent multipole magnets with oriented rare earth cobalt material. *Nucl. Instr. Meth.*, 169(1), 1980.

[51] S. Haroche. Nobel lecture: Controlling photons in a box and exploring the quantum to classical boundary. *Rev. Mod. Phys.*, 85:1083, 2013.

[52] S. Haroche and J.-M. Raimond. *Exploring the Quantum — Atoms, Cavities, and Photons*. Oxford University Press, 2006.

[53] P. Hauke, F. M. Cucchietti, A. Müller-Hermes, M.-C. Bañuls, J. I. Cirac, and M. Lewenstein. Complete devil's staircase and crystal-superfluid transitions in a dipolar XXZ spin chain: a trapped ion quantum simulation. *New Journal of Physics*, 12:113037, 2010.

[54] K. R. A. Hazzard, M. van den Worm, M. Foss-Feig, S. R. Manmana, E. G. Dalla Torre, T. Pfau, M. Kastner, and A. M. Rey. Quantum correlations and entanglement in far-from-equilibrium spin systems. *Phys. Rev. A*, 90:063622, 2014.

[55] R. Heidemann, U. Raitzsch, V. Bendkowsky, B. Butscher, R. Löw, L. Santos, and T. Pfau. Evidence for coherent collective Rydberg excitation in the strong blockade regime. *Phys. Rev. Lett.*, 99:163601, 2007.

[56] L. Isenhower, E. Urban, X. L. Zhang, A. T. Gill, T. Henage, T. A. Johnson, T. G. Walker, and M. Saffman. Demonstration of a neutral atom controlled-not quantum gate. *Phys. Rev. Lett.*, 104:010503, 2010.

[57] R. Islam, C. Senko, W. C. Campbell, S. Korenblit, J. Smith, A. Lee, E. E. Edwards, C.-C. J. Wang, J. K. Freericks, and C. Monroe. Emergence and frustration of magnetism with variable-range interactions in a quantum simulator. *Science*, 340:583, 2013.

[58] D. Jaksch, J. I. Cirac, P. Zoller, S. L. Rolston, R. Côté, and M. D. Lukin. Fast quantum gates for neutral atoms. *Phys. Rev. Lett.*, 85:2208, 2000.

[59] D. Jin and J. Ye. Polar molecules in the quantum regime. *Physics Today*, 64:27, 2011.

[60] A. M. Kaufman, B. J. Lester, and C. A. Regal. Cooling a single atom in an optical tweezer to its quantum ground state. *Phys. Rev. X*, 2:041014, 2012.

[61] T. Koch. *Enhancing the dipolar character of a Bose-Einstein condensate: From perturbative effects to a purely dipolar quantum gas.* PhD thesis, Universität Stuttgart, 2008.

[62] T. Koch, T. Lahaye, J. Metz, B. Fröhlich, A. Griesmaier, and T. Pfau. Stabilization of a purely dipolar quantum gas against collapse. *Nat. Phys.*, 4:218, 2008.

[63] D. L. Kovrizhin, G. V. Pai, and S. Sinha. Density wave and supersolid phases of correlated bosons in an optical lattice. *Europhys. Lett.*, 72:162, 2005.

[64] H. Kreutzmann, U. V. Poulsen, M. Lewenstein, R. Dumke, W. Ertmer, G. Birkl, and A. Sanpera. Coherence properties of guided-atom interferometers. *Phys. Rev. Lett.*, 92:163201, 2004.

[65] H. Labuhn and *et al.* Collective excitation of a mesoscopic number of atoms in the Rydberg blockade regime, 2015. In preparation.

[66] H. Labuhn, S. Ravets, D. Barredo, L. Béguin, F. Nogrette, T. Lahaye, and A. Browaeys. Single-atom addressing in microtraps for quantum-state engineering using Rydberg atoms. *Phys. Rev. A*, 90:023415, 2014.

[67] T. Lahaye. Measuring the eccentricity of the Earth's orbit with a nail and a piece of plywood. *Eur. J. Phys.*, 33:1167, 2012.

[68] T. Lahaye and A. Browaeys. Interacting cold Rydberg atoms: a toy many-body system. *Séminaire Poincaré*, 17:125, 2013.

[69] T. Lahaye, T. Koch, B. Fröhlich, M. Fattori, J. Metz, A. Griesmaier, S. Giovanazzi, and T. Pfau. Strong dipolar effects in a quantum ferrofluid. *Nature*, 448:672, 2007.

[70] T. Lahaye, P. Labastie, and R. Mathevet. Fizeau's "aether-drag" experiment in the undergraduate laboratory. *Am. J. Phys.*, 80:497, 2012.

[71] T. Lahaye, J. Metz, B. Fröhlich, T. Koch, M. Meister, a. Griesmaier, T. Pfau, H. Saito, Y. Kawaguchi, and M. Ueda. d-wave collapse and explosion of a dipolar Bose–Einstein condensate. *Phys. Rev. Lett.*, 101:080401, 2008.

[72] T. Lahaye, T. Pfau, and L. Santos. Mesoscopic ensembles of polar bosons in triple-well potentials. *Phys. Rev. Lett.*, 104:170404, 2010.

[73] T. Lahaye, J. Vogels, K. Günter, Z. Wang, J. Dalibard, and D. Guéry-Odelin. Realization of a magnetically guided atomic beam in the collisional regime. *Phys. Rev. Lett.*, 93:093003, 2004.

[74] T. Lahaye, Z. Wang, G. Reinaudi, S. Rath, J. Dalibard, and D. Guéry-Odelin. Evaporative cooling of a guided rubidium atomic beam. *Phys. Rev. A*, 72(3):033411, 2005.

[75] M. Lu, N. Q. Burdick, and B. L. Lev. Quantum degenerate dipolar Fermi gas. *Phys. Rev. Lett.*, 108:215301, 2012.

[76] M. Lu, N. Q. Burdick, S. H. Youn, and B. L. Lev. Strongly dipolar Bose–Einstein condensate of Dysprosium. *Phys. Rev. Lett.*, 107:190401, 2011.

[77] M. D. Lukin, M. Fleischhauer, R. Cote, L. M. Duan, D. Jaksch, J. I. Cirac, and P. Zoller. Dipole blockade and quantum information processing in mesoscopic atomic ensembles. *Phys. Rev. Lett.*, 87:037901, 2001.

[78] P. Martin, B. Oldaker, A. Miklich, and D. Pritchard. Bragg scattering of atoms from a standing light wave. *Phys. Rev. Lett.*, 60:515, 1988.

[79] C. Menotti, C. Trefzger, and M. Lewenstein. Metastable states of a gas of dipolar bosons in a 2D optical lattice. *Phys. Rev. Lett.*, 98:235301, 2007.

[80] J. Metz, T. Lahaye, B. Fröhlich, A. Griesmaier, T. Pfau, H. Saito, Y. Kawaguchi, and M. Ueda. Coherent collapses of dipolar Bose–einstein condensates for different trap geometries. *New J. Phys.*, 11:055032, 2009.

[81] M.-O. Mewes, M. R. Andrews, D. M. Kurn, D. S. Durfee, C. G. Townsend, and W. Ketterle. Output coupler for Bose–Einstein condensed atoms. *Phys. Rev. Lett.*, 78:582, 1997.

[82] Y. Miroshnychenko, W. Alt, I. Dotsenko, L. Förster, M. Khudaverdyan, D. Meschede, D. Schrader, and A. Rauschenbeutel. Quantum engineering: An atom-sorting machine. *Nature*, 442:151, 2006.

[83] D. Møller, L. B. Madsen, and K. Mølmer. Quantum gates and multiparticle entanglement by Rydberg excitation blockade and adiabatic passage. *Phys. Rev. Lett.*, 100:170504, 2008.

[84] O. Morsch and M. Oberthaler. Dynamics of Bose–Einstein condensates in optical lattices. *Rev. Mod. Phys.*, 78:179, 2006.

[85] I. Mourachko, D. Comparat, F. de Tomasi, A. Fioretti, P. Nosbaum, V. M. Akulin, and P. Pillet. Many-body effects in a frozen Rydberg gas. *Phys. Rev. Lett.*, 80:253, 1998.

[86] M. Mudrich, N. Zahzam, T. Vogt, D. Comparat, and P. Pillet. Back and forth transfer and coherent coupling in a cold Rydberg dipole gas. *Phys. Rev. Lett.*, 95:233002, 2005.

[87] M. Müller, I. Lesanovsky, H. Weimer, H. P. Büchler, and P. Zoller. Mesoscopic Rydberg gate based on electromagnetically induced transparency. *Phys. Rev. Lett.*, 102:170502, 2009.

[88] S. Müller, J. Billy, E. A. L. Henn, H. Kadau, A. Griesmaier, M. Jona-Lasinio, L. Santos, and T. Pfau. Stability of a dipolar Bose–Einstein condensate in a one-dimensional lattice. *Phys. Rev. A*, 84:053601, 2011.

[89] M. A. Nielsen and I. L. Chuang. *Quantum Computation and Quantum Information.* Cambridge University Press, 2000.

[90] J. Nipper, J. B. Balewski, A. T. Krupp, B. Butscher, R. Löw, and T. Pfau. Highly resolved measurements of Stark-tuned Förster resonances between Rydberg atoms. *Phys. Rev. Lett.*, 108:113001, 2012.

[91] J. Nipper, J. B. Balewski, A. T. Krupp, S. Hofferberth, R. Löw, and T. Pfau. Atomic pair-state interferometer: Controlling and measuring an interaction-induced phase shift in Rydberg-atom pairs. *Phys. Rev. X*, 2:031011, 2012.

[92] F. Nogrette, H. Labuhn, S. Ravets, D. Barredo, L. Béguin, A. Vernier, T. Lahaye, and A. Browaeys. Single-atom trapping in holographic 2d arrays of microtraps with arbitrary geometries. *Phys. Rev. X*, 4:021034, 2014.

[93] D. H. J. O'Dell, S. Giovanazzi, and C. Eberlein. Exact hydrodynamics of a trapped dipolar Bose–Einstein condensate. *Phys. Rev. Lett.*, 92:250401, 2004.

[94] Y. B. Ovchinnikov. A permanent Zeeman slower for Sr atomic clock. *Eur. Phys. J. Special Topics*, 163:95, 2008.

[95] A. Perrin. Private communication, 2012.

[96] D. Peter, S. Müller, S. Wessel, and H. P. Büchler. Anomalous behavior of spin systems with dipolar interactions. *Phys. Rev. Lett.*, 109:025303, 2012.

[97] D. Peter, K. Pawlowski, T. Pfau, and K. Rzazewski. Mean-field description of dipolar bosons in triple-well potentials. *J. Phys. B*, 45:225302, 2012.

[98] D. Peter, N. Y. Yao, N. Lang, S. D. Huber, M. D. Lukin, and H.-P. Büchler. Topological flat bands with Chern number $C = 2$ by dipolar exchange interactions. *arXiv:1410.5667*, 2014.

[99] W. D. Phillips and H. Metcalf. Laser deceleration of an atomic beam. *Phys. Rev. Lett.*, 48:596, 1982.

[100] L. P. Pitaevskii and S. Stringari. *Bose-Einstein condensation.* Clarendon Press, Oxford, 2003.

[101] S. E. Pollack, D. Dries, M. Junker, Y. P. Chen, T. A. Corcovilos, and R. G. Hulet. Extreme tunability of interactions in a ^{7}Li Bose–Einstein condensate. *Phys. Rev. Lett.*, 102:090402, 2009.

[102] G. Pupillo, A. Micheli, M. Boninsegni, I. Lesanovsky, and P. Zoller. Strongly correlated gases of Rydberg-dressed atoms: Quantum and classical dynamics. *Phys. Rev. Lett.*, 104:223002, 2010.

[103] S. Ravets. *Development of tools for quantum engineering using individual atoms: optical nanofibers and controlled Rydberg interactions.* PhD thesis, University Paris 11, 2014.

[104] S. Ravets and *et al.* Measurement of the angular dependence of the dipolar interaction between two Rybderg atoms at a Förster resonance, 2015. In preparation.

[105] S. Ravets, H. Labuhn, D. Barredo, L. Béguin, T. Lahaye, and A. Browaeys. Coherent dipole-dipole coupling between two single Rydberg atoms at an electrically-tuned Förster resonance. *Nature Phys.*, 10:914, 2014.

[106] A. Reinhard, K. C. Younge, and G. Raithel. Effect of Förster resonances on the excitation statistics of many-body Rydberg systems. *Phys. Rev. A*, 78:060702, 2008.

[107] I. I. Ryabtsev, D. B. Tretyakov, I. I. Beterov, and V. M. Entin. Observation of the Stark-tuned Förster resonance between two Rydberg atoms. *Phys. Rev. Lett.*, 104:073003, 2010.

[108] C. Ryu and M. G. Boshier. Integrated coherent matter wave circuits. arXiv:1410.8814, 2014.

[109] S. Sachdev. *Quantum phase transitions.* Cambridge University Press, 1999.

[110] C. A. Sackett, J. M. Gerton, M. Welling, and R. G. Hulet. Measurements of collective collapse in a Bose–Einstein condensate with attractive interactions. *Phys. Rev. Lett.*, 82:876, 1999.

[111] M. Saffman, T. G. Walker, and K. Mølmer. Quantum information with Rydberg atoms. *Rev. Mod. Phys.*, 82:2313, 2010.

[112] K. A. Safinya, J. F. Delpech, F. Gounand, W. Sandner, and T. F. Gallagher. Resonant Rydberg-atom-Rydberg-atom collisions. *Phys. Rev. Lett.*, 47:405, 1981.

[113] L. Santos, G. V. Shlyapnikov, and M. Lewenstein. Roton-maxon spectrum and stability of trapped dipolar Bose–Einstein condensates. *Phys. Rev. Lett.*, 90:250403, 2003.

[114] L. Santos, G. V. Shlyapnikov, P. Zoller, and M. Lewenstein. Bose–Einstein condensation in trapped dipolar gases. *Phys. Rev. Lett.*, 85:1791, 2000.

[115] P. Schauß, M. Cheneau, M. Endres, T. Fukuhara, S. Hild, A. Omran, T. Pohl, C. Gross, S. Kuhr, and I. Bloch. Observation of spatially ordered structures in a two-dimensional Rydberg gas. *Nature*, 491:87, 2012.

[116] P. Schauß, J. Zeiher, T. Fukuhara, S. Hild, M. Cheneau, T. Macrì, T. Pohl, I. Bloch, and C. Gross. Dynamical crystallization in a low-dimensional Rydberg gas. *arXiv:1404.0980*, 2014.

[117] M. Schlosser, J. Kruse, C. Gierl, S. Teichmann, S. Tichelmann, and G. Birkl. Fast transport, atom sample splitting and single-atom qubit supply in two-dimensional arrays of optical microtraps. *New J. Phys.*, 14:123034, 2012.

[118] N. Schlosser, G. Reymond, I. Protsenko, and P. Grangier. Sub-poissonian loading of single atoms in a microscopic dipole trap. *Nature*, 411:1024, 2001.

[119] C. Shen and L.-M. Duan. Correcting detection errors in quantum state engineering through data processing. *New J. Phys.*, 14:053053, 2012.

[120] K. Singer, M. Reetz-Lamour, T. Amthor, L. G. Marcassa, and M. Weidemüller. Suppression of excitation and spectral broadening induced by interactions in a cold gas of Rydberg atoms. *Phys. Rev. Lett.*, 93:163001, 2004.

[121] Y. R. P. Sortais, H. Marion, C. Tuchendler, A. M. Lance, M. Lamare, P. Fournet, C. Armellin, R. Mercier, G. Messin, A. Browaeys, and P. Grangier. Diffraction-limited optics for single-atom manipulation. *Phys. Rev. A*, 75:013406, 2007.

[122] J. Stuhler, A. Griesmaier, T. Koch, M. Fattori, T. Pfau, S. Giovanazzi, P. Pedri, and L. Santos. Observation of dipole-dipole interaction in a degenerate quantum gas. *Phys. Rev. Lett.*, 95:150406, 2005.

[123] J. D. Thompson, T. G. Tiecke, A. S. Zibrov, V. Vuletić, and M. D. Lukin. Coherence and Raman sideband cooling of a single atom in an optical tweezer. *Phys. Rev. Lett.*, 110:133001, 2013.

[124] D. Tong, S. M. Farooqi, J. Stanojevic, S. Krishnan, Y. P. Zhang, R. Côté, E. E. Eyler, and P. L. Gould. Local blockade of Rydberg excitation in an ultracold gas. *Phys. Rev. Lett.*, 93:063001, 2004.

[125] E. Urban, T. A. Johnson, T. Henage, L. Isenhower, D. D. Yavuz, T. G. Walker, and M. Saffman. Observation of Rydberg blockade between two atoms. *Nat. Phys.*, 5:110, 2009.

[126] C. S. E. van Ditzhuijzen, A. F. Koenderink, J. V. Hernández, F. Robicheaux, L. D. Noordam, and H. B. van Linden van den Heuvell. Spatially resolved observation of dipole-dipole interaction between Rydberg atoms. *Phys. Rev. Lett.*, 100:243201, 2008.

[127] F. Vermersch. *Etudes numériques sur la production, la diffusion et la manipulation d'ondes de matière*. PhD thesis, University Paul Sabatier, Toulouse, 2013.

[128] T. Vogt, M. Viteau, A. Chotia, J. Zhao, D. Comparat, and P. Pillet. Electric-field induced dipole blockade with Rydberg atoms. *Phys. Rev. Lett.*, 99:073002, 2007.

[129] H. Weimer, M. Müller, I. Lesanovsky, P. Zoller, and H.-P. Büchler. A Rydberg quantum simulator. *Nat. Physics*, 6:382, 2010.

[130] J. Werner, A. Griesmaier, S. Hensler, J. Stuhler, T. Pfau, A. Simoni, and E. Tiesinga. Observation of Feshbach resonances in an ultracold gas of ^{52}Cr. *Phys. Rev. Lett.*, 94:183201, 2005.

[131] T. Wilk, A. Gaëtan, C. Evellin, J. Wolters, Y. Miroshnychenko, P. Grangier, and A. Browaeys. Entanglement of two individual neutral atoms using Rydberg blockade. *Phys. Rev. Lett.*, 104:010502, 2010.

[132] D. J. Wineland. Nobel lecture: Superposition, entanglement, and raising Schrödinger's cat. *Rev. Mod. Phys.*, 85:1103–1114, 2013.

[133] H. Winter and H. W. Ortjohann. Simple demonstration of storing macroscopic particles in a Paul trap. *Am. J. Phys.*, 59:807, 1991.

[134] B. Yan, S. A. Moses, B. Gadway, J. P. Covey, K. R. A. Hazzard, A. M. Rey, D. S. Jin, and J. Ye. Observation of dipolar spin-exchange interactions with lattice-confined polar molecules. *Nature*, 501:521, 2013.